Nanostructures for emission control in organic light-emitting layers

Christian Kluge

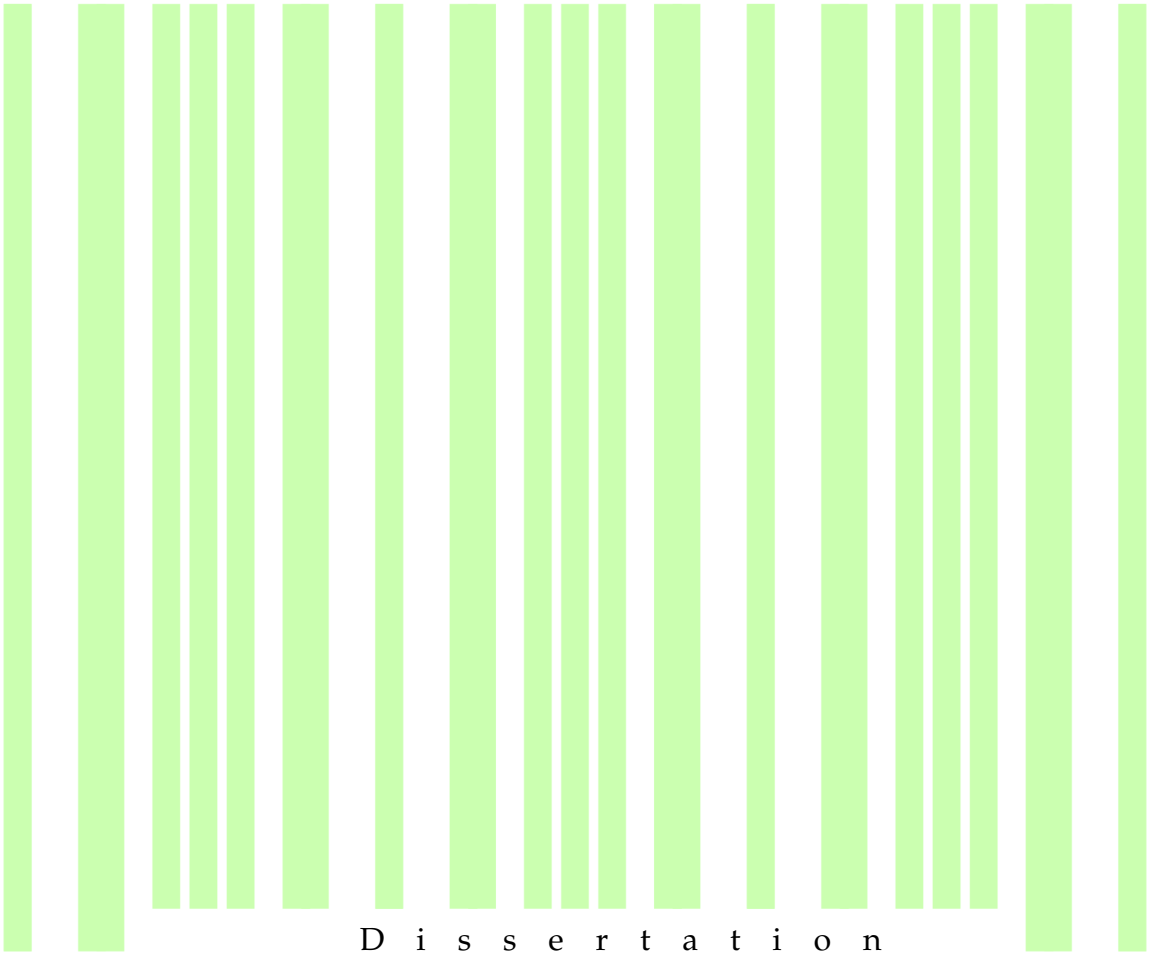

1. Gutachterin:	Prof. Martina Gerken
2. Gutachter:	Prof. Henri Benisty
3. Gutachter:	Prof. Jakob Kjelstrup-Hansen

Datum der mündlichen Prüfung: 16.05.2014

Nanostructures for emission control in organic light-emitting layers

Dissertation

zur Erlangung des akademischen Grades
Doktor der Ingenieurwissenschaften
(Dr.-Ing.)
der Technischen Fakulät
der Christian-Albrechts-Universität zu Kiel

Christian Kluge

Kiel
Januar 2014

Hiermit versichere ich, dass ich die Doktorarbeit

Nanostructures for emission control in organic light-emitting layers

selbständig und ohne unzulässige fremde Hilfe angefertigt habe und dass ich alle von anderen Autoren wörtlich übernommenen Stellen, wie auch die sich an die Gedankengänge anderer Autoren eng anlehnenden Ausführungen meiner Arbeit, besonders gekennzeichnet und die entsprechenden Quellen angegeben habe. Weiterhin wurde die Arbeit ausschließlich der Christian-Albrechts-Universität zu Kiel im Rahmen eines Prüfungsverfahrens vorgelegt, jedoch wurden Teile in Form von Beiträgen in Fachzeitschriften und Tagungsbänden veröffentlicht bzw. zur Veröffentlichung eingereicht (siehe Abschnitt zu Publikationen). Diese Arbeit ist unter Einhaltung der Regeln guter wissenschaftlicher Praxis der Deutschen Forschungsgemeinschaft entstanden.

Christian Kluge

Abstract

Organic light-emitting diodes (OLEDs) are promising light sources on their way into displays, general lighting, and optical sensing systems. However, a large portion of the generated light is trapped as guided modes in an OLED, due to its thin-film structure of high refractive index. These guided modes can be extracted with nanostructures in the thin films, but the extracted light modifies the OLED emission. Depending on the application, different emission characteristics are required and it is hence desirable to control the light outcoupling by the nanostructure's design.

This thesis investigates guided mode outcoupling with gratings, i.e. one-dimensional nanostructures, by modeling, simulations, and experiments for lighting and sensing applications.

A model is developed that gives physically insightful expressions for the intensity of guided mode scattering at a thin, binary grating. The intensity of each scattering order is shown to be proportional to the squared modulus of the corresponding grating's Fourier coefficient, the mode overlap with the grating region, the Airy factor of the cavity, the standing wave factors, and a directional term. By analysis of the TE_0-mode attenuation constant α with this model and rigorous coupled wave analysis (RCWA), it is demonstrated that the outcoupling intensity in a grating OLED-like waveguide strongly depends on the grating period and the waveguide thickness.

A drawback of guided mode outcoupling by single-period gratings is the induced color impression for the viewer as a guided mode is mainly scattered in a single wavelength-dependent direction. To overcome this limitation, this thesis introduces compound binary gratings as a novel multi-periodic nanostructure for use in OLED-like waveguides. The superposition of multiple single-period gratings yields a structure that scatters each wavelength into multiple directions. Photoluminescence measurements of an organic light-emitting layer structured by 24 different compound binary gratings show that the intensity of each scattering direction can be controlled by the duty cycle of the respective component grating.

The application of an organic emitter layer structured by a single-period grating as light source for refractive index sensing is presented. Due to the directionality introduced by Bragg scattering of guided modes, a 3.6 times higher sensitivity is achieved compared to an unstructured light source and a refractive index change of $4 \cdot 10^{-4}$ could be detected. Additionally, by using the angle- and wavelength-dependent Bragg scattering to spectrally encode the critical angle of total internal reflection, a sensitivity of 700 nm per refractive index unit is demonstrated.

In conclusion, this thesis provides a better understanding, greater design freedom and novel applications of guided mode outcoupling from OLEDs.

Zusammenfassung

Organische Leuchtdioden (OLEDs) sind vielversprechende Lichtquellen, die zur Zeit Eingang in Displaytechnik, Allgemeinbeleuchtung und optische Sensorik finden. Es besteht allerdings das Problem, dass ein großer Anteil des erzeugten Lichtes in Wellenleitermoden der OLED-Dünnschichtstruktur gefangen ist. Eine Möglichkeit, diese geführten Moden auszukoppeln ist die Nanostrukturierung der dünnen Schichten, allerdings wird hierdurch auch die Abstrahlung der OLED verändert. Da je nach Anwendung unterschiedliche Abstrahlcharakteristiken erforderlich sind, ist eine Kontrolle der Lichtauskopplung durch ein gezieltes Design der Nanostruktur wünschenswert.

Diese Arbeit untersucht daher mit Hilfe von Modellierung, Simulationen und Experimenten die Auskopplung von geführten Moden aus OLED-Wellenleitern mittels Beugungsgittern, d.h. eindimensionalen Nanostrukturen. Dabei werden Anwendungen des ausgekoppelten Lichtes für die Allgemeinbeleuchtung und Sensorik diskutiert.

Es wird ein Modell für die Intensität der Bragg-Streuung von Wellenleitermoden an dünnen, binären Gittern entwickelt. Dieses Modell beschreibt die Intensität jeder Beugungsordnung mittels der Gitter-Fourierkoeffizienten, der integralen Modenintensität im Bereich des Gitters, der Quellen-Interferenz in der Dünnschichtstruktur und eines Richtungsfaktors. Mit Hilfe dieses Modells und der RCWA-Methode wird gezeigt, dass die Wellenleiterdicke und die Gitterperiode entscheidend für die Auskopplungsstärke der TE_0-Mode in einem OLED-Wellenleiter sind.

Ein Nachteil der Modenauskopplung mittels eines einfach-periodischen Gitters ist der damit verbundene Farbeindruck, der durch die wellenlängenabhängige Richtung der Braggstreuung entsteht. Daher werden in dieser Arbeit multi-periodische Gitter für die Modenauskopplung vorgestellt, die durch die Überlagerung mehrerer einfach-periodischer Gitter gebildet werden. Es wird theoretisch und experimentell gezeigt, dass diese Gitter eine Wellenleitermode je Wellenlänge in mehrere Richtungen gleichzeitig auskoppeln. Anhand von Photolumineszenzmessungen einer organischen Emitterschicht mit 24 verschiedenen multi-periodischen Gittern wird zudem demonstriert, dass die Intensität der einzelnen Richtungen mittels der Tastverhältnisse der Gitterkomponenten gesteuert werden kann.

Des Weiteren wird eine gezielte Nutzung des ausgekoppelten Wellenleiterlichtes für einen Brechungsindexsensor gezeigt. Durch die verstärkte Abstrahlung in einen kleinen Winkelbereich bei der Auskopplung mittels eines einfach-periodischen Gitters konnte eine 3,6-fache Empfindlichkeit gegenüber einer unstrukturierten Emitterschicht erreicht werden und ein Brechungsindexunterschied von $4 \cdot 10^{-4}$ detektiert werden. Zudem wird eine

spektrale Messmethode vorgestellt, bei das ausgekoppelte Wellenleiterlicht dazu genutzt wird, eine Wellenlängenverschiebung bei einer Brechungsindexänderung zu messen. Dabei wurde eine Empfindlichkeit von 700 nm pro Brechungsindexeinheit erreicht.

Die in dieser Arbeit vorgestellten Methoden und Ergebnisse ermöglichen ein besseres Verständnis der Wellenleitermodenauskopplung aus OLEDs und zeigen Wege auf, diese Auskopplung vielfältiger zu entwerfen und einzusetzen.

Danksagung

Diese Arbeit entstand während meiner Tätigkeit als wissenschaftlicher Mitarbeiter in der Arbeitsgruppe “Integrierte Systeme und Photonik” (ISP). Ich möchte mich hiermit bei den vielen Menschen, die mich während dieser Zeit begleitet und unterstützt haben, bedanken.

Zu allererst danke ich meiner Betreuerin Prof. Dr. Martina Gerken, die mir die Möglichkeit gegeben hat, in dem spannenden Feld der Photonik zu forschen und zu promovieren. Ich bin dankbar für die vielen Diskussionen und hilfreichen Anregungen. Ich bedanke mich bei Prof. Henri Benisty des Institute d’Optique Paris und Prof. Jakob Kjelstrup-Hansen der Syddansk Universitet Sønderborg für die Begutachtung meiner Dissertation und dafür, dass sie die Anreise zu meiner Prüfung auf sich genommen haben.

Ein großes Dankeschön geht an die gesamte Arbeitsgruppe ISP für die gute Zusammenarbeit. Ganz besonders möchte ich mich bei meinen Bürokollegen Philipp Metz und Jost Adam für die gemeinsame Zeit und die hilfreichen Diskussionen bedanken, sowie bei Daniela Threm und Yousef Nazirizadeh. Für die Unterstützung bei der Probenherstellung bin ich Janine Greve, Hendrik Block, Arfat Pradana, Matthias Bremer und Sarah Schauer sehr dankbar. Ich danke zudem Andre Iwers, Moritz Paulsen und Roger Kwee für die tatkräftige Unterstützung beim Aufbau des Goniophotometers und den späteren Messungen. Ich danke Kai Körber, Julian Hauss, Lars Thorben Neustock und Priv.-Doz. Thomas Mussenbrock für die fachlichen Gespräche, sowie Sigrid Thielbörger für ihr offenes Ohr in allen anderen Fragen.

Den Mitarbeitern der Karlsruhe Nano Micro Facility (KNMF) danke ich für die Herstellung der multi-periodischen Nanostrukturen. Matthias Burmeister, Berndt Neumann und allen anderen Mitarbeitern der zentralen Werkstatt der Technischen Fakultät gilt ebenfalls ein großes Dankeschön für die Fertigung von Teilen für das Goniophotometer.

Ich danke Fabian Bergfeld und Felix Tiedemann für das Korrekturlesen. Bei meinen Eltern möchte ich mich bedanken, die mich uneingeschränkt unterstützen und mir viel ermöglicht haben. Ein ganz besonderer Dank geht an meine Freundin Anke, die jedes Hoch und Tief bei der Entstehung dieser Arbeit mit mir geteilt hat, für ihre unermüdliche Geduld.

Contents

Chapter 1

Introduction

Today, a large variety of electric light sources is used, e.g., in lighting, optical communications, sensors, and displays. These developments were enabled by a better understanding of physical phenomena and new fabrication techniques.

The history of electric light sources starts in the 19th century, when incandescent lamps were invented that emit light by heating a material with an electric current [1]. These lamps were mainly needed for a safer, more powerful, and more convenient lighting. Incandescent lamps, however, emit a large portion of radiation in the invisible infrared spectrum and hence exhibit a low energy efficiency. With the advent of semiconductor technology in the middle of the 20th century, new means for efficient light generation became possible. Semiconductors can be designed such that at an applied external voltage electron-hole recombinations lead to the emission of photons, which is a form of electroluminescence [2]. This electroluminescence is more energy efficient than incandescence, as it allows to built light sources that emit the main portion of radiation as visible light. Currently, the light-emitting diode (LED), an electric semiconductor light source, is underway to replace the inherently inefficient incandescent lamps for lighting [1, 3, 4]. Around the beginning of the 1990s, major breakthroughs in development of organic light-emitting diodes (OLEDs) have been reported [5, 6]. OLEDs consist of organic semiconducting materials, either polymers or so called small molecules, which can be fabricated and processed at potentially lower cost than inorganic semiconductors [7–9]. OLEDs first found application in displays and are now widely used in mobile devices [9, 10]. For general lighting, the possibility to fabricate large-area OLEDs and to use flexible substrates holds the promise of fundamentally new light sources [8, 11, 12]. Furthermore, OLEDs possess favorable properties for highly integrated sensor systems [13–20] such as their compatibility with a large range of

substrates.

OLED architecture and emission channels

The semiconducting organic materials are processed as a layer between two electrodes. A common material employed for the anode is the transparent indium-tin-oxide (ITO) while the cathode is commonly a thin layer of metal, e.g. aluminum. Further organic layers can be employed in the OLED layer stack to improve the electroluminescence efficiency, resulting in a stack thickness of typically 100 nm to 400 nm. Often, a glass substrate is used, so that the light generated in the OLED stack can leave the device through the ITO anode and the substrate. However, in a conventional OLED, approximately only 20 % of the photons leave the substrate as air modes. About 40 % of the photons are trapped in organic layers and the anode as (thin-film) guided modes or as surface plasmons near the metal cathode. The remaining 40 % are trapped in the substrate (see Fig. 1.1). These portions depend on the particular layer stack as reported in several

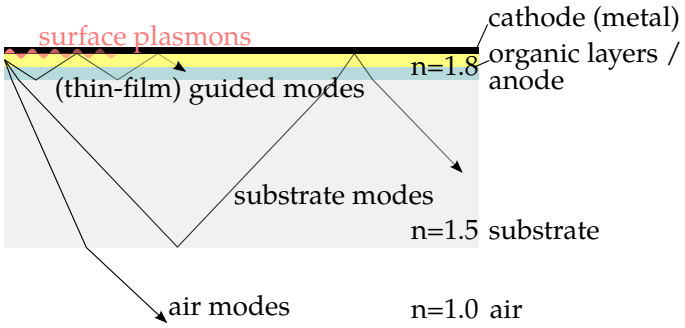

Figure 1.1: Emission channels in an OLED. Light generated inside the organic layers is guided in various pathways so that typically only 20 % leave the substrate as air modes.

numerical studies [21–25].

To understand the emission channels of an OLED, it is instructive to consider the emission as a superposition of rays with arbitrary directions. In a conventional OLED as shown in Fig. 1.1, only light that is emitted sufficiently close the layer normal will be able to leave the device through the substrate as air modes due to the high refractive indices of the thin films and the substrate compared to air. Light with a larger angle to the layer normal -but smaller than a particular angle- will be guided in the substrate by total internal reflection (TIR). Above a particular angle to the layer normal, light can only propagate in discrete guided states, which are either thin-film guided modes or surface plasmon modes. Due to the small

thickness of the thin-film stack, commonly only one or two thin-film guided modes exist per polarization.

Light emitted into the guided modes and surface plasmons is absorbed fast, i.e. typically on a length scale of 10 µm [26] and eventually lost to heat. It is therefore of great interest to extract light from these channels into useful directions. Today, the extraction of guided light is considered as the limiting factor in the overall OLED efficiency since the conversion ratio of injected electrons to photons, or internal quantum efficiency, has almost reached 100 % [27].

A straightforward method to suppress the thin-film guided modes is the use of a high refractive index substrate [28]. However, these substrates are generally considered too costly for mass production. A different and particularly promising approach is to introduce a nanostructure in the anode or the organic layers that leads to scattering of the guided modes. The scattering allows the guided mode to couple energy to non-guided modes, also termed radiation modes in the terminology of grating waveguides. This extraction of the guided modes is called guided mode outcoupling. In this respect, one dimensional gratings [29–34], two dimensional photonic crystals [35–37], and random scattering structures [38, 39] have been investigated.

Compound binary gratings for guided mode outcoupling

Gratings in OLEDs are periodic modulations of the refractive index in parallel lines. By design, gratings typically possess a dominant periodicity and are therefore called single-period gratings in the following. Incorporated in an OLED, a single-period grating mainly scatters the guided mode into a single, wavelength-dependent direction as shown in Fig. 1.2a. This wavelength dependency of the direction leads to an angular color impression for the viewer and is generally unwanted for general lighting. In this work, I will propose compound binary gratings for OLEDs that are obtained by the superposition of multiple singe-period gratings. Fig. 1.2b shows the principle of compound binary gratings for outcoupling of a guided mode. Due to the presence of multiple periodicities, multiple wavelengths are scattered into each direction. A possible application is the reduction of the color impression for general lighting OLEDs. Note that Fig. 1.2 only depicts one propagation direction of the guided mode. In an OLED, the counter-propagating guided mode is present as well, which leads to additional and symmetric scattering.

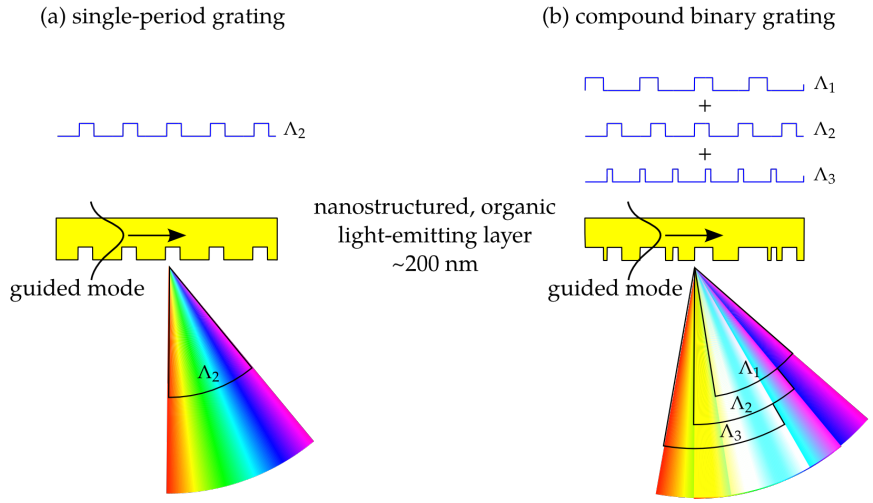

Figure 1.2: Scattering of a guided mode in an organic light-emitting layer. (a) A single-period grating possesses one dominant periodicity and scatters the guided mode mainly into a single, wavelength-dependent direction. (b) In contrast, a compound binary grating possesses multiple strong periodicities and scatters the guided mode in multiple directions for each wavelength. This wavelength mixing can reduce the angle-dependent color impression for the viewer.

Nanostructured source for sensors

When guided modes are extracted, the outcoupled light adds to the direct OLED emission. Periodic structures, i.e. gratings and photonic crystals, have the advantage that they offer the possibility to direct the scattering, compared to random scattering structures. By this control of the guided mode outcoupling, the light intensity can be increased in particular directions. Depending on the application of the OLED, the extracted light can thus be utilized. Fig. 1.3 shows two different OLED applications, which require different outcoupling directions. For an application in general lighting, the guided modes should be extracted into angles that are able to leave the substrate into air (see Fig. 1.3a). In contrast, Fig. 1.3b shows a sensing application of an OLED, in which the substrate serves as a light guide from the OLED to the analyte volume and to the detector. This thesis will demonstrate that the partially directional emission of an organic light-emitting layer with a single-period grating is beneficial for the sensing.

(a) general lighting

(b) sensing

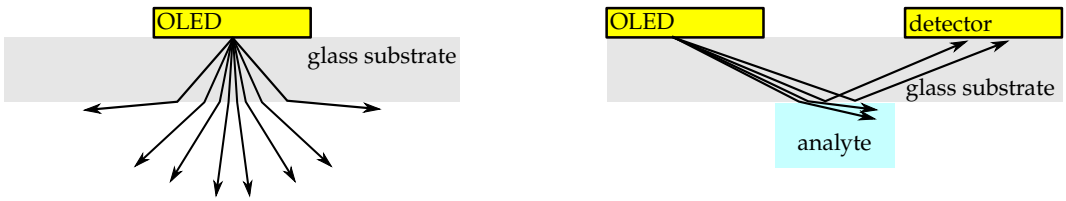

Figure 1.3: Two applications of an OLED with different required outcoupling directions. (a) In an OLED for general lighting, the guided modes should be scattered into angles that are able to leave the device through the substrate. (b) For this sensing application, a directional part of the emission towards the analyte is beneficial.

Theory of grating waveguides

Most experimental studies of guided mode outcoupling from OLEDs compare the nanostructured device with an unstructured reference device. While significant increases of the OLEDs emission intensity have been reported, separation of the individual optical and electrical effects is often difficult in these experiments as the nanostructure can also modify electrical characteristics and the internal quantum efficiency [40, 41]. In addition, nanostructures for guided mode outcoupling can also lead to extraction of substrate light [42, 43]. To understand and optimize the guided mode outcoupling with nanostructures it is therefore helpful to employ theoretical models.

One theoretical approach to nanostructured OLEDs is to numerically solve the full Maxwell's equations under dipole excitation in the device [32, 35, 36, 42]. Therefore, the complete geometry of the nanostructured OLED is entered, e.g., into a finite-difference time-domain (FDTD) program and the emission including the scattering intensities is obtained (see Fig. 1.4a). However, the assessment of individual parameters that influence the guided mode extraction can be difficult as the simulation yields only the solution for one particular case at a time. A more comprehensive picture of the parameters' influence can be obtained by the use of theoretical models. Here, a common approach is to approximate the nanostructured OLED as an unstructured waveguide and calculate the mode propagation constants [30, 33, 44]. Subsequently, the scattering directions can be calculated with Bragg's equation analytically from four parameters (see Fig. 1.4b). While treatment of the waveguide without nanostructure reduces the problem complexity considerably, this model is not capable of determining the intensity of the scattering. In this work, I will therefore develop an approximate

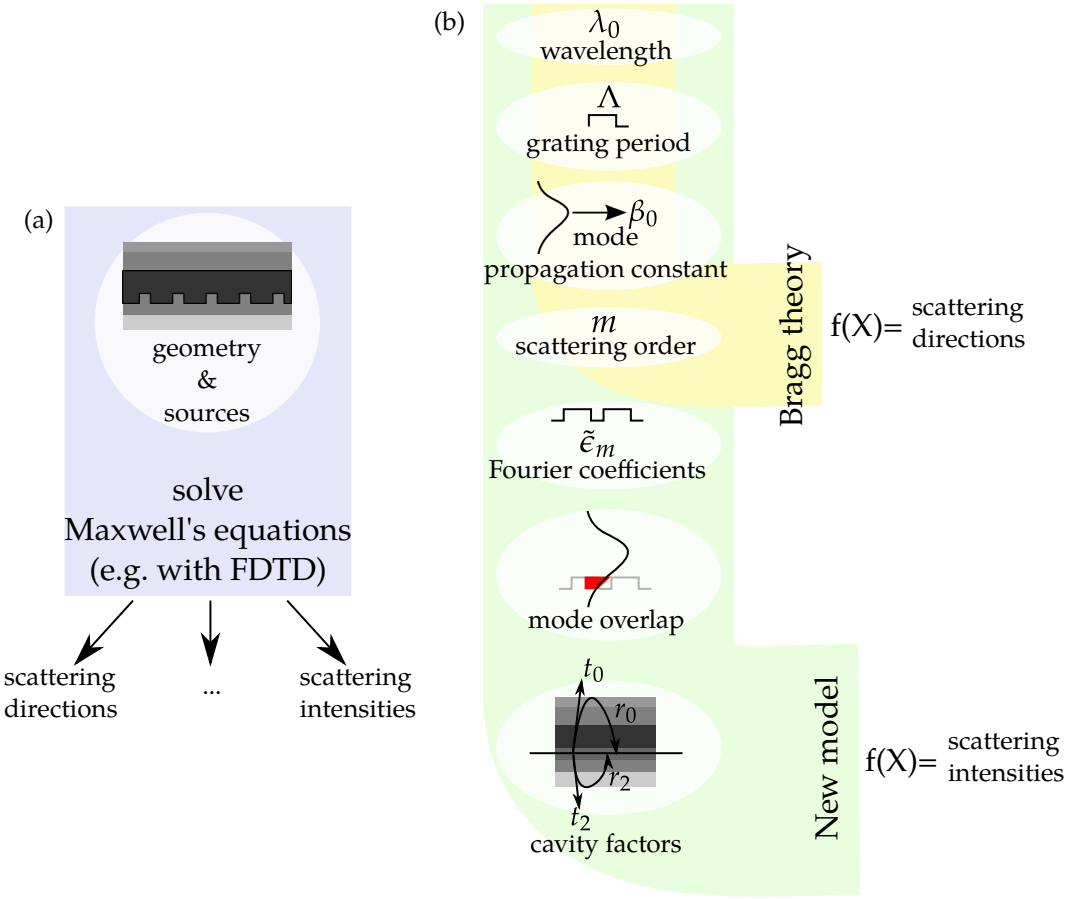

Figure 1.4: Two theoretical approaches to nanostructured OLEDs. (a) Solution of the full Maxwell's equations in the given geometry under excitation by the sources. From the electromagnetic field, one can calculate, e.g., the scattering directions and intensities. (b) The well-known Bragg theory provides an equation for the scattering direction with four input parameters. In this work, a new parameterized model is presented that provides an expression for the scattering intensities.

model for OLEDs with thin gratings that allows to determine the intensity of the scattering. By combining well-understood theories of grating waveguides [45] and cavity light extraction [46], the guided mode scattering is described as additional plane waves which emerge inside the grating layer and propagate to the outside. This model yields an (approximate) expression for the intensity of each scattering direction with physically meaningful factors (see Fig. 1.4b). The usefulness of the new model is subsequently demonstrated in the optimization of the thin-film stack thickness and the grating period for efficient guided mode outcoupling.

Aim and structure of this thesis

This thesis investigates how grating nanostructures can be designed to control the guided mode outcoupling in OLED-like waveguide structures. I investigate grating waveguides formed by an organic emitter layer on a corrugated glass substrate both theoretically and experimentally. A focus is on identification of the individual factors that determine the guided mode outcoupling. I further explore how the outcoupled guided modes can be applied, e.g., in sensors.

Chapter 2 reviews the relevant waveguide theory and numerical methods used in this thesis. Physically intuitive expressions for guided mode outcoupling are derived from grating coupler theory. These methods are applied in Chapter 3 to numerically study a grating structured OLED-like waveguide. A focus is on the influence of the grating period, the waveguide thickness, and the wavelength on the guided mode outcoupling. Chapter 4 describes the goniophotometer built within this work to measure the emission of OLED-like samples. The influence of the instrument on the measurement is analyzed. The width of outcoupling peaks from a grating structured organic emitter layer is investigated experimentally. In Chapter 5, the influence of the nanostructure's Fourier spectrum on the guided mode outcoupling is highlighted by the introduction of compound binary gratings obtained by the superposition of multiple binary gratings. The photoluminescence (PL) of organic emitter layers structured by these gratings is investigated experimentally and theoretically. Chapter 6 examines the benefits of nanostructures in the light source of a refractive index sensor. Here, the focus is laid on the application of the outcoupled light that renders the light source partially directional. Finally, Chapter 7 summarizes and concludes this thesis.

Following the main part of this thesis, Appendix A derives the Poynting vector of plane waves, Appendices B and C provide additional calculations for the goniophotometer, and Appendix D lists the parameters of the compound binary gratings and the fabricated samples. A nomenclature at the end of this document lists the meanings of the occurring symbols and abbreviations.

Chapter 2

Waveguide theory and numerical methods

Summary

This chapter discusses the basic concepts of light propagation as an electromagnetic wave in homogeneous materials, slab waveguides, and grating waveguides. The numerical methods used in this work to calculate the electromagnetic field in waveguides with and without gratings will be presented. I modify a grating waveguide method such that physically intuitive expressions for the scattering intensity of a guided mode are obtained.

2.1 Electromagnetic wave equation

Maxwell's equations for time-harmonic fields [47] describe monochromatic light as an electromagnetic wave by

$$\nabla \times \underline{\vec{E}}(\vec{r}) = -j\omega \underline{\vec{B}}(\vec{r}), \tag{2.1}$$

$$\nabla \times \underline{\vec{H}}(\vec{r}) = j\omega \underline{\vec{D}}(\vec{r}) + \underline{\vec{J}}(\vec{r}), \tag{2.2}$$

$$\nabla \cdot \underline{\vec{D}}(\vec{r}) = \underline{\rho}(\vec{r}), \text{ and} \tag{2.3}$$

$$\nabla \cdot \underline{\vec{B}}(\vec{r}) = 0, \tag{2.4}$$

where $\underline{\vec{E}}$ and $\underline{\vec{H}}$ are the electric and magnetic field strengths, respectively. $\underline{\vec{D}}$ represents the electric displacement and $\underline{\vec{B}}$ the magnetic flux density. $\underline{\vec{J}}$ is the current density, $\underline{\rho}$ is the space charge density, and $\vec{r} = x\vec{e}_x + y\vec{e}_y + z\vec{e}_z$ is the position in space. $\vec{e}_x$,$\vec{e}_y$, and $\vec{e}_z$ are the Cartesian unity vectors. The Cartesian components of vectors will be denoted with subscripts x, y, and z, e.g. $\underline{E}_z$ for the z-component of the electric field. The underlined quantities are peak value phasors and the corresponding physical quantities may be obtained by multiplying the phasor with the time dependence $\exp(+j\omega t)$ and taking the real part. ω is the angular frequency of the wave.

The complex Poynting vector is defined as

$$\underline{\vec{S}}(\vec{r}) = \underline{\vec{E}}(\vec{r}) \times \underline{\vec{H}}^*(\vec{r}), \tag{2.5}$$

where F^* denotes the complex conjugate of the function F. The magnitude and direction of energy flow per unit area of the electromagnetic field is given by the time-average Poynting vector [47]

$$\langle \vec{S} \rangle (\vec{r}) = \frac{1}{2} \mathrm{Re} \left\{ \underline{\vec{S}}(\vec{r}) \right\}. \tag{2.6}$$

This work assumes linear, isotropic, time-invariant and non-magnetic media, so that the permeability is the free-space permeability μ_0 and the permittivity ϵ is a scalar function of $\vec{r}$

$$\underline{\vec{B}}(\vec{r}) = \mu_0 \underline{\vec{H}}(\vec{r}) \tag{2.7}$$

$$\underline{\vec{D}}(\vec{r}) = \epsilon(\vec{r}) \underline{\vec{E}}(\vec{r}). \tag{2.8}$$

Note that for a geometry where discontinuous material properties occur, the electromagnetic field can be treated separately in the continuous regions under application of boundary conditions at the surfaces of discontinuity [48]. The boundary conditions require that, in the absence of surface charges and surface currents, the normal components of $\underline{\vec{B}}$ and $\underline{\vec{D}}$ and the tangential

components of $\vec{\underline{E}}$ and $\vec{\underline{H}}$ are continuous across the surface. In a source-free and non-conducting region, i.e. $\vec{\underline{J}}(\vec{r}) = 0$ and $\underline{\rho}(\vec{r}) = 0$, equations (2.1), (2.2), (2.7) and (2.8) yield the time-harmonic electromagnetic wave equation [47]

$$\nabla \times \nabla \times \vec{\underline{E}}(\vec{r}) = \omega^2 \mu_0 \epsilon(\vec{r}) \vec{\underline{E}}(\vec{r}), \tag{2.9}$$

a generalized eigenproblem. An equivalent wave equation can be formulated for $\vec{\underline{H}}$. However, as the magnetic and electric fields can be recovered from each other by use of (2.1) and (2.2), it is generally sufficient to solve only one of the wave equations. The following treatment of homogeneous media, slab waveguides, and nanostructured waveguides discusses solutions of (2.9) in special geometries characterized by their permittivity function $\epsilon(\vec{r})$.

2.2 Light propagation in homogeneous, lossless media

The most simple permittivity function is given for a homogeneous, i.e. space-invariant, medium. In this case $\epsilon(\vec{r}) = \epsilon$ is constant and real as we are considering only lossless media. The wave equation (2.9) then simplifies to

$$-\nabla^2 \vec{\underline{E}}(\vec{r}) = \omega^2 \mu_0 \epsilon \vec{\underline{E}}(\vec{r}), \tag{2.10}$$

also known as the Helmholtz equation [47]. Eq. (2.10) has a set of solutions comprised by the plane waves [48]

$$\vec{\underline{E}}\,(\vec{r}) = \vec{\underline{E}}_0 \exp\left(-j\vec{k} \cdot \vec{r}\right), \tag{2.11}$$

where $\vec{\underline{E}}_0$ is the position-independent plane wave amplitude. A plane wave is characterized by its wave vector $\vec{k}$ that has to fulfill the relation

$$\begin{aligned} \vec{k} \cdot \vec{k} = k_x^2 + k_y^2 + k_z^2 = \omega^2 \mu_0 \epsilon = (k_0 n)^2, \\ k_0 \equiv \frac{2\pi}{\lambda_0}, \end{aligned} \tag{2.12}$$

obtained by insertion of (2.11) into (2.10). λ_0 is the light wavelength in vacuum and

$$n = \sqrt{\epsilon/\epsilon_0} \tag{2.13}$$

is the refractive index of the propagation medium. A functional relation like (2.12) between the wave vector and the wave frequency ω is called dispersion relation.

It can be shown that $\vec{\underline{E}}$, $\vec{\underline{H}}$, and $\vec{k}$ are mutually perpendicular with $\vec{\underline{E}} \times \vec{\underline{H}}$ being in the direction of $\vec{k}$ [47]. In general, $\vec{k}$ can be complex and represented by real vectors $\vec{\beta}$ and $\vec{\alpha}$

$$\vec{k} = \vec{\beta} + j\vec{\alpha}. \tag{2.14}$$

By insertion of (2.14) into (2.11) one finds that the plane wave spatial variation splits up into two exponentials

$$\vec{\underline{E}}\,(\vec{r}) = \vec{\underline{E}}_0 \exp\left(\vec{\alpha} \cdot \vec{r}\right) \exp\left(-j\vec{\beta} \cdot \vec{r}\right), \tag{2.15}$$

the first, with real argument, being an amplitude variation and the second, with imaginary argument, being a phase term. The phase vector $\vec{\beta}$ points in direction of the most rapid phase change, often also called the wave propagation direction. However, this is not necessarily the direction of energy flow as will be shown later. The amplitude vector $\vec{\alpha}$ points in the direction of the most rapid amplitude change. Inserting (2.14) into the dispersion relation (2.12) yields directly

$$\vec{\alpha} \cdot \vec{\beta} = 0 \tag{2.16}$$

for lossless materials. This implies that the planes of equal amplitude and the planes of equal phase are orthogonal. If $\vec{\alpha} = 0$, i.e. $\vec{k}$ is real, one speaks of homogeneous plane waves. In the general case of complex $\vec{k}$ the plane waves are called inhomogeneous plane waves [49]. These play an important role in waveguides with nanostructures that leak energy away from the waveguide core.

For determination of the amount of energy carried by a plane wave and the direction of energy flow, the Poynting vector (2.5) of the plane wave field (2.11) is calculated (see Appendix A). In case of a homogeneous plane wave, or of an inhomogeneous plane wave with $\vec{\underline{E}}_0$ proportional to a real vector, the complex Poynting vector is

$$\vec{\underline{S}}(\vec{r}) = \frac{1}{\omega\mu_0} \left|\vec{\underline{E}}_0\right|^2 \left(\vec{\beta} - j\vec{\alpha}\right) \exp\left(2\vec{\alpha} \cdot \vec{r}\right). \tag{2.17}$$

In these cases the real part of the Poynting vector (2.17) gives an energy flow (2.6) in direction of $\vec{\beta}$.

2.3 Plane wave incidence on a plane boundary

At a plane boundary between two homogeneous media, an incident plane wave ($\vec{k}^{\text{inc}}$) is split into a reflected ($\vec{k}^{\text{refl}}$) and a transmitted ($\vec{k}^{\text{trans}}$) plane wave. An important result from the electromagnetic boundary conditions

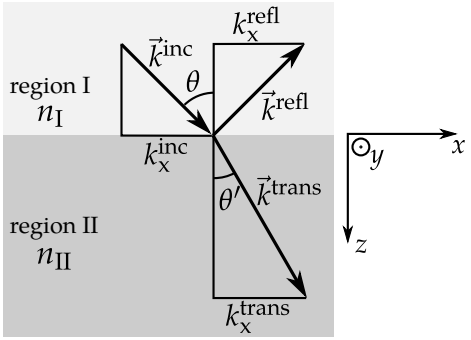

Figure 2.1: A plane wave incident from region I is split at the boundary to region II in a transmitted and a reflected plane wave. The figure shows the wave vectors in the plane of incidence.

(see section 2.1) is that the in-plane wave vector components are equal [47]. Consequently, $\vec{k}^{inc}$, $\vec{k}^{refl}$, and $\vec{k}^{trans}$ lie in the same plane, which is called the plane of incidence. In Fig. 2.1 the coordinate system is chosen such that the plane of incidence is the xz-plane. Thus, the tangential wave vector components are

$$k_x^{inc} = k_x^{refl} = k_x^{trans}. \tag{2.18}$$

As the wave vector modulus is proportional to n (see Eq. (2.12)), Eq. (2.18) yields Snell's law [47]

$$n_I \sin(\theta) = n_{II} \sin(\theta'). \tag{2.19}$$

If a plane wave is incident from the medium with higher refractive index, i.e. $n_I > n_{II}$, Eq. (2.19) yields real angle solutions only for incidence angles smaller than the critical angle

$$\sin(\theta_{cri}) = n_{II}/n_I. \tag{2.20}$$

For incidence angles higher than the critical angle, the requirement Eq. (2.18) leads to an in-plane wave vector that is larger than $k_0 n_{II}$. According to Eq. (2.12), the wave vector component normal to the boundary k_z^{trans} then becomes purely imaginary for the transmitted wave, which is then called an evanescent wave [47].

When calculating the plane wave fields at the boundary between two materials, it is helpful to separate the fields into components parallel and perpendicular to the plane of incidence and treating them separately [50]. In this work, transverse-electric (TE) polarization denotes the case of $\vec{E}$ being perpendicular to the plane of incidence and transverse-magnetic (TM)

polarization denotes the case of $\vec{H}$ being perpendicular to the plane of incidence. The amplitude reflection and transmission coefficients r and t are defined as the amplitude ratios of the respective waves to the incident wave and are determined by Fresnel's equations [50].

One speaks of total internal reflection (TIR) if a plane wave impinges upon a less dense material at an angle exceeding the critical angle (Eq. (2.20)). Fresnel's equations then yield a reflection coefficient of unity modulus and all incoming energy is reflected [50].

2.4 Cavity light extraction

Light inside planar films is reflected back and forth at each material boundary so that the partial waves interfere, a phenomenon called multiple beam interference [50]. The part of the structure in which the waves travel back and forth is often called a planar cavity. The interference can be used, e.g., for thin film filters with designed wavelength-specific reflectance when light is incident on the structure from outside [48]. Light generated inside the film can also be controlled by multiple-beam interference, e.g. in microcavity LEDs to increase the light extraction by redirection of dipole emission [51–53].

Consider the simple planar cavity in Fig. 2.2 formed by a high refractive index film of index n_{fi} bounded by semi-infinite regions I and II. As a source

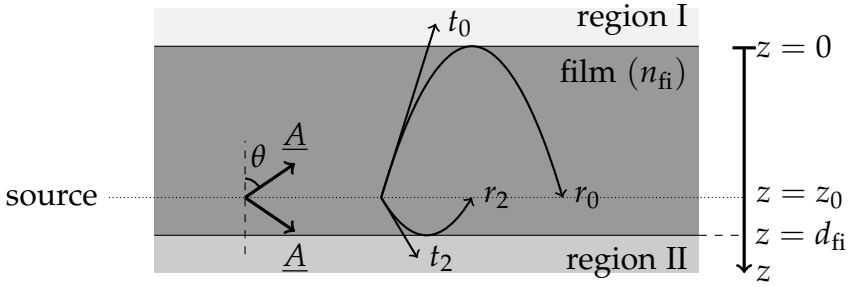

Figure 2.2: Schematic of a simple cavity with a plane wave source. The amplitude reflection coefficients r_0 and r_2 are defined from and to the source plane. The amplitude transmission constants t_0 and t_2 are defined from the source just to the outside of the film.

let us assume two plane waves of equal amplitude $\underline{A}$ inside the cavity at the source plane $z = z_0$. Both plane waves travel at an angle of θ with respect to the film normal but in opposite directions. Plane waves are commonly used as the expansion basis, e.g. to model dipole emission [52, 53]. Seen

from the source plane $z = z_0$, the amplitude reflection coefficients are r_0 and r_2, looking towards region I and region II, respectively. In the same way, the amplitude transmission coefficients t_0 and t_2 are defined from the source plane just to the film outside in region I and region II, respectively. Note that the amplitude coefficients are complex. In case of the amplitude reflection coefficients, we define the phase contributions via

$$r_0 = |r_0| \exp\left[j(2\phi_{0,\text{trip}} + \phi_{0,\text{refl}})\right], \tag{2.21}$$

$$r_2 = |r_2| \exp\left[j(2\phi_{2,\text{trip}} + \phi_{2,\text{refl}})\right], \tag{2.22}$$

where

$$\phi_{0,\text{trip}} = -k_0 n_{\text{fi}} \cos\theta z_0, \tag{2.23}$$

$$\phi_{2,\text{trip}} = -k_0 n_{\text{fi}} \cos\theta (d_{\text{fi}} - z_0) \tag{2.24}$$

are the phase changes due to path differences, while $\phi_{0,\text{refl}}$ and $\phi_{2,\text{refl}}$ are the phase changes occurring at reflection on the boundaries.

Calculating the outside fields, we find for the outgoing wave intensity [51] in region I

$$\left|\underline{E}^{(\text{I})}\right|^2 = |t_0|^2 \frac{|(r_2+1)|^2}{|1 - r_0 r_2|^2} |\underline{A}|^2, \tag{2.25}$$

and in region II

$$\left|\underline{E}^{(\text{II})}\right|^2 = |t_2|^2 \frac{|(r_0+1)|^2}{|1 - r_0 r_2|^2} |\underline{A}|^2. \tag{2.26}$$

Eqs. (2.25) and (2.26) take the interference of all partial waves into account. We find two important factors of the outgoing intensity in Eqs. (2.25) and (2.26). Firstly, the Airy factor

$$v_{\text{Airy}} \equiv 1/\left|1 - r_0 r_2\right|^2, \tag{2.27}$$

which is equal for both directions [52]. The Airy factor exhibits maxima at

$$2\phi_{0,\text{trip}} + \phi_{0,\text{refl}} + 2\phi_{2,\text{trip}} + \phi_{2,\text{refl}} = m2\pi \tag{2.28}$$

with m being an integer. At an Airy factor maximum, the cavity is said to be resonant [52]. Note that the Airy factor is determined by the complete round-trip phase and independent of the source position [52].

The second factors in Eqs. (2.25) and (2.26) are the standing wave factors

$$\zeta_{\text{I}} \equiv \left|(r_2+1)\right|^2, \tag{2.29}$$

$$\zeta_{\text{II}} \equiv \left|(r_0+1)\right|^2. \tag{2.30}$$

The standing wave factors strongly depend on the source position as they exhibit maxima when the reflected source wave interferes constructively with the other source wave. In other words, in a semi-infinite medium with only one boundary present, the standing wave factor will exhibit a maximum if the source is at an antinode of the standing wave pattern [52]. The maxima phase conditions are

$$2\phi_{2,\text{trip}} + \phi_{2,\text{refl}} = m2\pi \tag{2.31}$$

for the standing wave factor ζ_{I} and

$$2\phi_{0,\text{trip}} + \phi_{0,\text{refl}} = m2\pi \tag{2.32}$$

for the standing wave factor ζ_{II}.

2.5 Light propagation in slab waveguides

Slab waveguides are characterized by a permittivity that is a function of only one Cartesian coordinate. $\epsilon(\vec{r}) = \epsilon(z)$ is assumed in the following. Such a configuration is interesting for optical applications, as light can be guided due to total internal reflection. This means that the energy of the guided light is confined and the power flux is directed along the dielectric slab. I review the basics of the slab waveguide theory as described by Lee [47], Marcuse [54], and Lifante [55]. In these books, more information on this wide topic can be found.

Consider a simple three layer waveguide configuration as shown in Fig. 2.3. The waveguide is invariant in x- and y-direction and charac-

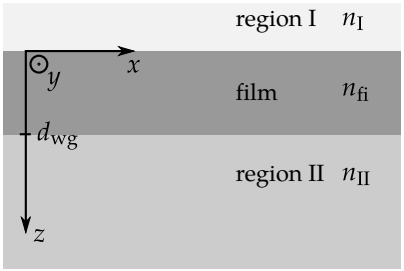

Figure 2.3: Geometry of the analyzed three layer slab dielectric waveguide with right-handed coordinate system.

terized by a refractive index dependence along z. The guiding film is of thickness d_{wg} and of refractive index n_f higher than n_I and n_{II}. Region I and region II extend infinitely in -z- and +z-direction. The film is also called

the waveguide core. Often, region II represents the substrate on which the film has been fabricated, and region I represents air, so that $n_{II} \geq n_I$.

A slab waveguide supports waves of the form

$$\underline{\vec{E}}\,(\vec{r}) = \underline{\vec{E}}(z)\exp\left(-jk_x x\right), \tag{2.33}$$

which are called modes. Note that the coordinate system is rotated so that the fields are independent of y. $\underline{\vec{E}}(z)$ is called the mode profile and is maintained as the mode propagates in x-direction. The wave vector component k_x is the mode propagation constant. Eq. (2.33) describes a guided mode if

$$k_x \geq k_0 n_{\mathrm{II}}, k_0 n_{\mathrm{I}} \tag{2.34}$$

and if the fields inside the waveguide core fulfill the transverse resonance condition [55]. By Eq. (2.34), the field of a guided mode is evanescent in region I and II and the mode energy is consequently guided in the waveguide core. Only a discrete set of fields satisfy the transverse resonance condition. These guided modes of a slab waveguide can be found by solving a transcendental relation [47] or with various numerical methods as for example the transfer matrix method (see Sec. 2.7.1).

The guided modes are commonly enumerated in the order of decreasing modulus of k_x and according to their field polarization. We use the same convention as for the plane wave incidence (see Sec. 2.3) to denote the mode polarization. E.g., the guided mode with $\underline{\vec{E}}(z)$ in y-direction that is propagating with the largest possible modulus of k_x is referred to as the TE_0-mode. Fig. 2.9 exemplarily depicts the first two TE-polarized guided mode profiles in a thin film waveguide.

To characterize a guided mode, the mode effective index

$$n_{\mathrm{eff}} \equiv k_x / k_0 \tag{2.35}$$

is often used. As given by Eq. (2.34), n_{eff} is higher than n_{I} and n_{II}, but it is smaller than n_{fi}, because the mode is not evanescent in the film itself [55]. The mode effective index n_{eff} is frequency-dependent and the relation between the light frequency and n_{eff} is called the dispersion relation. An important property of a guided mode is its cut-off frequency, which is the minimum frequency at which the particular mode is supported by the waveguide [47]. With increasing frequency, a waveguide supports an increasing number of guided modes.

2.6 Grating waveguides

In this section I review the basic theory of grating waveguides [45, 49, 56–59]. An excellent introduction to the topic is provided by Peng et al. [45].

Grating waveguides are important building-blocks for integrated optics. One can distinguish between guided mode to guided mode coupling and guided mode to radiation mode coupling. Typical applications of guided mode to guided mode coupling are distributed feedback lasers and filters [59]. Guided mode to radiation mode coupling is used in grating couplers that transfer a beam to a guided mode [60]. The grating period determines the change of the wave's momentum and thereby whether the mode can couple to another guided mode or to radiation.

Consider a grating waveguide as shown in Fig. 2.4. Similar to the

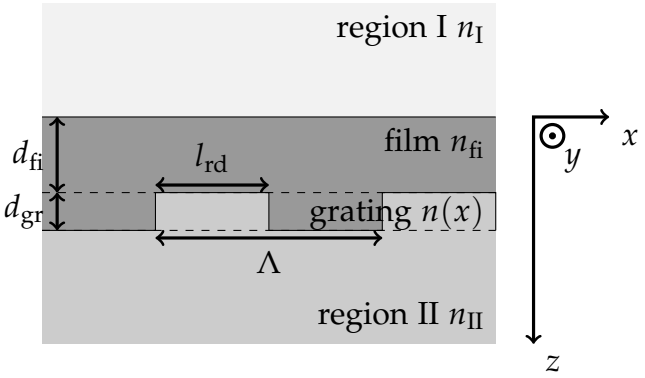

Figure 2.4: Grating waveguide with periodic permittivity modulation between the film and region II. The binary grating $n(x)$ is characterized by its period Λ and ridge width l_{rd} and present in a layer of thickness d_{gr}.

slab waveguide, the considered grating waveguide is structured by layers in z-direction. Additionally, the permittivity in the grating layer between region II and the film is periodically structured in x-direction and invariant in y- and z-direction. This rectangular permittivity modulation is a binary grating. A single-period binary grating is characterized by its period Λ and ridge width l_{rd} (see Fig. 2.4). In addition, the grating's duty cycle is defined as

$$f_{\mathrm{dc}} = l_{\mathrm{rd}} / \Lambda. \tag{2.36}$$

Note that regarding the fabrication, l_{rd} is the width of the ridges in the substrate's (region II) corrugation.

2.6.1 Unperturbed waveguide

If the grating is weak, i.e. sufficiently thin or of small permittivity modulation, the quasi-guided modes or leaky waves (see Sec. 2.6.2) supported by a grating waveguide can be regarded as modified guided modes of the unperturbed slab waveguide. The unperturbed slab waveguide, or basic structure, is obtained from the grating waveguide by averaging the permittivity in the grating layer [61, 62]. For example the averaged grating layer refractive index for the grating waveguide shown in Fig. 2.4 is

$$n_{\mathrm{gr}} = \sqrt{f_{\mathrm{dc}} n_{\mathrm{II}}^2 + (1 - f_{\mathrm{dc}}) n_{\mathrm{fi}}^2}. \tag{2.37}$$

The unperturbed waveguide is e.g. helpful to approximate the dispersion of the leaky waves in the grating waveguide.

2.6.2 Leaky waves

Grating waveguides have a discrete translational symmetry, e.g. the structure in Fig. 2.4 is invariant to a translation by Λ in x-direction. This symmetry in the permittivity function requires any solution of the electromagnetic wave equation (Eq. (2.9)) in the structure to be dependent on x by the product of a plane wave with a x-periodic function. This result is known as the Floquet or Bloch theorem [63]. I limit the analysis here to waves traveling in x-direction, i.e. perpendicular to the grating grooves, so that the fields are independent of y. Then, the field components in the i-th layer can be expressed by the sum of Floquet space harmonics

$$\begin{aligned} F(x,z) &= \sum_{m=-\infty}^{\infty} F_m^{(i)}(z) \exp(-jk_{xm}x), \\ k_{xm} &= k_{x0} + m \cdot K, \\ K &\equiv \frac{2\pi}{\Lambda}, \end{aligned} \tag{2.38}$$

where $F_m^{(i)}(z)$ is the z-dependent amplitude of the m-th space harmonic and K is the magnitude of the grating vector.

We are interested in field solutions that are supported by the grating waveguide in the absence of any impinging wave from outside. These solutions have to fulfill a transverse resonance condition similar to the guided modes in slab waveguides (see Sec. 2.5). Again, only a discrete set of fundamental mode propagation constants k_{x0} leads to transverse resonance. Depending on the grating period and the light frequency, the associated fields are guided modes or leaky waves [63]. This implies that despite the

grating, true guided modes can exist that propagate unattenuated along the grating waveguide. However, this work focuses on the leaky wave regime, i.e. the range of grating periods that leads to radiation loss from the grating waveguide in the light frequency range of interest.

If the grating is sufficiently weak, the k_{x0} of a leaky wave is closely given by the propagation constant of the guided mode in the unperturbed waveguide (see Sec. 2.6.1) [45]. However, the mode propagation constant of a leaky wave is complex

$$k_{x0} = \beta_0 + j\alpha, \tag{2.39}$$

and the leaky wave is attenuated along x. In the case without material absorption or gain, the attenuation constant α is due to energy leakage to radiation and occuring stopbands [45, 56]. The leaky-wave power varies as

$$P(x) = P_0 \exp(2\alpha x), \tag{2.40}$$

where P_0 is the leaky wave power at $x = 0$. The power change per unit length

$$\frac{dP}{dx} = 2\alpha P(x) \tag{2.41}$$

is proportional to the attenuation constant α [57]. This allows us to investigate the intensity of guided mode to radiation mode coupling by calculating α, if the stopband influence (see Sec. 2.6.3) is known.

In region $i = \mathrm{I}, \mathrm{II}$, the field space harmonics are plane waves and Eq. (2.38) becomes

$$F(x,z) = \sum_{m=-\infty}^{\infty} F_m^{(i)} \exp[-j(k_{xm}x + k_{zm}^{(i)}z)] \qquad \text{for } i = \mathrm{I,II}, \tag{2.42}$$

where $F_m^{(i)}$ is a constant field amplitude in the i-th region [45]. The transverse wave vectors are

$$k_{zm}^{(i)} = \pm\sqrt{\left(k_0 n^{(i)}\right)^2 - k_{xm}^2} \qquad \text{for } i = \mathrm{I,II} \tag{2.43}$$

according to Eq. (2.12). $n^{(i)}$ denotes the refractive index in the i-th layer. For a leaky wave with small attenuation α, we may assume $k_{x0} = \beta_0$. This assumption is instructive since the transverse wave vectors are then purely real or purely imaginary according to Eq. (2.43) (for lossless materials). This allows us to classify the space harmonics in region I and II into propagating and evanescent waves. A space harmonic is propagating in layer i, if $k_{zm}^{(i)}$ is real and it is evanescent if $k_{zm}^{(i)}$ is imaginary. Thus, the $m = 0$ spatial

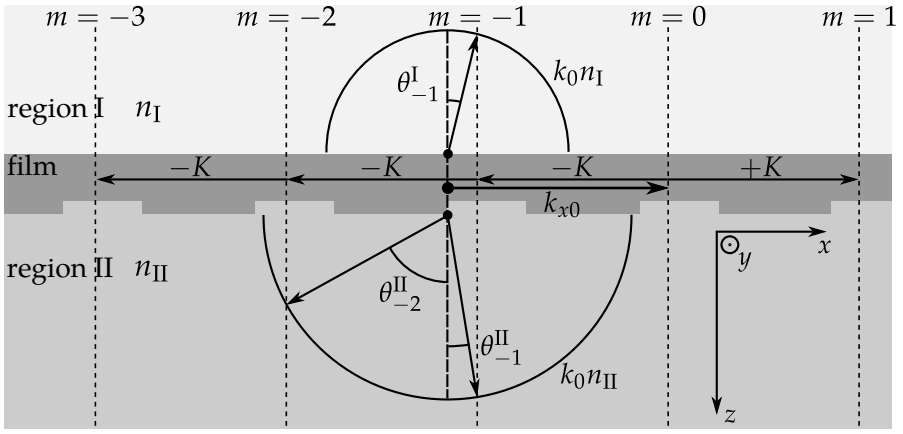

Figure 2.5: Floquet space harmonics in a grating waveguide. The leaky wave propagates along x with k_{x0}. Due to the periodic grating, space harmonics arise that are plane waves with tangential wave vectors $k_{x0} + mK$ in the homogeneous regions. These space harmonics are either propagating or evanescent in region I and II depending on the order m. In this case, the $m = -1$ space harmonic propagates in region I and the space harmonics $m = -1$ and $m = -2$ propagate in region II.

harmonics are evanescent in region I and II as k_{x0} is larger than $k_0 n^{(\mathrm{I,II})}$ and Eq. (2.43) yields purely imaginary transverse wave vectors. Spatial harmonics of negative m can, however, be propagating in region I and II as depicted in Fig. 2.5. The angles of the propagating space harmonics in layer i are given by

$$\sin\theta_m^{(i)} = k_{xm} / \left(k_0 n^{(i)}\right) = \left(n_\mathrm{eff} + m\frac{\lambda_0}{\Lambda}\right) / n^{(i)}, \tag{2.44}$$

as visible from Fig. 2.5. Eq. (2.44) is also referred to as the Bragg equation and expresses the conservation of momentum [64]. Physically, the formation of space harmonics can be explained by Bragg scattering of the "guided mode" with real n_eff at the periodical index modulation. It is therefore common to speak of outcoupling of the guided mode by Bragg scattering, although strictly the guided mode only exists in the unperturbed waveguide.

The conical case

At this point I briefly discuss the Bragg scattering angles for a guided mode traveling at an oblique angle ϕ to the grating normal (see Fig. 2.6), called the conical case. Although oblique incidence of a guided mode on the grating has been investigated for grating couplers [65, 66], I trigonometrically derive

simple expressions for the scattering angles from the wave vectors that cannot be found in these publications.

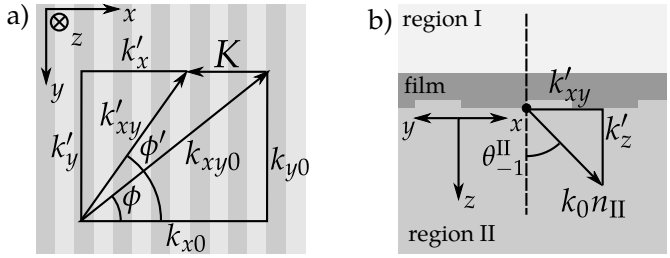

Figure 2.6: Bragg scattering of a guided mode traveling at an oblique angle to the grating normal. (a) xy-plane. The in-plane angle after scattering ϕ' differs from the guided mode direction ϕ. The grating causes a momentum change only normal to the grating grooves. (b) Plane defined by the new wave direction k'_{xy} and z. The Bragg scattering angle to the layer normal $\theta_m^{(i)}$ is defined by the tangential (in-plane) wave vector k'_{xy} and the wave vector modulus $k_0 n^{(i)}$ in region i.

The x- and y-components of the guided mode propagation constant $k_{xy0} = k_0 n_{\mathrm{eff}}$ are

$$k_{x0} = k_0 n_{\mathrm{eff}} \cos\phi \tag{2.45}$$

and

$$k_{y0} = k_0 n_{\mathrm{eff}} \sin\phi. \tag{2.46}$$

The Bragg scattering only affects the x-component of the wave vector [65], so that the wave vector after scattering $k'_{xy} = k'_x \vec{e_x} + k'_y \vec{e_y}$ is given by

$$\begin{aligned} k'_x &= k_{x0} + mK \\ k'_y &= k_{y0}. \end{aligned} \tag{2.47}$$

Thus, the scattered wave travels at the angle

$$\phi' = \arctan\left(\frac{k'_y}{k'_x}\right) \tag{2.48}$$

to the grating normal. By Eq. (2.45)-(2.47) and straightforward calculation, the Bragg scattering angle with respect to the layer normal (see Fig. 2.6) is

$$\begin{aligned} \sin(\theta_m^{(i)}) &= \sqrt{k_x'^2 + k_y'^2}/k_0 n^{(i)} \\ &= \sqrt{n_{\mathrm{eff}}^2 + 2\cos\phi n_{\mathrm{eff}} m\lambda_0/\Lambda + m^2\lambda_0^2/\Lambda^2}/n^{(i)}. \end{aligned} \tag{2.49}$$

2.6.3 Stopbands

A prominent effect of the grating is the emergence of stopbands near light frequencies that satisfy

$$\beta_0 \Lambda = N\pi, \tag{2.50}$$

where N is an integer. In a stopband, the electromagnetic field in the grating waveguide takes on the form of a standing wave. In addition, the attentuation constant α can increase significantly in a stopband due to coupling to the counter-propagating mode. Details about stopbands in periodic structures can be found in Joannopoulos et al. [63] and Peng et al. [45].

2.7 Simulation methods

2.7.1 Transfer matrix method

The transfer matrix method allows calculation of plane wave propagation in layered material and is described in detail in [67]. The approach describes the electromagnetic field by the amplitudes of two counter-propagating plane waves in each layer. Assume the given structure is layered in z-direction as in Fig. 2.3. The electric field parallel to the boundaries is represented in the layer i by the field amplitude vector

$$\begin{pmatrix} \underline{E}_{\uparrow}^{(i)} \\ \underline{E}_{\downarrow}^{(i)} \end{pmatrix},$$

where $\underline{E}_{\uparrow}^{(i)}$ is the forward-traveling (z-direction) wave amplitude, and $\underline{E}_{\downarrow}^{(i)}$ is the backward-traveling ($-z$-direction) wave amplitude at the beginning of the layer. The electric field parallel to the boundaries is then given by the sum [67]

$$\underline{E}_y(z) = \underline{E}_{\uparrow}^{(i)} \exp\left[-jk_z^{(i)}(z - z^{(i)})\right] + \underline{E}_{\downarrow}^{(i)} \exp\left[jk_z^{(i)}(z - z^{(i)})\right], \tag{2.51}$$

where $z^{(i)}$ denotes the beginning of the i-th layer and $k_z^{(i)}$ is the wave vector z-component in the i-th layer. The transfer matrix method relates the amplitude vectors at two different positions in the structure by the product of propagation- and boundary-matrices [67]. This reduces the plane wave solution of the electromagnetic wave equation (2.9) for layered structures to matrix multiplications and allows for fast computations even of structures with many layers.

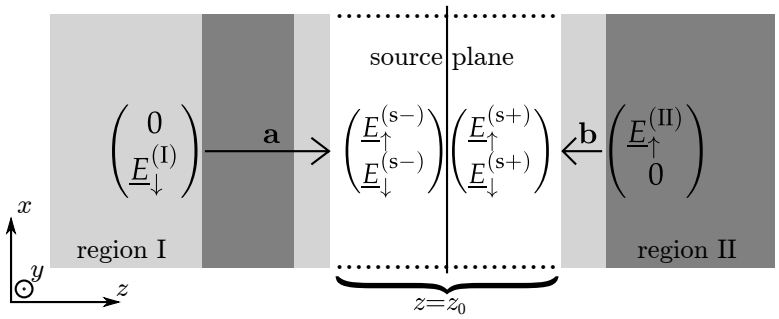

Figure 2.7: In order to calculate the outside fields in region I and II, the unperturbed waveguide is split at the source plane position. The two structures are then described by the product transfer matrices **a** and **b**. (Based on Fig. 2 in [46].)

Sources inside the structure

Usually, the transfer matrix method is used to calculate the electromagnetic fields for a plane wave impinging on the structure from outside. Nevertheless, the transfer matrix method can also be applied for plane wave sources inside the structure [46]. Benisty et al. [46] introduce the additive source terms $\underline{A}_{\uparrow}$ and $\underline{A}_{\downarrow}$ at $z = z_0$ to the forward- and backward-traveling wave, respectively. In order to calculate the field amplitudes outside, the structure is split at the source plane $z = z_0$ in layer $i = \mathrm{s}$ into two structures as shown in Fig. 2.7. The field on the left side of the source plane is described by the wave amplitudes $\underline{E}_{\uparrow}^{(\mathrm{s}-)}$ and $\underline{E}_{\downarrow}^{(\mathrm{s}-)}$, while the wave amplitudes on the right side are $\underline{E}_{\uparrow}^{(\mathrm{s}+)}$ and $\underline{E}_{\downarrow}^{(\mathrm{s}+)}$. The wave amplitudes on both sides of the source plane are related by the source terms [46]

$$\begin{pmatrix} \underline{E}_{\uparrow}^{(\mathrm{s}+)} \\ \underline{E}_{\downarrow}^{(\mathrm{s}+)} \end{pmatrix} - \begin{pmatrix} \underline{E}_{\uparrow}^{(\mathrm{s}-)} \\ \underline{E}_{\downarrow}^{(\mathrm{s}-)} \end{pmatrix} = \begin{pmatrix} \underline{A}_{\uparrow} \\ \underline{A}_{\downarrow} \end{pmatrix}. \tag{2.52}$$

The separation of the two structures in z-direction in Fig. 2.7 has been introduced only for illustration purposes as indicated by the dotted lines. The summed thickness of the source layer parts is preserved. As the source is inside the structure, only outgoing waves exist in region I and II. The outgoing wave amplitudes are connected to the wave amplitudes on both

sides of the source plane by the product transfer matrices **a** and **b** [46]

$$\begin{pmatrix} a_{11} & a_{12} \\ a_{21} & a_{22} \end{pmatrix} \begin{pmatrix} 0 \\ \underline{E}_{\downarrow}^{(\mathrm{I})} \end{pmatrix} = \begin{pmatrix} \underline{E}_{\uparrow}^{(\mathrm{s}-)} \\ \underline{E}_{\downarrow}^{(\mathrm{s}-)} \end{pmatrix},$$
$$\begin{pmatrix} b_{11} & b_{12} \\ b_{21} & b_{22} \end{pmatrix} \begin{pmatrix} \underline{E}_{\uparrow}^{(\mathrm{II})} \\ 0 \end{pmatrix} = \begin{pmatrix} \underline{E}_{\uparrow}^{(\mathrm{s}+)} \\ \underline{E}_{\downarrow}^{(\mathrm{s}+)} \end{pmatrix}. \tag{2.53}$$

The transfer matrices **a** and **b** of the two structure parts indicated in Fig. 2.7 can be calculated with standard transfer matrix techniques. From (2.52) and (2.53) the outside wave amplitudes can be calculated to be [46]

$$\underline{E}_{\downarrow}^{(\mathrm{I})} = \frac{b_{21}\underline{A}_{\uparrow} - b_{11}\underline{A}_{\downarrow}}{a_{22}b_{11} - b_{21}a_{12}} = \frac{t_0\left(r_2\underline{A}_{\uparrow} - \underline{A}_{\downarrow}\right)}{1 - r_0 r_2},$$
$$\underline{E}_{\uparrow}^{(\mathrm{II})} = \frac{a_{22}\underline{A}_{\uparrow} - a_{12}\underline{A}_{\downarrow}}{a_{22}b_{11} - b_{21}a_{12}} = \frac{t_2\left(r_0\underline{A}_{\downarrow} - \underline{A}_{\uparrow}\right)}{1 - r_0 r_2}, \tag{2.54}$$

with

$$t_0 = \underline{E}_{\downarrow}^{(\mathrm{I})}/\underline{E}_{\downarrow}^{(\mathrm{s}-)} = \frac{1}{a_{22}}, \qquad t_2 = \underline{E}_{\uparrow}^{(\mathrm{II})}/\underline{E}_{\uparrow}^{(\mathrm{s}+)} = \frac{1}{b_{11}},$$
$$r_0 = \underline{E}_{\uparrow}^{(\mathrm{s}-)}/\underline{E}_{\downarrow}^{(\mathrm{s}-)} = \frac{a_{12}}{a_{22}}, \qquad r_2 = \underline{E}_{\downarrow}^{(\mathrm{s}+)}/\underline{E}_{\uparrow}^{(\mathrm{s}+)} = \frac{b_{21}}{b_{11}}. \tag{2.55}$$

The amplitude transmission coefficients t_0 and t_2 are defined from the source position $z = z_0$ just to region I and region II, respectively. In the same way, the amplitude reflection coefficients r_0 and r_2 are defined as looking from the source position towards region I and region II, respectively.

Note that Eqs. (2.54) are a generalization of the cavity field extraction Eqs. (2.25) and (2.26) in Sec. 2.4. The advantage of the TMM approach is that it allows treatment of arbitrary planar cavities due to the numerical calculation of the amplitude reflection and transmission coefficients.

Guided modes

Matrix methods can also be used to find the guided modes and their propagation constants of a layered structure [68]. It is well known that the electromagnetic field in a structure resonates if the excitation's tangential wave vector matches the propagation constant of a guided mode supported by the structure [62, 68–74]. Experimentally, guided modes cannot be excited directly from the cladding by homogeneous waves, as the propagation constant of a guided mode is larger than the wave vector modulus in the waveguide cladding (see Sec. 2.5). Thus, a method to increase the excitation

wave vector is needed to experimentally observe the resonance, which can be achieved e.g., using a coupling grating or prism [60]. In a simulation, however, plane waves possessing arbitrary tangential wave vectors can be used to excite the structure from outside. Contrary to the method presented in [68], I use a transfer matrix formulation completely with tangential wave vectors instead of real-valued incidence angles [67], so that no artificial high-index layers are needed for evanescent coupling to the structure. It has to be noted though that arbitrary large wave vectors in the cladding can lead to unphysical reflection coefficients with moduli greater than one [71].

In order to find the guided modes of a layered structure, the tangential wave vector k_x is varied in a range near the expected guided mode propagation constant and the field amplitudes are calculated. At tangential wave vectors matching a guided mode's propagation constant, the field amplitude moduli in the structure will exhibit a Lorentzian peak [68]. Note that the field amplitude moduli in every layer will exhibit a peak simultaneously, as they are connected by the boundary conditions. The calculations in this work rely on analysis of the reflection amplitude. Fig. 2.8 shows the reflection amplitude modulus of the structure depicted in Fig. 2.3 with film layer refractive index $n_{\mathrm{fi}} = 1.8$ and thickness $d_{\mathrm{fi}} = 500\,\mathrm{nm}$ on a glass substrate ($n_{\mathrm{II}} = 1.52$) and air cladding ($n_{\mathrm{I}} = 1$). Clearly, two narrow peaks

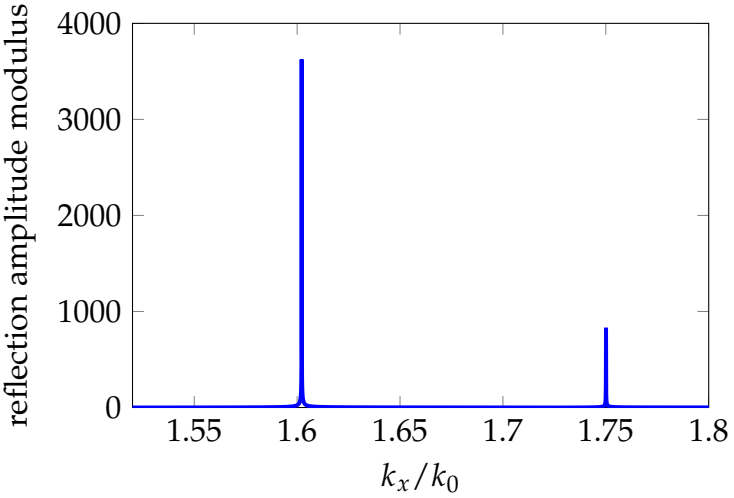

Figure 2.8: Reflection amplitude modulus of a high-index film on glass substrate for varying tangential wave vector excitation. Two narrow peaks arise that are associated with the TE_0 and TE_1 mode supported by the structure at $\lambda_0 = 550\,\mathrm{nm}$.

are present at $k_x/k_0 = 1.60$ and $k_x/k_0 = 1.75$. The peaks correspond to the TE_0 mode and the TE_1 mode supported by the structure with mode

propagation constants $k_x = 1.60k_0$ and $k_x = 1.75k_0$, respectively, at the given wavelength of 550 nm. To automatically determine the guided mode propagation constant, I use the Nelder-mead simplex minimization algorithm [75] (as implemented in the Matlab function *fminsearch*) to find the minimum of the inverse reflection amplitude modulus

$$1 / \left| \underline{E}_{\downarrow}^{(\mathrm{I})} / \underline{E}_{\uparrow}^{(\mathrm{I})} \right| .$$

The minimization start value is chosen manually as the expected mode propagation constant. Note that if multiple guided modes are supported by a structure, the minimization result might not be unique and great care has to be taken when choosing the start value. For most of the structures investigated throughout this work, only one guided mode per polarization will be present, thus making the start value choice less critical.

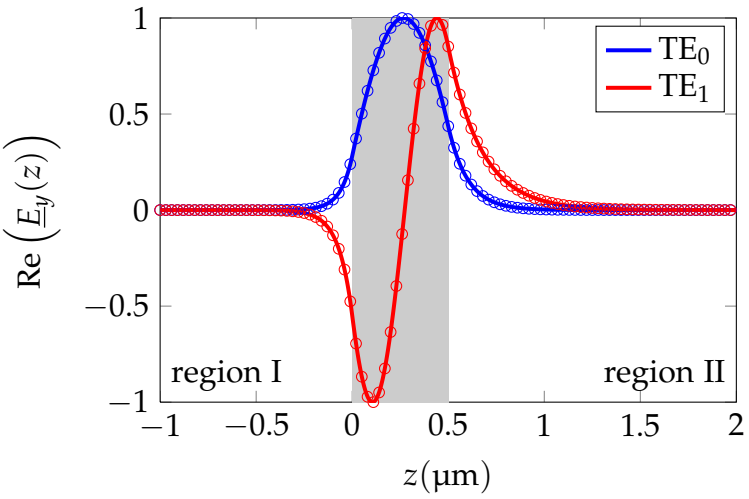

Figure 2.9: Guided mode electric field profiles calculated with the transfer matrix method (solid lines) and CAMFR (circle marks) ($n_{\mathrm{fi}} = 1.8$, $d_{\mathrm{fi}} = 500\,\mathrm{nm}$, $n_{\mathrm{II}} = 1.52$, $n_{\mathrm{I}} = 1$). Shown are the TE_0 mode and TE_1 mode supported by the structure at $\lambda_0 = 550\,\mathrm{nm}$. The transfer matrix method is in excellent agreement with CAMFR.

When the propagation constant of a guided mode has been found, the transfer matrix method can also be used to calculate the mode field profile. Consider the simple waveguide structure shown in Fig. 2.3. As the first step I calculate the fields in the structure beginning with the boundary between region I and the film, given a plane wave excitation of the resonant tangential wave vector. In order to remove the influence of the impinging excitation wave, I then calculate the fields in region I by propagating the backward traveling wave away from the film and assuming the forward-traveling

wave amplitude is zero. The mode profiles obtained with this transfer matrix method are in excellent agreement with CAMFR (see subsection of Sec. 2.7.3) as shown in Fig. 2.9. The guided modes shown in Fig. 2.9 are those identified in Fig. 2.8 for the same exemplary structure.

2.7.2 Perturbation source transfer matrix model

In this section, I will modify the perturbation analysis of dielectric gratings presented by Tamir and Peng [57], Handa et al. [61] to a transfer matrix model. The aim is to calculate the electromagnetic field of a leaky wave that arises from a guided mode of the structure when a periodic index modulation in the wave propagation direction is introduced. In [57, 61] transmission-line networks common in radio-frequency engineering are used to describe the electromagnetic fields. As the transfer matrix method is widely used for optical thin film calculations [48], an implementation of the grating model can be helpful to the optical engineer. Furthermore, the perturbation theory of gratings can provide significant physical insights to the determining factors of waveguide light outcoupling. The formulation will be restricted to TE polarization and propagation perpendicular to the grating grooves.

Perturbation ansatz

In the following, the perturbation analysis presented in [57] is reviewed. The analysis considers a thin-film structure with grating layer as shown in Fig. 2.4. The structure is described by a permittivity function $\epsilon(x,z)$. In order to calculate the electromagnetic fields, the permittivity of the actual structure is split in an unperturbed waveguide $\epsilon_{\mathrm{u}}(z)$ and a perturbation structure $\epsilon_{\mathrm{p}}(x,z)$

$$\epsilon(x,z) = \epsilon_{\mathrm{u}}(z) + \epsilon_{\mathrm{p}}(x,z). \tag{2.56}$$

For the unperturbed waveguide, the grating layer ($d_{\mathrm{fi}} \leq z < d_{\mathrm{fi}} + d_{\mathrm{gr}}$) is replaced with an uniform layer of averaged permittivity

$$\epsilon_{\mathrm{g}} = \epsilon_{\mathrm{fi}} \left(1 - \frac{l_{\mathrm{rd}}}{\Lambda}\right) + \epsilon_{\mathrm{II}} \frac{l_{\mathrm{rd}}}{\Lambda}, \tag{2.57}$$

so that an unperturbed structure

$$\epsilon_{\mathrm{u}}(z) = \begin{cases} \epsilon_{\mathrm{g}} & \text{if } d_{\mathrm{fi}} \leq z < d_{\mathrm{fi}} + d_{\mathrm{gr}} \\ \epsilon(z) & \text{else} \end{cases} \tag{2.58}$$

with uniform layers in x-direction is obtained. The superposed perturbation term $\epsilon_\mathrm{p}(x,z)$ is zero everywhere except in the grating layer. In the grating layer, $\epsilon_\mathrm{p}(x,z)$ is the permittivity modulation around the average permittivity ϵ_g (Eq. (2.57)). The electromagnetic fields in the actual structure are expressed by

$$\begin{aligned}\vec{E} &= \vec{E}_\mathrm{u} + \vec{E}_\mathrm{p},\\ \vec{H} &= \vec{H}_\mathrm{u} + \vec{H}_\mathrm{p},\end{aligned} \tag{2.59}$$

where $\vec{E}_\mathrm{u}$ and $\vec{H}_\mathrm{u}$ are the fields in the unperturbed waveguide and $\vec{E}_\mathrm{p}$ and $\vec{H}_\mathrm{p}$ are the perturbation fields. Let us assume that the field in the unperturbed waveguide is a guided mode with propagation constant k_{x0} given by

$$\underline{E}_{\mathrm{u}y}(x,z) = \underline{V}_\mathrm{u}(z)\exp(jk_{x0}x). \tag{2.60}$$

Introducing (2.59) and (2.56) into Maxwell's equations (2.1)-(2.2) one obtains for the perturbation fields, assuming time-harmonic fields and noting that $\vec{E}_\mathrm{u}$ and $\vec{H}_\mathrm{u}$ fulfill Maxwell's equations on the unperturbed waveguide separately [57],

$$\begin{aligned}\nabla\times\underline{\vec{E}}_\mathrm{p} &= -j\omega\mu_0\underline{\vec{H}}_\mathrm{p},\\ \nabla\times\underline{\vec{H}}_\mathrm{p} &= j\omega\left(\epsilon_\mathrm{u}\underline{\vec{E}}_\mathrm{p} + \epsilon_\mathrm{p}\underline{\vec{E}}_\mathrm{p} + \epsilon_\mathrm{p}\underline{\vec{E}}_\mathrm{u}\right).\end{aligned} \tag{2.61}$$

Here, $\epsilon_\mathrm{p}\underline{\vec{E}}_\mathrm{p}$ may be assumed as second-order compared to the other terms and is omitted in the approximation [57]. The term $\epsilon_\mathrm{p}\underline{\vec{E}}_\mathrm{u}$ is seen as a source term so that (2.61) expresses the inhomogeneous Maxwell's equations for the perturbation fields $\underline{\vec{E}}_\mathrm{p}$ and $\underline{\vec{H}}_\mathrm{p}$ along the unperturbed waveguide $\epsilon_\mathrm{u}(z)$. By taking the derivatives, the equations (2.61) can be brought into the wave equation form for TE polarization

$$\frac{\partial^2\underline{E}_{\mathrm{p}y}}{\partial z^2} + \frac{\partial^2\underline{E}_{\mathrm{p}y}}{\partial x^2} = -\omega^2\mu_0\left(\epsilon_\mathrm{u}\underline{E}_{\mathrm{p}y} + \epsilon_\mathrm{p}\underline{E}_{\mathrm{u}y}\right). \tag{2.62}$$

Note that the electromagnetic fields are y-invariant due to the infinitely extending geometry in this direction (Fig. 2.4). Now, the perturbation quantities are expressed by a Fourier series in x

$$\epsilon_\mathrm{p}(x,z) = \sum_{m\in\mathbb{Z}}\tilde{\epsilon}_m(z)\exp(j2\pi mx/\Lambda), \tag{2.63}$$

$$\underline{E}_{\mathrm{p}y}(x,z) = \sum_{m\in\mathbb{Z}}\underline{V}_m(z)\exp(jk_{xm}x), \tag{2.64}$$

$$k_{xm} = k_{x0} + 2\pi m/\Lambda, \tag{2.65}$$

where $\mathbb{Z}$ denotes the set of integers [57]. The summands in Eq. (2.64) are called (field) space harmonics with amplitude $\underline{V}_m$ where m is the diffraction order. Insertion of the ansatz Eq. (2.63)-(2.65), and Eq. (2.60) into the wave equation (2.62) yields

$$\begin{aligned}\sum_{m\in\mathbb{Z}} \frac{\partial^2 \underline{V}_m}{\partial z^2} \exp\left(jk_{xm}x\right) - \sum_{m\in\mathbb{Z}} \underline{V}_m k_{xm}^2 \exp\left(jk_{xm}x\right) = \\ -\omega^2\mu_0 \left(\sum_{m\in\mathbb{Z}} \left(\epsilon_\mathrm{u}\underline{V}_m + \tilde{\epsilon}_m \underline{V}_\mathrm{u}\right) \exp\left(jk_{xm}x\right) \right).\end{aligned} \tag{2.66}$$

As the functions $\exp\left(jk_{xm}x\right)$ form a fundamental system [76], Eq. (2.66) yields an independent wave equation for each space harmonic amplitude $\underline{V}_m$

$$-\frac{\partial^2 \underline{V}_m(z)}{\partial z^2} = \left(\omega^2\mu_0\epsilon_\mathrm{u}(z) - k_{xm}^2\right) \underline{V}_m(z) + \omega^2\mu_0\tilde{\epsilon}_m(z)\underline{V}_\mathrm{u}(z). \tag{2.67}$$

Tamir and Peng [57], Handa et al. [61] solve (2.67) by transmission-line methods and obtain the leaky-wave field as well as its attenuation constant. In the following, I will develop a formulation of the above model in the widely used transfer matrix framework (see Sec. 2.7.1).

Derivation of grating scattering source terms

The inhomogeneous wave equation (2.67) describes the perturbation field harmonics that arise due to guided mode scattering at the grating. In the following, I will show that Eq. (2.67) can be solved for each space harmonic amplitude $\underline{V}_m$ by the transfer matrix approach of two counter-propagating plane waves (Sec. 2.7.1). Usually, the transfer matrix method is used if the field is excited by externally impinging waves [67]. I will use a method proposed by Benisty et al. [46] and described in Sec. 2.7.1 that allows transfer matrix calculations with sources inside the planar structure, as is the case here. The sources are modeled as plane sources at the position $z = z_0$ inside the grating layer, which I will adopt here to approximate the distributed source term $\omega^2\mu_0\tilde{\epsilon}_m(z)\underline{V}_\mathrm{u}(z)$ in Eq. (2.67). This is a valid approximation in case of thin grating layers [61]. Thus, I make the following field ansatz

$$\begin{aligned}\underline{V}_m(z) =& \underline{E}_{m\uparrow}^{(i)} \exp(-jk_{zm}^{(i)}z) + \underline{E}_{m\downarrow}^{(i)} \exp(+jk_{zm}^{(i)}z), \\ \underline{E}_{m\uparrow}^{(i)} =& \underline{e}_{m\uparrow}^{(i)} + \underline{A}_{m\uparrow} \exp(+jk_{zm}^{(\mathrm{gr})}z_0)u(z-z_0), \\ \underline{E}_{m\downarrow}^{(i)} =& \underline{e}_{m\downarrow}^{(i)} + \underline{A}_{m\downarrow} \exp(-jk_{zm}^{(\mathrm{gr})}z_0)u(z-z_0),\end{aligned} \tag{2.68}$$

where $u(z)$ is the Heaviside step function [76] and $i = \mathrm{gr}$ is the index of the grating layer. The splitting of the wave amplitudes $\underline{E}_{m\downarrow}^{(i)}$ and $\underline{E}_{m\uparrow}^{(i)}$ in the i-th layer into a sum of a z-independent amplitude $\underline{e}_{m\downarrow}^{(i)}$ and $\underline{e}_{m\uparrow}^{(i)}$ and the z-dependent Heaviside function satisfies Eq. (2.52) and allows to express the wave amplitudes globally. Note that $\underline{e}_{m\downarrow}^{(i)}$ and $\underline{e}_{m\uparrow}^{(i)}$ will only be calculated implicitly.

The electric field amplitude $\underline{V}_m$ is required to be continuous at the source position $z = z_0$, which yields the source term condition

$$\underline{A}_{m\uparrow} + \underline{A}_{m\downarrow} = 0. \tag{2.69}$$

Insertion of the field ansatz (2.68) in the inhomogeneous wave equation (2.67) allows us to determine the source terms $\underline{A}_{m\uparrow}$ and $\underline{A}_{m\downarrow}$. Let us start with the calculation of the first and second derivate of $\underline{V}_m(z)$. The first derivation of Eq. (2.68) with respect to z yields

$$\begin{aligned}\frac{\partial \underline{V}_m(z)}{\partial z} = \quad & \underline{E}_{m\uparrow}^{(i)}(-jk_{zm}^{(i)})\exp(-jk_{zm}^{(i)}z) \\ & + \underline{E}_{m\downarrow}^{(i)}(+jk_{zm}^{(i)})\exp(+jk_{zm}^{(i)}z) \\ & + \Big(\underline{A}_{m\uparrow}\exp[-jk_{zm}^{(\mathrm{gr})}(z-z_0)] \\ & \qquad + \underline{A}_{m\downarrow}\exp[+jk_{zm}^{(\mathrm{gr})}(z-z_0)]\Big)\,\delta_0(z-z_0),\end{aligned} \tag{2.70}$$

where the third summand is zero due to the sifting property of the Dirac delta function [48, 77] and Eq. (2.69). The second derivative thus reads

$$\begin{aligned}\frac{\partial^2 \underline{V}_m(z)}{\partial z^2} =& -\underline{E}_{m\uparrow}^{(i)}(k_{zm}^{(i)})^2\exp(-jk_{zm}^{(i)}z) \\ & - \underline{E}_{m\downarrow}^{(i)}(k_{zm}^{(i)})^2\exp(+jk_{zm}^{(i)}z) \\ & - jk_{zm}^{(\mathrm{gr})}\Big(\underline{A}_{m\uparrow}\exp[-jk_{zm}^{(\mathrm{gr})}(z-z_0)] \\ & \qquad - \underline{A}_{m\downarrow}\exp[+jk_{zm}^{(\mathrm{gr})}(z-z_0)]\Big)\,\delta_0(z-z_0) \\ =& -(k_{zm}^{(i)})^2\underline{V}_m(z) - jk_{zm}^{(\mathrm{gr})}(\underline{A}_{m\uparrow} - \underline{A}_{m\downarrow})\delta_0(z-z_0).\end{aligned} \tag{2.71}$$

Insertion into the wave equation (2.67) confirms that each space harmonic amplitude $\underline{V}_m$ can be modeled by the transfer matrix ansatz (2.68) of two counter-propagating plane waves with the wave vector z-components

$$k_{zm}^{(i)} = \sqrt{\omega^2\mu_0\epsilon_{\mathrm{u}}^{(i)} - k_{xm}^2} \tag{2.72}$$

in the i-th layer. Here, $\epsilon_{\mathrm{u}}^{(i)}$ denotes the permittivity in layer i of the unperturbed waveguide. Furthermore, the insertion into Eq. (2.67) requires for

the source terms

$$\left(\underline{A}_{m\uparrow} - \underline{A}_{m\downarrow}\right) \delta_0(z - z_0) = -j\frac{\omega^2\mu_0}{k_{zm}^{(\mathrm{gr})}}\tilde{\epsilon}_m(z)\underline{V}_{\mathrm{u}}(z). \tag{2.73}$$

Recalling that $\tilde{\epsilon}_m(z)$ is non-zero only in the grating layer $d_{\mathrm{f}} \leq z < (d_{\mathrm{f}} + d_{\mathrm{g}})$, the right hand side of Eq. (2.73) can be approximated in the case of thin gratings by plane sources expressed by a Dirac delta function. Requiring the integral of both sides of Eq. (2.73) over z to be equal yields, together with the the source term condition (2.69),

$$\underline{A}_{m\uparrow} = -\underline{A}_{m\downarrow} = -j\frac{\omega^2\mu_0}{2k_{zm}^{(\mathrm{gr})}} \int_{d_{\mathrm{f}}}^{d_{\mathrm{f}}+d_{\mathrm{g}}} \tilde{\epsilon}_m(z)\underline{V}_{\mathrm{u}}(z)\,\mathrm{d}z. \tag{2.74}$$

For binary gratings the permittivity perturbation $\tilde{\epsilon}_m(z) = \tilde{\epsilon}_m$ in the grating layer $d_{\mathrm{f}} \leq z < (d_{\mathrm{f}} + d_{\mathrm{g}})$ is a constant and can thus be pulled out of the integral. The integral can then be interpreted as the mode overlap with the grating as will be discussed later. The source plane position z_0 is set to the center of the grating layer. Note that an off-center z_0 might improve the approximation if $\tilde{\epsilon}_m(z)\underline{V}_{\mathrm{u}}(z)$ varies strongly in the grating layer.

In order to calculate the source terms (2.74), the mode profile $\underline{V}_{\mathrm{u}}(z)$ and propagation constant k_{x0} of the guided wave in the unperturbed waveguide has to be determined. I use the transfer matrix resonant excitation method as described in Sec. 2.7.1 to find the guided mode with the profile $\underline{V}_{\mathrm{u}}(z)$. The mode profile is then normalized, such that the time-averaged power per unit length [54]

$$P_0 = \frac{|\,\mathrm{Re}(k_{x0})|}{2\omega\mu_0} \int_{-\infty}^{\infty} |\underline{V}_{\mathrm{u}}(z)|^2\,\mathrm{d}z \tag{2.75}$$

is 1 W/m.

Leaky wave radiation

We can now calculate the leaky wave radiation that arises from the outgoing space harmonics. Each space harmonic in Eq. (2.64) with real normal wave vector component $k_{zm}^{(I)}$ or $k_{zm}^{(II)}$ radiates energy away from the film. The outgoing wave amplitudes of the m-th space harmonic arising from the sources can be calculated with Eq. (2.52) to be

$$\underline{E}_{m\downarrow}^{(\mathrm{I})} = -\frac{t_0\,(r_2 + 1)}{1 - r_0 r_2}\underline{A}_{m\downarrow}$$

in region I and

$$\underline{E}_{m\uparrow}^{(\mathrm{II})} = \frac{t_2\,(r_0+1)}{1-r_0 r_2}\underline{A}_{m\uparrow} \tag{2.76}$$

in region II. The reflection and transmission coefficients r and t are calculated with the transfer matrix method as described in Sec. 2.7.1. Relations (2.17) and (2.6) yield for the m-th harmonic time-average power p_m carried by the outgoing waves

$$p_m^{(I)} = \langle \vec{S}_m^{(I)} \rangle \cdot (-\vec{e}_z) = \frac{1}{2\omega\mu_0}\left|\underline{E}_{m\downarrow}^{(I)}\right|^2 \mathrm{Re}(k_{zm}^{(I)})$$

in region I and

$$p_m^{(II)} = \langle \vec{S}_m^{(II)} \rangle \cdot \vec{e}_z = \frac{1}{2\omega\mu_0}\left|\underline{E}_{m\uparrow}^{(II)}\right|^2 \mathrm{Re}(k_{zm}^{(II)}) \tag{2.77}$$

in region II. The power p_m is per unit length in x- and y-direction. The leaky wave power loss due to radiation is given by

$$\frac{\mathrm{d}P}{\mathrm{d}x} = \sum_m (p_m^{(\mathrm{I})} + p_m^{(\mathrm{II})}), \tag{2.78}$$

where each radiating field harmonic contributes to the power loss [57]. Outside the stopbands and without material absorption, the power loss Eq. (2.78) relates to the leaky wave attenuation constant as [57]

$$\alpha = \frac{1}{2P_0}\frac{\mathrm{d}P}{\mathrm{d}x} = \frac{1}{2P_0}\sum_m (p_m^{(\mathrm{I})} + p_m^{(\mathrm{II})}). \tag{2.79}$$

Eq. (2.79) states that each radiating field harmonic contributes as a summand to α. For binary gratings, the relations (2.74), (2.76), (2.77), and (2.79) yield

$$\begin{aligned} p_m^{(I)} &= \frac{\omega^3\mu_0}{8\left|k_{zm}^{(\mathrm{gr})}\right|^2}|t_0|^2\left|\frac{r_2+1}{1-r_0r_2}\right|^2|\tilde{\varepsilon}_m|^2\left|\int_{d_\mathrm{f}}^{d_\mathrm{f}+d_\mathrm{g}}\underline{V}_\mathrm{u}(z)\,\mathrm{d}z\right|^2\mathrm{Re}(k_{zm}^{(I)}),\\ p_m^{(\mathrm{II})} &= \frac{\omega^3\mu_0}{8\left|k_{zm}^{(\mathrm{gr})}\right|^2}|t_2|^2\left|\frac{r_0+1}{1-r_0r_2}\right|^2|\tilde{\varepsilon}_m|^2\left|\int_{d_\mathrm{f}}^{d_\mathrm{f}+d_\mathrm{g}}\underline{V}_\mathrm{u}(z)\,\mathrm{d}z\right|^2\mathrm{Re}(k_{zm}^{(\mathrm{II})}). \end{aligned} \tag{2.80}$$

Now, the following physical factors of the leaky-wave radiation become clear: The m-th summand of α in Eq. (2.79) is proportional to

- the squared modulus of the unperturbed **mode overlap** with the grating region

$$v_\mathrm{mode} \equiv \left|\int_{d_\mathrm{f}}^{d_\mathrm{f}+d_\mathrm{g}}\underline{V}_\mathrm{u}(z)\,\mathrm{d}z\right|^2, \tag{2.81}$$

- the squared modulus of the m-th **grating Fourier coefficient**

$$|\tilde{\epsilon}_m|^2,$$

- the **standing wave factor** ζ as seen from the grating position and the cavity **Airy factor** v_{Airy} as introduced in Sec. 2.4

$$\left|\frac{r_2+1}{1-r_0r_2}\right|^2 = \zeta_{\text{I}} v_{\text{Airy}} \text{ for } p_m^{(\text{I})}, \tag{2.82}$$

$$\left|\frac{r_0+1}{1-r_0r_2}\right|^2 = \zeta_{\text{II}} v_{\text{Airy}} \text{ for } p_m^{(\text{II})}, \tag{2.83}$$

- and the **directional term**

$$v_{\text{dir,I}} \equiv |t_0|^2 \frac{\omega^3 \mu_0}{8\left|k_{zm}^{(\text{gr})}\right|^2} \text{Re}(k_{zm}^{(\text{I})}) \text{ for } p_m^{(\text{I})}, \tag{2.84}$$

$$v_{\text{dir,II}} \equiv |t_2|^2 \frac{\omega^3 \mu_0}{8\left|k_{zm}^{(\text{gr})}\right|^2} \text{Re}(k_{zm}^{(\text{II})}) \text{ for } p_m^{(\text{II})}. \tag{2.85}$$

Accuracy analysis

I will now analyze the accuracy of the perturbation source transfer matrix method (pTMM) described above. Due to the neglect of $\epsilon_{\text{p}}\vec{E}_{\text{p}}$ in the wave equation (2.62) and the plane source approximation of the extended sources as made in Eq. (2.73), the model is expected to be most accurate for small grating depths d_{gr}. As an example geometry I thus choose a binary grating with depth $d_{\text{gr}} = 10\,\text{nm}$ together with film thickness $d_{\text{fi}} = 190\,\text{nm}$, refractive indices $n_{\text{I}} = 1.00$, $n_{\text{fi}} = 1.80$, and $n_{\text{II}} = 1.52$, and a grating period of $\Lambda = 800\,\text{nm}$ (see Fig. 2.4). The fundamental TE mode attenuation constant of this structure at $\lambda_0 = 550\,\text{nm}$ wavelength has been calculated with pTMM and RCWA with results depicted in Fig. 2.10. At the given wavelength, the field space harmonics of orders $n = -1 \ldots -4$ radiate energy away from the film as they posses real normal wave vector components in both outside regions or region II only according to Eq. (2.65) and Eq. (2.72). All other perturbation field space harmonics are evanescent in region I and region II. Fig. 2.10 depicts the pTMM results with an increasing number of perturbation field space harmonics taken into account. Clearly, the pTMM result's deviation from the RCWA result decreases as the number of considered field harmonics is increased. If all four propagating field harmonics are taken into account, the pTMM result matches the RCWA

result almost exactly. Fig. 2.10 also shows that the first-order ($n = -1$) space harmonic causes the main radiation loss. This can be understood from Eq. (2.80) as grating's first Fourier coefficient modulus dominates.

In order to further quantify the pTMM accuracy, Fig. 2.11 depicts the fundamental TE mode attenuation constant α in the previously given grating waveguide with an increasing grating depth, while keeping the total thickness $d_{\mathrm{fi}} + d_{\mathrm{gr}} = 200\,\mathrm{nm}$ constant. Although the shown grating depths up to 100 nm clearly exceed the thin grating approximation, the general behavior of α (Fig. 2.11(a)) can be explained with pTMM. Thus the physical factors identified in Eq. (2.80) still play an important role even for large grating depths.

Fig. 2.11b depicts the maximal relative error of α in a given duty cycle range $\mathbb{F}$

$$\delta = \max_{f_{\mathrm{dc}} \in \mathbb{F}} \left| \frac{\alpha_{\mathrm{pTMM}}(f_{\mathrm{dc}}) - \alpha_{\mathrm{RCWA}}(f_{\mathrm{dc}})}{\alpha_{\mathrm{RCWA}}(f_{\mathrm{dc}})} \right| \cdot 100. \tag{2.86}$$

Clearly, pTMM suffers the largest errors for duty cycles below 0.25 and above 0.75. If only duty cycles in the range between 0.25 and 0.75 are considered, the maximal relative error δ is less than 10 % up to grating depths of 55 nm. Thus, the pTMM can provide a good approximation up to these grating depths with the intuitively accessible physical factors in Eq. (2.80).

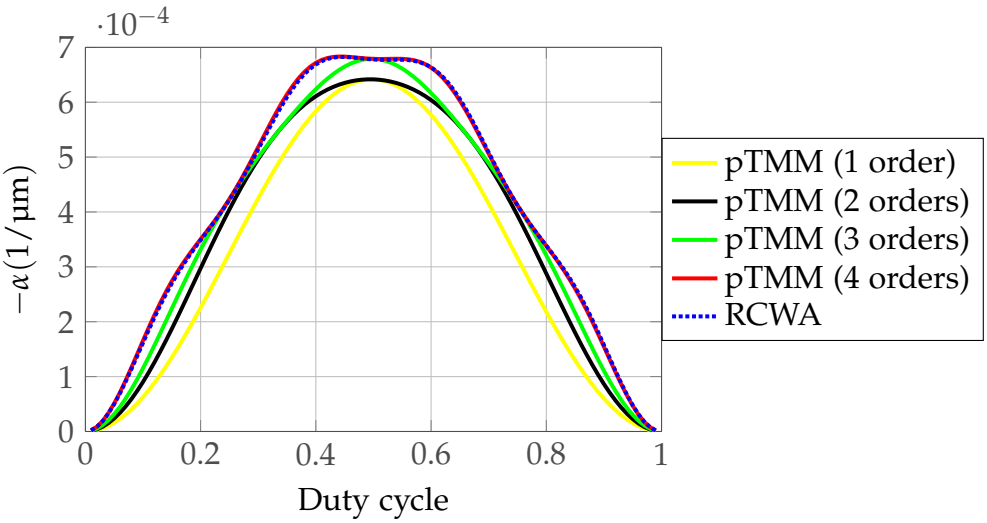

Figure 2.10: Fundamental TE mode attenuation constant of a waveguide with 10 nm grating depth, calculated with pTMM and RCWA at $\lambda_0 = 550$ nm. If all four propagating space harmonics ($m = -1... -4$) are taken into account, the pTMM matches the RCWA result almost exactly. The figure also shows the dominant contribution of the $m = -1$ space harmonic to α, which is responsible for the main part of radiation loss.

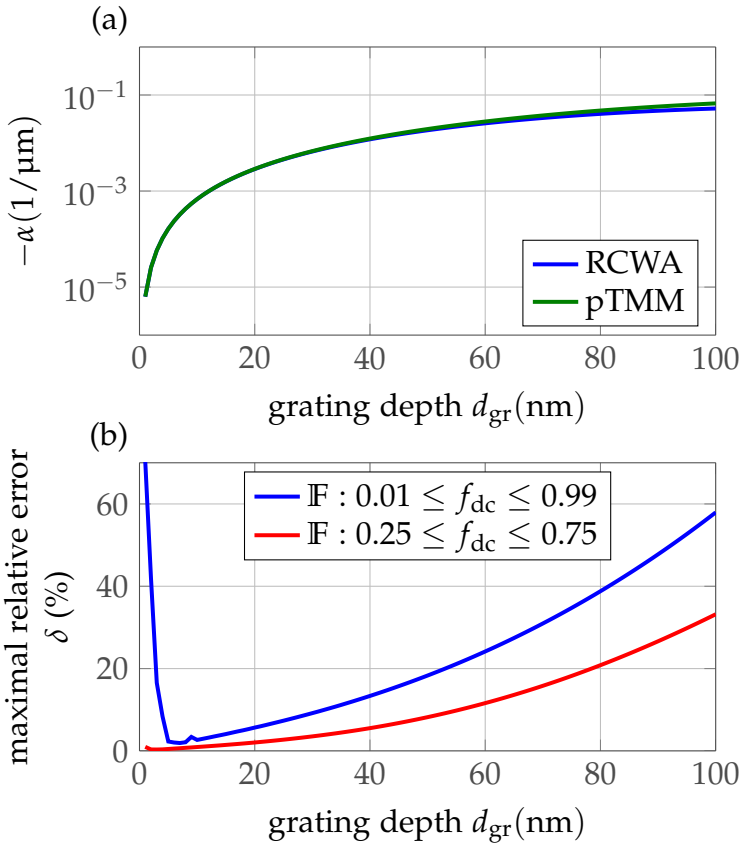

Figure 2.11: pTMM accuracy for exemplarily chosen grating waveguide with $\Lambda = 800\,\text{nm}$ period and total thickness $d_{fi} + d_{gr} = 200\,\text{nm}$ at $\lambda_0 = 550\,\text{nm}$. (a) TE_0 mode attenuation constant (logarithmic scale) for increasing grating depth and constant duty cycle of 0.5. The pTMM is capable of describing the general attenuation constant behavior at increasing grating depth. But the deviation from the rigorous result increases with increasing grating depth. (b) Maximal relative attenuation constant error δ in a range of duty cycles $\mathbb{F}$. The pTMM is more accurate in the range of duty cycles between 0.25 and 0.75. In this restricted duty cycle range, the pTMM yields attentuation constants with a maximal relative error less than 10 % up to grating depths of 55 nm.

2.7.3 Rigorous Coupled Wave Analysis

The rigorous coupled wave analysis (RCWA) is a method to solve the electromagnetic wave equation in grating structures. RCWA is a state variable method [78] that yields a linear equation system, which can be efficiently solved by matrix algebra software.

The general construction of the RCWA is [78]:

1. General solutions for the electromagnetic field in each region are formulated using amplitude-weighted waves. For example in a homogeneous region this is a sum of weighted Floquet plane waves (Eq. (2.42)). The wave amplitudes in all regions are represented in the vector X.

2. The electromagnetic boundary conditions are applied to the fields of adjacent regions.

3. The relations found in 2. are formulated in the matrix equation

$$\mathbf{A}X = E, \tag{2.87}$$

   where $\mathbf{A}$ is the coefficient matrix of the linear equation system and E is the excitation vector.

Solving the matrix equation yields the wave amplitudes for a given excitation and thereby the electromagnetic fields in the complete structure. Then, e.g., the diffraction efficiencies can be calculated.

I implemented the RCWA formulation for binary gratings given by Moharam et al. [79] in Matlab. In order to treat grating waveguides as shown in Fig. 2.4, I added a film layer to the implementation. I assume Floquet plane waves (Eq. (2.42)) of both z-directions as the general field solution in the film. The extended matrix system is then obtained by matching the tangential fields at the film's boundaries to the adjacent regions equivalently to the process described in [79].

RCWA is widely used to calculate the diffraction of an electromagnetic wave incident on a grating [79, 80]. The incident wave determines the tangential wave vector component k_{x0} so that the coefficient matrix is known. In contrast, if the transverse resonances of the grating waveguide are sought, i.e. the leaky waves (see Sec. 2.6.2), fields that are supported by the structure without external excitation have to be found and k_{x0} is unknown. Consequently, the problem statement is

$$\mathbf{A}(k_{k0})X = 0, \tag{2.88}$$

which is known as the homogeneous problem [62, 69, 72].

Similar to the method to determine the guided modes of a slab waveguide (Sec. 2.7.1), the leaky waves of a grating waveguide can be solved by varying excitation tangential wave vector k_{x0} and examining the amplitude coefficients [72]. If the structure is excited at a value of k_{x0} that allows for a non-trivial solution ($X \neq 0$) of the homogeneous problem, the amplitude coefficients will exhibit a pole [69]. Let us denote the outgoing wave amplitudes in region I by R_m^{I}. I use a Nelder-mead simplex minimization algorithm [75] to find a complex k_{x0} that minimizes

$$1 / \sum_m |R_m|. \tag{2.89}$$

This k_{x0} is the mode propagation constant of a leaky wave supported by the grating waveguide. The wave amplitudes X of this leaky wave are then obtained by solving Eq. (2.88), where $\mathbf{A}(k_{k0})$ is now known. However, as the minimization routine only yields an approximate value of k_{x0}, Eq. (2.88) cannot be solved exactly. Instead, I use a singular value decomposition (SVD) [81] of $\mathbf{A}(k_{k0})$ to minimize the left side of Eq. (2.88) in a least squares sense. Thus, X is the singular vector related to the smallest singular value of $\mathbf{A}(k_{k0})$ [82].

Comparison with CAMFR

Finally, I compare the results obtained by my RCWA implementation to the results of the freely available "cavity modelling framework" (CAMFR) [83, 84]. CAMFR is an eigenmode solver for Maxwell's equations and can be applied to a wide range of geometries due to the implementation of perfectly matched layers (PML) [83]. Fig. 2.12 depicts the TE_0 leaky wave dispersion in an exemplary grating waveguide calculated with RCWA and CAMFR. The depicted range of the mode propagation constant $\mathrm{Re}(k_{x0})$ is restricted to the first Brillouin zone [63]. The results obtained by RCWA and CAMFR are in excellent agreement. Note that $\mathrm{Im}(k_{x0})$ is the attenuation constant α and how the stopband at $\Lambda/\lambda_0 = 0.96$ results in a high modulus of α (see Sec. 2.6.3).

RCWA proved to be stable in parameter sweeps over large ranges, e.g. over the film thickness and the wavelength (see Chapter 3). CAMFR requires more manual correction of such sweeps as the PML strength has to be adjusted to the geometry and wavelength. However, I found CAMFR helpful to cross-check some results. In addition, with CAMFR new geometries can be evaluated much faster than with RCWA, since RCWA requires manual derivation of a new system matrix for each new layer configuration.

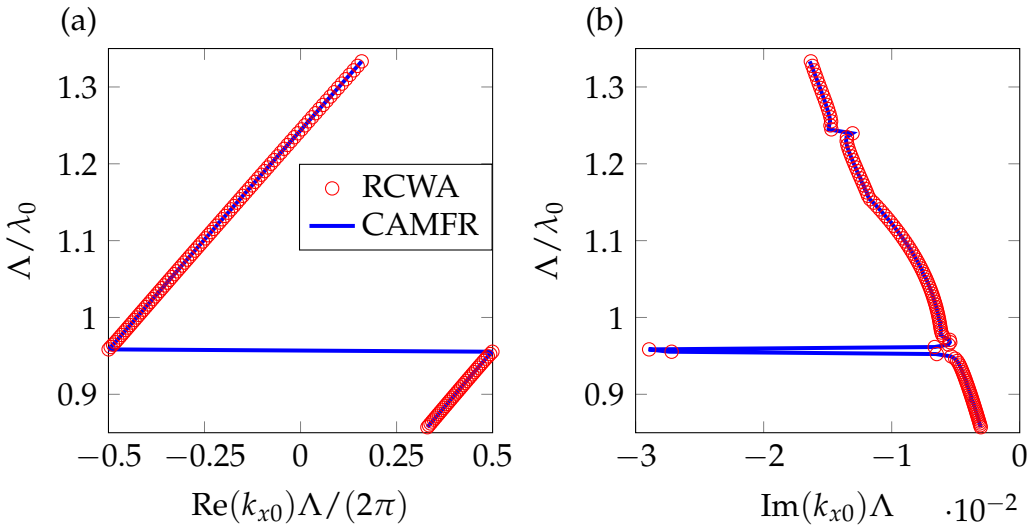

Figure 2.12: TE_0 leaky wave dispersion in a grating waveguide with $\Lambda = 600\,\mathrm{nm}$, $f_{\mathrm{dc}} = 0.5$, $d_{\mathrm{fi}} = 128\,\mathrm{nm}$, $d_{\mathrm{gr}} = 50\,\mathrm{nm}$, $n_{\mathrm{fi}} = 1.8$, $n_{\mathrm{I}} = 1.0$, and $n_{\mathrm{II}} = 1.52$ (see Sec. 2.6). a) Normalized real part of k_{x0} in the first Brillouin zone. b) Normalized imaginary part of k_{x0}.

Chapter 3

Single-period grating light extraction

Summary

This chapter introduces a simple grating OLED model comprising a homogeneous film layer on a glass substrate structured by a binary grating between the substrate and the film. Using the theoretical methods of Chapter 2, the influence of the film thickness, the grating period and the wavelength on the mode attenuation constant α due to radiation is discussed. I demonstrate that the standing wave factor towards the substrate and the mode overlap with the grating are crucial factors for α. An important design rule results that the guided mode outcoupling can be maximized by choosing the grating period depending on the waveguide thickness.

In this chapter, I investigate how the thin-film guided modes in OLED stacks can be efficiently transformed into radiating leaky waves by introduction of a grating layer. In Sec. 2.7.2, I identified the physical factors that determine the guided mode attenuation constant α due to radiation using a perturbation approach. As the radiated power per unit length is proportional to α outside the stopbands (see Sec. 2.6.2), the mode attenuation constant α is used to quantify the guided mode outcoupling. One could argue that any $\alpha < 0$ couples the guided mode to radiation eventually. However, in the presence of material absorption, the coupling to radiation competes with the absorption and hence a high value of α due to outcoupling is desirable. Although the importance of α for guided mode outcoupling from OLEDs has been recognized before [26, 85], systematic studies of α for OLED-like stacks are not available in literature.

Here, I will only consider single-period gratings, i.e. permittivity modulations with a dominant first Fourier coefficient. The waveguide thickness and the grating period are, at least in a limited range, available design parameters for a grating OLED. Understanding the influence of these design parameters on the guided mode outcoupling is thus of great interest. Furthermore, OLEDs are generally broad-wavelength devices, especially when used for general lighting. Hence I will discuss the influence of the waveguide thickness, the grating period, and the wavelength on α assuming a simple OLED-like grating waveguide structure. Using the expressions derived in Sec. 2.7.2 will allow us to identify the most influential factors on α. As these expressions can be physically interpreted, they provide a better understanding than for example the integral equations obtained by coupled mode theory [54]. At the end of this chapter, design rules to maximize the outcoupling will be given.

3.1 Simulation model

A large variety of OLED stacks is described in literature; three stacks are exemplary shown in Table 3.1. Although each OLED in Table 3.1 is comprised of different materials, the refractive indices and stack thicknesses are similar. The organic layers used in OLED stacks mostly have refractive indices of 1.7 to 1.9 in the visible wavelength range [88]. Nevertheless, there are also exceptions such as the conducting polymer poly(3,4-ethylenedioxythiophene) (PEDOT), which has a significantly lower refractive index. From Table 3.1, the overall thin film thickness without cathode is typically 150 nm to 350 nm.

In order to investigate the leaky-wave radiation from a general grating OLED, I model the grating OLED by the simple grating waveguide structure

Table 3.1: Three exemplary OLED stacks described in literature

layer	Frischeisen [86]			Lu and Sturm [22]			Ziebarth and McGehee [24]		
	material	t (nm)	n	material	t (nm)	n	material	t (nm)	n
cathode	MgAg	110		Ag			Ag/Ca	55	
2	Bphen	50	1.77[2][86]	Alq3	80	1.71	polymer	80	1.73[1]
3	CBP	10	1.83[2][86]	PVK	40	1.67	PEDOT	80	1.44[1][87]
4	TPD	40	1.79[2][86]	-	-				
anode	ITO	100	1.90[2][86]	ITO	200	2.00	ITO	150	1.78[1][87]

[1] in-plane at 600 nm
[2] at 475 nm

shown in Fig. 2.4. The organic layers and the anode are modeled by a homogeneous film layer of refractive index $n_{\mathrm{fi}} = 1.80$ and variable thickness d_{fi}. The grating with depth d_{gr}, period Λ and duty cycle f_{dc} is positioned between the substrate and the film. The glass substrate is of refractive index $n_{\mathrm{II}} = 1.52$ and the cladding material is air $n_{\mathrm{I}} = 1.00$. Material absorption and material dispersion are neglected. I speak of the waveguide thickness meaning $d_{\mathrm{fi}} + d_{\mathrm{gr}}$ because according to the unperturbed waveguide (see Sec. 2.6.1), the average refractive index in the grating region is higher than in region II and the grating layer thus contributes to the waveguide core for typical values of f_{dc}.

I simulate structures without top cathode. Clearly, neglecting the cathode is a deviation from real OLEDs as the metallic cathode modifies the cavity. Nevertheless, I will show that the model without cathode gives valuable insight to the guided mode scattering process in OLED-like grating waveguides. Surface plasmon waves, which may occur at the boundary between the metallic cathode and the dielectric layers and constitute another OLED loss mechanism [33, 89–91], are not considered in this work. However, scattering at gratings has also been demonstrated to be an efficient technique for outcoupling of surface plasmons in OLEDs [33, 89, 92].

3.2 Number of guided modes

If the grating layer is thin, the guided modes in the grating waveguide possess propagation constants closely given by the guided mode propagation constants of the unperturbed waveguide without grating [45]. Thus, I approximately calculate the number of guided modes supported by the OLED-like grating waveguide described in Sec. 3.1 and their propagation constants using the unperturbed waveguide with averaged permittivity grating layer (see Sec. 2.6.1). A constant grating layer thickness $d_{\mathrm{gr}} = 50\,\mathrm{nm}$ and a duty cycle of 0.5 are assumed yielding an averaged grating layer

refractive index of 1.67 (Eq. (2.37)). The modes' effective indices versus film thickness d_{fi} are shown in Fig. 3.1 for a wavelength of $\lambda_0 = 550\,\mathrm{nm}$. The waveguide supports an increasing number of guided modes with in-

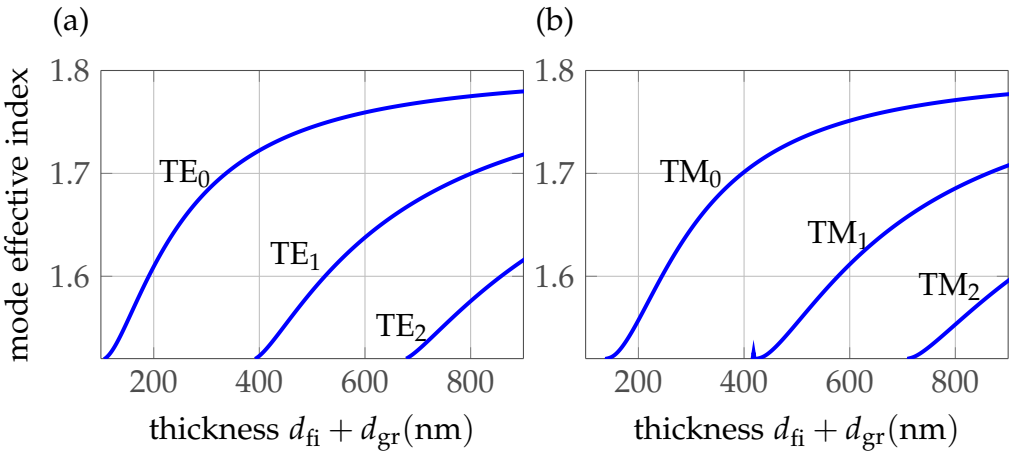

Figure 3.1: Effective mode indices versus waveguide thickness for $\lambda_0 = 550\,\mathrm{nm}$ in the grating OLED model. (a) TE modes and (b) TM modes. Only the film thickness d_{fi} is varied while the grating layer has a constant thickness of $d_{\mathrm{gr}} = 50\,\mathrm{nm}$.

creasing film thickness. In the range of typical thickness of an OLED stack between 100 nm and 400 nm only the fundamental TE_0 and TM_0 modes are supported. The following investigation is restricted to TE polarization and waveguide thicknesses $d_{\mathrm{fi}} + d_{\mathrm{gr}} \leq 400\,\mathrm{nm}$. By designing the grating waveguide such that the TE_0 mode attenuation constant α is high, TE polarized light cannot be guided in the thin films without radiating strongly. This reduces the amount of waveguide light and thereby one of the major OLED loss channels. I expect that many principles found for TE polarization can also be transferred to TM polarization.

3.3 Guided mode outcoupling intensity

This section discusses the leaky-wave radiation from the grating waveguide described in Sec. 3.1. I calculated the TE_0 mode attenuation constant α with RCWA (see Section 2.7.3) in a range of the film thickness d_{fi} from 50 nm to 350 nm and wavelengths in the visible range from 400 nm to 700 nm. The grating depth is chosen $d_{\mathrm{gr}} = 50\,\mathrm{nm}$ and the duty cycle is $f_{\mathrm{dc}} = 0.5$. The results for various grating periods are shown in Fig. 3.2.

The depicted mode attenuation constant exhibits multiple vertical line-shaped regions with high values, e.g. at $\lambda_0 = 650\,\mathrm{nm}$ and $d_{\mathrm{fi}} + d_{\mathrm{gr}} = 300\,\mathrm{nm}$

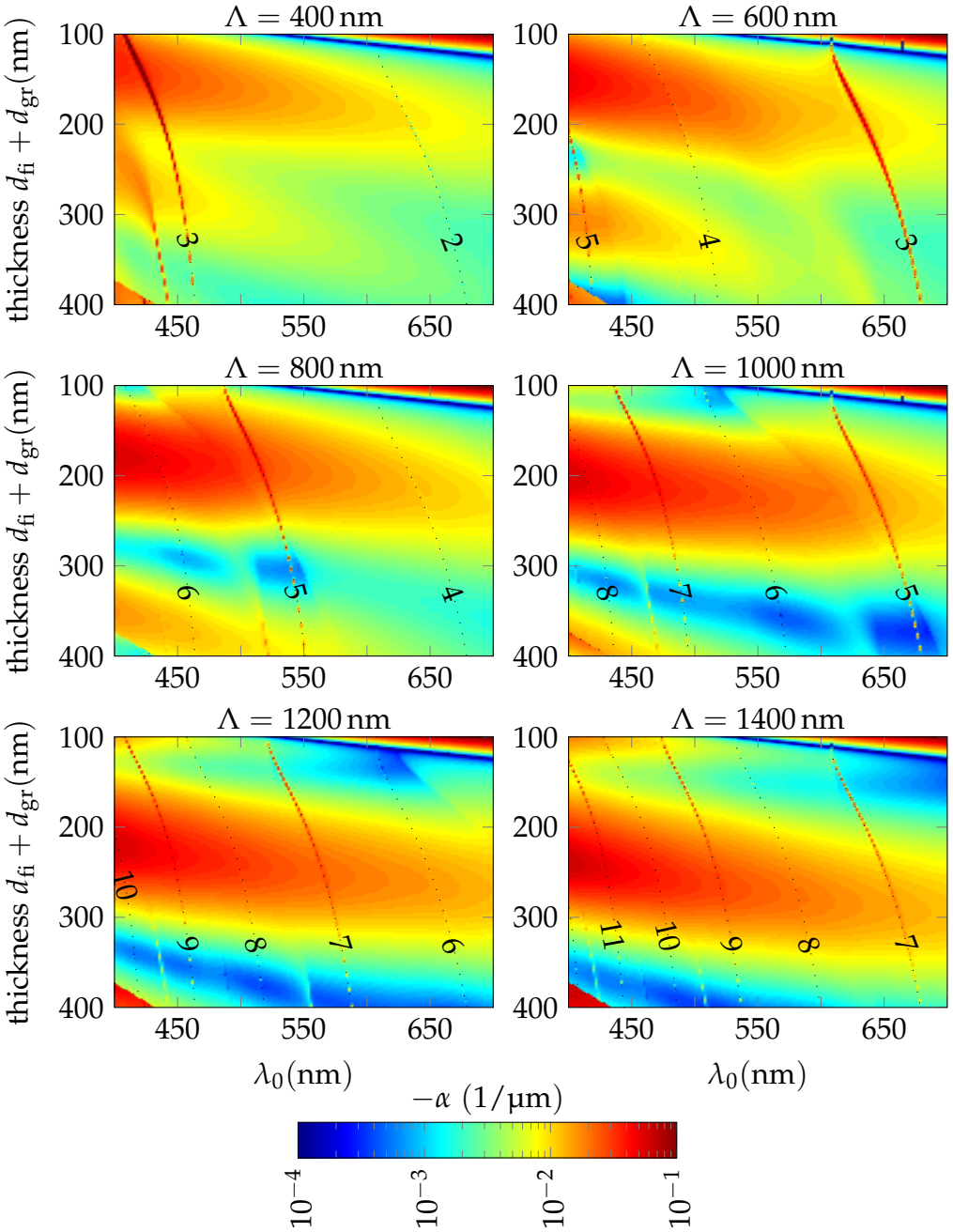

Figure 3.2: TE_0 attenuation constant α over wavelength and waveguide thickness ($d_{gr} = 50\,\text{nm}$, $f_{dc} = 0.5$). The dotted lines mark the Bragg condition numbered by the order N. Outside the stopbands, α at constant wavelength exhibits a maximum. As the grating period is increased, thicker waveguides are needed to obtain the maximum attenuation constant.

for $\Lambda = 600\,\text{nm}$ grating period. These are stopbands, which can occur when

the mode phase constant β_0 matches the Bragg condition

$$\beta_0 = \frac{\pi}{\Lambda} N, \tag{3.1}$$

with $(N \in \mathbb{Z})$ (see Sec. 2.6.3). The Bragg conditions are marked in Fig. 3.2 with black lines. Obviously, for the given grating with duty cycle 0.5, the mode attenuation constant α exhibits peaks only at stopbands with odd N values. For even values of N, the grating's Fourier coefficients $\tilde{\epsilon}_N$ are zero due to its symmetric shape. This can result in negligible coupling between the forward- and backward-propagating guided modes such that no α peak is observed [93]. Outside the stopbands the attenuation constant α is solely due to leaky-wave radiation [49].

Fig. 3.2 shows that the TE_0 attenuation constant α outside the stopbands exhibits a broad maximum with respect to the waveguide thickness, which has little wavelength dependence. As the wavelength decreases, the α-maximum value increases while the maximum position slightly shifts towards a smaller thickness. In the wavelength range shown, highest α values outside the stopbands occur at the shortest wavelength ($\lambda_0 = 400\,\text{nm}$). Clearly, in a region of thicknesses $d_{\text{fi}} + d_{\text{gr}}$ around the maximum, the deviation of α from its maximum value is small. E.g., at $\lambda_0 = 500\,\text{nm}$, α deviates from its maximum value less than 10 % in a region of about 40 nm thickness for $\Lambda = 400\,\text{nm}$ and $\Lambda = 800\,\text{nm}$ (see Fig. 3.3a). As the grating period increases, the α-maximum shifts towards a larger waveguide thickness. In order to explain this maximum and its location, I will use the pTMM perturbation model (Sec. 2.7.2). Sec. 3.3.1 discusses the α-maxima at constant wavelengths. Subsequently, Sec. 3.3.2 discusses the wavelength dependence.

Near the limits of the simulated waveguide thickness, the results exhibit two features. Firstly, all graphs in Fig. 3.2 show high α values in the region of small waveguide thickness $d_{\text{fi}} + d_{\text{gr}} \approx 100\,\text{nm}$ and large wavelength $\lambda_0 > 600\,\text{nm}$. This can be explained by the TE_0 mode cut-off occurring in this region (see Sec. 2.5). Secondly, the discontinuity of α in the lower left corner of all graphs (large thickness and small wavelength), results from a jump in the method's mode choice from the TE_0 mode to the TE_1 mode. As visible in Fig. 3.1, the structure supports a TE_1 mode at thicknesses $d_{\text{fi}} + d_{\text{gr}} \geq 400\,\text{nm}$ at $\lambda_0 = 550\,\text{nm}$. At shorter wavelengths, the TE_1 mode exists at smaller thicknesses, so that at $\lambda_0 = 400\,\text{nm}$, the TE_1 mode starts to exist in structures with $d_{\text{fi}} + d_{\text{gr}} \geq 245\,\text{nm}$. The RCWA algorithm, as implemented here, converges to a mode according to a given mode effective index start value (see Sec. 2.7.3). Here, I chose the start value $n_{\text{eff}} = 1.65$ and only in the small described regions of discontinuity, the TE_1-mode is calculated instead of the TE_0 mode.

3.3.1 Waveguide thickness and grating period

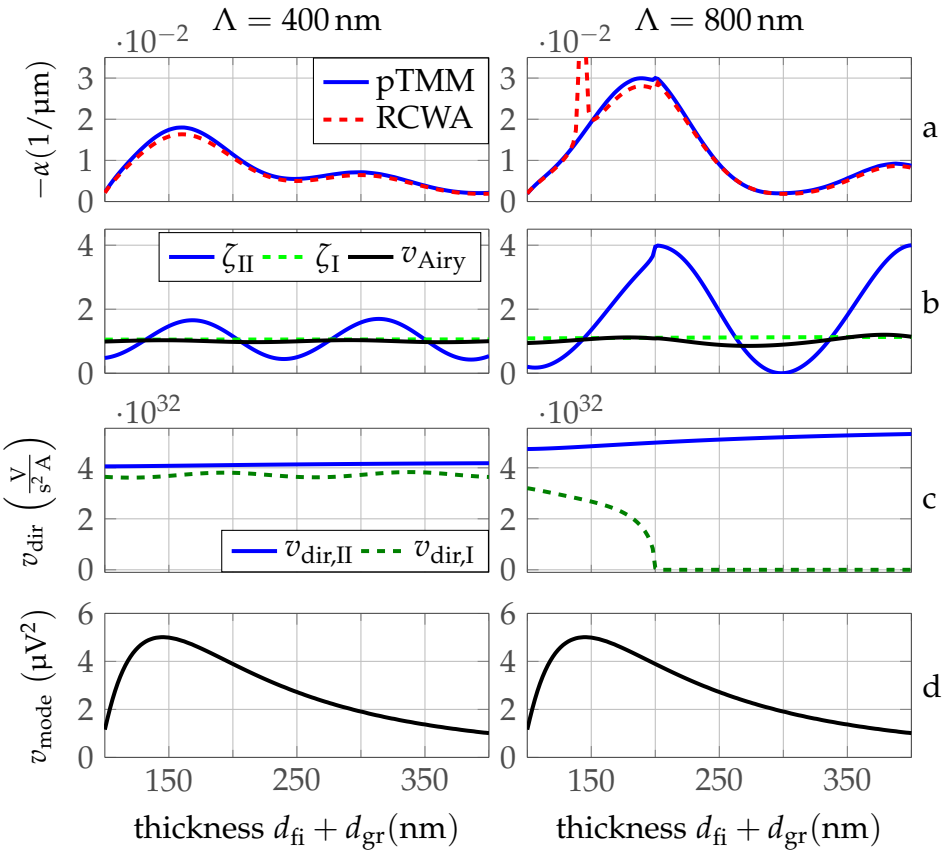

Figure 3.3: a) TE_0 attenuation constant α in grating waveguides with 400 nm and 800 nm period, $d_{gr} = 50$ nm depth and varying film thickness d_{fi} at $\lambda_0 = 500$ nm. For the pTMM result (blue line), only $m = -1$ is retained. b)-d) Physical factors of the radiation power terms into air (region I) and glass (region II) according to (2.80): b) The standing wave factors ζ_I and ζ_{II}, the cavity Airy factor v_{Airy}, c) the directional terms $v_{dir,I}$ and $v_{dir,II}$ and d) the modulus squared mode overlap v_{mode}. The standing wave factor ζ_{II} towards the glass substrate leads to the maxima in the α-curve. The decreasing mode overlap with the grating region at increasing film thickness causes the decrease of α.

Fig. 3.3a depicts the TE_0 attenuation constant α at $\lambda_0 = 500$ nm calculated with pTMM over the waveguide thickness retaining only the first diffraction order. Comparing the α pTMM result for 400 nm period and 800 nm period gratings with the rigorous RCWA result shows that the first diffraction order is sufficient for a good approximation of the attenuation constant. Only the narrow stopband peak at around 140 nm waveguide thickness for

the 800 nm period grating cannot be calculated with pTMM as this peak is not due to cladding or substrate radiation. The graphs b)-d) of Fig. 3.3 show the factors of the first-order space harmonic power in the cladding $p_{-1}^{(\mathrm{I})}$ (green dashed line) and the substrate $p_{-1}^{(\mathrm{II})}$ (blue solid line) according to Eq. (2.80). While the standing wave factors ζ_{I} and ζ_{II} and directional terms $v_{\mathrm{dir,I}}$ and $v_{\mathrm{dir,II}}$ are different for the region I and region II waves, the cavity Airy factor v_{Airy} and the mode overlap v_{mode} are common factors of $p_{-1}^{(\mathrm{I})}$ and $p_{-1}^{(\mathrm{II})}$. The grating Fourier coefficient $\tilde{\epsilon}_{-1} = -0.2959\epsilon_0$ is a constant factor of both first-order wave powers $p_{-1}^{(\mathrm{I})}$ and $p_{-1}^{(\mathrm{II})}$ and has therefore been omitted in Fig. 3.3. Note that in the first-order approximation, the TE_0 mode attenuation constant α is $(p_{-1}^{(\mathrm{I})} + p_{-1}^{(\mathrm{II})})/2$ according to Eq. (2.79), as P_0 has been normalized to $1\,\mathrm{W\,m^{-1}}$.

For a grating period of $\Lambda = 400\,\mathrm{nm}$, the factors ζ_{I}, v_{Airy}, $v_{\mathrm{dir,I}}$ and $v_{\mathrm{dir,II}}$ undergo only small changes over the waveguide thickness (see Fig. 3.3). On the contrary, the standing wave factor towards the substrate ζ_{II} and the mode overlap v_{mode} change by factors of 4 and 5, respectively, in the calculated waveguide thickness range and are thus responsible for the α-curve behavior. Obviously, the maxima of α at $d_{\mathrm{fi}} + d_{\mathrm{gr}} = 160\,\mathrm{nm}$ and $d_{\mathrm{fi}} + d_{\mathrm{gr}} = 300\,\mathrm{nm}$ arise from the standing wave factor towards the substrate, which peaks at $d_{\mathrm{fi}} + d_{\mathrm{gr}} = 168\,\mathrm{nm}$ and $d_{\mathrm{fi}} + d_{\mathrm{gr}} = 314\,\mathrm{nm}$. The shift between the maxima in the α-curve and the ζ_{II}-curve is due to the mode overlap decrease. The mode overlap factor is visible as a general trend in the α-curve, so that the second α-maximum at larger waveguide thickness is lower than the first at smaller thickness.

For a grating period of $\Lambda = 800\,\mathrm{nm}$, the standing wave factor towards the substrate ζ_{II} and the mode overlap v_{mode} again strongly influence the α-curve behavior (see Fig. 3.3). Additionally, the region I wave directional term $v_{\mathrm{dir,I}}$ decreases with waveguide thickness and vanishes for a thickness of 200 nm and above. This waveguide thickness is associated with a small kink in the α-curve, which is also visible in Fig. 3.2.

After identification of the most influential factor terms on the TE_0 mode attenuation constant if the waveguide thickness is changed, I will now investigate the factors in terms of their physical origins.

Standing wave factors and Airy factor

In the grating waveguide a guided mode is coherently scattered at the grating. The scattered light is generated inside the cavity formed by the thin film structure and will thus interfere with reflections. Although the grating waveguide is not a planar structure due to the grating corrugation,

it is approximately modeled by the planar unperturbed waveguide. In the pTMM approximation for thin grating layers, the scattered field is described by field space harmonics (Sec. 2.7.2). These harmonics are plane waves originating at the center of the grating layer $z = z_0$ as shown in Fig. 3.4 with amplitudes $\underline{A}_{m\uparrow}$ and $-\underline{A}_{m\downarrow}$ traveling towards region II and region I, respectively. Note that, according to the way $\underline{A}_{m\downarrow}$ was defined

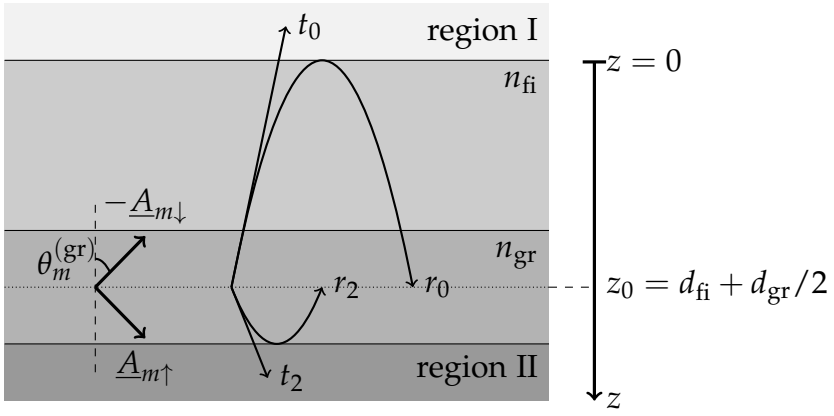

Figure 3.4: Schematic of the grating scattering sources in a simple pTMM OLED model. Each diffraction order m is modeled as two source plane waves originating from the center of the grating layer. The film and grating layer form a cavity with amplitude reflection constants r_0 and r_2 and amplitude transmission constants t_0 and t_2 seen from the source position.

in Eq. 2.68, the source wave traveling in $-z$-direction in Fig. 3.4 has a negative sign. The source wave propagation direction is given by the in-plane wavevector, which depends on the diffraction order m according to Eq. (2.65). Its angle $\theta_m^{(i)}$ with respect to the boundary normal is given by Eq. (2.44), where $i \in \{\mathrm{II}, \mathrm{gr}, \mathrm{fi}, \mathrm{I}\}$ denotes the layer. Besides the diffraction order, the propagation angle depends on the guided mode effective index n_{eff}. As visible in Fig. 3.1, an increased waveguide thickness leads to a higher n_{eff} of the guided mode. With increasing n_{eff}, the propagation angles change according to Eq. (2.44). This is visible in Fig. 3.5a for the angle of the first-order diffracted wave inside the film $\theta_{-1}^{(\mathrm{fi})}$ for the grating periods $\Lambda = 400\,\mathrm{nm}$ and $\Lambda = 800\,\mathrm{nm}$. In these exemplary cases, $\theta_{-1}^{(\mathrm{fi})}$ increases slightly with the waveguide thickness.

The standing wave factors (Eq. (2.30)) and the cavity Airy factor (Eq. (2.27)) describe the interference of the source amplitudes $\underline{A}_{m\uparrow}$ and $-\underline{A}_{m\downarrow}$ inside the cavity (see Sec. 2.4). They are determined by the reflection coefficients relative to the source position. Fig. 3.5b,c depicts the amplitude reflection coefficients r_0 and r_2 for the exemplary cases. Due to the small refractive

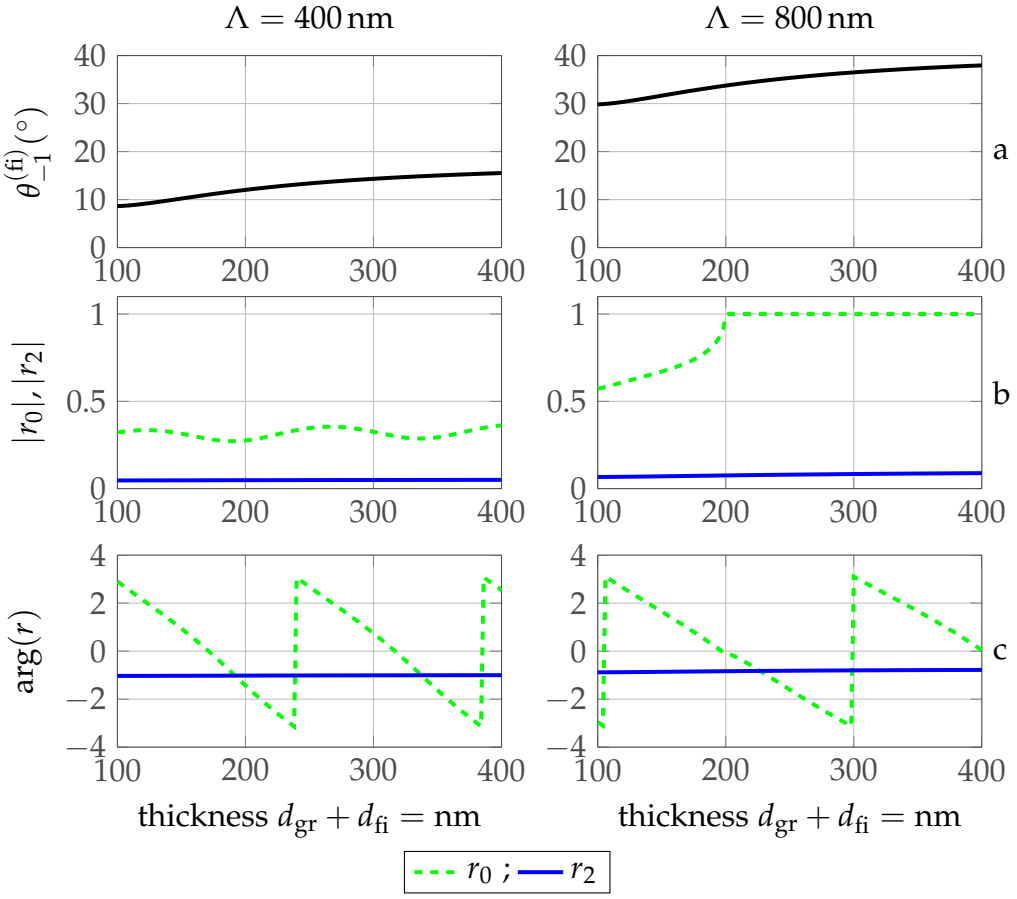

Figure 3.5: a) First diffraction order wave angle in the film and b),c) corresponding amplitude reflection coefficients (TE_0 mode, $\lambda_0 = 500\,\mathrm{nm}$). The reflection at the film-air boundary is much higher than at the grating-glass boundary. Above film angles of 34°, total internal reflection occurs at the film-air boundary.

index difference between the grating layer and the substrate, r_2 is small. On the other hand, the reflection r_0 from the structure part above the source is much higher because of the greater refractive index difference between the film and air. For film angles $\theta_m^{(\mathrm{fi})} > 34°$, the upwards traveling wave is even completely reflected by TIR so that $|r_0| = 1$. This can be observed in Fig. 3.5b for the $\Lambda = 800\,\mathrm{nm}$ grating at a waveguide thickness larger than 200 nm. Thus, the standing wave factor towards the glass substrate ζ_{II} (Fig. 3.3b) reaches values up to 4 according to Eq. (2.30), depending on the phase of r_0.

Constructive source wave interference towards the substrate occurs if the phase of r_0 is an integer multiple of 2π as given in Eqs. (2.31) and (2.32) corresponding to $\arg(r_0) = 0$. Thus, each regular zero-crossing of $\arg(r_0)$

in Fig. 3.5 leads to a maximum of ζ_{II} in Fig. 3.3b. Destructive source wave interference towards the substrate occurs if the phase of r_0 is an uneven integer multiple of π corresponding to $\arg(r_0) = \pm\pi$. Thus, each $\pm\pi$-crossing of $\arg(r_0)$ in Fig. 3.5 leads to a minimum of ζ_{II} in Fig. 3.3b. Note that the arg-operator gives the phase of a quantity in the range between $-\pi$ and π.

The reflection phases $\arg(r_0)$ and $\arg(r_2)$ depend on the wave propagation angle $\theta_m^{(i)}$ and the layer thicknesses. The phase changes due to the wave's traveled path length $2\phi_{0,\mathrm{trip}}$ and $2\phi_{2,\mathrm{trip}}$ are

$$\begin{aligned} 2\phi_{0,\mathrm{trip}} &= -2k_0 \left(n_{\mathrm{gr}} \cos\theta_{-1}^{(\mathrm{gr})} d_{\mathrm{gr}}/2 + n_{\mathrm{fi}} \cos\theta_{-1}^{(\mathrm{fi})} d_{\mathrm{fi}} \right), \\ 2\phi_{2,\mathrm{trip}} &= -2k_0 n_{\mathrm{gr}} \cos\theta_{-1}^{(\mathrm{gr})} d_{\mathrm{gr}}/2, \end{aligned} \tag{3.2}$$

equivalent to Eq. (2.24) but considering the additional grating layer. As the film thickness d_{fi} is increased the path length of the upward traveling wave is highly affected because the source distance to the film-air boundary increases. This leads to a decreasing $2\phi_{0,\mathrm{trip}}$ via Eq. (3.2). Thus, $\arg(r_0)$ strongly depends on the waveguide thickness as visible in Fig. 3.5b. On the other hand, the path length of the downward traveling wave is not directly dependent on d_{fi} (see Eq. (3.2)). Indirectly, $2\phi_{2,\mathrm{trip}}$ depends on d_{fi} via the thickness effect on the propagation angle described above. But as visible in Fig. 3.5b, $\arg(r_2)$ is nearly constant over the waveguide thickness. Here, the indirect influence of d_{fi} on the reflection phase via the change of the propagation angle $\theta_{-1}^{(i)}$ is only small compared to the direct influence of d_{fi} in Eq. (3.2).

Note that the reflection phases possess the additional component ϕ_{refl}, the phase change upon reflection as expressed in Eq. (2.22). For the exemplary cases considered in Fig. 3.5, ϕ_{refl} is only non-zero for the $\Lambda = 800\,\mathrm{nm}$ grating and waveguide thicknesses above 200 nm. In this case, TIR occurs at the film-air boundary (see Fig. 3.5b) and ϕ_{refl} increases from 0 at the critical angle of $\theta_{-1}^{(\mathrm{fi})} = 34^\circ$ to $\pi/4$ at $\theta_{-1}^{(\mathrm{fi})} = 39^\circ$. In Fig. 3.5c, ϕ_{refl} is visible as a small offset of $\arg(r_0)$ but the reflection phase curve is dominated by the path length phase change.

Considering the nearly constant modulus and phase of r_2 with respect to the waveguide thickness, Eq. (2.27) and Eq. (2.30) yield that the cavity Airy factor v_{Airy} and the standing wave factor towards air ζ_{I} are also nearly constant. This explains why v_{Airy} and ζ_{I} have only a small influence on α when the waveguide thickness is changed. On the contrary, the standing wave factor towards the substrate ζ_{II} depends strongly on the film thickness, as the reflection coefficient r_2 has a significant modulus and a phase that

varies strongly with the film thickness. In order to obtain a high α value at a given wavelength and grating period, the film thickness should therefore be designed such that the first-order source waves interfere constructively towards the substrate.

The reflection phase change due to path length $2\phi_{0,\mathrm{trip}}$ can also explain the α-maximum shift towards a thicker waveguide for increasing grating period observed in Fig. 3.2. An increased grating period leads to a larger propagation angle according to Eq. (2.44). In the case of positive propagation angles $\theta_{-1}^{(i)}$, this decreases $\cos\theta_{-1}^{(i)}$. If $2\phi_{0,\mathrm{trip}}$ is an integer multiple of 2π for the smaller grating period at a given d_{fi}, so that the constructive interference condition is met, then, according to Eq. (3.2), the smaller $\cos\theta_{-1}^{(i)}$ requires a larger value of d_{fi} to yield the same phase change and thereby constructive interference again. Note that in case of negative propagation angles $\theta_{-1}^{(i)}$, $\cos\theta_{-1}^{(i)}$ increases with the angle and the α-maximum shifts towards a thinner waveguide for increasing grating period.

Finally note the kink in the standing wave factor towards the substrate ζ_{II} at $d_{\mathrm{gr}} + d_{\mathrm{fi}} = 200\,\mathrm{nm}$ visible in Fig. 3.3b for $\Lambda = 800\,\mathrm{nm}$. As the propagation angle inside the film $\theta_m^{(\mathrm{fi})}$ approaches the critical angle of TIR (Sec. 2.3), the modulus of the reflection coefficient r_0 steeply increases as shown in Fig. 3.5b for $\Lambda = 800\,\mathrm{nm}$ at $d_{\mathrm{gr}} + d_{\mathrm{fi}} = 200\,\mathrm{nm}$. At the same time, the first-order wave in air vanishes. The onset of TIR is associated with a kink in the RCWA and pTMM α-curve in Fig. 3.3a. In Fig. 3.2 for the grating periods $\Lambda = 800\,\mathrm{nm}$ and $\Lambda = 1000\,\mathrm{nm}$ the rapid change of ζ_{II} becomes visible as lines of discontinuity in the α-plot that are not parallel to the Bragg lines. In the study of grating reflection, the rapid changes occurring at the onset or disappearance of a diffraction order are called Rayleigh anomalies [62, 69, 94]. In the study of guided waves in grating waveguides, peaks in the α-curve have also been observed at the onset of a diffraction order [93].

Directional term

The directional terms $v_{\mathrm{dir,I}}$ and $v_{\mathrm{dir,II}}$ depend on the source wave propagation direction via the normal wave vector component in the outside region $k_{zm}^{(I)}$ and $k_{zm}^{(II)}$, respectively, and via the amplitude transmission coefficient to this outside region t_0 and t_2, respectively (see Eq. (2.85)). As noted previously, the source wave propagation direction is influenced by the waveguide thickness via n_{eff}. Fig. 3.3c for $\Lambda = 800\,\mathrm{nm}$ shows that the directional term $v_{\mathrm{dir,I}}$ decreases strongly as the propagation angle approaches the critical angle of TIR (see Fig. 3.5). Above the critical angle, the real part of the

normal wave vector in the outside region vanishes and according to Eq. (2.85) v_{dir} is zero. Consequently, the upwards traveling wave does not transport power into the air region according to Eq. 2.80.

Mode overlap

In Fig. 3.6, the unperturbed mode overlap with the grating region as defined in Eq. (2.81) is shown for different film thicknesses d_{fi} in the unperturbed waveguide (see Sec. 2.6.1). The grating duty cycle is 0.5. Note that the (unperturbed) mode overlap does not depend on the grating period, as the average grating layer permittivity is only a function of the duty cycle and the adjacent layer permittivities according to Eq. (2.57).

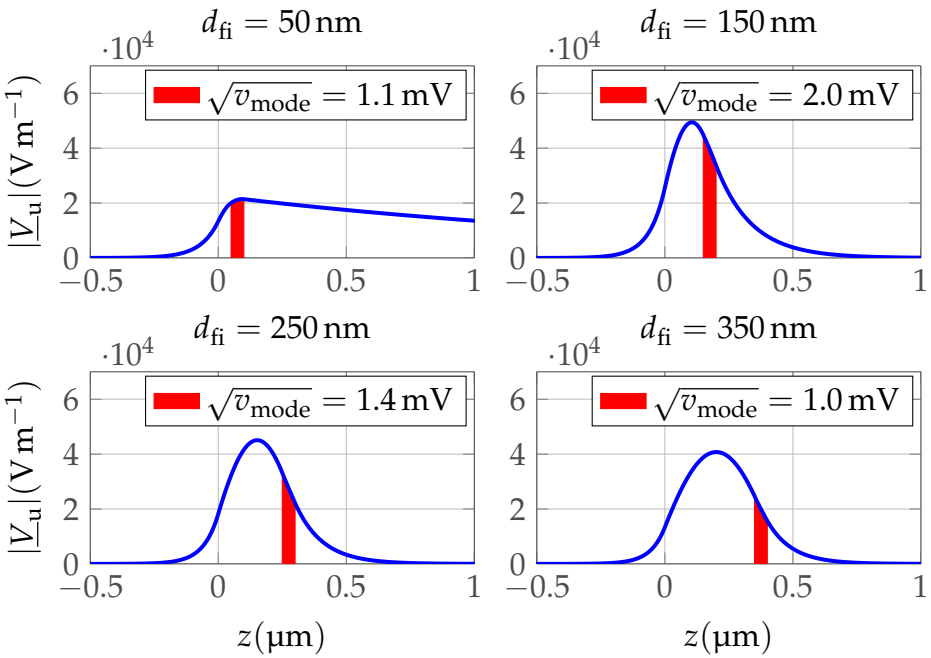

Figure 3.6: TE_0 mode profiles in the unperturbed waveguide with various film thicknesses normalized to $1\,\mathrm{W\,m^{-1}}$ ($\lambda_0 = 500\,\mathrm{nm}$). The air-film boundary is at $z = 0\,\mu\mathrm{m}$. The mode overlap $\sqrt{v_{\mathrm{mode}}}$ with the grating layer is the marked area in red. Around $d_{\mathrm{fi}} = 150\,\mathrm{nm}$ the mode is well confined near the grating layer, resulting in a high mode overlap.

Fig. 3.6 allows us to understand the mode overlap curve in Fig. 3.3. In case of $d_{\mathrm{fi}} = 50\,\mathrm{nm}$, the mode is hardly confined so that the mode overlap with the grating is low. As the film thickness increases, the mode becomes more confined near the grating layer, resulting in a high mode overlap at $d_{\mathrm{fi}} = 150\,\mathrm{nm}$. Further increase of the film thickness leads to a decreasing mode confinement and a shift of the mode energy away from the grating

layer. Thus, the mode overlap at $d_{\mathrm{fi}} = 350\,\mathrm{nm}$ is comparably low as at $d_{\mathrm{fi}} = 50\,\mathrm{nm}$.

3.3.2 Wavelength

The RCWA results depicted in Fig. 3.2 show the general trend of decreasing TE_0 attenuation constant α with larger wavelength, independent of the grating period. Furthermore, the α-maximum shifts towards a thicker waveguide at larger wavelengths. In order to discuss the most influential wavelength effects on α, I will consider two exemplary waveguide gratings of fixed thickness and periods $\Lambda = 400\,\mathrm{nm}$ and $\Lambda = 800\,\mathrm{nm}$. I chose the film thickness such that ζ_{II} exhibits a maximum at $\lambda_0 = 500\,\mathrm{nm}$ yielding constructive interference of the first-order wave towards the substrate. Thus, the film thicknesses are $d_{\mathrm{fi}} = 122\,\mathrm{nm}$ ($d_{\mathrm{fi}} + d_{\mathrm{gr}} = 172\,\mathrm{nm}$) for the 400 nm grating and $d_{\mathrm{fi}} = 150\,\mathrm{nm}$ ($d_{\mathrm{fi}} + d_{\mathrm{gr}} = 200\,\mathrm{nm}$) for the 800 nm grating.

One important effect causing wavelength dependence is angular dispersion. As the mode effective index n_{eff} is a function of the wavelength (see Sec. 2.5), the propagation angles $\theta_m^{(i)}$ of the m-th field space harmonics are also wavelength dependent according to Eq. (2.44). Fig. 3.7a depicts the first-order propagation angle in the film $\theta_m^{(\mathrm{fi})}$. As a consequence of the $\theta_m^{(\mathrm{fi})}$ wavelength dependence, the amplitude reflection and transmission coefficients of the first-order wave are a function of the wavelength as shown in Fig. 3.7b,c. The most prominent change of the reflection coefficients' modulus occurs at the critical angle $\theta_{-1}^{(\mathrm{fi})} = 34^\circ$ as the waves are completely reflected at the film-air boundary. Away from the critical angle, angular dispersion causes only slight changes of $|r_0|$ and $|r_2|$. The reflection coefficient phase is $(2\phi_{\mathrm{trip}} + \phi_{\mathrm{refl}})$ as given in Eq. (2.22). By Eqs. (3.2) and (2.12), the traveled path phase change ϕ_{trip} is proportional to $-1/\lambda_0$, visible as hyperbolic trend in $\arg(r)$. At the same time, the angular dispersion affects ϕ_{trip} through $\cos\theta$ (see Eq. (3.2)). Additionally, a phase change upon reflection ϕ_{refl} for angles above the critical angle occurs as is observable below $\lambda_0 = 500\,\mathrm{nm}$ in the r_0-curve depicted in Fig. 3.7c for $\Lambda = 800\,\mathrm{nm}$. It is interesting to note that in this case, the onset of ϕ_{refl} leads to a broader wavelength region in which constructive source wave interference is closely met.

Fig. 3.8 shows the pTMM factors at varying wavelength for the exemplarily chosen grating waveguides. Clearly, all pTMM factors are functions of the wavelength. Due to the weak reflection from the substrate, the Airy factor v_{Airy} and the standing wave factor towards air ζ_{I} undergo only small changes (see Fig. 3.8b) as discussed previously. Also v_{mode} varies only

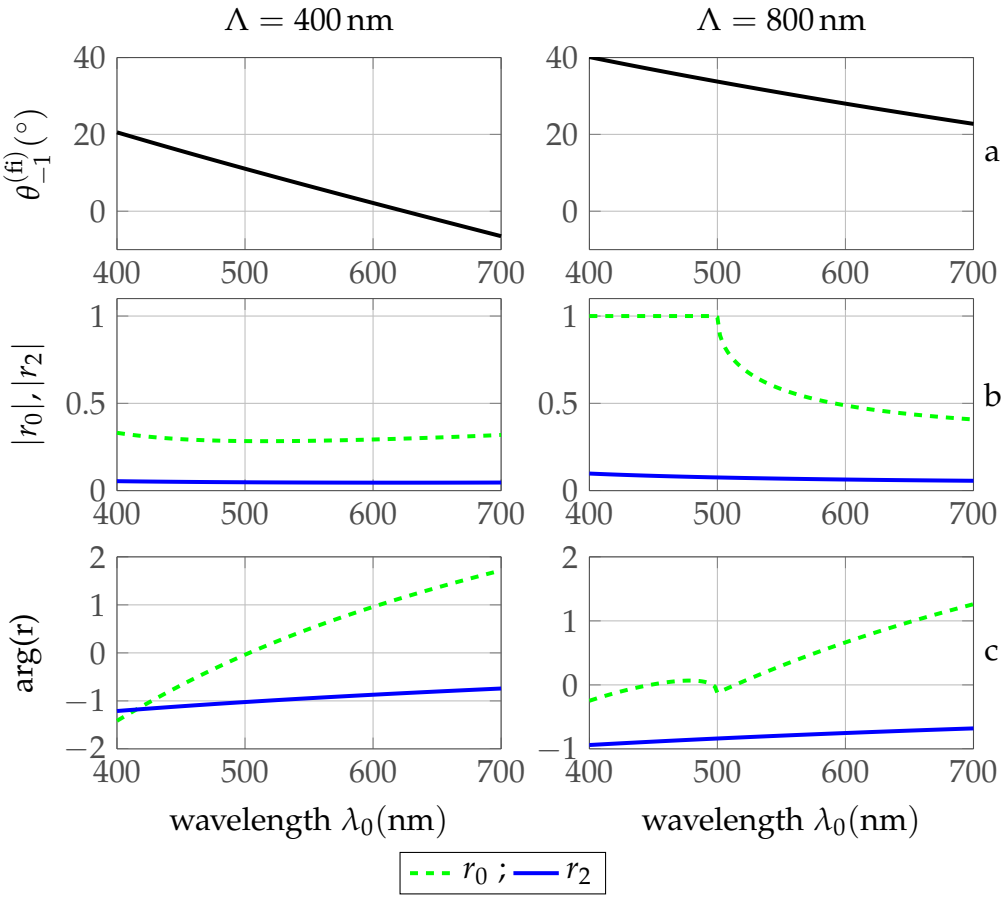

Figure 3.7: a) Wavelength dependence of the first-order diffraction wave film angle and b) reflection coefficients in grating waveguides with 400 nm and 800 nm period, $d_{gr} = 50$ nm depth. The film thickness is $d_{fi} = 122$ nm for the 400 nm grating and $d_{fi} = 150$ nm for the 800 nm grating.

slightly with the wavelength as visible in Fig. 3.8d.

Clearly, the directional terms $v_{dir,I}$ and $v_{dir,II}$ have the greatest influence on the α wavelength dependence. Eq. (2.12) and Eq. (2.85) yield that $v_{dir,I}$ and $v_{dir,II}$ are proportional to ω^2 for a fixed angle. As visible in Fig. 3.8c, for $\Lambda = 400$ nm both $v_{dir,I}$ and $v_{dir,II}$ and for $\Lambda = 800$ nm $v_{dir,II}$ fit well to a squared frequency function. In these cases, angular dispersion has only a small effect on $v_{dir,I}$ and $v_{dir,II}$. However, in case of a film angle close to the critical angle of TIR, angular dispersion can have a dominant effect on the directional term. This can be observed for $\Lambda = 800$ nm above $\lambda_0 = 500$ nm, where the air wave transforms from an evanescent wave to a propagating wave causing a steep rise of $v_{dir,I}$.

Regarding the standing wave factors, we have already seen in in Sec. 3.3.1 that ζ_{II} has a large influence on α as the reflection from the film top is

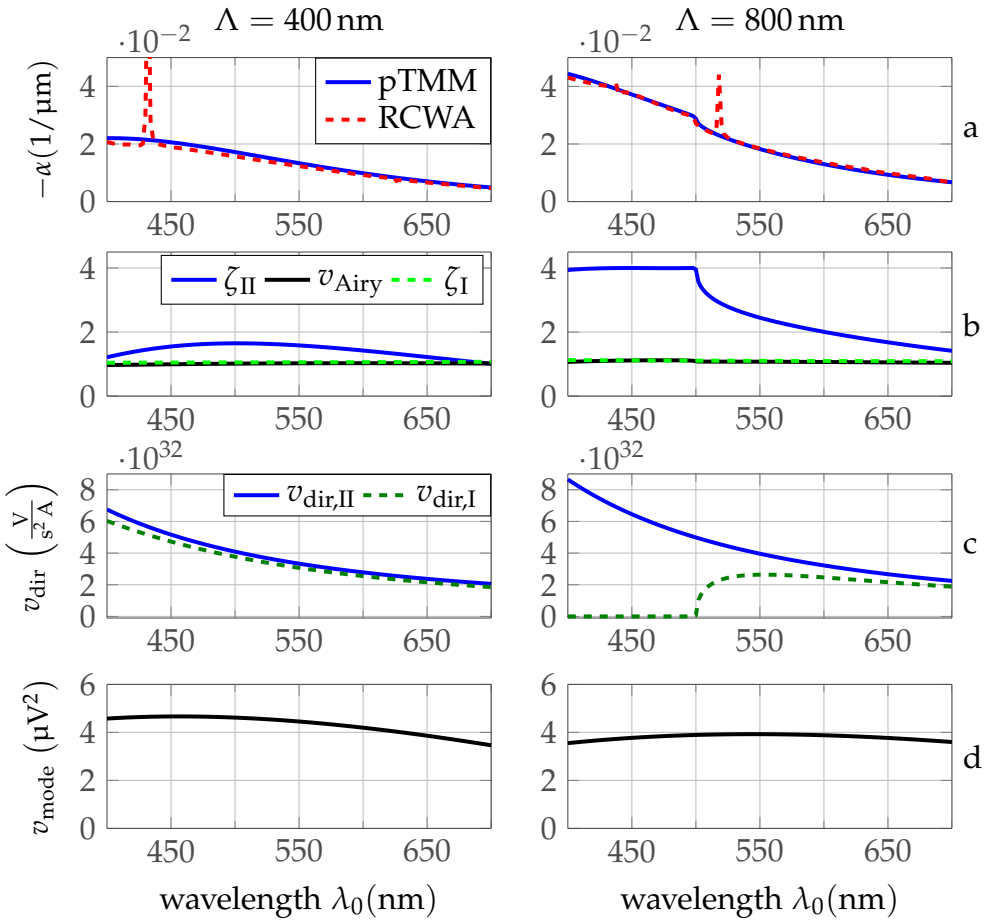

Figure 3.8: a) Wavelength dependence of the TE_0 attenuation constant α in grating waveguides with 400 nm and 800 nm period, and $d_{gr} = 50$ nm depth. b)-d) pTMM physical factors of the leaky-wave radiation. The film thickness was chosen to be $d_{fi} = 122$ nm for the grating with $\Lambda = 400$ nm and $d_{fi} = 150$ nm for the grating with $\Lambda = 800$ nm, so that the standing wave factor ζ_{II} exhibits a maximum at $\lambda_0 = 500$ nm.

generally high. According to Eq. (2.30), ζ_{II} is a function of the amplitude reflection coefficient r_0 and strongly varies with its phase. The phase $\arg(r_0) = 0$ causes constructive interference as is visible in Fig. 3.8b in combination with Fig. 3.7c. Consequently, the remarkably constant ζ_{II} between 400 nm and 500 nm wavelength in case of $\Lambda = 800$ nm is caused by the closely met constructive interference condition of r_0 in this wavelength range.

3.4 Design rules

In the application for grating OLED light extraction, the physical factors of guided mode outcoupling given by pTMM can be used to design the grating and OLED stack.

Certainly, one of the first design decisions is the grating period as it determines the propagation angle of the scattered light. If a direct outcoupling to air of the m-th diffraction order is desired, its in-plane wave vector must be small enough to leave the film and substrate to the air region. Hence Eq. (2.44) yields the condition

$$-m\frac{\lambda_0}{1+n_{\text{eff}}} \leq \Lambda \leq m\frac{\lambda_0}{1-n_{\text{eff}}} \tag{3.3}$$

for the grating period. To make things concrete, assume that the TE_0 mode in the grating waveguide of Sec. 3.1 with $d_{\text{fi}} = 250\,\text{nm}$, $d_{\text{gr}} = 50\,\text{nm}$, and $f_{\text{dc}} = 0.5$ is to be scattered such that the $m = -1$-order can escape to air for the visible wavelength range between $\lambda_0 = 400\,\text{nm}$ and $\lambda_0 = 700\,\text{nm}$. A TMM simulation yields that the effective index is between $n_{\text{eff}} = 1.647$ ($\lambda_0 = 700\,\text{nm}$) and $n_{\text{eff}} = 1.722$ ($\lambda_0 = 400\,\text{nm}$). Thus, Eq. (3.3) yields that the grating period should be between $\Lambda = 264\,\text{nm}$ and $\Lambda = 554\,\text{nm}$. Note that there are also OLED applications in which a coupling into substrate modes is desirable. One example will be discussed in Chapter 6. It is also conceivable to scatter the guided mode first into substrate modes and employ substrate outcoupling techniques [95, 96] to couple the light to the air region eventually.

In order to achieve a high mode attenuation constant α and thus strong coupling between the guided mode and radiation, generally all space harmonic powers in the exterior regions p_m^{I} and p_m^{II} have to be maximized according to Eq. (2.79) via their factors given in Eq. (2.80). In the case of a single period grating with a dominant first-order Fourier coefficient

$$|\tilde{\epsilon}_{-1}|^2 \gg |\tilde{\epsilon}_m|^2 \quad (|m| > 1),$$

p_{-1}^{I} and p_{-1}^{II} will be the largest summands in Eq. (2.79) and it is generally sufficient to maximize these. It is important to note that an optimization of one OLED stack parameter, e.g. the layer thicknesses, will generally affect more than one factor in Eq. (2.80). Nevertheless, for the grating waveguide given by Fig. 2.4 and the assumed refractive indices (see Sec. 3.1), I have identified dominating factors. I found that the strongest reflection occurs at the film-air boundary. Thus, in order to achieve high α-values, the ζ_{II} should be maximized while the mode overlap is high (Sec. 3.3).

This can be achieved, e.g., by choice of the film thickness (see Sec. 3.3.1). Although the exact phase condition for constructive interference will be met only for particular wavelengths, it is nevertheless beneficial to optimize the waveguide thickness so that the phase condition is closely met in a range of wavelength. This can be verified from Fig. 3.2 as for example a grating period $\Lambda = 1000\,\mathrm{nm}$ together with $d_{\mathrm{fi}} + d_{\mathrm{gr}} = 200\,\mathrm{nm}$ leads to higher α-values than $d_{\mathrm{fi}} + d_{\mathrm{gr}} = 300\,\mathrm{nm}$ in a large region of wavelengths.

The mode overlap with the grating region has to be considered together with the standing wave factors, when high α-values are desired. In Sec. 3.3.1, I have shown that the waveguide thickness also affects the mode overlap factor v_{mode}. The thickness that causes a v_{mode}-maximum does not necessarily coincide with a maximum in the standing wave factor, so that a compromise needs to be found. The grating depth has been assumed as constant here, but directly determines the mode overlap and thus is another important factor for α [57].

The Airy factor v_{Airy} in the investigated grating waveguide (Sec. 3.1) is small due to the small reflection from the substrate. Nevertheless, different stack designs might be employed to design a cavity with a high v_{Airy}. This makes large α-values conceivable, at least for particular wavelengths and lossless materials. Another interesting design could be made by designing a thin-film mirror at one end of the cavity yielding a reflection phase ϕ_{refl} that compensates the wavelength-dependence of the phase change due to the traveled path ϕ_{trip}. Thus, a high standing wave factor over a larger wavelength range could be obtained.

Finally, I want to note that the grating outcoupling design has to be in compromise with the overall OLED design. It is known that the OLED cavity and the position of the recombination zone alters the spontaneous emission [22, 53, 97, 98]. Especially the amount of emission into waveguide modes, substrate modes, and free space depends on the layer thicknesses [23, 91]. The electrical characteristics, the available materials and the fabrication of an OLED put further bounds to the feasible design space.

Chapter 4

Goniophotometer

Summary

In order to measure the angularly and spectrally resolved emission from samples, I built a goniophotometer. In this chapter, I describe the instrument and give details how photoluminescence measurements were recorded for this work. Subequently, the goniophotometer's influence on the measurements is analyzed and described by its angular instrument response function. It is shown that the angular sample emission can be approximately recovered from the measured signal by a deconvolution. Afterwards, I describe the methods used throughout this work to analyze the wavelength and angular peaks in the emission of emitting grating waveguides. Finally, I present experimental results of the angular peak width in the emission of organic emitter layers structured by single-period gratings which indicate that the peak width in wavenumber units is related to the Bragg-scattered mode's attenuation constant.

A goniophotometer is an opto-mechanical instrument to measure the angular distribution of the emission or reflection from a sample [99]. The angular resolution is achieved by measuring the radiation in a small solid angle and sampling the angle-space by either rotating the sample or the detector. Goniophotometers are, e.g., used to measure the emission angular distribution of light sources [100], the reflection properties of hair [101], and the scattering characteristics of general surfaces [102].

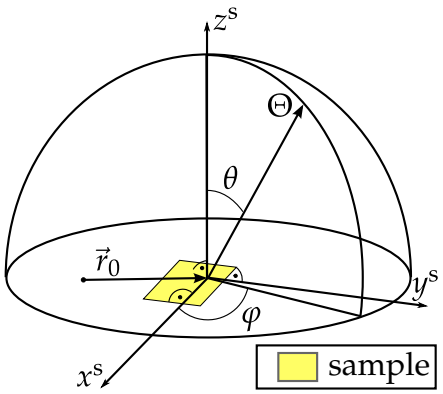

Figure 4.1: Sample coordinate and emission direction. The emission direction Θ is defined by the spherical coordinates θ and φ. Note that the coordinate system's origin $\vec{r}_0$ is the analyzed position on the sample.

In the experimental part of this work, I compare the emission from organic light-emitting layers with different nanostructures. Fig. 4.1 depicts the sample coordinate system. The samples are fabricated on flat glass substrates and the aim is to measure the emission from a small area at $\vec{r}_0$ into a subset of Θ-directions. Thus, a goniophotometer has been developed and built in the course of this work. The requirements were:

- analysis area on sample down to 300 µm diameter to allow sample designs with multiple different nanostructures on adjacent areas on one sample,
- variable and precise sample positioning to select analysis area,
- angular resolution higher than 1° and,
- spectrally-resolved detection as the expected Bragg scattering depends on wavelength and angle,
- θ-independent laser excitation for photoluminescence measurements to achieve a constant excitation independently of the sample rotation,

- versatile sample holder to facilitate measurements on various sample types and also optical sensor configurations (see Chapter 6).

I describe the built instrument in the following. Subsequently, I discuss the measurement data characteristics and data processing.

4.1 The instrument

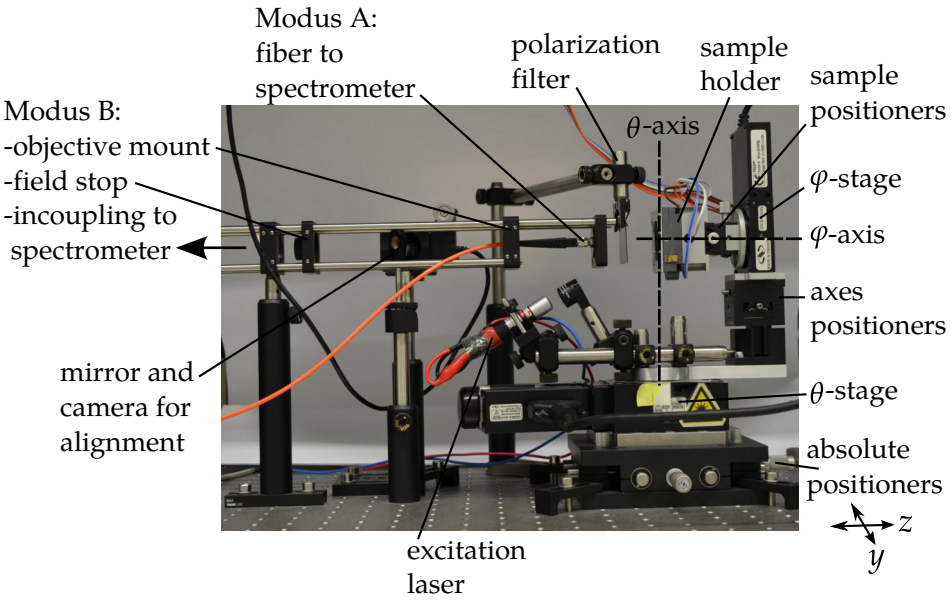

Figure 4.2: Goniophotometer (photograph). The sample is mounted on two rotational stages. The emission is collected at a fixed position either by a fiber (Modus A) or an objective (Modus B) and additional optics.

Fig. 4.2 depicts the goniophotometer setup. Two motorized rotational stages allow to scan the emission half space. The vertical θ-axis is driven by a Newport URS75BPP stage with $\pm 0.015°$ absolute accuracy, while the horizontal φ-axis is driven by a Newport PR50PP stage with $\pm 0.05°$ absolute accuracy. The θ-axis and the φ-axis form an angle of $90°$ and the φ-axis is normal to the sample surface. In order to measure the emission from a fixed position $\vec{r}_0$ on the sample as the axes rotate, the θ-axis, the φ-axis, and the optical axis must intersect at $\vec{r}_0$ as shown in Fig. 4.3. The optical axis is defined by the fiber (Modus A) or the objective (Modus B). This alignment can be achieved by using the three orthogonal axes positioners between the axes and the y-absolute-positioner beneath the complete setup. The z-absolute-positioner allows to adjust the sample-fiber or sample-objective distance. Additionally, two orthogonal sample positioners allow to select the

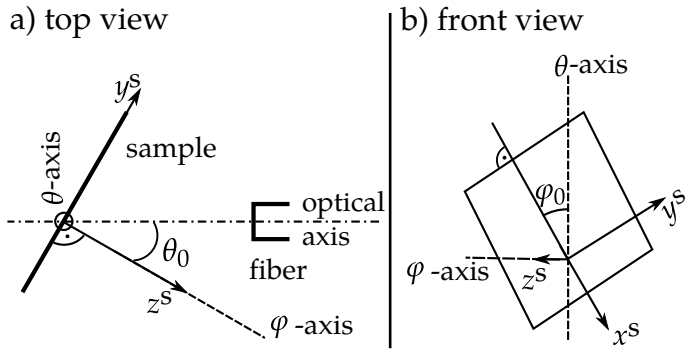

Figure 4.3: Goniometer axes alignment and definition of the measurement angles φ_0 and θ_0. a) The φ-axis, the optical axis (fiber symmetry line), and the θ-axis intersect at the analyzed position $\vec{r}_0$ on the sample surface (see Fig. 4.1). The sample tilt angle θ_0 is defined between the φ-axis and the optical axis. b) The sample rotation angle φ_0 is the angle between the θ-axis and the x^s-axis.

analyzed position $\vec{r}_0$ on the sample. The sample holder is easily demountable by opening two clips so that the sample can be inserted into the holder on the table horizontally.

To collect the sample light, two modes have been realized. In both modes, the polarization filter shown in Fig. 4.2 allows to select the polarization of the detected light. For TE-polarization, the filter allows the vertical electric field component to pass (parallel to the θ-axis). For TM-polarization, the filter was rotated by 90°, so that the horizontal electric field component can pass (perpendicular to the plane subtended by the θ-axis and the optical axis).

4.1.1 Modus A: Bare fiber light collection

In Modus A, a multi-mode fiber with 205 µm diameter and numerical aperture (NA) of 0.22 is mounted in front of the sample. The sample-fiber distance l can be roughly adjusted by moving the fiber mount on two rods. The fiber guides the collected light to the spectrometer, where additional in-coupling optics provide efficient coupling of the fiber light to the spectrometer slit. Note that due to the large sample-fiber distance typically used, the fiber's NA does not determine the angular range of the detected sample emission. In Sec. 4.2 it will be shown that the sample and fiber extent as well as the sample-fiber distance are the determining factors for the angular range of the detected sample emission. On the other hand, the fiber's NA determines the size of the area on the sample from which

light is collected for $\theta_0 = 0°$. A straightforward trigonometric calculation yields for the diameter of this area

$$2b = 2\frac{\mathrm{NA} \cdot l}{\sqrt{(1 - \mathrm{NA}^2)}}, \tag{4.1}$$

if the fiber's end is assumed to be a point. Given the standard sample-fiber distance $l = 50\,\mathrm{mm}$ used in this work, Eq. (4.1) yields a diameter of $2b = 22.6\,\mathrm{mm}$. Thus, if smaller areas on the sample are to be analyzed separately, the size of the emitting area has to be limited. For photoluminescence measurements, the small size of the excitation laser spot limits the emitting area on the sample as described in Sec. 4.1.4. Furthermore, black textile was used to mask the sample's edges in order to prevent stray light contributing to the measurement.

4.1.2 Modus B: Microscope objective light collection

In Modus B, a telecentric microscope objective from Mitutoyo is mounted at the position indicated in Fig. 4.2 instead of the fiber. The objective provides a 5x magnification, NA of 0.13, and a large working distance of 61 mm so that there is sufficient space for the sample during rotation. In this modus, a field stop in the intermediate image plane allows to limit the analyzed area on the sample to diameters between 0.14 mm and 1 mm for $\theta_0 = 0°$. From the intermediate image plane the light is coupled to the spectrometer, while an additional aperture stop (not shown in Fig. 4.2) allows to limit the angular range of the detected sample emission. Note that due to this aperture stop, the objective's NA does not determine the angular range of the detected sample emission.

The advantage of this modus over Modus A is that the analyzed area can be selected by the field stop while a larger area of the sample may be emitting light. This is important, e.g., for electroluminescence measurements if multiple different nanostructures are present in one OLED and the emission from each nanostructured area has to be determined separately.

On the other hand, Modus B is highly sensitive to alignment errors of the axes. For well aligned axes, a nearly symmetric reflection from a Lambertian reflector for $-80° < \theta_0 < 80°$ could be measured, as expected. However, even the change of the sample can result in a misalignment and significant changes in the measured emission intensity become visible. For this reason, Modus A was used for the measurements throughout this work as it is much less susceptible to alignment errors of the axes.

The Modus B additionally allows to flip a mirror into the beam path to image the sample onto a complementary metal–oxide–semiconductor (CMOS) camera as visible in Fig. 4.2.

4.1.3 Axes alignment

As discussed above, the θ-axis and the φ-axis have to be aligned to intersect at the analyzed position $\vec{r}_0$ on the sample so that a rotation of the axes induces a pure sample rotation around $\vec{r}_0$ without any translation of this point. Furthermore, the optical axis has to go through $\vec{r}_0$, so that the emission from the pure-rotation point $\vec{r}_0$ is analyzed. The alignment is performed in two steps with the printed cross shown in Fig. 4.4 in the sample holder. Both steps are done with the microscope objective mounted (Modus B).

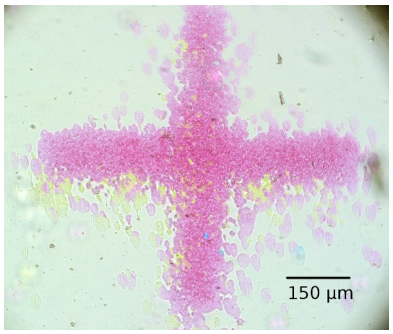

Figure 4.4: Microscope image of a printed cross used for the axes alignment.

Firstly, light from an LED is coupled into the goniophotometer's light path at the spectrometer-side of the in-coupling optics, so that it is focused on the sample holder. Then the printed cross is moved by the sample positioners and the z-absolute-positioner into the beam focus. Subsequently, the axes positioners are adjusted so that the printed cross remains at a fixed position while the axes rotate.

Secondly, the printed cross is viewed with the CMOS camera while rotating the sample. This allows further refinement of the axes alignment.

4.1.4 Photoluminescence: Laser excitation

For photoluminescence measurements of the organic emitter layers, a diode laser emitting at $\lambda_0 = 405\,\text{nm}$ excites the sample. The laser is driven by a constant current of 100 mA provided by a source-measurement unit Keithley 2400. The laser optical output power is approximately 15 mW. Using an achromatic doublet lens with a focal length of 75 mm, the laser is focused

onto the sample. The laser beam width at the sample is 256 µm horizontally and 214 µm vertically ($1/e^2$-irradiance value [50]) as determined by taking camera images of different integration times. Thus, the laser spot is small enough to excite the required area size on the samples separately, which is especially important for the fiber light collection (Modus A).

4.1.5 Spectrometer

In both Modus A and B, the collected light is analyzed by a spectrometer (Andor Shamrock SR-500i) with a cooled back-illuminated charge-coupled device (CCD) detector (Andor DU920P-OE) at $-60\,^{\circ}\mathrm{C}$ and typical integration times between 0.5 s and 1 s.

For automatic emission measurements with the goniophotometer, a LabView program was developed that controls the rotation stages and the spectrometer[1]. The spectrum, a time stamp, and the respective CCD detector temperature are saved in a plain text file for each φ- and θ-angle. Additionally, the integration time and the dark spectrum are saved.

Before further data analysis, the dark spectrum is subtracted from each measured spectrum. The dark spectrum is obtained by averaging ten spectrum recordings without any signal or ambient light at the integration time used for the subsequent measurement.

4.2 Instrument response function

In the following, I analyze the goniophotometer's effect on the measured angular signal in case of fiber light collection (Modus A). An approximation will be presented that allows to express the measured signal as a convolution of the sample emission with an instrument response function (IRF) . I will determine the dependence of the IRF on the measurement angle. This will be important for the interpretation of the measured intensities. Additionally, the IRF will reveal how the fiber-to-sample distance influences the signal intensity, which is important for the goniophotometer's set-up. A deconvolution method and the determination of the "real" width of the angular emission peaks will be presented in Sec. 4.4 and Sec. 4.4.2.

In case of a point-like sample and point-like fiber, the measured signal comprises only light from the $\Theta = (\theta_0, \varphi_0)$ direction of the sample emission. But due to the finite extent of both sample and fiber compared to their distance, light of not only a single emission direction reaches the fiber from

[1]The LabView programming was done by the assistant students André Iwers and Moritz Paulsen, whose help I greatly appreciate.

the sample. Instead, the collected light is comprised by a range of emission angles, causing an averaging in the angular measurement signal. Especially in case of angularly narrow emission peaks, it is of interest to determine the "real" angular peak width not affected by the instrument.

The determination or estimation of function of interest from the measured signal can be considered an inverse problem [103]. In order to solve the inverse problem, the functional relation between the function of interest and the measured quantity must be known. Often, the instrument's effect on the measured signal can be described by a convolution of the function of interest with the IRF, e.g. in spectroscopy [104, 105].

4.2.1 The inverse problem

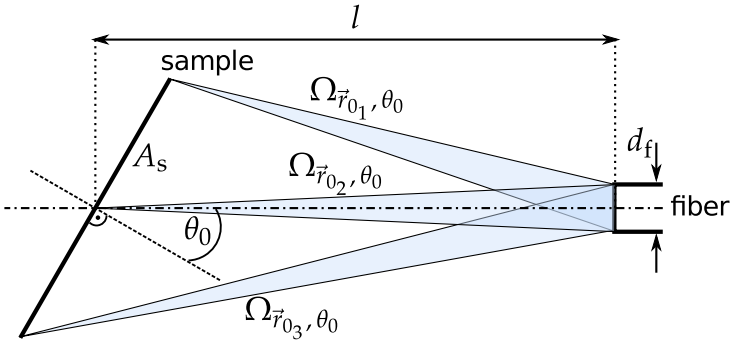

Figure 4.5: Light collection from sample by the fiber. Depending on the position $\vec{r_0}$ on the sample, the solid angle $\Omega_{\vec{r_0}}$ reaching the fiber varies. Light within this solid angle contributes to the radiant flux collected by the fiber at the given sample tilt angle θ_0.

I am analyzing here a goniophotometer measurement at a fixed sample angle φ_0 and a variable sample tilt θ_0 (see Fig. 4.3). The measured signal then is the (spectral) radiant flux $\Phi_f(\theta_0)$ at the fiber end and the function of interest is the sample radiance L_s. At this point, I neglect the conversion of Φ_f to the spectrometer signal as this process is assumed to be angle-independent. Depending on the position $\vec{r}_0$ on the sample and θ_0, the fiber end subtends the solid angle $\Omega_{\vec{r}_0,\theta_0}$ seen from $\vec{r}_0$ (see Fig. 4.5). Light emitted into this solid angle contributes to the collected radiant flux Φ_f at the fiber. The sample area is denoted by A_s.

The radiance of an emissive or reflective surface is defined as

$$L = \frac{\mathrm{d}^2\Phi}{\mathrm{d}\Omega\,\mathrm{d}A\cos\theta'} \tag{4.2}$$

where $\mathrm{d}A$ denotes an infinitesimal area on the surface and θ is the angle between the emission direction and the surface normal [106]. By rearrangement of Eq. (4.2), the infinitesimal radiant flux $\mathrm{d}\Phi$ into the infinitesimal solid angle $\mathrm{d}\Omega$ is

$$\mathrm{d}^2\Phi = L\,\mathrm{d}\Omega\,\mathrm{d}A\cos\theta. \tag{4.3}$$

Integration of Eq. (4.3) over the sample area and the solid angle subtended by the fiber end yields

$$\Phi_f(\theta_0) = \int_{A_\mathrm{s}} \int_{\Omega_{\vec{r}_0,\theta_0}} L_\mathrm{s}\left(\vec{r}_0, \Theta\right) \cos\theta\,\mathrm{d}\Omega\,\mathrm{d}A. \tag{4.4}$$

The sample radiance L_s is generally dependent on $\vec{r}_0$ and the emission direction Θ. The three-dimensional direction Θ is defined from $\vec{r}_0$ as depicted in Fig. 4.1. Note also, that the inner integral's boundaries depend on the integration variable $\vec{r}_0$ of the outer area integral. Eq. (4.4) is the general goniophotometer's inverse problem. The equation characterizes the radiation exchange between two plane surfaces and can be reformulated as an integral over the emitting and receiving surface [102, 106]. Alternatively, I will show next that in certain cases, Eq. (4.4) can be approximately reformulated by an integration over the emission angle θ only. This allows the recovery of $L_s(\theta)$ from the measured signal $\Phi_f(\theta_0)$.

4.2.2 Two-dimensional approximation

Let us consider a two-dimensional cut through the sample and the fiber perpendicular to the θ-axis and coinciding with the φ-axis as shown in Fig. 4.6. Here, I use a coordinate system with the y-axis along the sample in the cut plane and the z-axis normal to the sample. The analyzed position $\vec{r}_0$ is the sample center. Denoting the sample extent in y-direction with d_s, let us assume that

$$\begin{aligned} l &\gg d_\mathrm{s}, d_\mathrm{f}\,, \\ \Delta x_\mathrm{s}, \Delta x_\mathrm{f} &\ll d_\mathrm{s}, d_\mathrm{f}\,, \end{aligned} \tag{4.5}$$

where Δx_s and Δx_f are the extents in x-direction of sample and fiber, respectively. This implies that the sample and fiber are now considered as small stripes of length d_s and d_f, respectively.

Assuming further a sample with position-independent radiance

$$L_{\mathrm{s},\varphi_0}\left(y, \theta\right) = L_{\mathrm{s},\varphi_0}\left(\theta\right) \neq f(y), \tag{4.6}$$

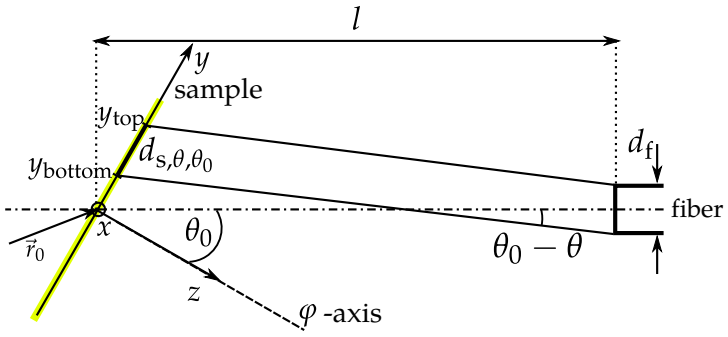

Figure 4.6: In this two-dimensional approximation, the sample y-region d_{s,θ,θ_0} contributing to the fiber flux can be calculated trigonometrically. d_{s,θ,θ_0} is the sample region between y_{bottom} and y_{top}. This calculation allows a straightforward approximation of the goniophotometer's angular response function $f_E(\theta, \theta_0)$.

allows to approximate Eq. (4.4) by

$$\Phi_f(\theta_0) \approx \Delta x_s \Delta x_f \int_{-\pi}^{\pi} L_{s,\varphi_0}(\theta) \cos\theta \, f_E(\theta, \theta_0) \, d\theta, \tag{4.7}$$

with the goniophotometer's IRF

$$f_E(\theta, \theta_0) = \int_{d_{s,\theta,\theta_0}} \frac{1}{r} \, dy \tag{4.8}$$

as derived in Appendix B. Note that the integral in Eq. (4.7) resembles a convolution of the function of interest with f_E, if f_E is dependent only on the argument difference $\theta_0 - \theta$.

Angular instrument response function

The assumptions Eq. (4.5) further allow an approximation of $1/r$ by $1/l$ in Eq. (4.8) so that

$$f_E(\theta, \theta_0) \approx \frac{1}{l} \int_{d_{s,\theta,\theta_0}} dy. \tag{4.9}$$

At this point, the approximated goniophotometer's angular IRF Eq. (4.9) can be calculated trigonometrically.

The integration region d_{s,θ,θ_0}, as defined in Appendix B, is the y-range on the sample that contributes to the fiber flux at a given goniophotometer tilt angle θ_0 and sample emission angle θ. Fig. 4.6 schematically depicts the

relevant angles and lengths. As shown in Appendix C , the y-limits in the sample plane potentially contributing to the fiber flux are

$$y_{\text{top}}, y_{\text{bottom}} = \frac{\pm d_{\text{f}}/2 + \tan(\theta_0 - \theta) l}{\cos(\theta_0) + \tan(\theta_0 - \theta) \sin(\theta_0)}. \tag{4.10}$$

Only the length actually filled by the sample between y_{bottom} to y_{top} contributes to the integral in Eq. (4.9), so that the goniophotometer's IRF is

$$f_{\text{E}}(\theta, \theta_0) \approx (y'_{\text{top}} - y'_{\text{bottom}})/l, \tag{4.11}$$

where y'_{bottom} and y'_{top} are limited to the sample's extent according to

$$y' = \begin{cases} d_{\text{s}}/2 & : y > d_{\text{s}}/2 \\ -d_{\text{s}}/2 & : y < -d_{\text{s}}/2 \\ y & : \text{else} \end{cases}.$$

Note that analyzed position is the sample center.

The $f_{\text{E}}(\theta, \theta_0)$ trigonometric approximation calculated by Eq. (4.11) is depicted in Fig. 4.7 together with Zemax [107] non-sequential ray-tracing results. The results are based on the a sample-fiber distance $l = 50\,\text{mm}$, sample edge length $d_{\text{s}} = 500\,\mu\text{m}$, and fiber diameter $d_{\text{f}} = 205\,\mu\text{m}$. This is the configuration used to obtain most of the goniophotometric measurement results in this work. Note that, opposed to the approximation, the Zemax simulation results have been obtained for the full-sized sample and fiber, both assumed as square areas with edge length d_{s} and d_{f}, respectively.

To calculate $f_{\text{E}}(\theta, \theta_0)$ with Zemax, I simulated the radiant intensity $I_{\text{e}}(\theta')$ incident on the detector at an angle $\theta' = -(\theta_0 - \theta)$ to the detector normal (see Fig. 4.6). An isotropic sample emission characteristic has been used with normalized power, i.e.

$$L_{\text{s}} \cos\theta = 1\,\text{W}\,\text{sr}^{-1}\,\text{m}^{-2}. \tag{4.12}$$

Eq. (4.7) can also be interpreted as an integration of the radiant flux on the detector, so that

$$I_{\text{e}}(\theta') \frac{\Delta x_{\text{s}}}{l} = \Delta x_{\text{f}} \Delta x_{\text{s}} L_{\text{s},\varphi_0}(\theta) \cos\theta \; f_{\text{E}}(\theta, \theta_0). \tag{4.13}$$

The additional factor $\Delta x_{\text{s}}/l$ stems from the approximative integration over the solid angle subtended by the sample as seen from the fiber (see Eq. (B.2)). Thus, by insertion of Eq. (4.12) into Eq. (4.13), we find that $f_{\text{E}}(\theta, \theta_0)$ is proportional to $I_{\text{e}}(\theta')$

$$f_{\text{E}}(\theta, \theta_0) = \frac{1}{d_{\text{f}} l} I_{\text{e}}(-(\theta_0 - \theta)). \tag{4.14}$$

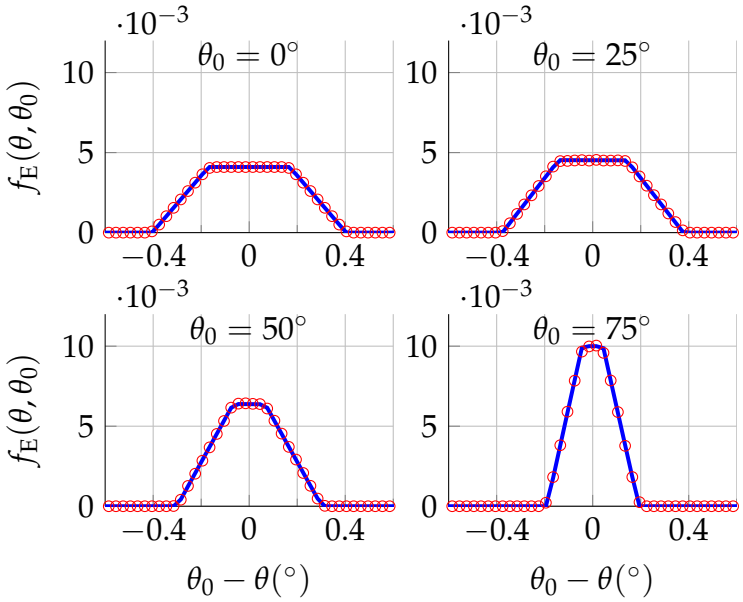

Figure 4.7: Goniophotometer's angular response function $f_E(\theta, \theta_0)$ for $l = 50\,\text{mm}$, $d_s = 500\,\mu\text{m}$, and $d_f = 205\,\mu\text{m}$. Four different sample tilt angles θ_0 are shown. Solid lines: trigonometric equation Eq. (4.11) (approximation: small sample and small fiber x-extent). Red circles: Zemax ray-tracing simulation (full sample and full fiber extent). Approximated and simulated curves are in excellent agreement. In this configuration the fiber collects an angular range of about 0.4° to 0.8°.

I set $\Delta x_f = d_f$ here. Due to this simulation scheme, each Zemax curve in Fig. 4.7 could be obtained by a single simulation run at the given sample tilt. I used $500 \cdot 10^6$ rays distributed in a 2°-range centered at θ_0 in order to minimize the number of rays that cannot hit the detector. The detector discretization was set to 2000 pixel × 6000 pixel to resolve the small angular range of $I_e(\theta')$.

Fig. 4.7 shows that the approximation given by Eq. (4.11) and the Zemax simulation are in excellent agreement. This validates the assumptions made in Sec. 4.2.2 to develop the approximation for the given configuration.

Angular resolution

Furthermore, Fig. 4.7 shows that the fiber collects light from the sample in an angular range of about 0.4° to 0.8° width. At higher θ_0, the angular resolution increases. This resolution range achieved at $l = 50\,\text{mm}$ proved to be sufficient for the measurements made throughout this work.

Angular responsivity

Although the approximated $f_{\mathrm{E}}(\theta, \theta_0)$ depends on θ_0, its integral over θ is independent of θ_0 in the range $|\theta_0| \leq 89.0°$. For an isotropic sample emission, e.g., this results in a detected signal intensity that is constant over θ_0 as obtained by Eq. (4.7).

Influence of sample-fiber distance

The angular IRF $f_{\mathrm{E}}(\theta, \theta_0)$ is helpful to choose the sample-fiber distance l. Fig. 4.8 shows that, in the analyzed configurations, $f_{\mathrm{E}}(\theta, \theta_0)$ doubles its

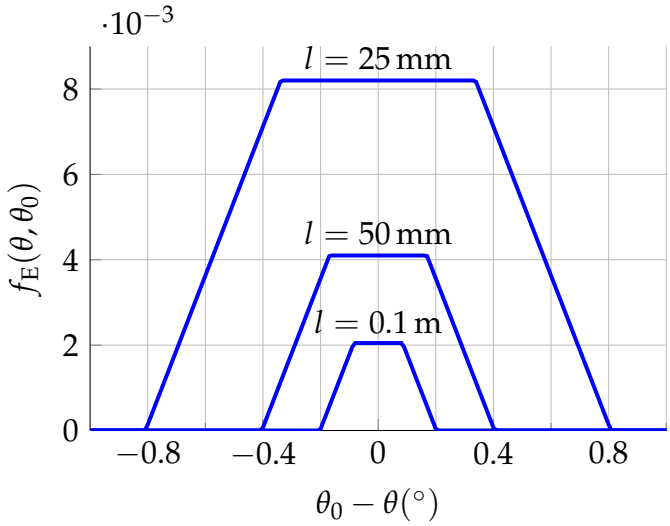

Figure 4.8: Goniophotometer's angular response function $f_{\mathrm{E}}(\theta, \theta_0)$ for $d_{\mathrm{s}} = 500\,\mu\mathrm{m}$, $d_{\mathrm{f}} = 205\,\mu\mathrm{m}$ and three different sample-fiber distances l. Increase of l leads to a higher angular resolution but lower signal at the fiber.

width and area if l is halved. While the increase in width leads to a loss of angular resolution, the increase in area corresponds to a higher signal $\Phi_f(\theta_0)$ at the fiber according to the inverse-square law [50]. Thus, the choice of l is a compromise between angular resolution and required signal strength. Most measurements in this work have been done at $l = 50\,\mathrm{mm}$ as this yielded maximum spectrometer intensities about 2/3 the spectrometer saturation value of 2^{16} counts at practical integration times of 0.2 s to 1 s. This reduces the influence of noise on the recorded spectra compared to measurements with lower intensities.

Convolution formulation

The knowledge of $f_{\mathrm{E}}(\theta, \theta_0)$ allows to recover the "true" angular peak width. $f_{\mathrm{E}}(\theta, \theta_0)$ depends not only on the argument difference $\theta_0 - \theta$ but also on the absolute value of θ_0, as shown in Fig. 4.7. Nevertheless, in case the function of interest $L_{\mathrm{s},\varphi_0}(\theta)$ is a peak with small width, the detected signal $\Phi_f(\theta_0)$ will also be a peak of small angular width due to the limited range of $f_{\mathrm{E}}(\theta, \theta_0)$ being non-zero. Thus, we can approximate $f_{\mathrm{E}}(\theta, \theta_0)$ around the measured peak position $\theta_{0,\mathrm{p}}$ by a function $f_{\mathrm{E},\theta_{0,\mathrm{p}}}(\theta_0 - \theta)$ and reformulate Eq. (4.7) as

$$\Phi_f(\theta_0) \approx \Delta x_{\mathrm{s}} \Delta x_{\mathrm{f}} \int_{-\pi}^{\pi} L_{\mathrm{s},\varphi_0}(\theta) \cos\theta \, f_{\mathrm{E},\theta_{0,\mathrm{p}}}(\theta_0 - \theta) \, \mathrm{d}\theta. \tag{4.15}$$

We could thus express the functional relation between the function of interest $L_{\mathrm{s},\varphi_0}(\theta)$ and the measured quantity $\Phi_f(\theta_0)$ through Eq. (4.15) as a convolution. The approximation of $f_{\mathrm{E}}(\theta, \theta_0)$ by a Gaussian function $f_{\mathrm{E},\theta_{0,\mathrm{p}}}(\theta_0 - \theta)$ and the (approximate) recovery of L_{s,φ_0} by a deconvolution will be described in Sec. 4.4.

4.3 Outcoupling peak analysis

So far, the outcoupled light from a grating waveguide has been considered as plane wave space harmonics (see Sec. 2.6.2). However, goniophotometer measurements of the emission of a nanostructured organic emitter layer show that the guided mode outcoupling results in narrow but finite peaks in the emission, both in the wavelength spectrum as well as in the angular distribution. Fig. 4.9 depicts a typical sample TE-polarized emission spectrum measured with the goniophotometer. This sample is comprised of the organic emitter Superyellow on a grating with period 400 nm. The complete sample structure and fabrication is described in Sec. 5.2. The emission has been measured perpendicular to the grating grooves, i.e. $\varphi_0 = 0°$ and the y^{s}-axis perpendicular to the grating grooves (Fig. 4.3). To visualize the emission, each spectrum recorded at θ_0 is plotted as a column in Fig. 4.9. The intensity counts are mapped to colors according to the colormap shown.

Two strong outcoupling features are visible in Fig. 4.9 due to Bragg scattering of the forward- and backward-traveling TE_0 mode (see Sec. 2.6.2). This is distinctive of single-period gratings. In Chapter 5 it will be shown that more outcoupling features arise if the grating possesses multiple strong frequency components. One feature at a time will be analyzed by the methods presented in the following. The outcoupling symmetry of the

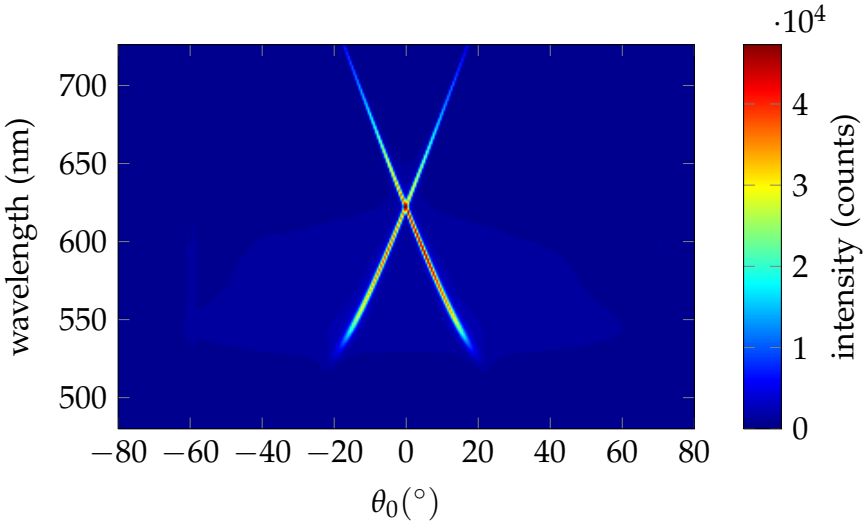

Figure 4.9: Angularly and spectrally resolved TE emission from an organic emitter layer structured by a grating with period $\Lambda = 400\,\text{nm}$ (K15, field C9). The emission was measured with the goniophotometer.

forwards- and backwards-traveling mode is discussed in Sec. 5.7.2 and will generally allow to limit the analysis to one direction.

The angular discretization is 0.5° given by the θ_0-step size and the wavelength discretization is 0.344 nm given by the spectrometer grating groove density $150\,\text{mm}^{-1}$. I determine the peak position and intensity in the wavelength spectrum, as this spectrum provides a higher discretization than the angular spectrum. Nevertheless, the wavelength peak fitting described in Sec. 4.3.3 allows to interpolate the angular spectrum. Afterwards, the peak width in the angular spectrum can be robustly determined as described in Sec. 4.4.

4.3.1 Background removal and normalization

Before the emission peaks can be further analyzed, the background signal has to be removed. The background signal is the part of the emission that does not emerge from waveguide outcoupling, but is emitted directly. I assume that the background signal of the grating waveguide is equal to the unstructured waveguide emission. By this assumption, I neglect the grating's influence on the dipole emission. The unstructured waveguide emission (Fig. 4.10) is measured separately for each sample at an unstructured area with the same angular and spectral discretization and polarization as the grating areas. To match the background intensity in the grating area with the intensity in the unstructured area, I integrate the in-

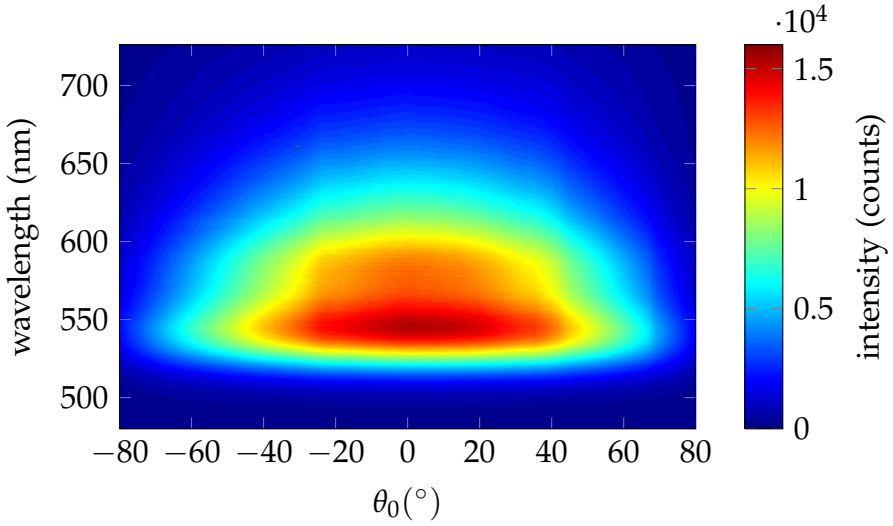

Figure 4.10: Angularly and spectrally resolved TE emission from an unstructured Superyellow layer. This spectrum is used to remove the background emission from the grating measurements.

tensity in a region of typically 5° angle and 7 nm wavelength and determine the ratio as a matching factor. The region has to be chosen individually for each grating, as it has to be uninfluenced by the peaks but exhibit sufficient background intensity. For the emission depicted in Fig. 4.9, the matching region is centered at $\theta_0 = 0°$ and $\lambda_0 = 560\,\text{nm}$. By subtraction of the intensity-matched background signal I approximately separate the scattered guided mode light and obtain isolated peaks in the spectrum (Fig. 4.11).

When analyzing the outcoupling peaks, I am interested in their intensity relative to the excitation. Thus, I divide each measured spectrum by the spectrum of the unstructured area at $\theta_0 = 0°$. The intensities in the following plots will consequently be normalized to the Superyellow spectrum.

4.3.2 Position

The wavelength peak position is the wavelength at which the peak corresponding to one feature is maximum. I determine the peak position by choosing about five wavelength-angle-points on a feature manually. These points are then interpolated by a spline. Subsequently, the maximum in the wavelength spectrum is automatically found at each θ_0 in a window of 20 nm wavelength around the interpolated positions. The blue asterisks in Fig. 4.12a depict the peak position determined by this maximum search method. Angles with feature crossings are excluded manually from the maximum search because a unique maximum cannot be found if the an-

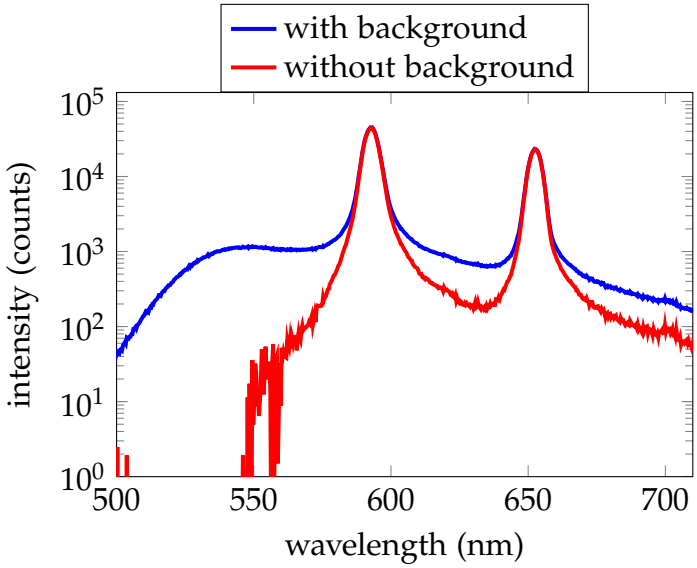

Figure 4.11: Background removal from single-period grating emission spectrum (K15 C9, TE-polarization, $\theta_0 = 5.2°$). The TE_0-mode outcoupling peaks are separated by subtracting the unstructured waveguide spectrum.

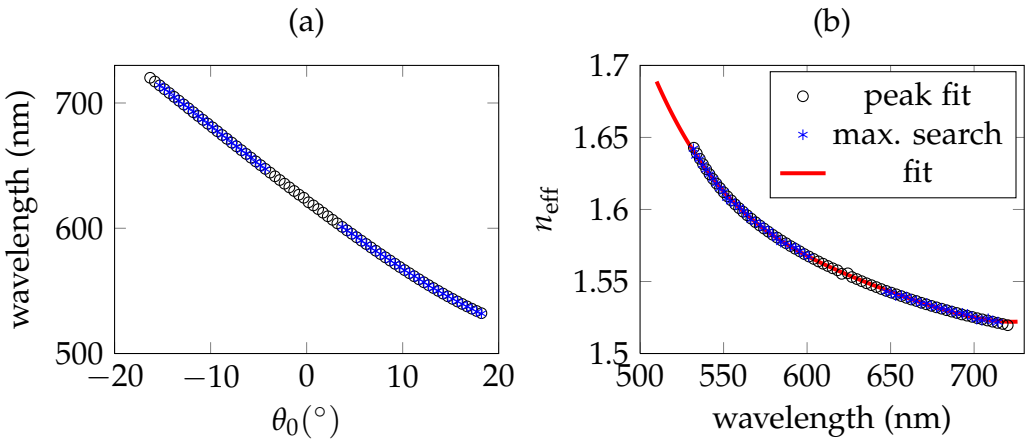

Figure 4.12: (a) Wavelength peak position. A direct maximum search (blue asterisks) and a wavelength peak fitting method (black circles) lead to the same results. (b) Mode effective index n_{eff} calculated from the peak position. A 3rd order polynomial fit (red line) is well suited to interpolate n_{eff}.

alyzed window contains more than one peak. This is visible in Fig. 4.12a around $\theta_0 = 0°$.

After determining the peak positions, the mode effective index n_{eff} can be calculated with relation Eq. (2.44) (Fig. 4.12b - blue asterisks). To approximate n_{eff} in the crossing regions, n_{eff} over θ_0 is interpolated by a 3rd order

polynomial (Fig. 4.12b - red line).

A further refinement of the peak positions is obtained, when a peak model is fitted to the wavelength peaks as described in Sec. 4.3.3. However, Fig. 4.12 indicates that the peak fitting results (black circles) differ negligibly from the maximum search (blue asterisks). This shows that the wavelength discretization is sufficiently fine for the typical peak width.

4.3.3 Intensity

To determine the peak intensity in the wavelength spectrum, I implemented two different methods. One method is to fit a peak model to the spectrum, while the other method is to integrate the area under the peak directly.

Wavelength peak fitting

After background removal, peaks can be fitted to the wavelength spectrum at each θ_0. The weighted Voigt profile

$$V_{c,\lambda_{\mathrm{pos}},\sigma,\gamma}(\lambda' = \lambda_0 - \lambda_{\mathrm{pos}}) = c\frac{\exp(-\lambda'^2/(2\sigma^2))}{\sigma\sqrt{2\pi}} \otimes \frac{\gamma}{\pi(\lambda'^2+\gamma^2)}, \qquad (4.16)$$

a convolution ($\otimes$) of a Gaussian and Lorentzian profile [108], is used to model the spectral outcoupling peaks. In order to save computational time, I use a Feddeeva function numerical implementation written by Steven G. Johnson [109] to compute the Voigt profile. The fitting is performed by a Nelder-mead simplex minimization [75] of the summed squared difference between the measured spectrum and the computed Voigt profile. The fitting parameters are the peak intensity c, position λ_{pos}, Gaussian parameter σ, and Lorentzian parameter γ. Fig. 4.13 depicts a typical fitting result, showing the close agreement between the measured peak and the fitted Voigt profile. Note that only the small asymmetry in the measured peak is lost due to the fit.

The method fits the peak corresponding to each outcoupling feature separately. That is, for the measurement data shown in Fig. 4.9, two subsequent fittings are made, one for each mode propagation direction. Special attention has to be paid to the peak crossing regions, e.g. around $\lambda_0 = 620\,\mathrm{nm}$ and $\theta_0 = 0^\circ$ in Fig. 4.9. In these regions, two summed peaks are fitted simultaneously.

If the angular peak width is to be determined (Sec. 4.4), a finer angular discretization is needed. Therefore, the fitting parameters $c, \lambda_{\mathrm{pos}}, \sigma,$ and γ are linearly interpolated to an angular discretization of 0.01°. Thus, I obtain a Voigt profile model of each outcoupling feature as is exemplarily depicted

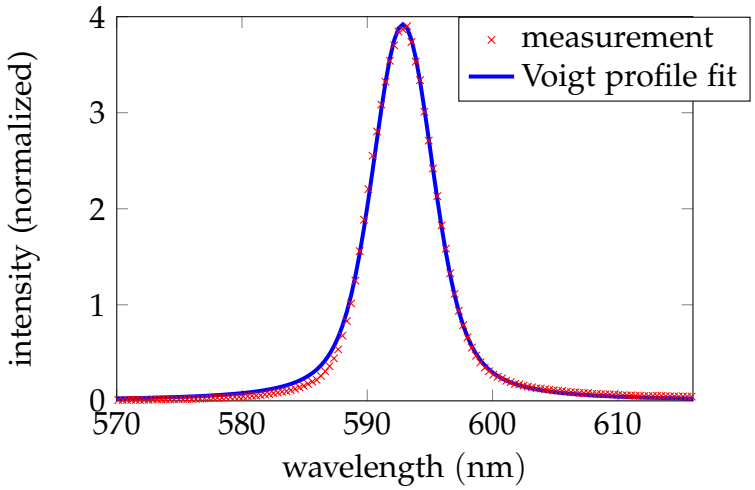

Figure 4.13: Voigt profile fit to wavelength peak (K15 C9, TE-polarization, $\theta_0 = 5.2°$). The Voigt profile is well suited to model the measurement data. Only the small asymmetry in the measured peak is lost due to the fit.

in Fig. 4.14. The interpolated spectra can then be used to analyze the peaks

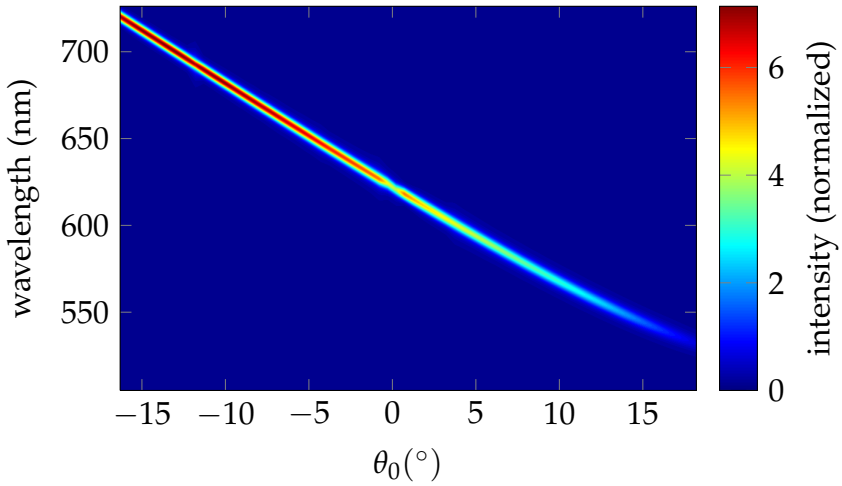

Figure 4.14: TE-polarized model emission spectrum of first-order Bragg-scattered, forward-traveling TE_0 mode (K15,C9). The Voigt profile parameters fitted to the measurement have been interpolated to a fine angular discretization to compute this model spectrum.

in the angular spectrum as described in Sec. 4.4.

Peak integration

Alternatively to the peak fitting, the peak intensities in the wavelength spectrum can be determined by integration. I numerically integrate in a wavelength region around the peak position by trapezoidal integration [76]. The peak position is found by the maximum search described in Sec. 4.3.2.

The size of the integration region has to be chosen according to the peak width. I found that a wavelength region of 20 nm centered at the peak position yielded good results for the typical peak width in my analyses. The choice of the integration region is a compromise between the inclusion of the theoretically infinitely wide peaks and the suppression of not completely removed background signal. Furthermore, the region has to be small enough to allow a separate analysis of adjacent peaks.

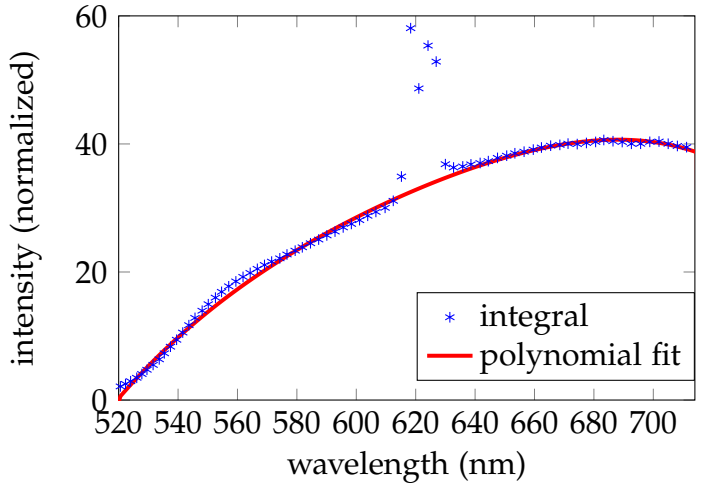

Figure 4.15: Wavelength peak intensity (blue asterisks) obtained by integration and plotted over the peak position. The peak crossing leads to a steeply increasing intensity around $\lambda_0 = 620\,\text{nm}$. A polynomial fit (red line) with non-quadratic cost function allows separation of the peak intensity in the peak crossing region.

After the wavelength peak intensity has been calculated at each θ_0, the intensities can be plotted versus the peak position as shown in Fig. 4.15. Clearly, the integration method cannot separate the intensities of the two peaks in the crossing regions, as visible in Fig. 4.15 around $\lambda_0 = 620\,\text{nm}$. The peak crossings lead to a steeply increasing intensity as both peaks lie in the integration region. To estimate the peak intensity in the crossing regions nevertheless, I fit a polynomial with a non-quadratic cost function to the intensity curve with a Matlab program provided by Mazet et al. [110]. This method has been originally proposed for background estimation

in spectroscopy [110]. It is, however, also applicable to remove the rapid intensity changes in the peak crossing regions as visible, e.g., from the 4th-order polynomial fit of the peak intensity depicted in Fig. 4.15.

Comparison

I compare the peak intensity determined with both methods in Fig. 4.16. The peak integration mostly yields smaller intensities than the peak fitting

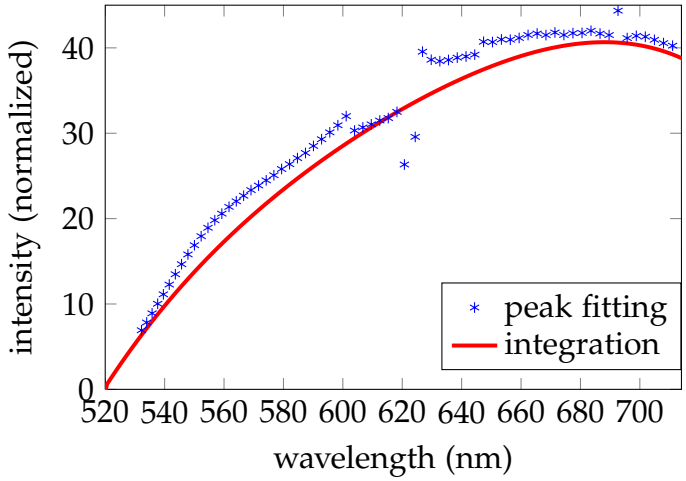

Figure 4.16: Wavelength peak intensity determined by peak fitting (blue asterisks) and peak integration (red line). The peak integration slightly underestimates the intensity, but is simpler and more robust.

method. This can be explained by the finite integration region of 20 nm wavelength, that does not include the complete peak tails. The deviation outside the crossing region is smaller than 15 % from the peak fitting result. Inside the crossing region around $\lambda_0 = 620\,\text{nm}$, the peak fitting model reveals a dip in the intensity that is also visible in Fig. 4.14. This dip is not recognized by the integration method as it simply interpolates the intensity in the crossing regions.

The advantage of the integration method is that it is stable and requires no manual control of the convergence as is necessary in the peak fitting method. Especially, when the measured emission exhibits more than one crossing per feature, the peak fitting method requires manual adjustments of the start values. Furthermore, the integration method yields interpolated intensity values at each wavelength so that intensity ratios between different features can be directly calculated. I therefore use the integration method for analysis of compound binary gratings (see Chap. 5).

On the other hand, the peak fitting method yields more accurate results, as the peaks are modeled in their full extent and discretization errors are minimized. Furthermore, the fitting compensates background residuals that can distort the peak shape. Additionally, information about the peak intensities in the crossing regions is preserved. The peak fitting method finally allows to interpolate the angular spectrum, which is necessary to analyze the angular peak width (Sec. 4.4).

4.4 Angular peak width

To conclude this chapter, I investigate the angular peak width in the emission of organic emitter layers structured by gratings. It is well known that grating waveguides exhibit resonances in transmission and reflection both over wavelength and incidence angle [62, 69, 70, 73, 74, 94, 111–114]. The resonance arises if the grating waveguide is illuminated by a plane wave with a particular wavelength and incidence angle such that a diffracted excitation wavevector matches the wavevector of a leaky mode supported by the waveguide. Under this condition, light couples to the leaky mode and the re-scattered mode interferes with the directly reflected and transmitted light [112]. This phenomenon is of practical interest for filters and switching applications [112, 113].

It has been shown, that the resonance in the reflectivity over angle is described by a Lorentzian curve if the angle is expressed in wavevector units [62, 113], i.e. the reflected intensity is

$$I_\mathrm{r} = \frac{c}{(k_\mathrm{t} + (\beta_0 - \frac{2\pi}{\Lambda}))^2 + \gamma^2} \tag{4.17}$$

with

$$\gamma = |\alpha|,$$

where c is an arbitrary constant, k_t is the tangential component of the incident wavevector, and $\beta_0 + j\alpha$ is the complex propagation constant of the leaky waveguide mode that causes the resonance. According to Eq. (4.17), the resonance's width is determined by the mode attenuation constant α.

Most papers study the resonance in case of an incident wave or beam from outside the grating waveguide. For external excitation, the resonance in the reflection and transmission can be described by a pole in the scattering matrix of the grating waveguide [111]. However, as the electromagnetic fields inside the grating waveguide can be related to the scattered fields by linear matrices [70], it is reasonable to assume that the relation between the internal fields and the scattered fields exhibits the same pole. Consequently,

the resonance in the scattered field intensity in a configuration with sources inside the grating waveguide can be described by the same Lorentzian curve as for external excitation. Such a configuration is, e.g., given for the grating waveguides investigated in this work, as light is generated inside the organic emitter layer. Thus, the scattered field intensity is assumed to be given by Eq. (4.17), where $-k_t$ is the tangential component of the scattered wavevector.

4.4.1 Fitting and deconvolution

In order to remove the goniophotometer's influence on the angular peaks, the measured angular spectrum is deconvolved. First of all, the angular spectrum is interpolated using the wavelength peak fitting method described in Sec. 4.3.3. Afterwards, peaks can be fitted to the angular spectrum (fixed λ_0) in order to determine the angular peak width. Fig. 4.17 depicts an

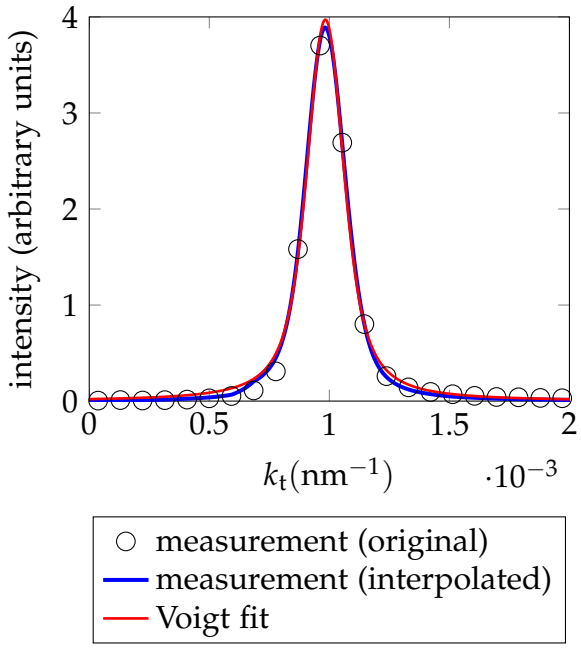

Figure 4.17: Exemplary angular peak given by the original measurement, the interpolated values and the Voigt fit.

exemplary angular peak given by the original measurement, the interpolated values and the Voigt fit. Clearly, the angular interpolation is necessary to provide enough data points inside the peak for the subsequent fitting. The deconvolution is achieved by fitting a Voigt profile to the measured signal as is described in the following.

With the emission tangential wave vector

$$\begin{aligned} k_\mathrm{t} &= k_0 \sin(\theta), \\ \mathrm{d}k_\mathrm{t} &= k_0 \cos(\theta)\,\mathrm{d}\theta \\ &= \sqrt{k_0^2 - k_\mathrm{t}^2}\,\mathrm{d}\theta, \end{aligned} \tag{4.18}$$

the convolution integral in Eq. (4.15) can be reformulated to the wave vector formulation

$$\Phi_f(k_{\mathrm{t}_0}) \approx \Delta x_\mathrm{s} \Delta x_\mathrm{f} \int_{-k_0}^{k_0} \frac{L_{\mathrm{s},\varphi_0}(k_\mathrm{t}) \cos\theta}{\sqrt{k_0^2 - k_\mathrm{t}^2}}\, f_{\mathrm{E},\theta_{0,\mathrm{p}}}(k_{\mathrm{t}_0} - k_\mathrm{t})\,\mathrm{d}k_\mathrm{t}, \tag{4.19}$$

where k_{t_0} is obtained from θ_0 by Eq. (4.18). The fraction in the convolution integral of Eq. (4.19)

$$I_\mathrm{e} \equiv \frac{L_{\mathrm{s},\varphi_0}(k_\mathrm{t}) \cos\theta}{\sqrt{k_0^2 - k_\mathrm{t}^2}} \tag{4.20}$$

is the sought sample emission intensity expressed as radiance per unit wave vector k_t (instead of angle θ) and freed from the $\cos\theta$ term (see definition of radiance in Eq. (4.2)). As discussed above, I assume that the angular guided mode outcoupling peaks in the so defined sample emission to be Lorentzians. Our deconvolution approach of Eq. (4.19) relies on an approximation of the angular IRF $f_{\mathrm{E},\theta_{0,\mathrm{p}}}(k_{\mathrm{t}_0} - k_\mathrm{t})$ by a Gaussian profile with parameter σ_IRF. As I_e is assumed to be of Lorentzian profile, the convolution results in Voigt profiles (see Eq. (4.16)). Consequently, least-squares fitting a Voigt profile with fixed Gaussian parameter σ_IRF to the measured signal intensity yields the approximate "true" Lorentzian peak with the angular IRF removed. σ_IRF is obtained by calculation of the IRF (Eq. (4.11)) for each wavelength at the given peak position $\theta_{0,\mathrm{p}}$ and equaling the Gaussian's FWHM to the IRF's FWHM. Thus, by the definition of the Gaussian profile [76],

$$\sigma_\mathrm{IRF} = \mathrm{FWHM}_\mathrm{IRF} / (2\sqrt{2\ln 2}), \tag{4.21}$$

where the IRF's FWHM is denoted by $\mathrm{FWHM}_\mathrm{IRF}$. A typical instrument response function FWHM value is e.g. $\mathrm{FWHM}_\mathrm{IRF} = 1.08 \times 10^{-4}\,(1/\mathrm{nm})$ at $l = 50\,\mathrm{mm}$, $\lambda_0 = 539.5\,\mathrm{nm}$ and peak position $\theta_{0,\mathrm{p}} = 16.07^\circ$ as shown in Fig. 4.18. Although the trapezoidal form of the IRF matches the Gaussian profile only roughly, the width is retained.

Finally, the result of the deconvolution is shown in Fig. 4.19. The obtained Lorentzian curve is the "true" signal that has been extracted from the

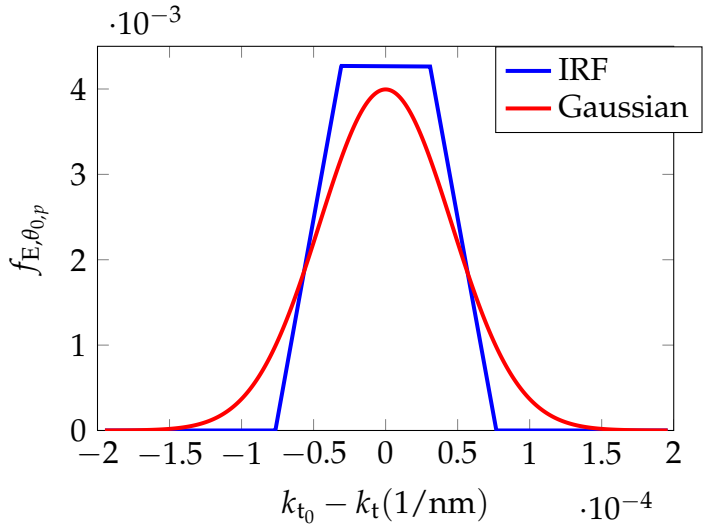

Figure 4.18: Exemplary Gaussian approximation of the IRF Eq. (4.11). FWHM and area of IRF and Gaussian profile are equal. The Gaussian profile facilitates a convenient deconvolution of the measured signal.

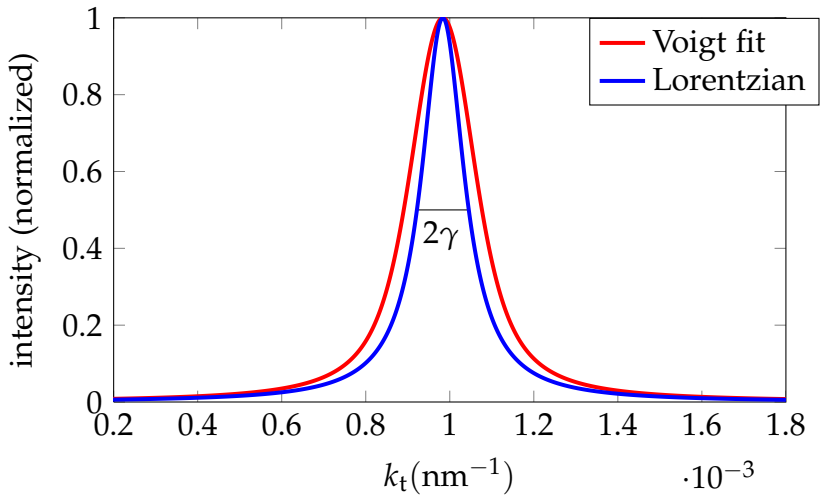

Figure 4.19: Exemplary deconvolution result of an angular peak. A Voigt peak with fixed Gaussian parameter is fitted to the measured intensity. The Gaussian profile is chosen to model the IRF. Consequently, the obtained Lorentzian peak approximates the emission intensity without the influence of the goniophotometer. The Lorentzian's FWHM value relates to the waveguide mode's attenuation constant by $2|\alpha| = 2\gamma$.

measurement by removal of the IRF. In Fig. 4.19 it becomes visible that, in the used configuration, the goniophotometer influences the angular peak width only moderately.

4.4.2 Experimental results

I applied the method described above to the measured emission of samples with single-period gratings. An emitter layer of 65 nm Superyellow has been deposited on a corrugated imprint resist as described in Sec. 5.2. The emitter layer is protected by a 70 nm thick layer of silicon monoxide. These thicknesses are chosen such that only the fundamental order TE and TM modes are supported. Fig. 4.20a depicts the determined γ from the angular peaks in the emission intensity associated with the Bragg-scattered TE_0-mode. All measurements shown in Fig. 4.20a were conducted on the sample K15 at the indicated grating fields (see Appendix D).

A general trend of decreasing γ with increasing wavelength can be observed in Fig. 4.20a. For each grating waveguide, two γ-curves were obtained, one for each mode propagation direction. As visible in Fig. 4.20a both curves are nearly equal as expected due to the symmetry of the waveguide. This indicates that the method for determining γ is stable. The simulated TE_0-mode attenuation constant α_a due to material absorption describes the general trend of the measured γ-curves well. α_a has been obtained by a TMM simulation with the parameters given in Sec. 5.3.

Fig. 4.20b shows the simulated TE_0-mode attenuation constant α_c due to mode coupling. These curves are obtained by simulation of the lossless structure with RCWA. Then, α_c solely originates from coupling to radiation modes as well as to the counter-propagating guided mode in the stop-band regime. The α-curves are almost independent of the grating period, except for the form and position of the rapid fluctuations (see Fig. 4.20b). These rapid fluctuations are due to stop-bands, whose positions depend on the grating period [45]. Clearly, these stop-band fluctuations are also visible in the measured γ-curves at positions that agree to good extent with the simulation. The α_c due to mode coupling is a factor of ten smaller than the α_a due to absorption.

The mode attenuation α is approximately the sum $\alpha_a + \alpha_c$, if the interplay between absorption and mode coupling is neglected. Obviously, $\alpha_a + \alpha_c$ resembles the γ-curves well. This indicates that the width of the angular peaks in the emission intensity is determined by α of the corresponding mode as expressed by Eq. (4.17).

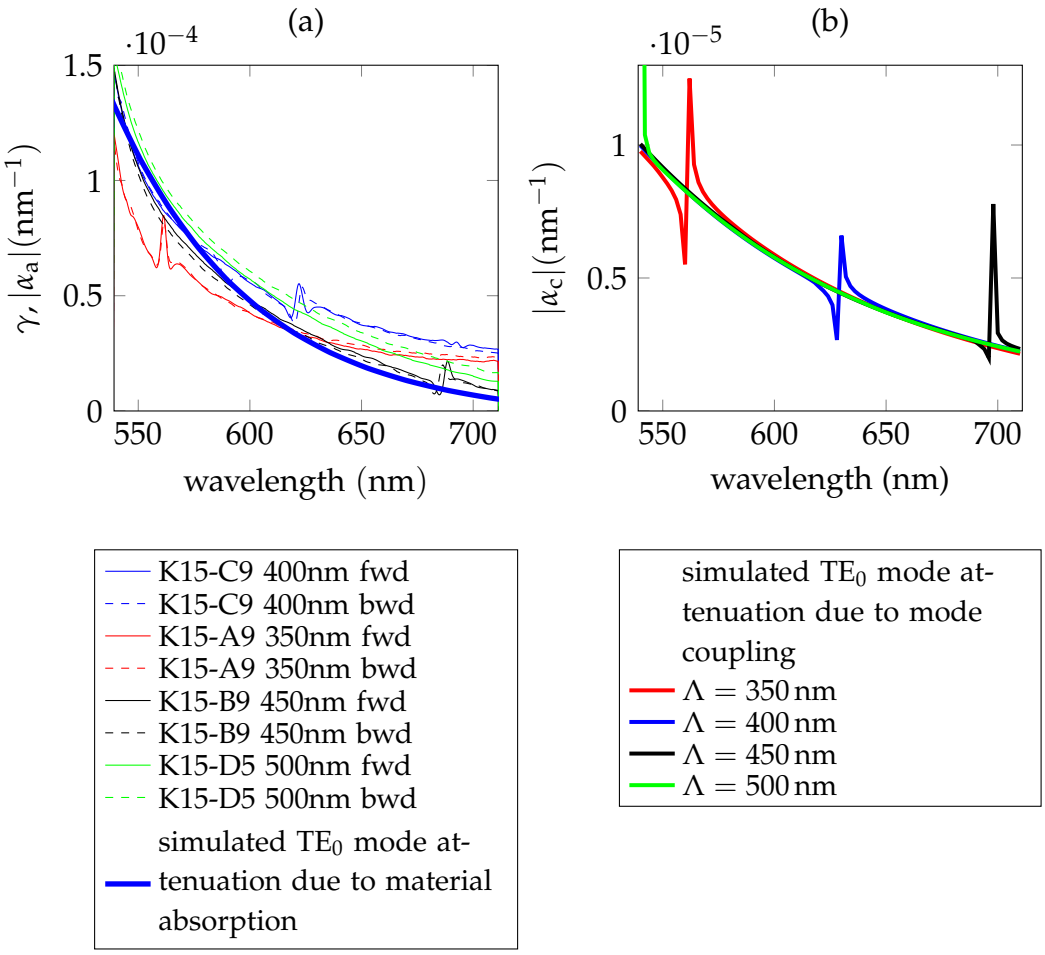

Figure 4.20: (a) Experimentally determined Lorentzian peak widths γ in the emission intensity from four grating waveguides with different grating periods. In each measured emission the angular Bragg scattering peak originating from the forward- (fwd) and backward- (bwd) propagating TE_0-mode are analyzed. The general trend of the measured γ-curves is described well by the simulated TE_0-mode attenuation constant α_a due to material absorption. (b) The TE_0-mode attenuation constant due to mode coupling is one order of magnitude smaller than the attenuation constant due to absorption. The rapid fluctuations in the α_c-curves are due to stop-bands and the positions of these features agree well with the measurement.

Chapter 5

Compound binary grating light extraction

Summary

Compound binary gratings are structures yielded by the combination of multiple binary gratings with different periods. Incorporated into a slab waveguide, these structures scatter a guided mode into multiple directions. The structure's Fourier coefficients and the waveguide cavity determine the intensity of each direction. In this chapter I demonstrate that the intensity ratio between the directions can be controlled by changing the duty cycle of a grating component. I present photoluminescence measurements of organic emitter samples with 24 different compound binary gratings and show that the measured emission is in good agreement with RCWA simulations and a theoretical model.

As discussed in Chapter 1 and 3, gratings can be employed to extract light from waveguide modes in OLEDs and thereby increase the OLED efficiency. At a single-period grating, a waveguide mode is Bragg scattered to particular directions depending on the light wavelength. Hence the OLED emission over the angle is modified and becomes partly directional. An exemplary photoluminescence measurement is depicted in Fig. 5.1a for an organic emitter layer structured by a single-period grating. The lines of

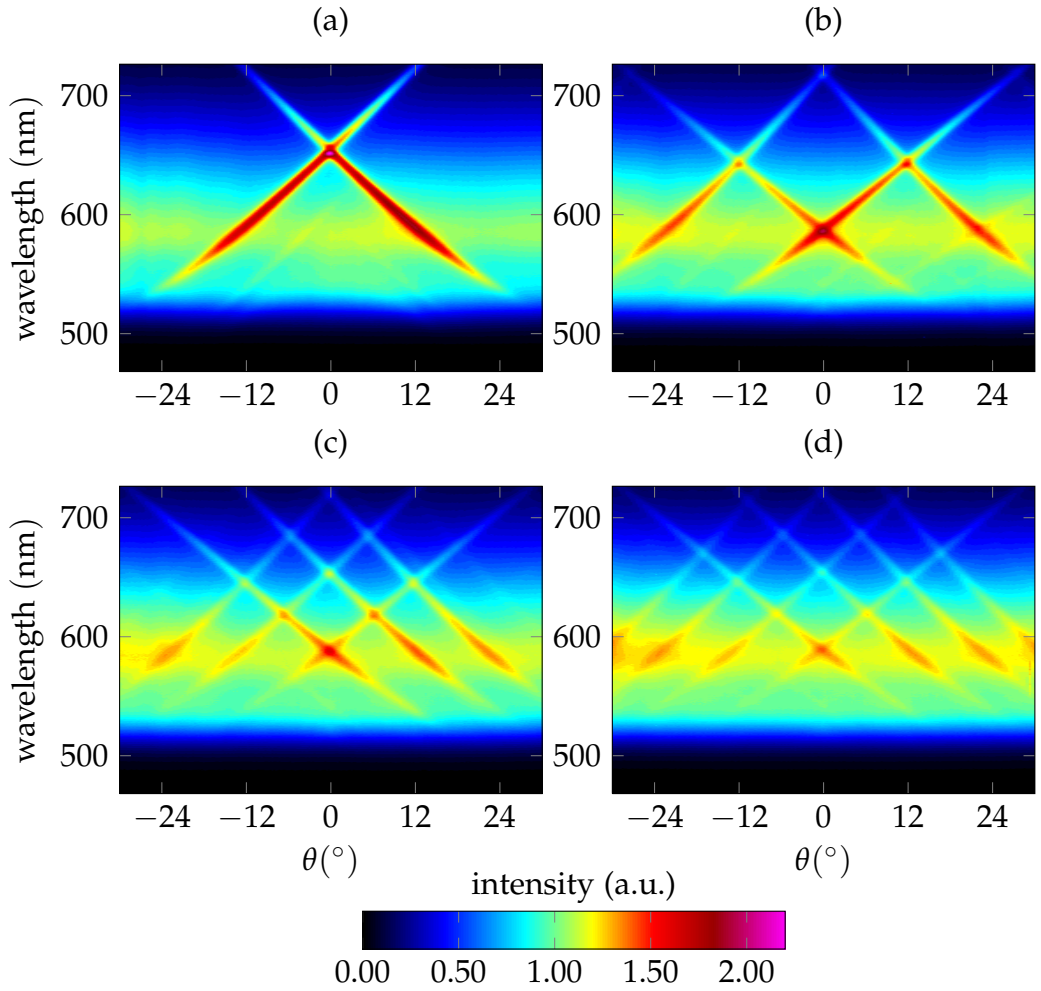

Figure 5.1: Angle-resolved PL spectra of an organic emitter layer structured by (a) single-period grating, and compound binary gratings with (b) two superimposed grating periods, (c) three superimposed grating periods, and (d) four superimposed grating periods. An increased number of period components increases the number of Bragg scattering directions into which the TE_0 waveguide mode is extracted.

high intensity in Fig. 5.1a are the wavelength and angle-dependent peaks of the Bragg scattered TE_0-mode. Besides single-period gratings, random

scattering structures have been investigated for outcoupling of waveguide modes from OLEDs [38, 115, 116]. While a single-period grating has one dominant space-frequency, random structures have a broad distribution of space-frequencies. Depending on the space-frequency distribution, a guided mode is scattered either to a distinct pair of peaks (see Fig. 5.1a), as is the case for single-period gratings, or to a broad range of directions, as is the case for random scattering structures. These two extreme cases limit the OLED outcoupling designs reported to date.

In this chapter, I investigate structures with multiple strong space frequencies for waveguide light outcoupling. By superimposing multiple binary gratings with various periods, a binary grating can be constructed that dominantly comprises the space frequencies of its components. I call the resulting grating a compound binary grating. In contrast to random scattering structures, compound binary gratings allow the control of the Bragg scattered waves' directions and intensities as I will investigate in this chapter. Fig. 5.1b-d exemplarily show the angularly-resolved spectral emissions of an organic emitter layer structured by compound binary gratings with increasing number of period components. The waveguide mode is now Bragg scattered to multiple directions.

A possible application of compound binary gratings is to reduce the color impression of grating OLEDs for general lighting [117]. One drawback of single-period gratings is the introduced spectral change that results in an angle-dependent color impression for the viewer [118]. For an OLED application in general lighting, such color change might be unwanted. Compound binary gratings, on the other hand, produce multiple wavelength peaks in the emission at a given viewing angle as visible in Fig. 5.1, so that the color impression is reduced. I exemplarily calculated the angular color change CD_{avg} defined as the average Euclidian distance between the CIE (Commission Internationale de l'Eclairage) 1976 u'v' color points at all angles [119] for the emissions shown in Fig. 5.1. I found that the color change yielded by the compound binary grating sample with the emission depicted in Fig. 5.1c is a factor 11 smaller than that of the single-period grating with emission of Fig. 5.1a [117]. The calculated values of $1000CD_{avg}$ in the angle range between $\theta = 0°$ and $\theta = 30°$ in Fig. 5.1 are (a) 6.52, (b) 1.64, (c) 0.58, and (d) 0.74. Note that smaller values correspond to less color change.

On the other hand, a directional emission can be beneficial for applications other than general lighting. E.g., I investigate in Chapter 6 an optical detection system using the directionality of a single-period grating structured emitter layer. It is conceivable that additional Bragg scattering

directions and control of their intensity provided by compound binary gratings can be expedient in optical detection systems and other applications.

Gratings with multiple superimposed periods have already been investigated in other contexts than OLED waveguide light outcoupling, such as their application as multiwavelength grating reflectors [120–122], and effective selective absorbers [123]. Also their general diffraction properties [124, 125] have been studied. Combining two grating periods in a metal grating, a band gap for surface plasmon polaritons has been made observable in outcoupled light [126, 127]. For optical detection systems, it has been shown that two superimposed grating periods in a waveguide sensor allow the decoupling of the excitation light from the signal light [128, 129]. Furthermore, Peng [130] investigated the guided waves in doubly periodic structures but without treating the guided mode to radiation coupling explicitly.

This chapter begins with the definition of compound binary gratings and their geometry (Sec. 5.1). The fabrication of organic emitter samples with compound binary gratings is described in Sec. 5.2. In order to compare the experimental results with simulations, the optical constants of the materials used in the samples have to be determined as is elaborated in Sec. 5.3. After a discussion of the compound binary grating Fourier spectrum (Sec. 5.4), and the required number of retained orders in the RCWA simulation (Sec. 5.5), I investigate the angular emission pattern of waveguides with compound binary gratings (Sec. 5.7).

5.1 Geometry of compound binary gratings

The idea how to combine multiple binary gratings with various periods is to superimpose the gratings in position-space by a logical disjunction operation. The result is again a binary grating, which I refer to as a compound binary grating. In contrast to more complex grating relief forms, binary structures can be directly written with electron beam lithography, which is the method of choice to fabricate an irregular sequence of grooves and ridges (see Sec. 5.2.1).

Assume we want to combine N binary gratings with periods Λ_i and ridge widths $l_{\mathrm{rd},\Lambda_\mathrm{i}}$ as defined in Sec. 2.6. To construct the compound binary grating, each component grating with index i is represented as a relief function $g_i : x \to [0, 1]$, where x is the position perpendicular to the grating lines as given in Fig. 2.4. g_i is 0 where the grating has a groove and 1 where the grating has a ridge as seen from the substrate. This means that the grooves are of the film material and the ridges are of the substrate material (see Fig. 2.4). The component gratings are aligned before the superposition,

so that at $x = 0$ each g_i exhibits a rising edge. The compound binary grating relief function g_t is then defined as

$$g_\mathrm{t} = g_1 \vee g_2 ... \vee g_N, \tag{5.1}$$

where $\vee$ is the logical disjunction operator yielding 0 only when both operands are 0, and 1 otherwise. The component periods Λ_i in nanometers must be integer values. Then, the superposition defined in Eq. (5.1) yields a periodic g_t with integer total period Λ_t given by the least common multiple of all Λ_i. The assumption of all Λ_i being of integer value guarantees that g_t is periodic. The non-commensurate case in which no integer least common multiple exists and an aperiodic structure results, occurs only if one or more Λ_i is of irrational value [130].

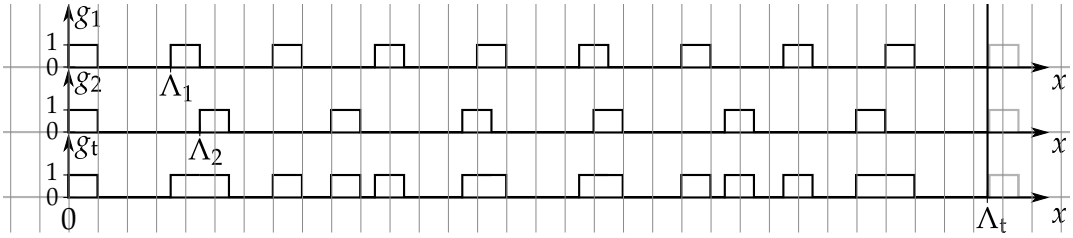

Figure 5.2: Construction of an example compound binary grating. The grating relief function g_1 represents the component $\Lambda_1 = 350\,\mathrm{nm}$ with $l_{\mathrm{rd},350\,\mathrm{nm}} = 100\,\mathrm{nm}$ and g_2 represents the component $\Lambda_2 = 450\,\mathrm{nm}$ with $l_{\mathrm{rd},450\,\mathrm{nm}} = 100\,\mathrm{nm}$. The relief function g_t is obtained by a logical disjunction operation at every x-position and represents the compound binary grating.

Fig. 5.2 depicts the compound binary grating construction according to Eq. (5.1) for two components: $\Lambda_1 = 350\,\mathrm{nm}$ with $l_{\mathrm{rd},350\,\mathrm{nm}} = 100\,\mathrm{nm}$ and $\Lambda_2 = 450\,\mathrm{nm}$ with $l_{\mathrm{rd},450\,\mathrm{nm}} = 100\,\mathrm{nm}$. For this example, the total period is $\Lambda_\mathrm{t} = 3150\,\mathrm{nm}$ and we see how nine periods of g_1 and seven periods of g_2 fit in Λ_t.

The short notation

$$\Lambda_1(l_{\mathrm{rd},\Lambda_1})|\Lambda_2(l_{\mathrm{rd},\Lambda_2})|...|\Lambda_N(l_{\mathrm{rd},\Lambda_\mathrm{N}}) \tag{5.2}$$

denotes the compound binary grating with components of periods Λ_1, Λ_2, ..., Λ_N and ridge widths $l_{\mathrm{rd},\Lambda_1}$, $l_{\mathrm{rd},\Lambda_2}$, ..., $l_{\mathrm{rd},\Lambda_\mathrm{N}}$. All lengths are written in nanometers without units. E.g., the compound binary grating of Fig. 5.2 is abbreviated as $350(100)|450(100)$. Note that the notation Eq. (5.2) implies all component duty cycles $f_{\mathrm{dc},i}$ via Eq. (2.36). If specification of the ridge width is omitted in notation Eq. (5.2), it refers to a type of compound binary grating with a particular period combination.

Finally, we define the duty cycle of a compound binary grating by

$$f_{\mathrm{dc}} = \frac{1}{\Lambda_{\mathrm{t}}} \int_0^{\Lambda_{\mathrm{t}}} g_{\mathrm{t}} \, \mathrm{d}x. \tag{5.3}$$

5.2 Sample fabrication

In order to study the principles of waveguide mode outcoupling by compound binary gratings, I decided to fabricate samples for photoluminescence measurements. As these samples are excited externally by a laser, no electrodes are required as would be the case for a fully functional OLED. The omission of the electrodes facilitates a sample fabrication with less potentially unstable process factors, still allowing us to investigate the general principles of guided mode outcoupling from OLED-like structures. The waveguide was designed to support only the fundamental TE_0- and TM_0-mode. Thus, the Bragg scattering of a single guided mode could be studied in polarized measurements.

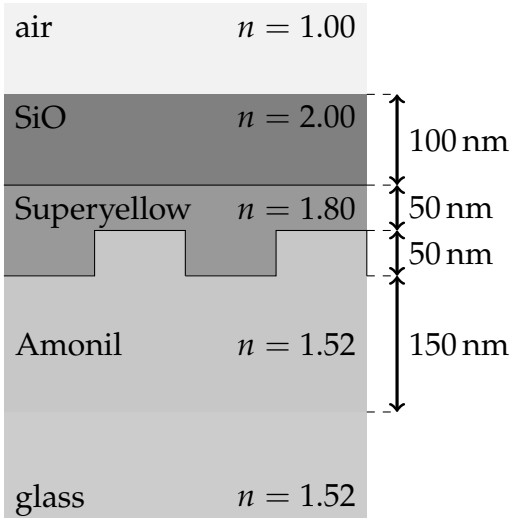

Figure 5.3: The sample design. The organic emitter Superyellow is structured by the Amonil imprint resist. The SiO layer on top of the Superyellow completes the waveguide core and protects the Superyellow against oxygen from air. The sample is fabricated on a glass substrate. The given refractive indices are approximate values at $\lambda_0 = 550\,\mathrm{nm}$.

Fig. 5.3 depicts the sample design. The conjugated polymer Superyellow (Merck KGaA), a phenylene substituted poly(para-phenylenevinylene) derivative, serves as emitter. The emitter layer is protected by a silicon monoxide (SiO) layer that also forms the waveguide core together with

the emitter. As a patterning technique to incorporate the grating into the structure, I use nanoimprint lithography (NIL) to pattern the Amonil (AMO GmbH) imprint layer on the glass substrate. NIL facilitates a high-throughput pattern transfer from a master pattern into the samples [131] and has been successfully employed to fabricate grating OLEDs and two-dimensional photonic crystal OLEDs [30, 132]. With NIL, a once fabricated master pattern, e.g. by electron beam lithography, can be replicated many times by a much faster process (see Sec. 5.2.2). The substrate containing the master pattern is called master stamp. The details of the sample fabrication and NIL process are given in Sec. 5.2.2. Before this, I will describe the master pattern design and fabrication.

5.2.1 Grating masters for nanoimprint lithography

For the purpose of assessing a large parameter space given by the geometry of compound binary gratings, I designed a NIL master pattern containing 36 different binary gratings on a single master stamp. The master stamp was chosen to be 25 mm × 25 mm, which is the size of the glass substrates used in our laboratory for OLED fabrication. Therefore, I arranged four groups each of nine grating fields on the master stamp. Each grating field is a square of 500 µm × 500 µm. The spacing between the fields' edges is 1000 µm in each direction. The fabricated master stamp contains eight type 350|450, eight type 350|400|450, and eight type 300|400|500 compound binary gratings with varied component duty cycles. Furthermore, six single-period gratings and six additional compound binary gratings were fabricated. The gratings are denoted with A,B,C,D for the group and a following number from one to nine for the field, for example B4. A complete list of the gratings with specified ridge widths can be found in Appendix D. The component periods and ridge widths have been chosen under the condition that all resulting ridges and grooves in the compound binary grating are at least 50 nm long. This was the limit set by the master stamp fabrication process.

Because of the complex geometry of the compound binary gratings, I wrote a Python program to calculate and draw the grating patterns. With the Python library dxfwrite [133] the grating patterns were saved in the "Drawing Interchange Format" as black and white graphics. These graphics then served as the input for electron beam lithography to transfer the black and white regions into ridges and grooves, respectively, to the master stamp. Initially, the master pattern was electron beam written in a 50 nm PMMA layer on a silicon wafer. The PMMA thickness determines the grating depth. Subsequently, on top of the PMMA layer, layers of 7 nm

chromium and 15 nm gold were evaporated. Afterward, approximately 1 mm nickel was deposited on the metallic layers by galvanization, similar to the process described in [134]. Finally, the silicon and the PMMA were removed, yielding a nickel shim with the master pattern on its surface that acts as the master stamp. The electron beam lithography and the pattern transfer to the nickel shim have been carried out by the Karlsruhe Nano Micro Facility (KNMF) at the Karlsruhe Institute of Technology. Overall, the KNMF fabricated eight master stamps of which I chose one for the sample fabrication.

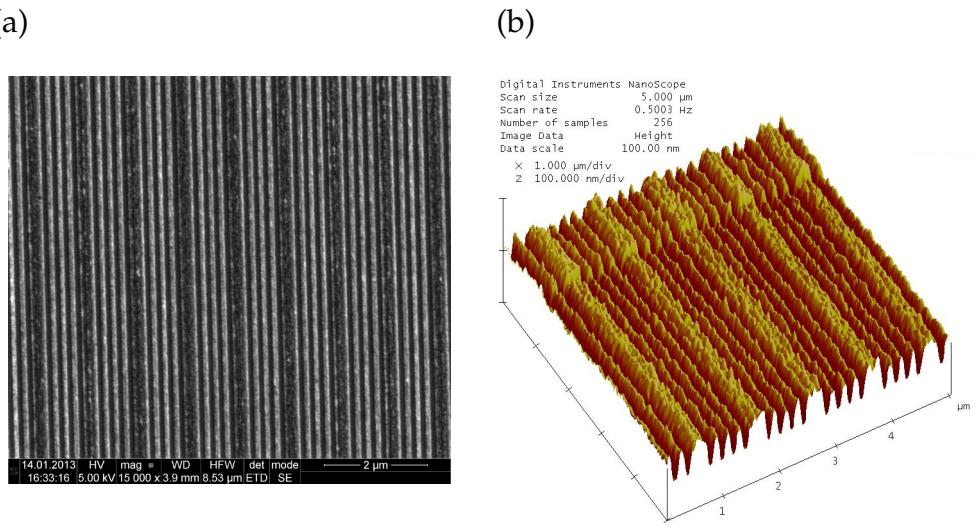

Figure 5.4: Nickel master stamp. Exemplarily shown is the compound binary grating 196(98)|490(98) (field D9). (a) SEM image (b) AFM height profile. In both (a) and (b) the desired structure is visible. Additionally, we observe a significant surface roughness. The AFM measurement has been performed by the Karlsruhe Institute of Technology.

Figure 5.4 shows a scanning electron microscope (SEM) image and an atomic force microscope (AFM) measurement of the height profile of a fabricated nickel master stamp. The grating structure is clearly visible. The structure depth measured with AFM is between 35 nm and 65 nm, depending on the position on the master stamp. We observe a slight deviation from a binary structure, as the ridges are not purely rectangular. Furthermore, the AFM measurement reveals a roughness of approximately 10 nm peak-to-valley amplitude superimposed onto the grating structure. The surface roughness is associated with the observation that two different surface types are present on the master stamps as shown in Fig. 5.5. In Fig. 5.5, the surface on the right side appears brighter and rougher than on the left side. One explanation could be that the chromium and gold layers

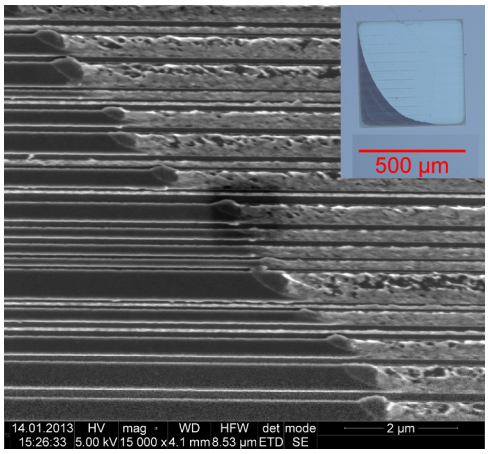

Figure 5.5: SEM image of a grating field on the master stamp showing two different surface types present. The ridges on the left are darker than the ones the right. At the border between the two surface types, the ridges are raised. Possibly, the chromium and gold layer became detached from the underlying nickel in the brighter areas. The inset shows a light microscope image of the complete grating field. The areas that appear brighter in the SEM image also appear brighter under the light microscope.

possibly became detached from the nickel shim in the brighter areas. SEM images of the tilted master stamp revealed that the darker ridges on the left side of Fig. 5.5 are indeed higher than on the right side. As seen from the inset of Fig. 5.5, there are coherent areas of both surface types on the grating fields. Unfortunately, the rougher surface type is present on the majority of the area on the master stamps. I therefore decided to use the master stamp with the smallest fraction of the darker surface area so that the later measurements are less influenced by the difference in the surface structure.

5.2.2 Process details

Before the samples could be fabricated, the master pattern had to be transferred from the master stamp to a polydimethylsiloxane (PDMS) stamp for the NIL process. I used Sylgard 184 PDMS (Dow Corning Corporation) and mixed basis and curing agent in a ratio of 8:1 for 20 min at a mixing rotation speed of 4500 min^{-1}. After removal of bubbles from the PDMS in vacuum, the PDMS was poured in a casting mold with the master stamp forming the bottom. Finally, the PDMS was cured at 80 °C for 135 min yielding a PDMS stamp with the desired pattern at the bottom.

The samples (Fig. 5.3) were fabricated on a quadratic float glass substrate

of 25 mm · 25 mm area and 1 mm thickness. Before further processing, the glass substrates were cleaned using an ultrasonic cleaner for 5 min in acetone and subsequently for 5 min in isopropyl alcohol. Afterwards the remaining moisture was reduced by heating the glass substrates to 160 °C for 10 min.

As NIL imprint material the UV curable Amonil (AMO GmbH) was used. To improve the adhesion between the glass substrate and the Amonil, I initially spin-coated the adhesion promoter Amoprime (AMO GmbH). Then a 200 nm-thick layer of Amonil was spin-coated onto the substrate. Both Amonil and Amoprime were spin-coated at 3000 min^{-1} for 30 s. At this point, the previously fabricated PDMS stamp was applied onto the sample without pressure. After curing the Amonil under an UV-lamp for 3 min, the PDMS stamp was carefully removed. As a result of the twofold transfer from the master pattern to the PDMS stamp and the imprint resist afterwards, the structure transfer to the imprint resist is non-inverting.

Following this, 230 ml toluene-dissolved Superyellow was spin-coated onto the structured imprint resist with a program starting with 500 min^{-1} for 5 s and spinning then at 1000 min^{-1} for 60 s. This step was done in a glovebox with inert nitrogen atmosphere to protect the Superyellow from oxygen and moisture.

Finally, the sample was brought into an evaporation machine without exposing it to air. There, a 100 nm layer of SiO was evaporated onto the Superyellow at a rate of 0.12 $\mathrm{nm\,s}^{-1}$.

All fabrication steps were performed in the clean room of the Technical Faculty at the Christian-Albrechts-University of Kiel.

5.2.3 Fabricated structure examination

In order to examine the fabricated sample structure, a focused ion beam (FIB) was used to cut into the layers of exemplary fields on a sample. The FIB cut allows the subsequent imaging of the cut edge with the SEM as shown in Fig. 5.6. Note that the FIB process required evaporation of a silver layer on top of the sample as is visible in Fig. 5.6b at the topmost layer. Fig. 5.6 reveals that all layers above the Amonil imprint resist are corrugated by the grating. It is clearly visible that the corrugation is not a pure binary grating, but is significantly rounded. Nevertheless, the period is preserved. From the examined FIB cuts, the thickness of the fabricated layers could be estimated to the values given in Fig. 5.6b. Note that the layer thicknesses could only be approximated since the boundaries between the layers are blurred. The grating depth is approximately 30 nm. The fabricated SiO layer is thinner than it was designed, which could be due to calibration

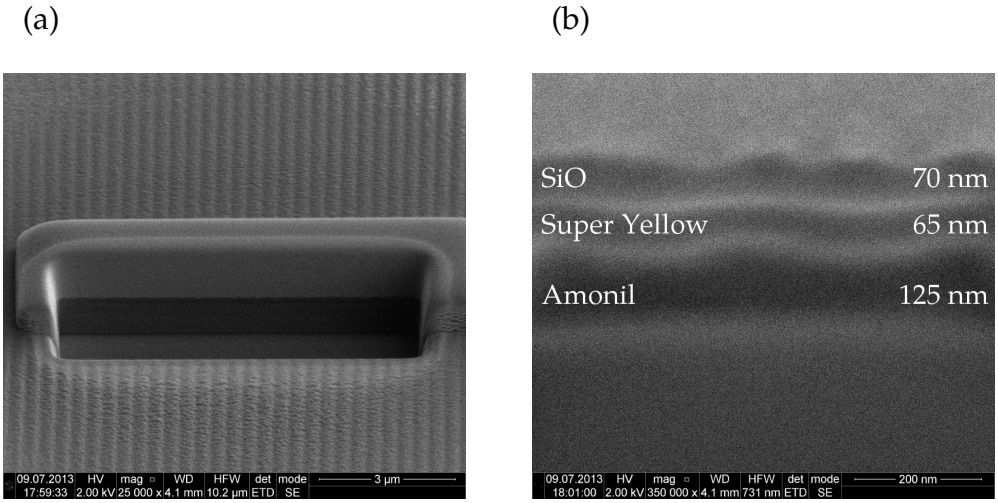

Figure 5.6: Field A9 with single-period grating $\Lambda = 350\,\text{nm}$. (a) FIB cut into a sample to examine the sample layer structure. (b) SEM image of the FIB cut. The layer thicknesses could be estimated from the SEM images to the given values. The grating structure is present in all layers above the Amonil imprint resist.

inaccuracy of the evaporation process.

5.3 Determination of optical constants

The optical constants of the used materials are necessary to compare the experimental results with the simulations. Although many OLED materials have been characterized in the literature [86–88, 135–138], the optical constants given for each material may vary. One possible explanation is that the process parameters during fabrication can influence the optical properties of a material. Notably, the molecular orientation of small-molecule OLED materials depends on the vacuum-deposition rate and temperature and has significant effects on the material's optical properties [88]. It is also known for SiO, which I used in the samples, that its optical properties depend appreciably on the deposition conditions [139]. In the samples, two materials of unknown refractive index are present: the Superyellow and the SiO. I will assume two layer stacks with different layer refractive indices and compare the TMM simulation results. Although the refractive indices of the materials cannot be uniquely determined, I show that both layer stacks are capable of describing the measured TE_0-mode propagation.

I began with the determination of the real parts of the refractive indices. As first step, I determined the TE_0-mode effective index n_{eff} (Fig. 5.7a)

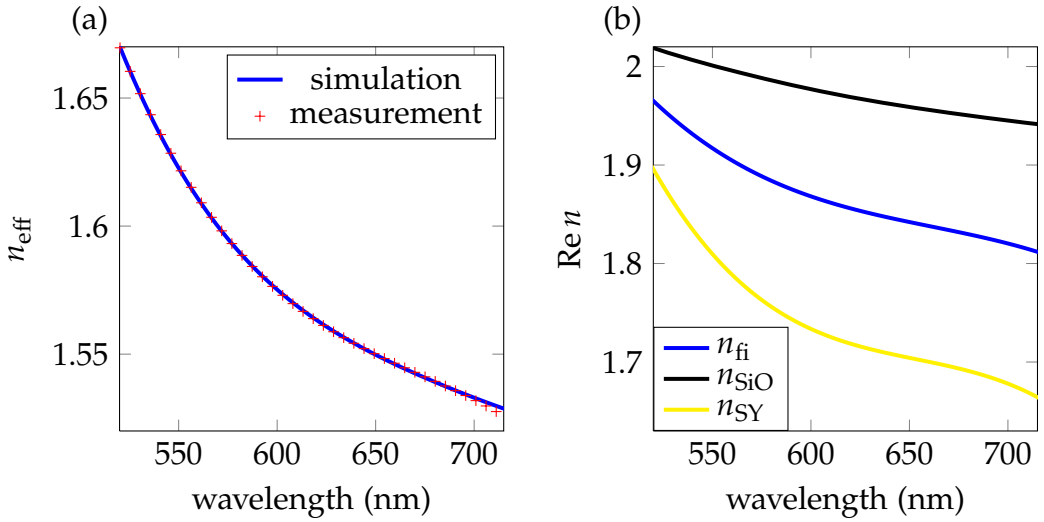

Figure 5.7: (a) Measured TE_0-mode effective index used to determine the film refractive index (red marks). The blue line is the TMM simulation result after fitting the refractive index of one layer in the model stack. (b) Real parts of fitted refractive indices. Yellow line: Fitted Superyellow refractive index n_{SY} if SiO refractive index n_{SiO} is given. Blue line: Fitted film refractive index n_{fi} if Superyellow and SiO layer are modeled as one film layer. Black line: n_{SiO} for comparison.

from an outcoupling peak position in the measured emission of the grating 350(100)|450(100) on sample K15 (see Appendix D) with the method described in Sec. 4.3.2. I then used the unperturbed waveguide model (Sec. 2.6.1) to match the TMM simulation of n_{eff} to the measured value. I assumed the layer thicknesses determined from Fig. 5.6. Thus, the refractive index of one layer could be determined for each wavelength with the TMM by least-squares fitting the simulated n_{eff} to the measured value. The averaged grating layer refractive index was calculated by Eq. (2.37) with $f_{\text{dc}} = 0.444$.

I compared two layer stacks. Stack A: Air, 70 nm SiO, 35 nm Superyellow, 30 nm grating, Amonil/glass. Here, the Superyellow refractive index n_{SY} is the fitting-variable while the SiO refractive index n_{SiO} is taken from [140] (SOPRA Data:2). The fitting result is shown in Fig. 5.7a and the obtained n_{SY} is shown in Fig. 5.7b. Stack B: Air, 105 nm film, 30 nm grating, Amonil/glass. Here, only one film layer is assumed for the Superyellow layer and the SiO layer together. The film refractive index n_{fi} is now the fitting-variable and the film thickness is the sum of both layers. The resulting n_{fi} is shown in Fig. 5.7b. The n_{eff} fitting result is equal to that of Stack A shown in Fig. 5.7a. Both layer stacks yield a high level of agreement between the measured and the simulated n_{eff}.

For comparison, Fig. 5.7b also shows n_{SiO} as given in [140] (SOPRA Data:2). Evidently, the fitted layer refractive index in both stacks is smaller than n_{SiO}. Furthermore, the layer refractive indices exhibit a significant dispersion. This material dispersion adds to the waveguide dispersion, which both lead to the decrease of n_{eff} with increasing wavelength (Fig. 5.7a). In the Stack B, n_{fi} is an average value of the two material refractive indices. My RCWA implementation only allows the simulation of structures with a single waveguide layer (see Sec. 2.7.3). Thus, only Stack B is compatible with my RCWA implementation. As the fitted refractive indices yield equal values of the TE_0-mode effective index n_{eff} in both layer stacks, I will use the obtained n_{fi} of Stack B for the RCWA simulations.

Note that the refractive indices are valid for an in-plane electric field as they were determined from the TE-polarized mode. Conjugated polymer thin films have been shown to be optically anisotropic [137], and the refractive index for TM-polarized light will therefore be different.

The imaginary part of the SiO refractive index was taken from [140] (SOPRA Data:2) and is depicted in Fig. 5.8b. I initially simulated Stack A with the real parts of the refractive indices obtained above, but with lossy SiO. Simultaneously, the Superyellow was assumed lossless, as reports about similar conjugated polymers indicate that these materials absorb strongest at wavelengths shorter than 550 nm [135, 141]. This yielded

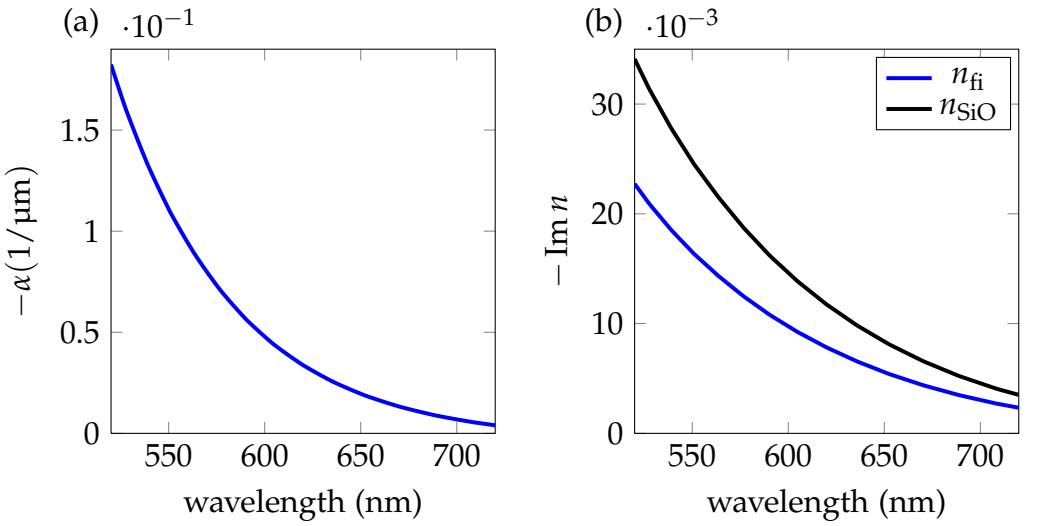

Figure 5.8: (a) Simulated TE_0 attenuation constant α due to material absorption. (b) Imaginary parts of refractive indices. Black line: SiO as given in [140]. Blue line: Merged film layer yielding the same α as in the layer stack with separate Superyellow layer and SiO layer.

the TE_0 attenuation constant α due to material absorption as depicted in

Fig. 5.8a. To obtain a layer stack compatible with my RCWA implementation, the imaginary part of the film refractive index in Stack B has then been adjusted by the factor 70/105 to obtain the same α (Fig. 5.8b). Clearly, the material absorption increases at shorter wavelengths.

Note that the results obtained above depend on the assumed layer thicknesses, which are not exactly known and can vary over the sample surface. Thicker layers in the simulation would result in a lower refractive index.

5.4 Fourier spectrum of compound binary gratings

We have already seen in Sec. 2.7.2 that the Fourier coefficients $\tilde{\epsilon}_m$ of the grating permittivity function are a determining factor for the diffracted wave intensities. Recalling that the idea of compound binary gratings is to obtain a grating structure that possesses the diffraction properties of multiple gratings, the spectrum of compound binary gratings is therefore of great interest. The question is: How much of the individual component's spectra will be present in the compound grating's spectrum? In addition, RCWA requires the Fourier coefficients for calculation of the electromagnetic field in a grating waveguide (Sec. 2.7.3).

The grating permittivity function $\epsilon(x)$ is related to the grating relief function $g_t(x)$ (Sec. 5.1) by

$$\epsilon(x) = \epsilon_{\mathrm{grv}} + (\epsilon_{\mathrm{rdg}} - \epsilon_{\mathrm{grv}}) g_t(x), \tag{5.4}$$

where ϵ_{grv} and ϵ_{rdg} are the permittivities in the grating groove and ridge, respectively. The permittivities are related to the refractive indices by Eq. (2.13).

If all component periods Λ_i are integer values, then $g_t(x)$ is periodic (see Sec. 5.1) and consequently $\epsilon(x)$ is also a periodic function. Thus, $\epsilon(x)$ can be represented by a Fourier series with coefficients $\tilde{\epsilon}_m$. Note that $\tilde{\epsilon}_m$ of Eq. (5.4) are equal to the Fourier coefficients of the grating perturbation defined in Eq. (2.63), except for the average term $\tilde{\epsilon}_0$. This is because the permittivity function in Eq. (2.63) describes the perturbation from the average permittivity. Nevertheless, all Fourier coefficients $m \neq 0$ of Eq. (5.4) can be used in the pTMM.

For a qualitative understanding of the Fourier spectrum of compound binary gratings, let us consider the Fourier transform of $\epsilon(x)$

$$\mathcal{F}\left(\epsilon(x)\right) = \epsilon_{\mathrm{grv}}\delta_0 + (\epsilon_{\mathrm{rdg}} - \epsilon_{\mathrm{grv}})\mathcal{F}\left(g_t(x)\right). \tag{5.5}$$

Due to the periodicity of $\epsilon(x)$, $\mathcal{F}(\epsilon(x))$ is a discrete frequency spectrum comprising Dirac impulses δ_0 at the harmonic frequencies weighted by the coefficients $2\pi\tilde{\epsilon}_m$ [142]. In order to calculate $\mathcal{F}(g_\mathrm{t}(x))$, it is beneficial to reformulate the defining equation (5.1) outside Boolean algebra. Assuming only two component gratings g_1 and g_2, Eq. (5.1) is equivalent to

$$g_\mathrm{t} = g_1 + g_2 - g_1 \cdot g_2 \tag{5.6}$$

as is directly verifiable from the four possible value combinations at a given x-position. The superposition of more than two component gratings can be calculated afterwards by inserting g_t and one new component iteratively into Eq. (5.6). The Fourier transform of g_t can thus be expressed with Eq. (5.6) as

$$\begin{aligned}\mathcal{F}(g_\mathrm{t}) &= \mathcal{F}(g_1) + \mathcal{F}(g_2) - \mathcal{F}(g_1 \cdot g_2) \\ &= \mathcal{F}(g_1) + \mathcal{F}(g_2) - \frac{1}{2\pi}\mathcal{F}(g_1) \otimes \mathcal{F}(g_2),\end{aligned} \tag{5.7}$$

where the frequency convolution theorem of the Fourier transform has been used [142]. Consequently, the Fourier spectrum of the compound binary grating is the sum of the component gratings' spectra plus a spectrum convolution term. This is also valid for more component gratings, but the number of convolution terms will rapidly grow with the number of component gratings.

As an example Fig. 5.9 depicts the spectrum of the compound binary grating $350(100)|450(100)$ together with the extended component gratings' spectra. Clearly, the summed component gratings' spectra dominate the resulting spectrum of the compound binary grating in this case. The spectrum convolution term of Eq. (5.6) reduces the amplitudes of the component gratings' Fourier coefficients moderately. Additionally, the convolution term becomes visible as the intermediate Fourier coefficients that are not present in the individual component spectra. The intermediate Fourier coefficients in the component spectra are zero, because the periodicity of the component gratings is increased to $\Lambda_\mathrm{t} = 3150\,\mathrm{nm}$. For this reason, the "first-order" Fourier coefficient is $\tilde{\epsilon}_9$ for the 350 nm-grating and $\tilde{\epsilon}_7$ for the 450 nm-grating in this example. Generally, the m^comp-th Fourier coefficient of the i-th component grating based on its original period Λ_i occurs at the order

$$m = \frac{\Lambda_\mathrm{t}}{\Lambda_i} \cdot m^\mathrm{comp} \tag{5.8}$$

in the compound grating's spectrum.

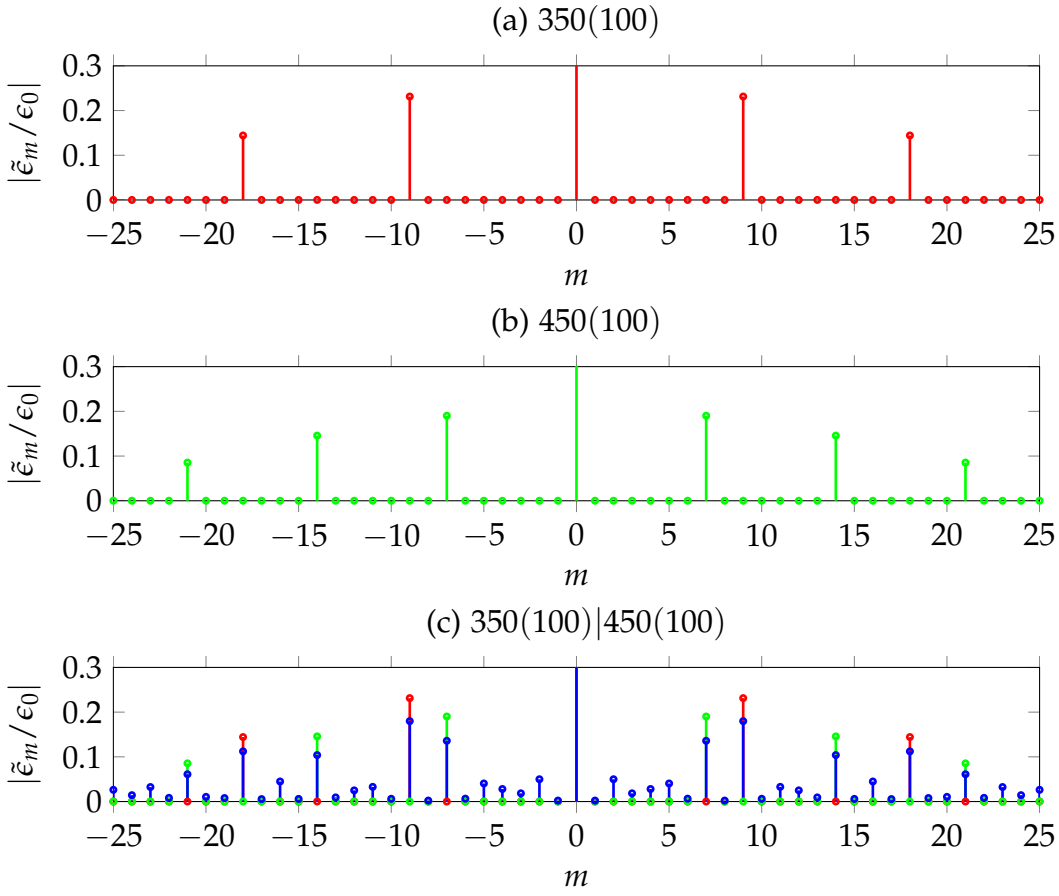

Figure 5.9: (a),(b) Amplitude Fourier spectra of two single-period gratings and (c) the amplitude Fourier spectra of the corresponding compound binary grating (blue lines). Note that all three spectra have been calculated with respect to the total period $\Lambda_t = 3150\,\text{nm}$. This results in the intermediate zeros visible in the spectra of the single-period gratings. In (c), both component spectra (a) and (b) have been plotted in their original colors to illustrate the spectrum superposition.

In the example given above the superposition through logical disjunction yields a spectrum that is dominated by the sum of the components' spectra. This is different when the spectrum convolution term in Eq. (5.7) is of high magnitude. The convolution term's magnitude increases with the overlap of the component gratings. In the limiting case of any grating component having a ridge at every x-position, Eq. (5.1) yields a relief function g_t that is 1 everywhere. Then the convolution terms arising from the iterative use of Eq. (5.7) cancel out every $\tilde{\epsilon}_m$ except for $\tilde{\epsilon}_0$. Consequently, the compound binary grating will not act as a grating in this limiting case, which shows that the number of grating components is limited for the logical disjunction

superposition.

The Fourier spectra are calculated in Matlab with the fast Fourier transform algorithm [143].

5.5 Number of retained space harmonics in RCWA

The accuracy of grating diffraction calculations with RCWA depends on the number of retained space harmonics [79]. For an exemplary single period grating, it has been found that not more than 100 space harmonics are needed for the convergence of RCWA [79]. In the following, N denotes the number of retained space harmonics. Compared to single-period gratings, compound binary gratings posses a broader spectrum (Sec. 5.4). We thus expect that the RCWA calculation of compound binary gratings requires more retained space harmonics. Note that the single-period gratings' spectra in Fig. 5.9a,b are artificially broadened due to the increase of the period and could equivalently be represented with five and seven Fourier coefficients, respectively, in the depicted spectral range.

I define the error of diffraction efficiency to the substrate as

$$\delta = \left| \mathrm{DE}_m^{\mathrm{sub}}(N) - \mathrm{DE}_m^{\mathrm{sub}}(N_{\max}) \right|, \tag{5.9}$$

where m is the space harmonic order and $N_{\max}$ is the highest N in the particular comparison. The error δ over N is depicted in Fig. 5.10a,b,c for three different compound binary gratings. Each curve in Fig. 5.10a,b,c represents a different space harmonic order. There is a clear trend of decreasing error δ with increasing N. For a small error, it is especially important to include the first two orders of the original component gratings. This is, e.g., the case if the highest included order $(N-1)/2$ fulfills $(N-1)/2 > 2 \cdot 9 = 18$ for the $350(100)|450(150)$ grating, yielding $\delta < 0.3$. Consequently, the $350(100)|400(100)|450(150)$-grating requires significantly more retained space harmonics, as the original gratings' first Fourier coefficients occur at orders 56, 63, and 72 in the compound spectrum (see Eq. (5.8)). Thus, the original second orders are only included for $(N-1)/2 > 2 \cdot 72 = 144$, yielding $\delta < 0.8$.

The choice of N for the RCWA calculations is a trade-off between accuracy and computation time. Fig. 5.10d shows that the computation time per RCWA simulation increases with more than N^2. I therefore chose N as given in Table 5.1.

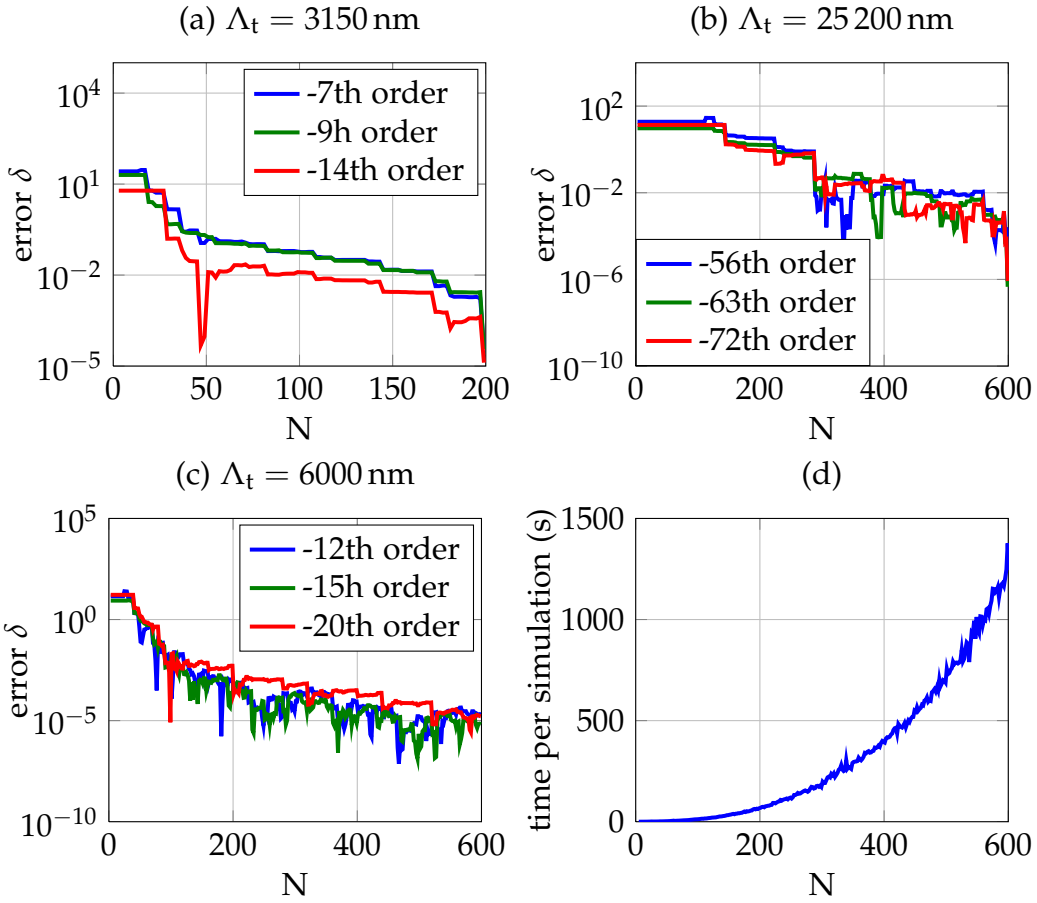

Figure 5.10: RCWA error with increasing number of retained space harmonics N for compound binary gratings at $\lambda_0 = 550\,\mathrm{nm}$. (a) 350(100)|450(150). (b) 350(100)|400(100)|450(150). (c) 300(100)|400(100)|500(150). The error of diffraction efficiency as defined in Eq. (5.9) is shown for three different orders. Clearly, more space harmonics have to be retained for increasing total grating period if a particular error level is to be achieved. (d) Simulation time per step.

5.6 Guided mode outcoupling intensity

To evaluate the intensity of guided mode to radiation coupling in a compound binary grating waveguide, I simulated the exemplary case given in Fig. 5.11 with the RCWA model (Sec. 2.7.3). The assumed grating depth is 50 nm and the film is characterized by $d_{\mathrm{fi}} = 150\,\mathrm{nm}$ and $n_{\mathrm{fi}} = 1.8$ (wavelength-independent and lossless). Clearly, the compound binary grating's α-curve is populated with many stopband peaks. These arise due to the intermediate Fourier coefficients that lead to stopbands at wavelengths fulfilling the Bragg condition Eq. (2.50). Outside the stopbands, α in the

grating	Λ_t	N
350|450	3150	100
350|400|450	25200	300
300|400|500	6000	150

Table 5.1: Number of retained space harmonics N used for RCWA of compound binary gratings.

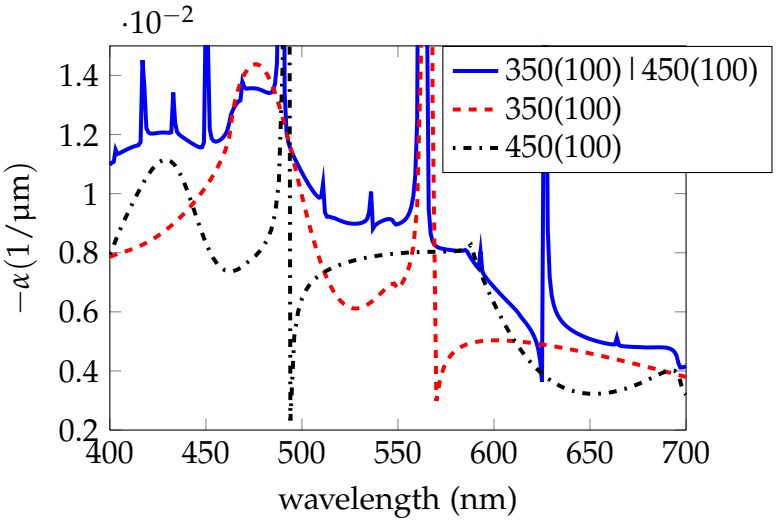

Figure 5.11: TE_0-mode attenuation constant in a compound binary grating waveguide compared to a waveguide structured by the single-period component gratings. The compound binary grating couples the guided mode to radiation comparably strong as its single-period component gratings in this example.

waveguide structured by a compound binary grating is comparably strong as for the single-period component gratings in the given example. On the other hand, the single-period gratings would couple stronger to radiation if the duty cycle was increased to 0.5 (see Fig. 2.10).

In order to finally assess the guided mode to radiation coupling in a compound binary grating waveguide in comparison to single-period gratings as one extreme and random scattering structures as the other extreme, an analysis like that made by Payne and Lacey [144] might be necessary. Payne and Lacey [144] derived analytical expressions for the scattering loss in slab waveguides depending on the autocorrelation function of the surface roughness.

5.7 Angular emission pattern

The photoluminescent emission from the samples with compound binary gratings will now be investigated. The leading question will be: How do the parameters of a compound binary grating influence the angular emission pattern?

The sample emission was measured with the goniophotometer as described in Chapter 4. All spectra were recorded perpendicular to the grating lines, i.e. $\varphi_0 = 0^\circ$ and the y^s-axis perpendicular to the grating grooves (Fig. 4.3).

5.7.1 Polarization

Fig. 5.12 depicts the emission from a typical grating field. A polarization filter was used to measure the TE- and TM-polarized emission separately.

Strong TE-polarized peaks are present in the visible emission. It has been reported that the peaks in the emission of grating structured films are polarized as they arise from Bragg-scattered waveguide modes [26, 29]. Further evidence that the peaks originate from Bragg-scattered waveguide modes are the peak positions and intensities, which will be discussed in Sec. 5.7.2 and Sec. 5.7.3.

From the absence of TM-polarized peaks I conclude that an insignificant amount of light is guided in TM-waveguide modes in the sample. Nevertheless, a CAMFR simulation yields that the TM_0-mode is supported for wavelengths below $\lambda_0 = 600\,\text{nm}$ in the assumed Stack B (Sec. 5.3) with the n_{fi} from Fig. 5.7b. Even if the out-of-plane refractive index of the film is significantly lower than its in-plane value due to optical anisotropy, the TM_0-mode would still be supported at $\lambda_0 = 550\,\text{nm}$ for a refractive index as low as 1.81. It is thus reasonable to assume that the TM_0-mode is supported at least at the short wavelengths of the measurement (Fig. 5.12). Consequently, the absence of TM-polarized peaks in the measurement indicates that the TM-mode is only weakly excited. This is in agreement with reports that the dipoles in a spin-coated polymer emitter tend to lie in the film plane [21, 145] and in-plane dipoles couple stronger to TE-modes than to TM-modes [90].

The following analyses will therefore be limited to the TE-polarized peaks.

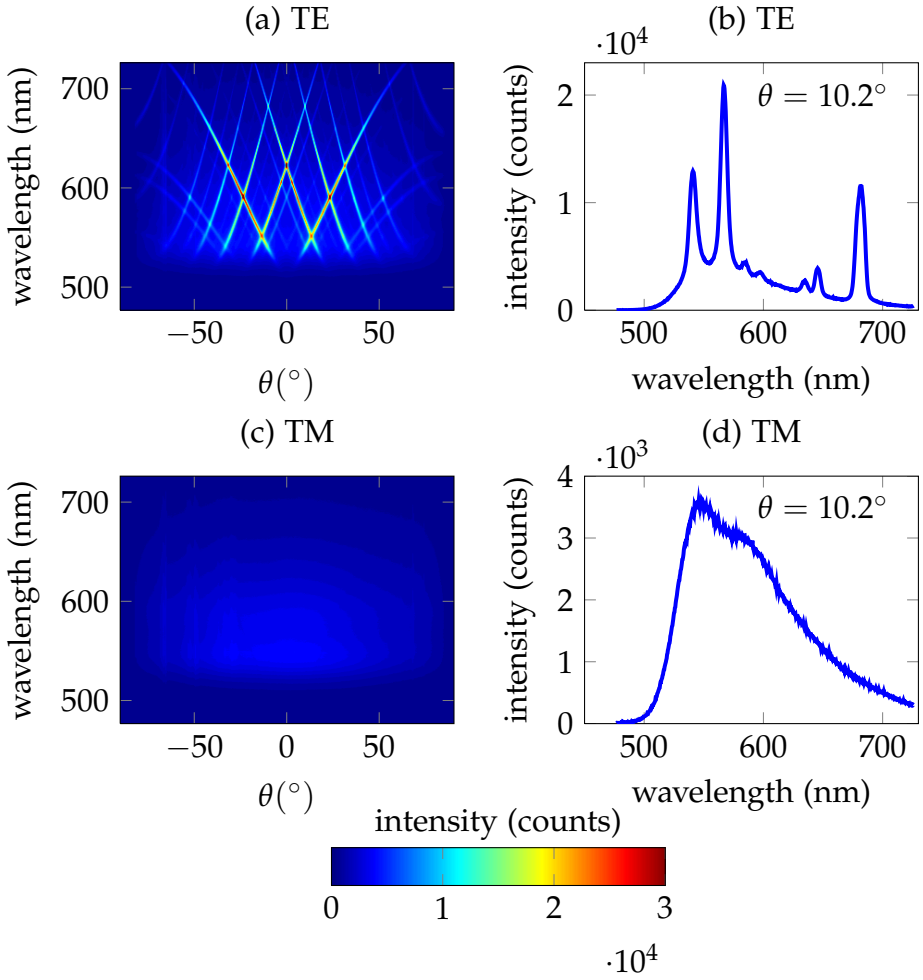

Figure 5.12: Goniophotometric emission measurement of the sample K15 C6 with the compound binary grating 300(100)|400(100)|500(100). In the TE-polarized emission depicted in (a) and (b), strong outcoupling peaks arising from the TE_0-mode are visible. On the contrary, no outcoupling features are visible in the TM-polarized emission. The spectra in (b) and (d) are exemplarily given at $\theta = 10.2°$.

5.7.2 Peak position

The emission of polymer films structured by compound binary gratings exhibits multiple TE-polarized wavelength peaks with angle-dependent position as shown in Fig. 5.12. In the following, the measured peak positions are investigated.

I initially chose one Bragg scattering order and determined the corresponding wavelength peak position with the peak maximum search described in Sec. 4.3.2 from the photoluminescence measurement. Concurrently, the mode effective index n_{eff} was obtained. The other orders' peak

positions were subsequently calculated by the Bragg equation (Eq. (2.44)).

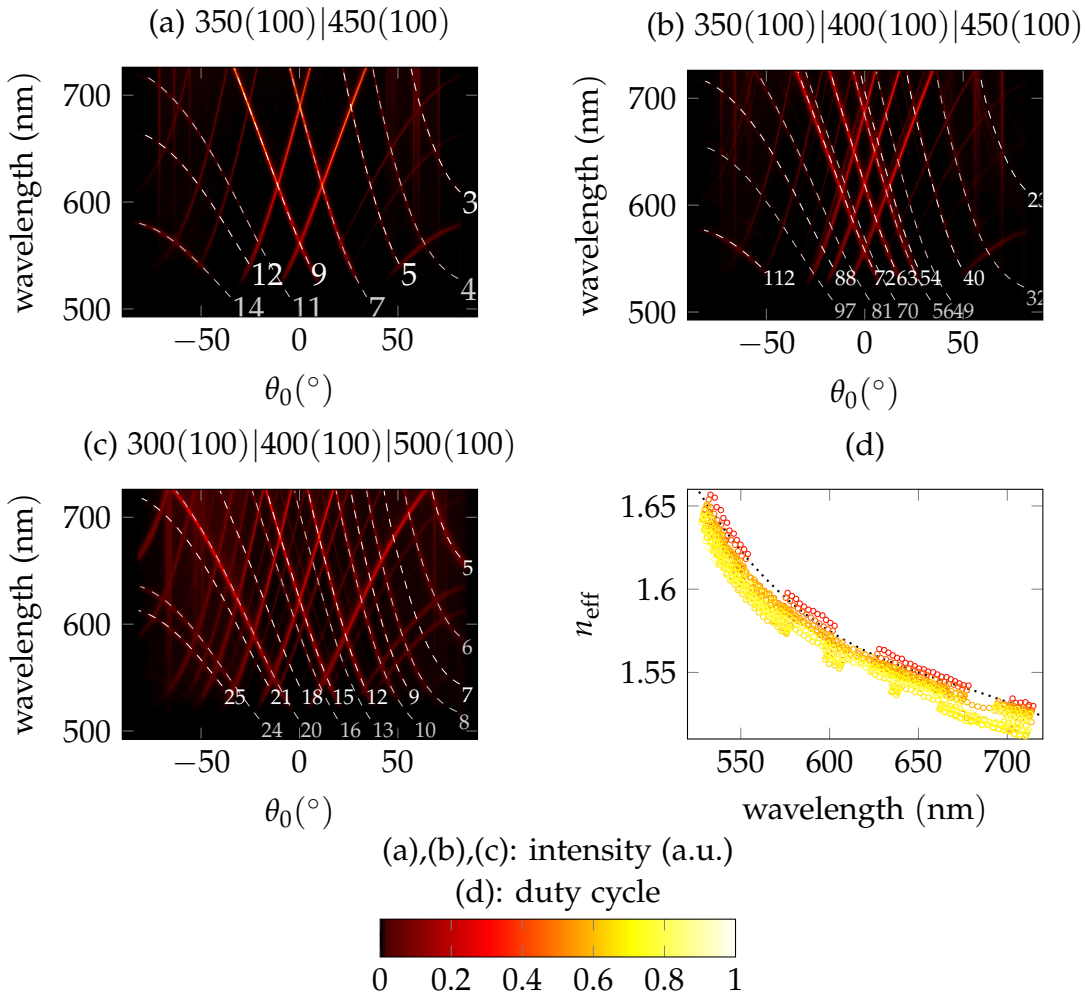

Figure 5.13: Peak positions in the measured emission of exemplary gratings (a) A6, (b) B6, and (c) C6. The dashed lines were calculated by the Bragg equation and are numbered according to the scattering order $|m|$. (d) Mode effective indices n_{eff} at the 24 gratings A1-8, B1-8, and C1-8. The marker colors visualize the corresponding grating duty cycle and show the trend of decreasing n_{eff} with increasing duty cycle. The dotted line is the TE_0-mode's n_{eff} matched with the simulation in Sec. 5.3.

I analyzed the gratings A1 to A8, B1 to B8, and C1 to C8 and show one example of each field in Fig. 5.13a,b,c. The results of all 24 gratings can be found in Appendix E. Only peaks originating from one mode propagation direction are analyzed, as the counter-propagation direction generates symmetrical peaks (see Sec. "Symmetry" below). The peak maximum search was performed on the 9th order for gratings 350|450, the 63rd order for

gratings 350|400|450 and the 12th order for gratings 300|400|500. These orders were chosen because they are of sufficient intensity in every measured emission, so that the peak maximum search is stable.

As shown in Fig. 5.13a,b,c, the positions of these initially determined orders and of the subsequently calculated orders are in excellent agreement with the measured peak positions. This evidences that each peak arises from mode Bragg scattering with the indicated order $|m|$. The m-th order Bragg scattering occurs at the grating's m-th Fourier component.

In Fig. 5.13a,b,c, additional vertical peaks are visible, e.g. in Fig. 5.13c at $\theta_0 = -65°$. These unpolarized peaks cannot be explained by mode Bragg scattering, although they were not observed in the emission from the unstructured regions on the sample. The origin of these additional vertical peaks could not be determined in the course of this work.

Fig. 5.13d depicts the values of n_{eff} over wavelength obtained for the 24 gratings. The determined n_{eff} curves are similar to the curve that matched the fundamental TE_0-mode in the simulation of the fabricated structure (Sec. 5.3). This evidences that the peaks originate from the fundamental TE_0-mode.

The mode's effective index n_{eff} varies with the measured grating, although all gratings are on the same sample. The grating duty cycle - indicated by the marker color- reveals a trend of the n_{eff}-curve shifting towards smaller values with increased duty cycle. This trend is explainable by Eq. (2.37) as the increased duty cycle decreases the average permittivity in the grating layer. I attribute the not perfectly monotonic shifting of the n_{eff}-curve with the duty cycle to layer inhomogeneities and measurement inaccuracy.

Symmetry

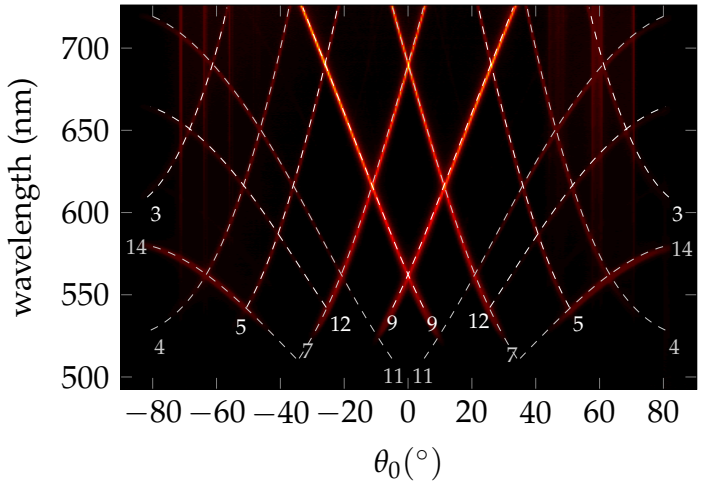

Figure 5.14: Peak position symmetry. The two counter-propagating modes generate angle-mirrored peaks in the emission.

The two counter-propagating TE_0-modes are Bragg-scattered to the plane of measurement simultaneously. Fig. 5.14 shows the peak positions of both propagation directions. Besides the peak positions shown already in Fig. 5.13, the angle-mirrored positions are shown to match the measurement excellently. This is also in agreement with Bragg-theory as the scattering angles of the counter-propagating modes only differ by their signs as the right side of Eq. (2.44) is negated.

5.7.3 Peak intensity control by component duty cycle

I will now discuss how the duty cycles of the component gratings influence the peak intensities and how the emission spectrum can thereby be controlled.

Measurements and RCWA simulations

All compound binary grating measurements were made with 0.75 s spectrometer integration time and equal laser excitation (see Sec. 4.1.4). Initially, the emission spectra are normalized to their background to correct a possibly varying excitation due to sample inhomogeneities or influence of the grating on the excitation. Note that only if the ratio of waveguide light to background light is equal for all gratings, this normalization yields comparable absolute peak intensities. Subsequently, the background has been removed from the emission spectra and the emission spectra are divided by the Superyellow spectrum to obtain a ratio relative to the excitation as described in Sec. 4.3. The resulting peak intensities are depicted in Figs. 5.15, 5.16, and 5.17. The eight spectra depicted in each Figure are ordered according to the components' ridge widths and consequently their duty cycles. We refer to a particular peak by its corresponding Bragg scattering order as given in Fig. 5.13 and Appendix E.

Note that every emission depicted in Figs. 5.15, 5.16, and 5.17 exhibits a trend of increasing peak intensity relative to the Superyellow spectrum at longer wavelengths. This is contrary to the wavelength dependence of the guided mode to radiation coupling discussed in Sec. 3.3.2 and the exemplary α-curve shown in Fig. 5.11 for the lossless case that suggest weaker peaks at longer wavelengths. On the other hand, the material absorption introduced by the SiO has to be considered. With the data from [140], the TE_0-mode attenuation constant in the samples due to absorption in the SiO has been shown to increase towards shorter wavelengths from $\alpha = 7\,\mathrm{mm}^{-1}$ ($\lambda_0 = 700\,\mathrm{nm}$) to $\alpha = 150\,\mathrm{mm}^{-1}$ ($\lambda_0 = 530\,\mathrm{nm}$) (see Fig. 5.8). At the same time, the α due to guided mode to radiation coupling approximately evolves between $\alpha = 3\,\mathrm{mm}^{-1}(\lambda_0 = 700\,\mathrm{nm})$ and $\alpha = 9\,\mathrm{mm}^{-1}(\lambda_0 = 530\,\mathrm{nm})$ (see Fig. 5.11). As the mode extraction relative to the mode absorption is much higher at longer wavelengths, higher peak intensities are observed at longer wavelengths. The general competition between mode extraction and mode absorption is also a crucial factor in grating OLEDs [26, 85].

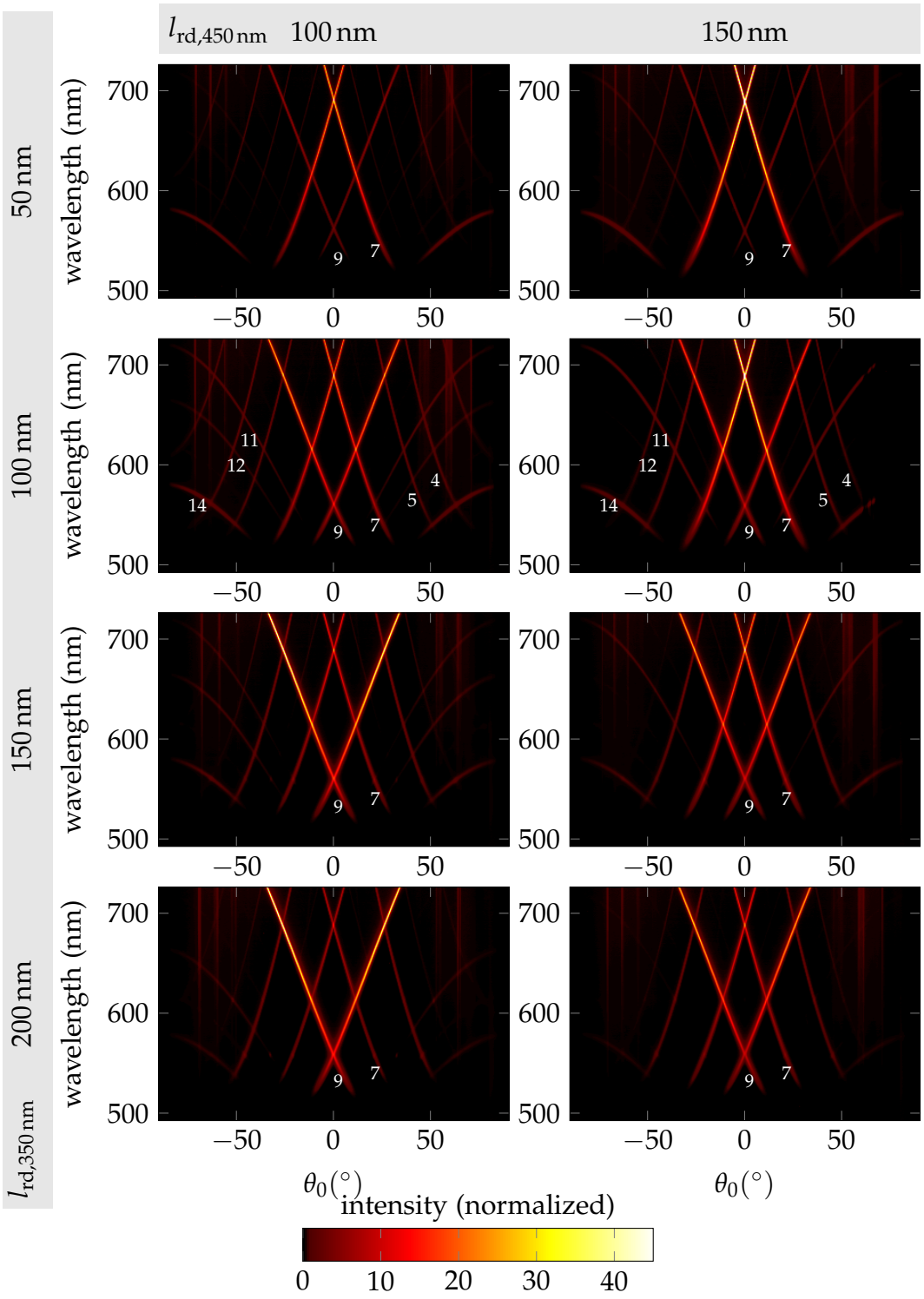

Figure 5.15: Peak intensities measured for compound binary gratings of type 350|450 (Group A) with varying $l_{\mathrm{rd,350\,nm}}$ and $l_{\mathrm{rd,450\,nm}}$. The components' ridge widths primarily influence the peak order corresponding to the component's first Fourier order.

Fig. 5.15 depicts the peak intensities for the compound binary gratings of type 350|450. Beginning with the left column of Fig. 5.15, the 450 nm-component has a fixed ridge width of $l_{\mathrm{rd},450\,\mathrm{nm}} = 100\,\mathrm{nm}$, corresponding to a duty cycle of approximately 0.222. The ridge width of the 350 nm-component increases from $l_{\mathrm{rd},350\,\mathrm{nm}} = 50\,\mathrm{nm}$ ($f_{\mathrm{dc}} \approx 0.143$) in the first row of Fig. 5.15 to $l_{\mathrm{rd},350\,\mathrm{nm}} = 200\,\mathrm{nm}$ ($f_{\mathrm{dc}} \approx 0.571$) in the last row. Note that the 9th order peak corresponds to the first Fourier order of the 350 nm-component and the 7th-order to that of the 450 nm-component (see. Eq. (5.8)).

Clearly, the 9th order peak intensity increases in the first three rows. At the same time, the 7th order peak intensity decreases. As $l_{\mathrm{rd},350\,\mathrm{nm}}$ is further increased from 150 nm to 200 nm, the 9th order peak intensity is nearly constant, while the 7th order peak intensity decreases further. At ridge widths $l_{\mathrm{rd},350\,\mathrm{nm}}$ of 150 nm and 200 nm, the peak corresponding to the 350 nm-component's first Fourier order is dominating.

In the right column of Fig. 5.15, the 450 nm-component has a fixed ridge width of $l_{\mathrm{rd},450\,\mathrm{nm}} = 150\,\mathrm{nm}$, corresponding to a duty cycle of $1/3$. This higher ridge width leads to an increase of the 7th order peak irrespective of the 350 nm-component's ridge width. Again, the increase of $l_{\mathrm{rd},350\,\mathrm{nm}}$ increases the 9th order peak intensity. Here, the peak intensity increases further for $l_{\mathrm{rd},350\,\mathrm{nm}} = 200\,\mathrm{nm}$, in contrast to the left column.

Besides the 7th and 9th order peaks, the peak order 14, corresponding to the second Fourier order of the 450 nm-component, is visible in every emission depicted in Fig. 5.15. Further peak orders with non-vanishing intensity are 3, 4, 5, 11, and 12, which arise from the spectrum convolution as described in Sec. 5.4.

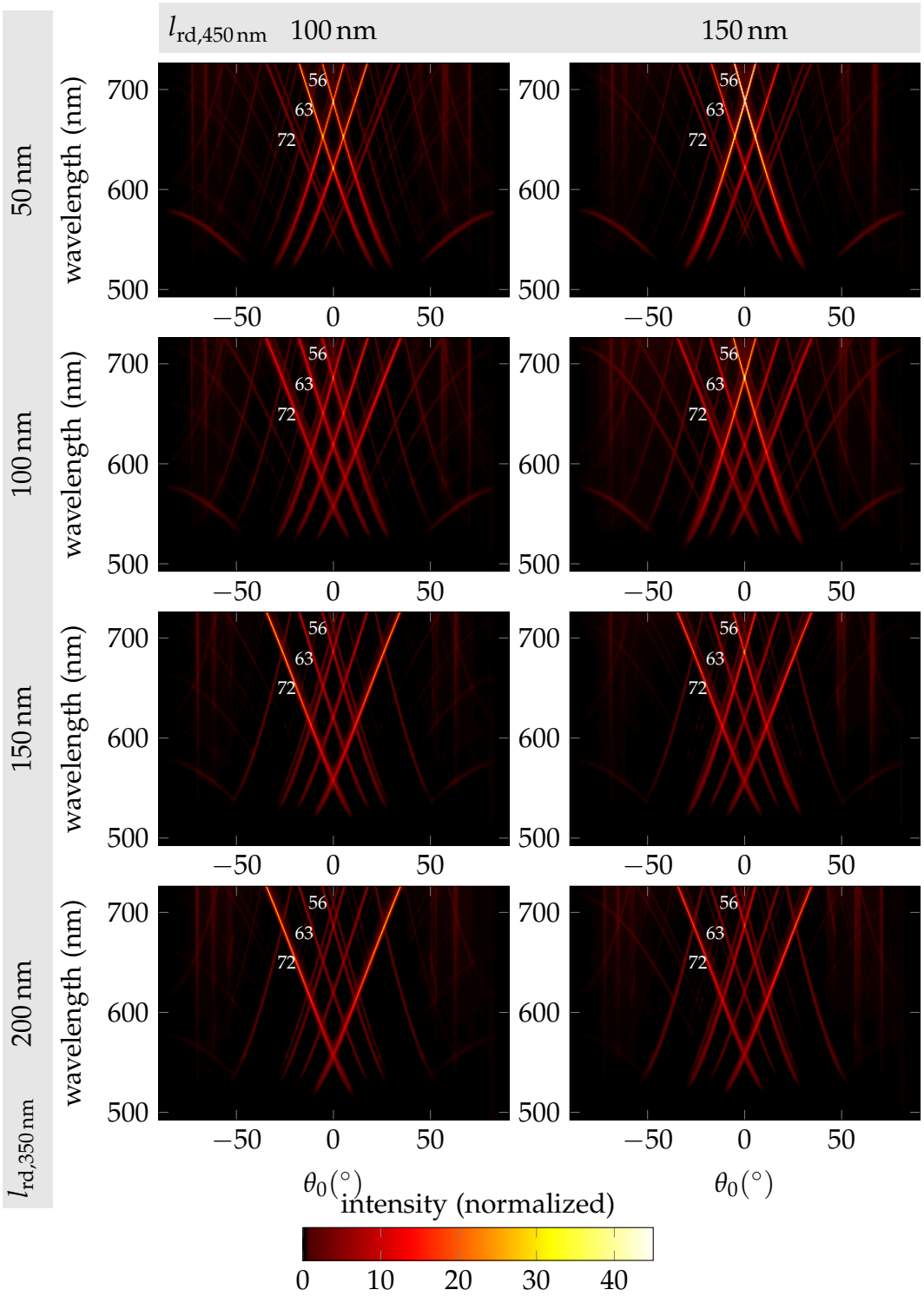

Figure 5.16: Peak intensities measured for compound binary gratings of type 350|400|450 (Group B) with varying $l_{rd,350\,nm}$ and $l_{rd,450\,nm}$ and fix $l_{rd,400\,nm} = 100\,nm$.

Fig. 5.16 depicts the peak intensities for the compound binary gratings of type 350|400(100)|450. For this grating type with $\Lambda_t = 25\,200\,\text{nm}$, the 56th Bragg scattering order corresponds to the first Fourier order of the 450 nm-component, the 63rd order corresponds to the first Fourier order of the 400 nm-component, and the 72nd order corresponds to the first Fourier order of the 350 nm-component.

The ridge width of the 350 nm-component again controls the intensity of the peak order corresponding to the first Fourier order of the 350 nm-component, i.e. the 72nd order. As $l_{\text{rd},350\,\text{nm}}$ is increased, the intensity of the 72nd peak increases. At the same time, the peak intensities of the orders 56 and 63 decrease.

Equivalent observations are made for the gratings of type 300|400(100)|500 (Group C) with total period $\Lambda_t = 6000\,\text{nm}$ (Fig. 5.17). For these gratings, the 12th Bragg scattering order corresponds to the first Fourier order of the 500 nm-component, the 15th order corresponds to the first Fourier order of the 400 nm-component, and the 20th order corresponds to the first Fourier order of the 300 nm-component. Here, the ridge width of the 300 nm-component is changed along the rows of Fig. 5.17 and the ridge width of the 500 nm-component is changed along the columns. Similar to the gratings of type 350|450, the peak intensity of the controlled peak increases only up to a ridge width of 150 nm. For gratings of type 300|400|500, the 20th order peak intensity even decreases as $l_{\text{rd},300\,\text{nm}}$ is increased from 150 nm to 200 nm (Fig. 5.17). Additionally to the three strong components' first-order peaks 12, 15, and 20, the measured emission shown in Fig. 5.17 exhibits the most peaks with significant intensity of the three grating types investigated. This indicates that the convolution term in Eq. (5.7) creates many strong intermediate Fourier components in the Fourier spectrum of the grating type 300|400|500.

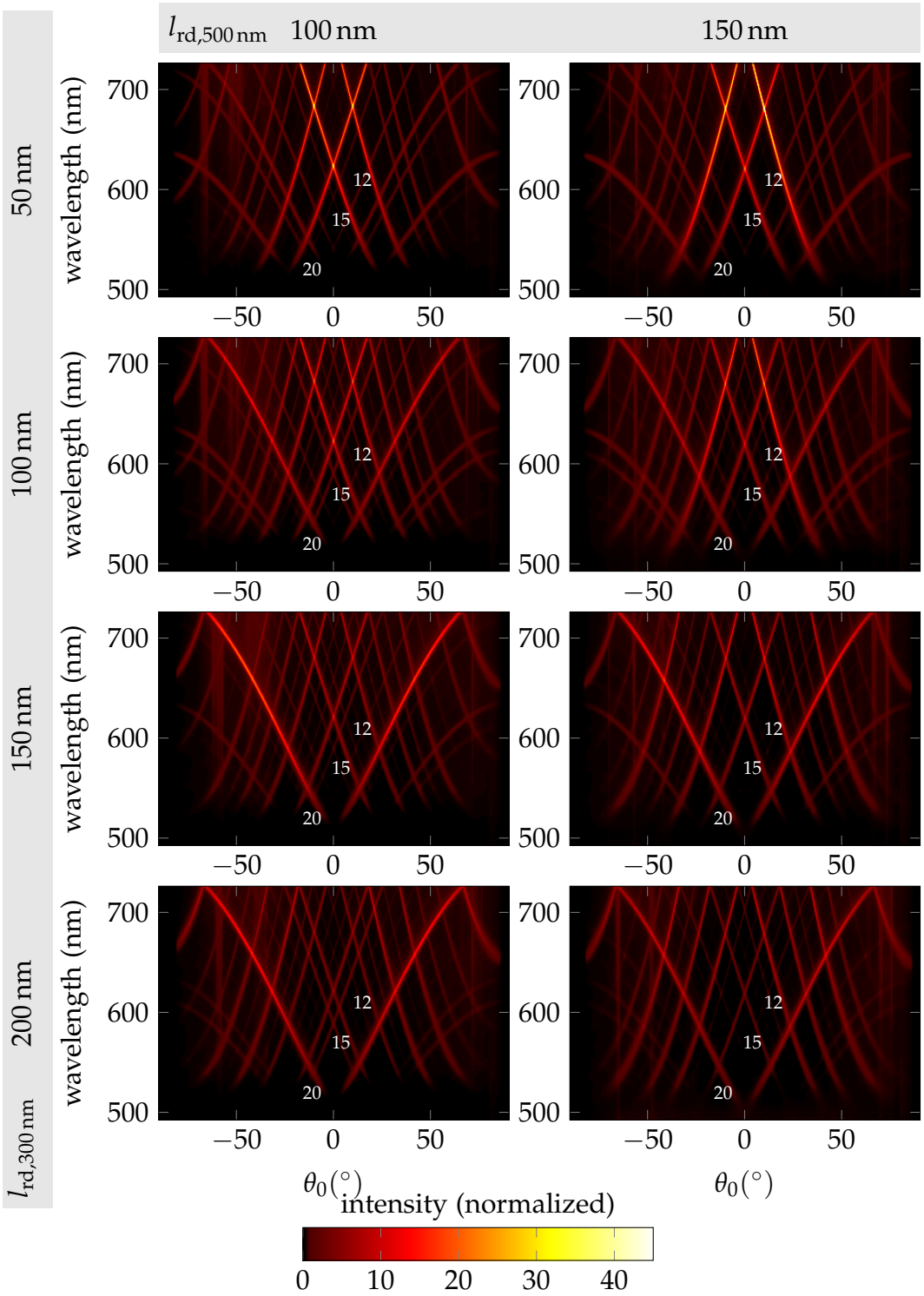

Figure 5.17: Peak intensities measured for compound binary gratings of type 300|400|500 (Group C) with varying $l_{rd,300\,nm}$ and $l_{rd,500\,nm}$ and fix $l_{rd,400\,nm} = 100\,nm$.

In order to quantify the peak intensities and their dependence on the components' ridge widths, I integrated the measured spectrum in a wavelength region of 20 nm around each peak position and removed the crossing regions as described in Sec. 4.3.3. Additionally, I simulated the grating waveguide with RCWA according to the model parameters given in Sec. 5.3 for Stack B. As the RCWA simulation does not provide absolute intensities, I compare the relative measured peak intensities and the simulated diffraction efficiencies. The reference base for the measured peak intensities is the summed intensity of the peak orders 3 to 14 at each wavelength. The simulated diffraction efficiencies were corrected by the Fresnel equations at the glass-air boundary and related to the new reference base of the summed intensities in air. The reference base comprises only waves scattered towards the substrate (region II), while waves towards region I are neglected (see Fig. 2.4).

Figs. 5.18 and 5.19 depict the measured relative peak intensities and simulated diffraction efficiencies for the grating type 350|450 over the wavelength. Simulation and measurement are in reasonable agreement. This evidences that the peaks originate from Bragg scattering of the simulated TE_0-mode. The rapid changes in the simulated intensities at particular wavelengths are due to stopbands (see Sec. 2.6.3), occurring at outcoupling feature crossings. Outside the stopbands, I attribute the deviations of simulation and measurement to the idealizations made in the simulation model such as the assumed pure binary geometry of the grating and the corrugation of only the film bottom in the model. Recalling the SEM picture shown in Fig. 5.6, it becomes clear that these model assumptions are approximate.

Both measurement and simulation depicted in Figs. 5.18 and 5.19 confirm that the 9th peak intensity increases with $l_{\mathrm{rd,350\,nm}}$. By choosing $l_{\mathrm{rd,350\,nm}}$ and $l_{\mathrm{rd,450\,nm}}$, the 9th order peak intensity can thus be controlled to have a relative intensity between less than 20 % and higher than 70 % in the complete wavelength range. Concurrently, as the relative 9th order peak intensity increases, the relative intensity of the 7th order peak decreases.

An interesting feature visible in Figs. 5.18 and 5.19 is the onset of the 14th order peak at wavelengths below 580 nm. This Bragg scattering order cannot be coupled out of the substrate at longer wavelengths as is visible in Fig. 5.15. Cleary, the onset wavelength of the 14th order peak is well predicted by the simulation.

Figs. 5.18 and 5.19 indicate that equal peak intensities of the 7th and 9th order can be achieved if both components have equal ridge widths as observable for the combinations $l_{\mathrm{rd,350\,nm}} = 100\,\mathrm{nm}$ and $l_{\mathrm{rd,450\,nm}} = 100\,\mathrm{nm}$ or $l_{\mathrm{rd,350\,nm}} = 150\,\mathrm{nm}$ and $l_{\mathrm{rd,450\,nm}} = 150\,\mathrm{nm}$.

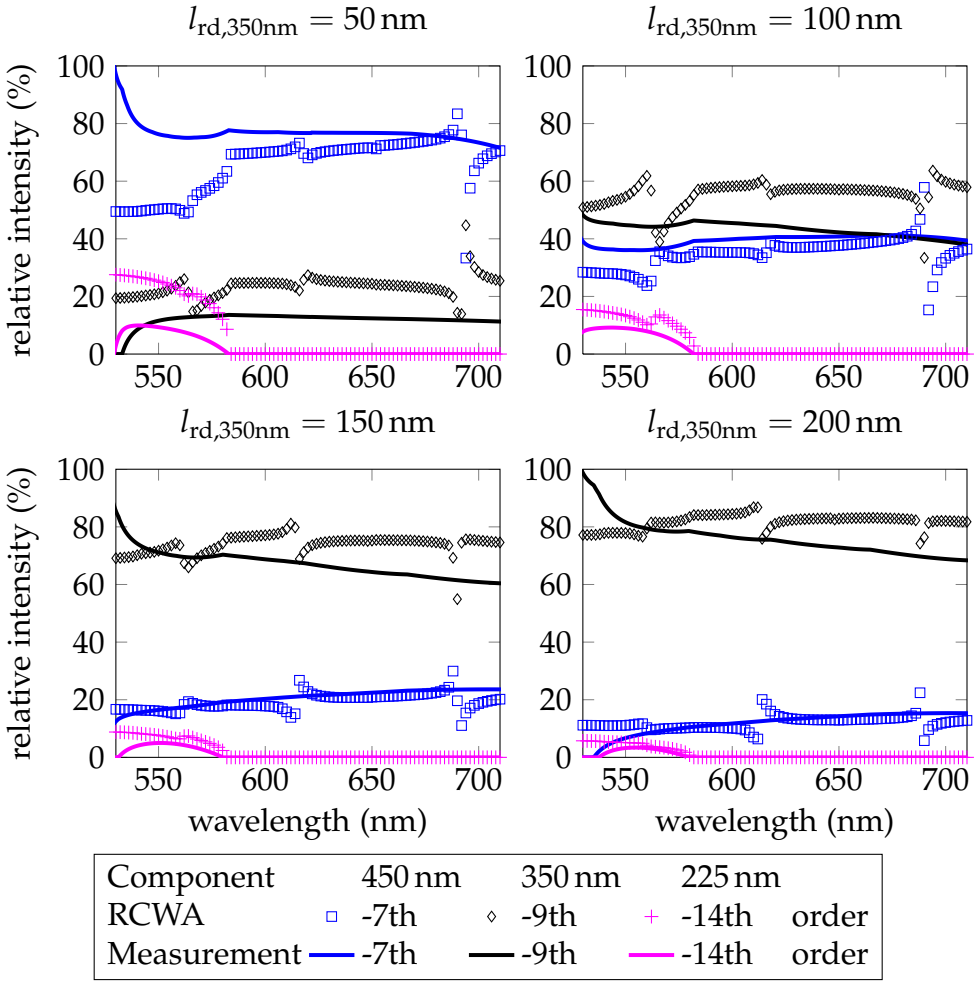

Figure 5.18: Relative measured peak intensities (solid lines) and simulated diffraction efficiencies (markers) for the grating $350(l_{\mathrm{rd,350\,nm}})|450(100)$ with total period $\Lambda_t = 3150\,\mathrm{nm}$.

The relative measured peak intensities of the groups B and C are shown together with RCWA simulations in Appendix E. While measurement and RCWA simulation are still in reasonable agreement, the deviation of the measured 20th order peak intensity from simulation is significant, possibly due to the fabricated grating geometry.

Theory

I will now discuss how the pTMM model introduced in Sec. 2.7.2 can explain the observed peak intensities. In Sec. 2.7.2, it has been shown that the intensity of the m-th field space harmonic in the substrate p_m^{II} is proportional to the squared modulus of the m-th grating Fourier coefficient

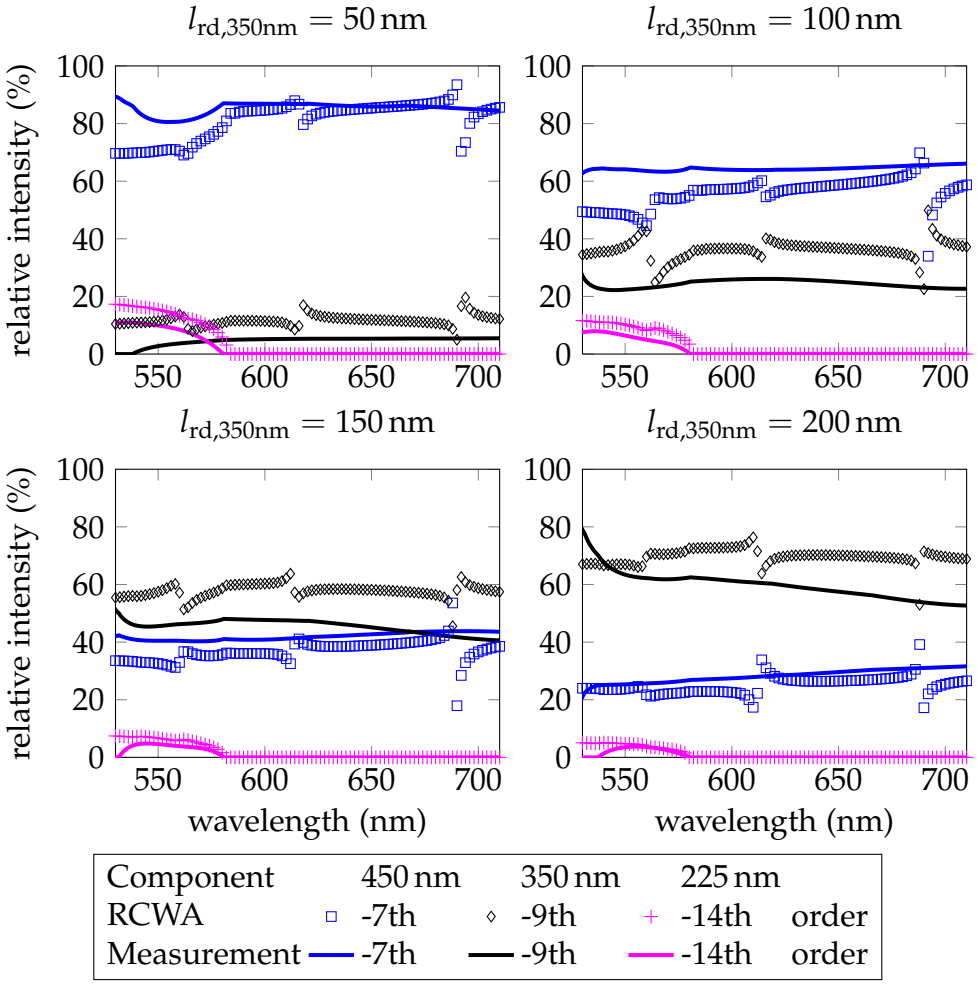

Figure 5.19: Relative measured peak intensities (solid lines) and simulated diffraction efficiencies (markers) for the grating $350(l_{\mathrm{rd,350\,nm}})|450(150)$ with total period $\Lambda_t = 3150\,\mathrm{nm}$.

$\tilde{\epsilon}_m$. Fig. 5.20 therefore exemplarily depicts the strongest Fourier coefficients of the compound binary grating $350|450(100)$ versus $l_{\mathrm{rd,350\,nm}}$. The Fourier coefficient $|\tilde{\epsilon_9}|^2$ exhibits a bell-shaped curve with its maximum at $l_{\mathrm{rd,350\,nm}} = 175\,\mathrm{nm}$ corresponding to a component's duty cycle of 0.5. The curve behavior of $|\tilde{\epsilon_9}|^2$ is typical for a single-period binary grating, which is the reason why many single-period, binary grating waveguides radiate strongest close to a grating duty cycle of 0.5 [57, 93]. It is noteworthy that this first-order Fourier harmonic of the 350 nm-component is well preserved in the compound binary grating spectrum.

Now it becomes clear that the observed increase of the 9th-order peak intensity, as $l_{\mathrm{rd,350\,nm}}$ increases from 50 nm to 150 nm, is caused by the increasing Fourier coefficient modulus $|\tilde{\epsilon}_9|$. A further increase to $l_{\mathrm{rd,350\,nm}} =$

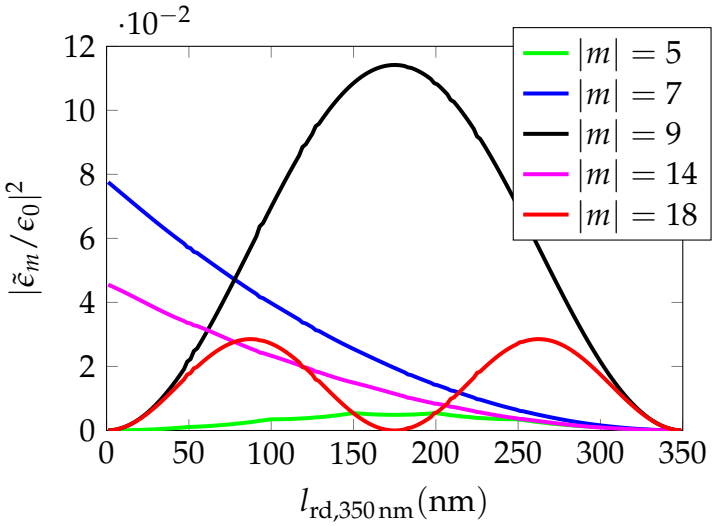

Figure 5.20: Fourier coefficients of the compound binary grating 350|450(100) versus $l_{\mathrm{rd,350\,nm}}$. The first Fourier order of the 350 nm-component corresponds to $m = 9$. $|\tilde{\epsilon}_9|^2$ shows the typical curve of the first Fourier harmonic of a binary grating with a maximum at 0.5 duty cycle.

200 nm leaves $|\tilde{\epsilon}_9|$ unchanged and thus no further increase of the 9th-order peak intensity is visible in the emission (Fig 5.15). As the maximum ridge width in the fabricated samples was $l_{\mathrm{rd,350\,nm}} = 200\,\mathrm{nm}$, the effect of the decreasing $|\tilde{\epsilon}_9|$ could not be observed in the measurements. But in Fig. 5.17, where the ridge width of the $l_{\mathrm{rd,300\,nm}}$-component is changed, $l_{\mathrm{rd,300\,nm}} = 200\,\mathrm{nm}$ corresponds to a duty cycle well beyond 0.5 and we thus observe a decreasing 20th-order peak intensity. Concurrently with the increasing $|\tilde{\epsilon}_9|$, the grating Fourier coefficients $|\tilde{\epsilon}_7|$ and $|\tilde{\epsilon}_{14}|$ decrease at higher $l_{\mathrm{rd,350\,nm}}$. This explains the observed decrease of the 7th-order and 14th-order peak intensities in Fig. 5.15. However, the Fourier coefficients alone cannot explain the outcoupling peak intensities. As discussed in Sec. 2.7.2, the other factors of the m-th field space harmonic's intensity in the substrate are the mode overlap v_{mode}, the standing wave factor ζ_{II}, the cavity's Airy factor v_{Airy} and the directional term $v_{\mathrm{dir,II}}$. The product of these factors is thus $p_m^{\mathrm{II}}/|\tilde{\epsilon}_m|^2$ (see Eq. (2.80)). Fig. 5.21 shows $p_m^{\mathrm{II}}/|\tilde{\epsilon}_m|^2$ for the sample structure at $\lambda_0 = 550\,\mathrm{nm}$.

The ratio $p_m^{\mathrm{II}}/|\tilde{\epsilon}_m|^2$ originally depends on the field space harmonic propagation direction described by the tangential wave vector k_{xm}. As this propagation direction is determined by the grating period Λ_t and the diffraction order m according to Eq. (2.65), $p_m^{\mathrm{II}}/|\tilde{\epsilon}_m|^2$ can also be plotted versus the inverse grating space frequency Λ_t/m as shown in Fig. 5.21. The advantage of this representation is that positions of the component's periods on the

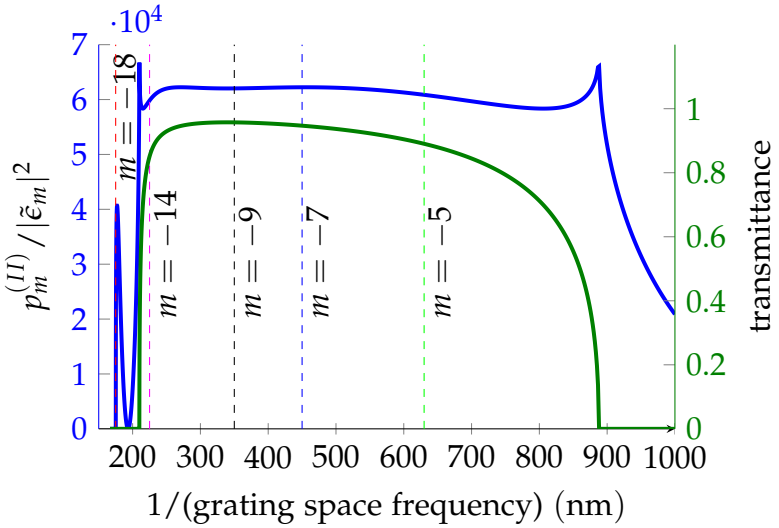

Figure 5.21: Field space harmonic power ratio $p_m^{\mathrm{II}}/|\tilde{\epsilon}_m|^2$ in the substrate versus the inverse grating space frequency (blue line) in the sample structure (Stack B in Sec. 5.3, assumed $f_{\mathrm{dc}} = 0.5$). Glass-air transmittance (green line). The film layer was assumed lossless and the calculation was done at $\lambda_0 = 550\,\mathrm{nm}$. The product of both curves determines the outcoupled intensity of a wave that arises from diffraction at a given Fourier harmonic of the grating.

x-axis are directly visible. Additionally, vertical lines indicate the positions of the relevant diffraction orders.

We find that $p_m^{\mathrm{II}}/|\tilde{\epsilon}_m|^2$ is nearly equal for the diffraction orders between -5 and -14. Consequently, the field space harmonic intensities of these orders in the substrate differ only due to differences in the corresponding Fourier coefficients. On the contrary, $p_m^{\mathrm{II}}/|\tilde{\epsilon}_m|^2$ is zero for the diffraction order $m = -18$ so that the intensity of this order in the substrate is zero, even though the corresponding Fourier coefficient is significant (see Fig. 5.20). This is due to a large tangential wave vector of this order, that causes an evanescent field in the substrate.

Although the $p_m^{\mathrm{II}}/|\tilde{\epsilon}_m|^2$-curve in this example does not seem particularly interesting due to the small changes for the relevant orders, I want to emphasize that the presented method can be used for a large variety of grating waveguides. Especially if the geometry forms a cavity with higher boundary reflectivities, stronger variations of $p_m^{\mathrm{II}}/|\tilde{\epsilon}_m|^2$ can occur, which make the choice of the grating space frequencies more important. This is also relevant for OLEDs with metallic electrodes.

In order to calculate the peak intensity in air, Fresnel's equations have to be applied at the glass-air boundary. The calculated transmittance of

the substrate waves to air is depicted in Fig. 5.21 (green line). Clearly, the glass-air boundary has only a small effect on the relevant diffraction orders here. The most important effect of this boundary is that it defines a window of grating space frequencies that can potentially escape to air.

I finally compare the pTMM model (Sec. 2.7.2) applied above with RCWA and the measurement results. Therefore, I calculated each field space

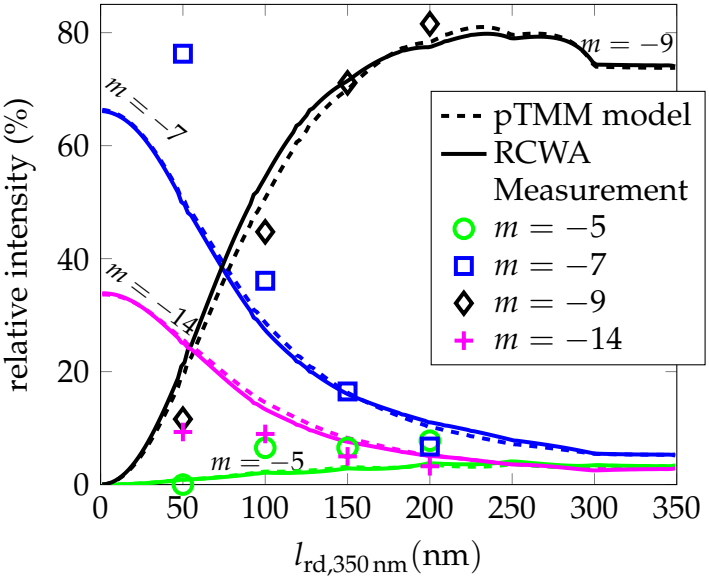

Figure 5.22: Comparison of the relative peak intensity outside the substrate for the pTMM model, RCWA simulation and measurement for a 350|450(100) grating at $\lambda_0 = 550\,\mathrm{nm}$. The reference base is the summed intensity of all field space harmonics leaving the substrate. The pTMM model, the RCWA, and the measurement clearly show how the relative intensities can be controlled by the component's ridge width.

harmonic power outside the substrate as the product of the curves in Fig. 5.21 and the corresponding Fourier coefficient (Fig. 5.20). The thereby obtained relative intensities are in close agreement with the RCWA simulation results (Fig. 5.22). Although some measurement data points deviate significantly from the theoretical values, the measured emission supports the theory and the simulation well. In conclusion, Fig. 5.22 shows how the emission from compound binary gratings can be controlled by the duty cycle of a grating component.

Chapter 6

Nanostructured emitter for lab-on-a-chip systems

Summary

Organic emitters are promising for highly integrated sensing applications and lab-on-chip systems due to cost and processing advantages. In this chapter, I experimentally demonstrate how a nanostructuring of the organic emitter layer can be used to improve refractive index sensing of a fluid analyte. I present two approaches to achieve Bragg scattering of a thin film mode into guided substrate modes. Subsequently, by measuring an analyte refractive index via the critical angle of TIR, a signal increase of 45 % *is achieved with the nanostructured emitter. Making use of the wavelength- and angle-dependent Bragg scattering, a spectral method to determine the refractive index is presented with a remarkably high sensitivity of* 700 nm*/RIU (RIU: refractive index unit). Finally, I show that by measuring the intensity at a fixed angle, the analyte refractive index can be determined with a* 3.6 *times higher sensitivity using the nanostructured emitter compared to the unstructured emitter. A refractive index change of* $5 \cdot 10^{-4}$ *is readily detectable.*

We have seen in the two preceding chapters how gratings can be incorporated into organic emitter layers to Bragg-scatter guided modes. It was shown that the Bragg scattering leads to wavelength- and angle-dependent peaks in the emission. In this chapter, I will demonstrate that this directionality in the emission can be used to enhance the sensitivity of refractive index measurements. A setup will be presented that integrates the nanostructured emitter on one substrate together with the detection volume and hence facilitates an application for lab-on-a-chip systems.

Lab-on-a-chip systems integrate multiple functions required for chemical, biological, or medical analysis on a small chip [146, 147]. The advantages of the high integration are the small amount of analyte needed, the portability of the device that allows for point-of-care diagnostics and the potentially low cost [18, 147]. Typically, an optical lab-on-a-chip combines a light source, a microfluidic system with detection volume and a light detector [148]. Many detection principles can be used in lab-on-a-chip systems, e.g. measurement of absorbance, fluorescence and refractive index [146, 149]. Although measuring a refractive index change is inherently unspecific regarding the analyte, a specific detection can be achieved by measuring the refractive index change due to a specific binding at a receptor-coated surface [149, 150]. This detection principle is label-free and makes refractive index measurements suited for biochemical sensing [151].

Organic semiconductors are especially promising for lab-on-a-chip applications as they can be processed on a large variety of materials and can thus be directly integrated on the microfluidic chip where needed. Furthermore, the scalability of organic optoelectronic components and potentially low-cost mass production render them attractive for lab-on-a-chip applications. Hence, several papers address the application of OLEDs as a light source for highly integrated detection systems [13–20]. An often encountered challenge is to couple the OLED emission towards the detection element efficiently. This channeling can be achieved, e.g., by coupling the OLED light into a waveguide evanescently [152] or by embedding a waveguide in the OLED layers [153]. However, if the OLED's far field radiation is used for the detection, the efficiency is limited by the Lambertian emission, as only light emitted in the solid angle that reaches the detection region contributes to the measurement signal.

In the following, I will demonstrate that the directional emission of grating structured organic layers can be employed to increase the amount of detection light in a setup proposed by Ratcliff et al. [17] and shown in Fig. 6.1. In this setup, the amount of light reflected at the glass-analyte boundary decreases as the analyte refractive index n_a is increased. By

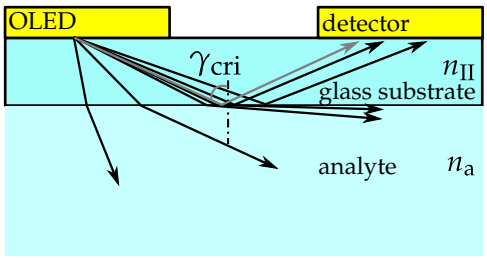

Figure 6.1: Integrated OLED and detector setup for refractive index measurements of the analyte fluid. As proposed by Ratcliff et al. [17] the amount of reflected light at the glass-analyte boundary is measured to determine the analyte's refractive index. As indicated, this signal can be increased with a directional light source that emits more light close to the critical angle of total internal reflection γ_{cri}.

detecting the amount of reflected light, n_a can be determined.

I will demonstrate that the Bragg scattering of guided modes from the organic thin films can be designed to couple into the substrate at angles close to the critical angle of total internal reflection. Subsequently, I show how this substrate coupling can improve the refractive index sensing.

6.1 Coupling to substrate modes

With substrate modes we denote light in the substrate traveling at an angle greater than the critical angle of total internal reflection

$$\gamma_{cri} = \arcsin(n_a/n_{II}) \tag{6.1}$$

(see Fig. 6.1) as obtained by Snell's law (Eq. (2.19)). According to Eq. (6.1), γ_{cri} depends on the analyte refractive index n_a. For example, if the analyte is water then $n_a = n_{H_2O} \approx 1.33$ and $\gamma_{cri}(n_{H_2O}) \approx 61°$.

6.1.1 Direct coupling

In this approach, I investigate an organic emitter layer structured by a grating as a light source directly processed on a glass substrate as depicted in Fig. 6.2. The first-order Bragg scattering of the waveguide modes supported by the thin films is designed to radiate into the substrate modes at an angle close to $\gamma_{cri}(n_{H_2O})$ of water analyte. For a waveguide mode traveling perpendicular to the grating grooves, this typically requires very large or very small periods. E.g., a grating period of $\Lambda = 184\,\text{nm}$ or $\Lambda = 1719\,\text{nm}$ is required according to Eq. (2.44) for $n_{eff} = 1.65$, $n_a = 1.33$, and $\lambda_0 = 550\,\text{nm}$.

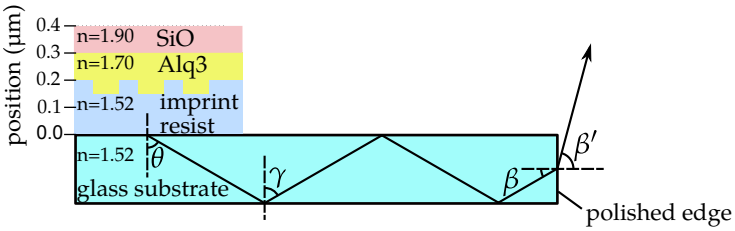

Figure 6.2: Coupling thin film waveguide modes to the substrate: direct coupling approach. In this setup, the Bragg scattering of thin film modes is designed to radiate into an angle $\theta = \gamma > \gamma_{\mathrm{cri}}(n_{\mathrm{a}} = 1.0)$. The scattered light is then observed through the polished substrate edge.

When the samples were fabricated, I did not have grating masters for the NIL process with such periods available. Alternatively, I designed the samples such that the observed Bragg-scattered mode traveled at an oblique angle to the grating grooves prior to the scattering. This allowed me to use a grating master with period $\Lambda = 740\,\mathrm{nm}$ as explained in the following.

The samples were fabricated as described in Sec. 5.2, with the only exception that tris (8-hydroxy quinioline) aluminum (Alq3) was used as the emitter layer. Alq3 is a organic small molecular emitter [88] that is commonly used for OLEDs. A 100 nm-thick layer was deposited on the imprint resist by thermal evaporation under high vacuum. Assuming that the Alq3 refractive index is similar to the refractive index of Superyellow, the TE_0-mode effective index is approximately $n_{\mathrm{eff}} = 1.62$ ($\lambda_0 = 550\,\mathrm{nm}$) according to Fig. 5.7.

As described in Sec. 2.6.2, the Bragg scattering angle θ depends on the mode propagation direction to the grating normal. If the organic emitter is excited by a laser, modes propagating in every direction will be present in the thin films. Thus, the direction of observation to the grating normal has to be chosen such that the Bragg scattering angle θ is close to the desired value. For this experiment, I did not aim at the exact adjustment of θ to, e.g., $\gamma_{\mathrm{cri}}(n_{\mathrm{H_2O}}) \approx 61^\circ$ because only a proof-of-principle should be made. I measured the Bragg scattering at an angle of 74.0° to the grating normal. According to Eq. (2.49), the TE_0-mode traveling under an angle of $\phi = 48.3^\circ$ to the grating grooves prior to the scattering will be first-order Bragg-scattered into the substrate at an angle of $\theta = 55.7^\circ$ and $\phi' = 74.0^\circ$, for $\lambda_0 = 550\,\mathrm{nm}$, $n_{\mathrm{eff}} = 1.62$, $\Lambda = 740\,\mathrm{nm}$, and $n_2 = 1.52$. Note that Fig. 6.2 depicts the cut plane at the observation angle $\phi' = 74.0^\circ$ to the grating normal. Here, $\gamma = \theta$ as these are alternating angles of the ray intersecting the parallel surface normals at the top and bottom glass boundary (see Fig. 6.2).

In order to observe the substrate modes, the substrate edge was polished with a polishing machine so that scattering at this edge was minimized. The photoluminescence in β'-direction was measured with the goniophotometer using a microscope objective (Modus B - see Sec. 4) and a specially designed sample holder. The measurement angle β' is converted to γ by

$$\gamma = 90° - \arcsin\left(\sin(\beta')/1.52\right), \tag{6.2}$$

as obtained by Snell's law (Eq. (2.19)).

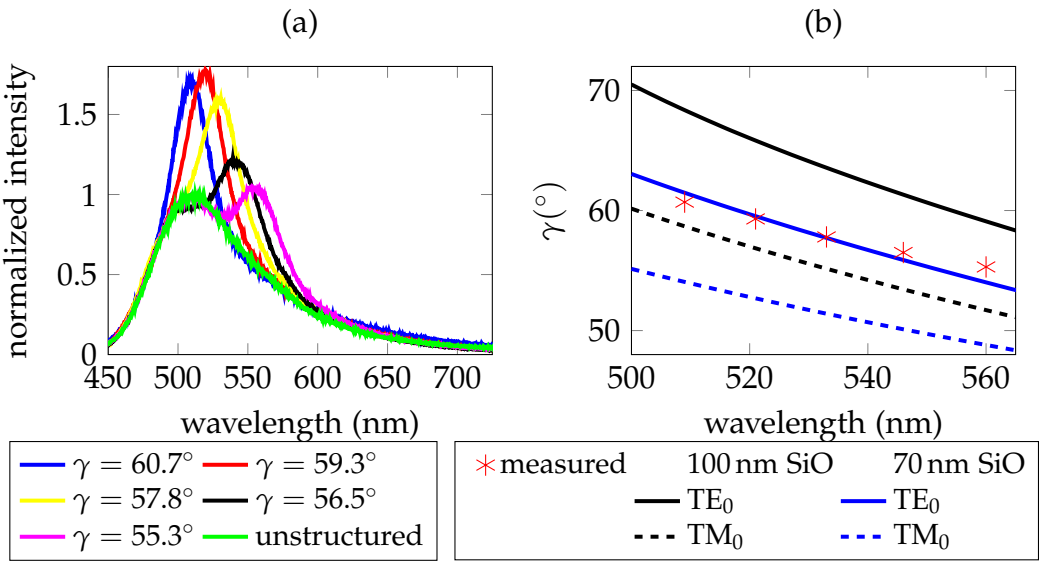

Figure 6.3: (a) Unpolarized photoluminescence spectra for five different angles γ measured through the polished substrate edge. Due to the grating, peaks arise in the spectra and the emission to substrate modes is enhanced for $55° < \gamma < 61°$. (b) Comparison of the measured and simulated peak position. The agreement in slopes of the measured and simulated curves evidences that the peaks originate from Bragg scattering of a guided mode. A concluding prediction of the absolute peak position is not possible due to the the uncertainty in the stack parameters.

Fig. 6.3a depicts the measured unpolarized spectra at five different angles γ together with the photoluminescence spectrum of an unstructured Alq3-layer. The spectra exhibit a wavelength peak that shifts towards shorter wavelengths with increasing γ. The dispersion of the peak position is shown in Fig. 6.3b together with the theoretical curves obtained with the Bragg equation (Eq. (2.49)) and TMM simulations of two different waveguide stacks. Due to the uncertainty of the exact layer thicknesses and the unpolarized measurement, it cannot be concluded whether the TE_0 or the TM_0 leads

to the observed peaks. Even though the absolute peak position is not conclusively determined by the theory, the agreement in slope of the theoretical curves and the measured curve evidences that the peaks arise due to Bragg scattering of a guided thin film mode. As γ is well above the critical angle of total internal reflection at the glass-air boundary $\gamma_{\text{cri}} = 41.1°$, the observed light comes from the substrate modes. Consequently, the Bragg scattering couples light from the thin films to substrate modes. Fig. 6.3 shows that the intensity is increased in a range of approximately 5° for the analyzed wavelength range between $\lambda_0 = 500\,\text{nm}$ to $\lambda_0 = 560\,\text{nm}$. The emission of the nanostructured organic emitter layer is thus partially directional.

6.1.2 Prism coupling

In order to investigate the application of the partially directional emission for refractive index sensing, it is helpful to study a configuration where the emitted light is observed after a single reflection at the substrate-analyte boundary. As a ray emitted at, e.g., $\theta = 61°$ travels only some millimeters laterally in the 1 mm-thick substrate before it hits the substrate's top boundary again, the direct coupling setup shown in Fig. 6.2 is not well suited for such an experiment. To increase the traveled path length and make the observation of reflected light after a single reflection more convenient, I used a right-angle prism in a setup shown in Fig. 6.4. The sample substrate, the

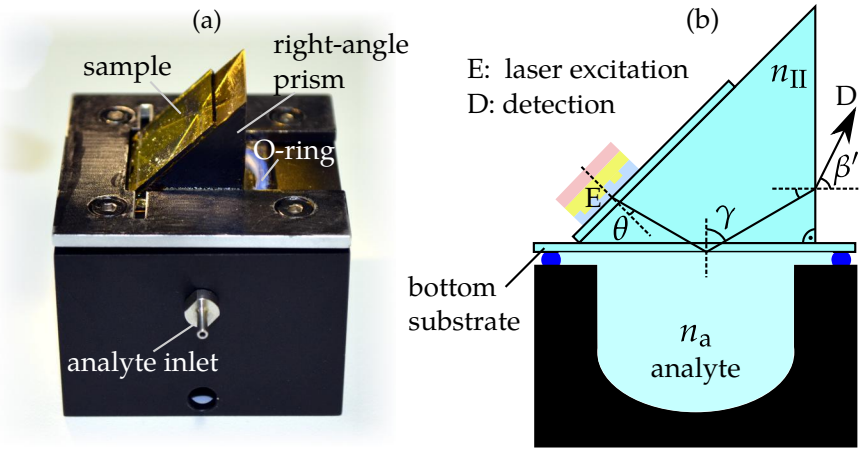

Figure 6.4: Setup for refractive index sensing using a grating structured organic emitter layer. (a) Photograph of the goniophotometer sample holder with analyte volume. (b) Schematic drawing. The emission from the sample is reflected from the substrate-analyte boundary once at the angle γ and observed outside the prism at the angle β'. The bottom substrate closes the analyte volume with an O-ring.

right-angle prism, and the bottom substrate are approximately of refractive index $n_{\mathrm{II}} = 1.52$ and attached to each other by index matching fluid, to prevent reflections at the junctions. The complete setup is mountable to the goniophotometer, so that the reflected light spectrum can be measured angularly resolved. The analyte volume beneath the bottom substrate holds 8 ml and can be filled via two inlets at the sides (see Fig. 6.4a) using two syringes. The surface of the analyte volume is dull black anodized to minimize light reflections.

As the sample is inclined relatively to the bottom substrate by an angle of 45°, we obtain for the relation between the measured angle β' and the reflection angle γ using Snell's Law

$$\begin{aligned} \gamma &= 45^\circ + \theta \\ &= 90^\circ - \arcsin\left(\sin\beta'/n_{\mathrm{II}}\right). \end{aligned} \tag{6.3}$$

According to Eq. (6.3), we now require an enhanced sample emission at approximately $\theta = 16^\circ$ to increase the amount of light close to the critical angle $\gamma_{\mathrm{cri}}(n_{\mathrm{H_2O}}) \approx 61^\circ$ of water analyte. Grating field D5 on sample K13 (see Appendix D and Sec. 5.2 for fabrication details) possesses a period of $\Lambda = 500\,\mathrm{nm}$ and provides the required emission pattern. Fig. 6.5 depicts

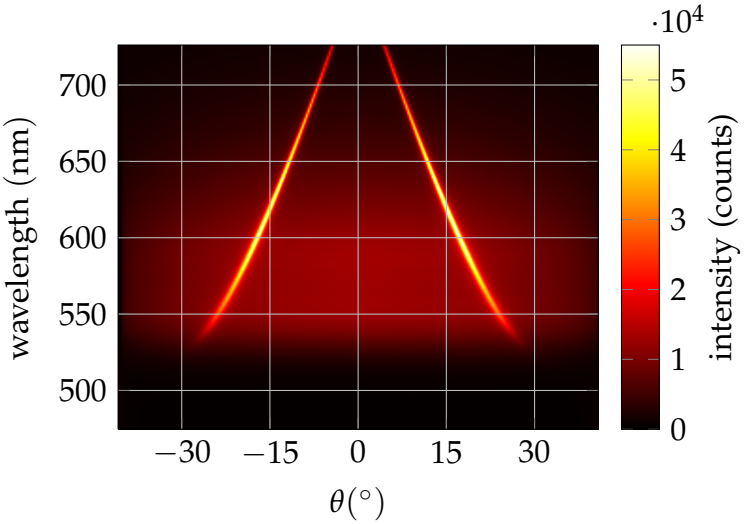

Figure 6.5: Emission pattern in glass of an organic emitter layer structured by the single-period grating field D5 of period $\Lambda = 500\,\mathrm{nm}$. This emitter layer provides an enhanced emission at the required angles for the prism refractive index sensing setup.

its emission pattern in glass recorded with the goniophotometer. The angle θ and the intensity have been converted to the values in glass by Snell's law

(Eq. (2.19)) and Fresnel's equations [50], respectively. As visible in Fig. 6.5, the emission is strongly enhanced due to mode Bragg scattering around $\theta = 16°$, which corresponds to the critical angle $\gamma_{\mathrm{cri}}(n_{\mathrm{H_2O}})$ in the prism setup. Note that in contrast to the experiment in Sec. 6.1.1, here the light is observed perpendicular to the grating grooves, i.e. $\phi = \phi\prime = 0°$.

Using the goniophotometer, the reflected intensity versus β' was measured in the prism setup (Fig. 6.4) for field D5 ($\Lambda = 500\,\mathrm{nm}$) and an adjacent unstructured area on the same sample. Fig. 6.6 depicts the spectral re-

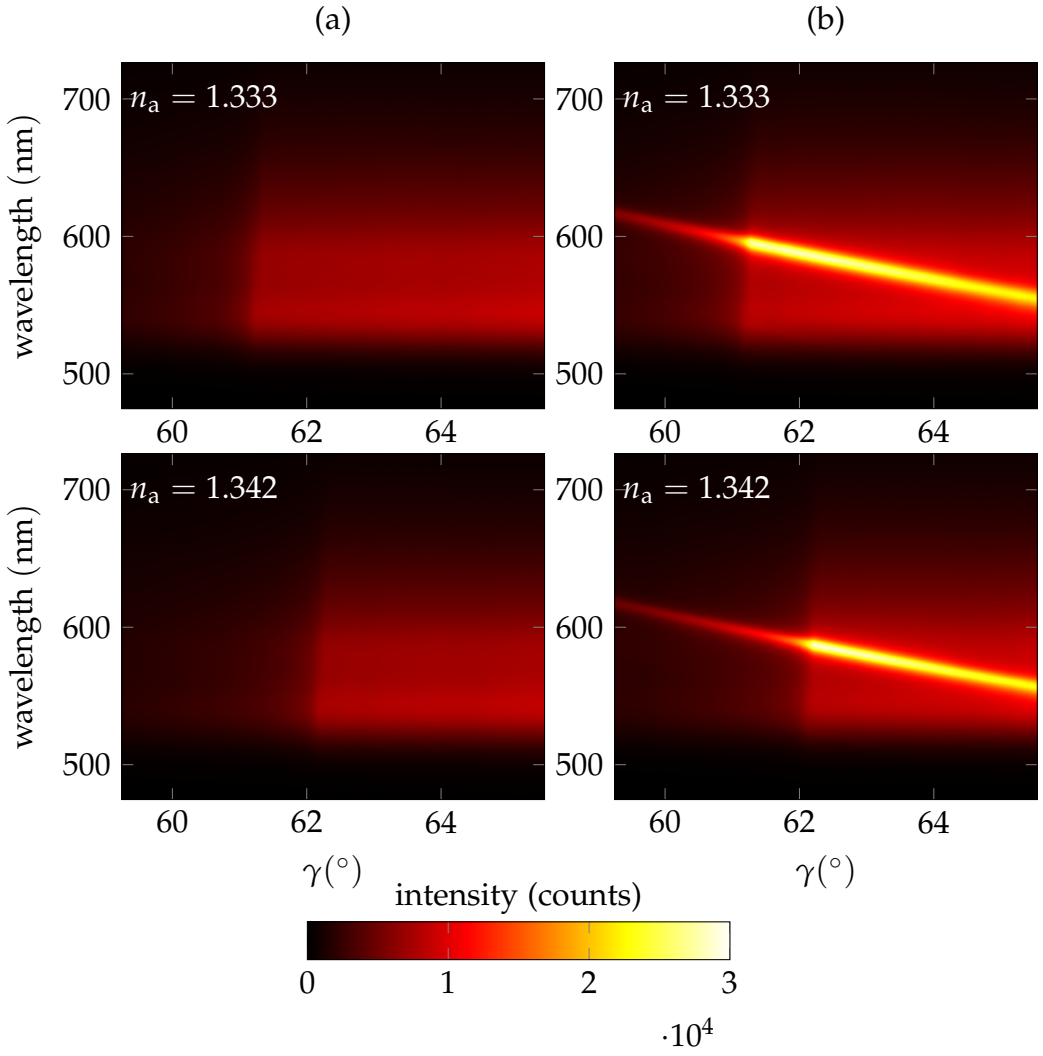

Figure 6.6: Measured unpolarized spectral light intensity over the reflection angle γ for (a) an unstructured emitter layer and (b) an emitter layer structured with a grating of period $\Lambda = 500\,\mathrm{nm}$. A change of the analyte refractive index from $n_a = 1.333$ (top row) to $n_a = 1.342$ (bottom row) results in shift of the TIR critical angle. The grating structured emitter enhances the intensity in a small, γ-dependent wavelength range.

flection intensity as a function of γ, which has been obtained from β' by Eq. (6.3). The TIR critical angle becomes clearly visible as an edge in the intensity. An offset of approximately 5° was applied on β' to adjust the measured TIR critical to the expected value of water analyte. This adjustment was necessary because the goniophotometer's mechanics did not allow to center the point where the observed ray leaves the prism (see Fig. 6.4).

Fig. 6.6 shows that the structured emitter enhances the reflected light intensity significantly in the required γ-range. Two different analytes are compared: pure water (top row) and a volume mixture of 80 % water and 20 % isopropyl alcohol. The calculation of the resulting refractive indices is described in Sec. 6.2.1. Independent of the emitter, γ_{cri} increases with increasing n_{a} as is expected from Eq. (6.1). Additionally, we observe an inclination of the total internal reflection edge towards higher angles at longer wavelengths in each measurement (Fig. 6.6). This wavelength-dependence of γ_{cri} is due to the normal glass dispersion [48] that causes an increase of $n_{\mathrm{a}}/n_{\mathrm{II}}$ in Eq. (6.1).

In the following, three different approaches of analyte refractive index sensing are presented along with a comparison between the structured and the unstructured emitter.

6.2 Refractive index detection

6.2.1 Analyte mixture

We use a mixture of water and isopropyl alcohol as analyte and control the mixture's refractive index n_{a} by the volume ratio of the components. The component's refractive indices are taken from [154] to be $n_{\mathrm{H_2O}} = 1.333$ for water and $n_{\mathrm{IPA}} = 1.377$ for isopropyl alcohol at the Fraunhofer D-line ($\lambda_0 = 589.29\,\mathrm{nm}$) and 20 °C. Using the Arago-Biot equation

$$n_{\mathrm{a}} = v_{\mathrm{H_2O}} \cdot n_{\mathrm{H_2O}} + (1 - v_{\mathrm{H_2O}}) n_{\mathrm{IPA}}, \tag{6.4}$$

n_{a} is obtained approximately [155], where $v_{\mathrm{H_2O}}$ denotes the volume ratio of water in the analyte.

6.2.2 Critical angle

Measurement of the critical angle is a common method to determine the refractive index. Already in 1874 Ernst Abbe described the Abbe-refractometer that allows a convenient and accurate determination of the TIR critical angle [156].

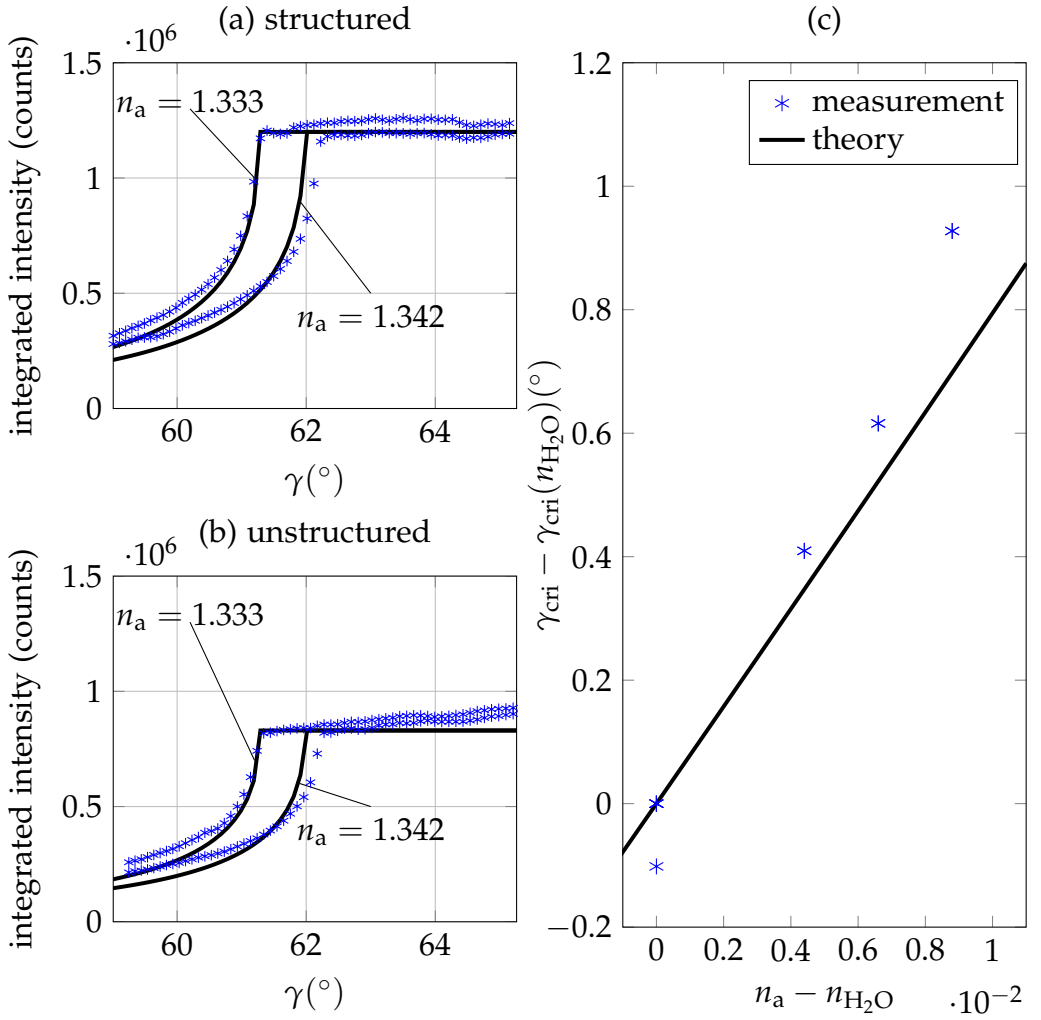

Figure 6.7: Refractive index determination from the integrated intensity versus γ. The measured values are in good agreement with Fresnel's equation (black line). The signal using (a) the structured emitter is approximately 45 % higher than using (b) the unstructured emitter. (c) γ_{cri} increases with n_{a} as predicted by Snell's law at a rate of approximately 80°/RIU (refractive index unit).

Determination of the critical angle requires an angularly resolved measurement, but no spectral information is required. Thus, after measurement of the reflected spectral intensity with the goniophotometer, I integrate the spectra from $\lambda_0 = 500\,\mathrm{nm}$ to $\lambda_0 = 700\,\mathrm{nm}$ for each γ. For a more accurate measurement of γ_{cri} the spectral range would have to be reduced, as material dispersion causes γ_{cri} to be wavelength-dependent (see Eq. (6.1)). In order to assess the grating's influence on the critical angle measurement in the prism setup (Fig. 6.4), analyte mixtures with water ratios $v_{\mathrm{H_2O}}$ be-

tween 0.8 and 1.0 were prepared. Fig. 6.7a,b depicts the intensity curves for $v_{H_2O} = 1.0$ and $v_{H_2O} = 0.8$ obtained for the structured and the unstructured emitter layer. The indicated n_a are calculated by Eq. (6.4). The TIR shifting towards higher γ is clearly visible for both the structured and the unstructured emitter. However, the intensity provided by the structured emitter is approximately 45 % higher than for the unstructured emitter. Note that all measurements were conducted at the same spectrometer integration time and the same excitation laser power.

Additionally, Fig. 6.7a,b depicts the theoretical reflection from the glass-analyte boundary obtained by Fresnel's equations [50], scaled by an arbitrary constant. These theoretical curves are in very good agreement with the measurement.

In total, eleven measurements were made with the structured emitter in the following sequence of analytes: $v_{H_2O} = 1.0$; 0.9; 1.0; 0.8; 1.0; 0.9; 1.0; 0.8; 1.0[1]; 0.85; 1.0; 0.85. γ_{cri} was automatically calculated from the integrated intensity by determining the minimum of the second derivative. The measured shift is excellently reproducible within the angular discretization, as the data points for each n_a coincide except for one data point of $v_{H_2O} = 1.0$ (Fig. 6.7c). I attribute the moderate deviation between the theoretical curve obtained by Eq. (6.1) and the measurement to inaccuracies in the analyte mixing. Nevertheless, a good agreement between theory and experiment is observed. As a sensitivity figure, I define the shift of γ_{cri} per refractive index unit (RIU), which is approximately 80°/RIU from Fig. 6.7c. Note that the sensitivity is independent of the emitter. Nevertheless, the structured emitter is capable of providing a stronger signal and thus a higher signal-to-noise ratio in a sensing application.

6.2.3 Spectrum

Here, I present a method to determine n_a that makes use of the spectral feature caused by the guided mode Bragg scattering (see Fig. 6.6). Consider a spectral detector that collects the reflection in the γ-range depicted range in Fig. 6.6. If only the outcoupling feature was present and if we assumed a perfectly sharp TIR onset, γ_{cri} would be encoded in the falling edge of the spectrum, due to the angular- and wavelength-dependent Bragg scattering as can be seen from Fig. 6.6.

Fig. 6.8a depicts the measured emission integrated in the γ-range between 59.5° and 65.8° and normalized to the curve maximum. Eleven

[1]Omitted from the analysis due to missing data caused by problems with the spectrometer shutter.

measurements are shown according to the analyte sequence described in Sec. 6.2.2. Clearly, the expected spectral edge due to the combination of

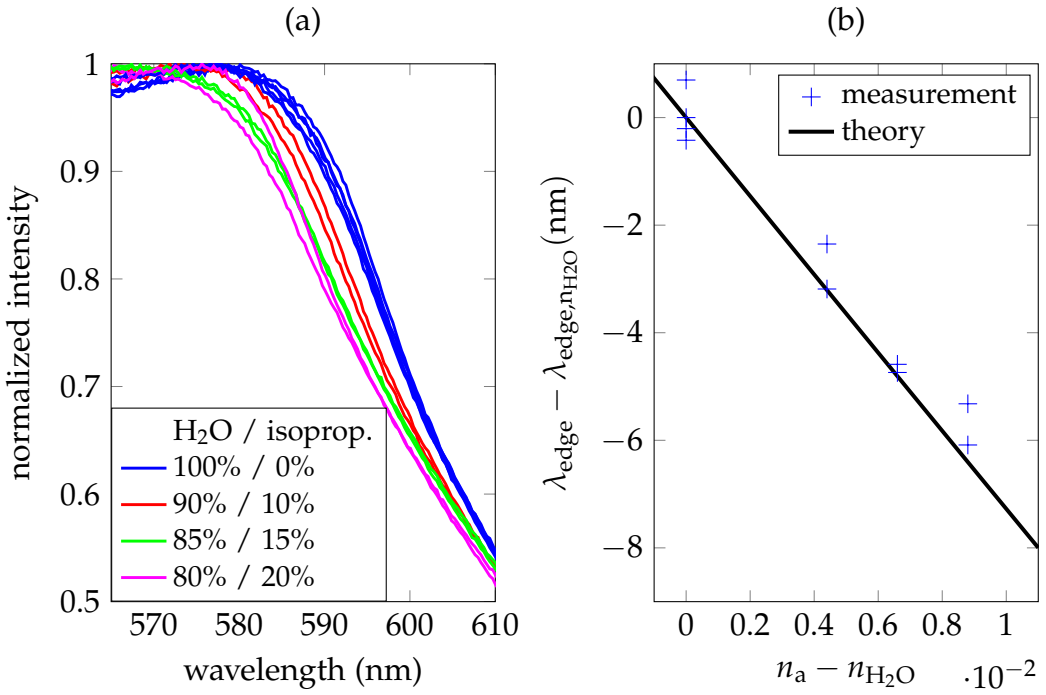

Figure 6.8: Refractive index detection making use of the wavelength- and angle-dependent mode Bragg scattering in combination with TIR. (a) Reflected intensity at the glass-analyte boundary in the γ-range between 59.5° and 65.8°. The falling edge shifts towards shorter wavelengths as n_a increases. (b) The measured shift follows the calculated trend. A remarkably high sensitivity of approximately 700 nm/RIU is observed.

the onset of TIR and the angular- and wavelength-dependent outcoupling feature becomes visible in the spectra. The position of the falling edge is, however, not uniquely defined due to the not-perfectly sharp TIR onset and the background light. Nevertheless, I arbitrarily defined the position λ_{edge} as the wavelength at which the intensity has fallen to 80 % of its maximum value. The shift of the thus obtained edge positions as a function of the refractive index change is depicted in Fig. 6.8b. Although the variance is significant, a clear trend of decreasing λ_{edge} with increasing n_a is observed.

Theoretically, λ_{edge} is determined by the first-order mode Bragg scattering to γ_{cri}

$$n_{eff} - \lambda_{edge}/\Lambda = \sin(\gamma_{cri} - 45°) n_{II}, \tag{6.5}$$

where γ_{cri} depends on n_a as given by Eq. (6.1). The black line in Fig. 6.8b depicts the solution of Eq. (6.5) with Eq. (6.1) and the experimentally deter-

mined n_{eff} of a similar sample (see Fig. 5.7). Clearly, the theoretical shift of λ_{edge} is in good agreement with the measured values. Defining the sensitivity of this detection method as the edge shift in wavelength per RIU, a value of approximately 700 nm/RIU has been achieved. This sensitivity value is remarkably high as it is comparable to the sensitivities of current photonic crystal sensors [150]. It has to be noted, however, that in most photonic crystal sensors, the position of a narrow resonance peak is detected [157] instead of a wavelength edge as is the case here. Nevertheless, there are also reports about successful detections of a falling edge in photonic crystal sensors [158]. Peak detection is potentially more robust as the position of a narrow peak is well defined and it is insensitive to variations in the intensity.

During the measurement, the photoluminescence intensity decreased considerably due to degradation of the organic emitter, thereby making a normalization necessary. The decrease is, e.g., a factor of 0.74 from the first pure water measurement to the last pure water measurement in the analyte sequence. Furthermore, the spectra changed over time even for the same analyte as is visible in the normalized curves (Fig. 6.8). Thus, further research is needed to investigate the robustness of the spectral detection method presented here.

6.2.4 Intensity

Finally, I demonstrate a method to measure n_{a} by the reflected intensity at a fixed angle close to $\gamma_{\text{cri}}(n_{\text{H}_2\text{O}})$. As visible from Fig. 6.6, the intensity decreases at a fixed observation angle γ near $\gamma_{\text{cri}}(n_{\text{H}_2\text{O}})$ as n_{a} increases.

In this experiment, a step-wise change of n_{a} is achieved by adding 1 ml analyte mixture with $v_{\text{H}_2\text{O}} = 0.8$ (see Sec. 6.2.1) and refraction index $n_{\text{a},\infty}$ (see Eq. (6.4)) to the analyte volume each minute. At the start of the experiment (step 0), the analyte volume is filled with 8 ml pure water. Assuming that by the injection, 1 ml of the previous analyte is extruded at the opposing analyte inlet and a mixing with the injected analyte of index $n_{\text{a},\infty}$ takes place afterwards, the analyte refractive index at step m can be modeled with

$$n_{\text{a},m} = \left(\frac{7}{8} n_{\text{a},m-1} + \frac{1}{8} n_{\text{a},\infty}\right). \tag{6.6}$$

$n_{\text{a},m}$ starts with $n_{\text{a},0} = n_{\text{H}_2\text{O}}$ and converges to $n_{\text{a},\infty}$ with increasing m. The green line in Fig. 6.9 depicts the thus obtained change of n_{a} with each injection at the indicated time steps (step $m = 1$ at 20 s, step $m = 2$ at 80 s, and so forth).

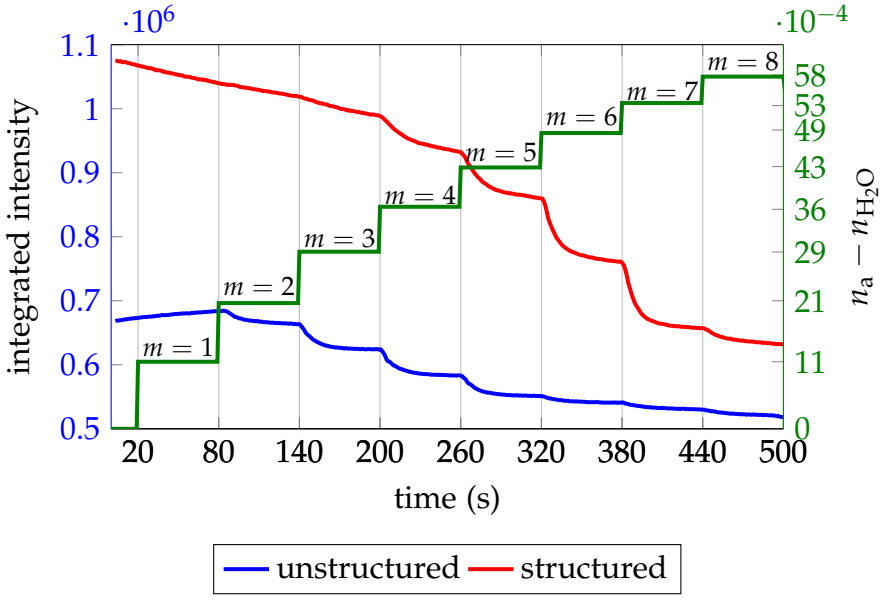

Figure 6.9: Reflection intensity for varied analyte measured in the prism setup at a fixed angle close to $\gamma_{cri}(n_{H_2O})$. At the indicated time steps, the analyte is varied resulting in a step-wise change of n_a (green curve). By using a structured emitter layer, higher signal changes per RIU are observed than for the unstructured emitter layer.

The reflection intensity was recorded over time in the prism setup at approximately $\gamma = 61°$ for a structured and an unstructured emitter layer. As shown in Fig. 6.9, the intensity decreases for both emitters at most injections. The intensity decrease is most rapid at the time of injection and almost vanishes after 60 s. This signal form indicates that an almost complete mixing takes place in the chosen injection interval of 60 s. Additionally to the rapid changes associated with the analyte variations, a drift over time is visible in both signals. A drift with negative slope is clearly visible in the red line up to 200 s and a drift with positive slope is visible in the blue line up to 80 s. I attribute these drifts to changes in the emitters' photoluminescence and note that the drift is superimposed on the changes due to the analyte throughout the measurement.

Defining the sensitivity as the amount of intensity change per RIU, we observe a varying sensitivity in Fig. 6.9 with the step number or analyte refractive index. E.g., the first three injections (0 s to 200 s), do not result in rapid signal changes for the structured emitter measurement (red line). This is also the case for the unstructured emitter measurement (blue line) at the first injection. Up to these points, the measured intensities exhibit only the described drift. For the unstructured emitter, the highest sensitivity is

measured at the $m = 4$ injection. The highest sensitivity for the structured emitter is measured after at the $m = 7$ injection, i.e. at a higher value of n_a than for the unstructured emitter. The change of the sensitivity with the analyte refractive index can be understood from the Fresnel reflection curves shown in Fig. 6.7a,b. Assuming the fixed observation angle is higher than γ_{cri,H_2O} and assuming an analyte with n_a increasing from n_{H_2O}, the measured reflected intensity is constant until n_a is high enough so that the observation angle is equal to the TIR critical angle (Eq. (6.1)). At this n_a, the sensitivity is high due to the rapidly falling reflection intensity. Increasing n_a further results in a further decrease of the measured intensity but with decreasing rate of change. This behavior can be observed for both emitters in Fig. 6.9. The difference in n_a at which the sensitivity is maximal can be explained by small differences in the observation angle. Although the measurements with the structured and the unstructured emitter were recorded at the same goniophotometer tilt angle, the different positions on the sample lead to a deviation in the actual observation angle. The observation angle is approximately $\gamma = 61.4°$ for the structured emitter layer and $\gamma = 61.1°$ for the unstructured emitter. This explains why the sensitivity maximum for the structured emitter occurs at higher values of n_a.

In conclusion, an approximately fourfold sensitivity is achieved with the structured emitter compared to the unstructured emitter in this refractive index measurement. Using the structured emitter, a change in n_a as small as $5 \cdot 10^{-4}$ is readily detectable as visible in step $m = 7$ in Fig. 6.9.

Chapter 7

Summary and conclusion

OLEDs are light sources of great interest since the employed organic light-emitting materials facilitate new applications and low-cost production. Yet, the thin-film structure of an OLED comprises a waveguide that traps significant amounts of the generated light in guided modes. For lighting applications, the guided modes reduce the OLED's efficiency. One way to recover the trapped light are Bragg gratings, which scatter the guided modes into the emission direction. The strength of the scattering, however, significantly depends on the combination of the grating period and the thin-film thickness as this work has shown. In addition, the often employed single-period gratings mainly scatter the guided mode in a single, wavelength-dependent direction, which leads to an angular color impression for the viewer. Besides the grating period, single-period gratings offer no further control over the scattering direction. This limits the optimization of a grating OLED, e.g. for a minimal angular color impression. In this thesis, I investigated the guided mode outcoupling from OLED-like waveguides with gratings and demonstrated that novel nanostructures can be used to obtain more control over the guided mode scattering.

On the theoretical side, I developed an approximative model for guided mode extraction in grating waveguides. I derived source terms for the fields scattered at the grating, by combining two formulations: the grating perturbation theory of Tamir and Peng [57], which treats the grating as a perturbation source inside the cavity formed by the waveguide and the transfer matrix formulation of Benisty et al. [46], which allows to calculate the fields in planar structures for internal sources. I thereby obtained physically intuitive expressions for the intensity of the scattered waves outside the thin films. These expressions show that the intensity of the radiated plane waves is proportional to the squared modulus of the mode overlap with the grating region, the grating Fourier coefficients, the cavity

factors, and a directional term. Without material absorption and outside the stopbands, evaluation of the given expressions with transfer matrix methods further allows to calculate the mode attenuation constant α efficiently. In addition, I implemented a RCWA formulation to rigorously calculate α in grating waveguides.

Using RCWA and the developed model, I systematically studied the guided mode attenuation constant α in an OLED-like waveguide without cathode. The mode attenuation constant α is directly related to the intensity of the radiated plane waves. Although the α obtained by RCWA comprises radiation and stopbands, α could be used to quantify the total radiation as the stopbands affected α only in narrow regions. I demonstrated the importance of the waveguide thickness and grating period for efficient guided mode outcoupling. Although the studied cavity is weak due to the small reflection at the film-substrate interface, α was found to exhibit pronounced and broad maxima at particular waveguide thicknesses, which coincide with the maxima of the standing wave factor towards the substrate. These maxima are caused by constructive interference of the "source" waves originating at the grating and were explained by the readily assessable reflection factors inside the waveguide. In addition, the mode overlap with the grating region was found to decrease with the waveguide thickness, which leads to lower values of α for thicker waveguides. The obtained methods and results provide a powerful tool to optimize the layer thicknesses of grating OLEDs. Of particular interest for guided mode extraction may be the strong interference effects found in "cavity OLEDs" [159], which comprise a metallic cathode in combination with a reflector at the film-substrate boundary. Typically, the cavity is optimized regarding emission from the recombination zone. With the insights brought by this work, a cavity grating OLED is conceivable that simultaneously optimizes the cavity for sources at the recombination zone and the scattering sources at the grating.

The goniophotometer built in this work allowed me to measure the emission of samples with a high angular resolution. I derived the instrument response function of the goniophotometer and could thereby measure the angular peak width of the Bragg-scattered guided mode precisely. While the angular peak width is known to be associated with the guided mode's attenuation constant α in grating waveguides when the reflection is measured, I found evidence that this relation is also valid for emission from nanostructured light-emitting layers.

Addressing the limited design space of single-period gratings, I introduced compound binary gratings for guided mode extraction from OLED-like waveguides in this work. A compound binary grating is obtained

by the superposition of multiple binary gratings and possesses the dominant Fourier coefficients of its components. With photoluminescence measurements, I experimentally demonstrated that compound binary gratings scatter a guided mode to multiple strong outcoupling directions, which is in contrast to single period gratings. I found that each dominant Fourier coefficient is associated with a particular outcoupling feature and direction given by the Bragg equation. Due to the presence of a forward- and a backward-traveling wave, pairs of angle-symmetric outcoupling features were observed. Furthermore, I demonstrated that the intensity of the individual outcoupling features can be controlled by the component gratings' duty cycle. By gradually increasing the duty cycle of one grating component, the intensity of the corresponding features generally increased up to a component duty cycle of 0.5. The experimental results were found to be in good agreement with my developed model and RCWA. The control of the individual outcoupling feature intensities could be mainly attributed to the corresponding Fourier coefficients. In conclusion, compound binary gratings facilitate numerous designs of guided mode outcoupling. With the freedom to combine various grating periods weighted by their duty cycles, wide control over the emission is possible. The control of the outcoupling features is desirable to design grating OLEDs with highly efficient guided mode outcoupling, which at the same time minimize the color impression for the viewer. Additionally, the emission control may facilitate new applications of the polarized, outcoupled light, e.g., for sensors or displays.

As an application of nanostructured organic layers for sensors, I experimentally investigated refractive index sensing with a light source structured by a single-period grating. I employed the directionality of the emission due to Bragg scattering of guided modes to increase the sensor signal. Additionally, I showed that the angular- and wavelength dependence of the outcoupled light can also facilitate new sensing methods such as the spectral encoding of the reflection angle in a refractive index sensor based on total internal reflection.

In conclusion, the methods and results presented in this work allow to design OLEDs with better efficiencies, higher color quality and wider application possibilities.

Appendix A

Plane wave Poynting vector

In the following, the Poynting vector of a general plane wave with complex $\vec{k}$ described by Eq. (2.11) is calculated. The first Maxwell equation (2.1)

$$\nabla \times \underline{\vec{E}}(\vec{r}) = -j\omega \underline{\vec{B}}(\vec{r}) \overset{(2.7)}{=} -j\omega\mu_0 \underline{\vec{H}}(\vec{r}) \tag{A.1}$$

relates the electric and the magnetic field. For the plane wave, the rotation of the electric field vector can be expressed as

$$\begin{aligned}
\nabla \times \underline{\vec{E}}(\vec{r}) &\overset{(2.11)}{=} \nabla \times \underline{\vec{E}}_{0,\vec{k}} \exp\left(-j\vec{k}\cdot\vec{r}\right) \\
&\overset{[76]}{=} \left(\frac{\partial}{\partial x}\vec{e}_x + \frac{\partial}{\partial y}\vec{e}_y + \frac{\partial}{\partial z}\vec{e}_z\right) \times \underline{\vec{E}}_{0,\vec{k}} \exp\left[-j(k_x x + k_y y + k_z z)\right] \\
&= -j\left(k_x\vec{e}_x + k_y\vec{e}_y + k_z\vec{e}_z\right) \times \underline{\vec{E}}(\vec{r}) \\
&= -j\vec{k} \times \underline{\vec{E}}(\vec{r}).
\end{aligned} \tag{A.2}$$

Now, insertion of (A.2) into (A.1) yields the plane wave magnetic field for (2.11)

$$\underline{\vec{H}}(\vec{r}) = \frac{1}{\omega\mu_0}\vec{k} \times \underline{\vec{E}}(\vec{r}). \tag{A.3}$$

Making use of the formula for the double vector product [76]

$$\vec{a} \times (\vec{b} \times \vec{c}) = \vec{b} \cdot (\vec{a} \cdot \vec{c}) - \vec{c} \cdot \left(\vec{a} \cdot \vec{b}\right), \tag{A.4}$$

the complex Poynting vector (2.5) is

$$\begin{aligned}
\underline{\vec{S}}(\vec{r}) &\overset{(2.5)}{=} \underline{\vec{E}}(\vec{r}) \times \underline{\vec{H}}^*(\vec{r}) \\
&\overset{(2.11),(A.3)}{=} \underline{\vec{E}}_{0,\vec{k}} \times \left(\frac{1}{\omega\mu_0}\vec{k} \times \underline{\vec{E}}_{0,\vec{k}}\right)^* \exp\left(-j\vec{k}\cdot\vec{r}\right)\left[\exp\left(-j\vec{k}\cdot\vec{r}\right)\right]^* \\
&\overset{(A.4)}{=} \left[\left(\underline{\vec{E}}_{0,\vec{k}}\cdot\underline{\vec{E}}^*_{0,\vec{k}}\right)\frac{1}{\omega\mu_0}\vec{k}^* - \left(\frac{1}{\omega\mu_0}\underline{\vec{E}}_{0,\vec{k}}\cdot\vec{k}^*\right)\underline{\vec{E}}^*_{0,\vec{k}}\right]\left|\exp\left(-j\vec{k}\cdot\vec{r}\right)\right|^2 \\
&\overset{(2.14)}{=} \frac{1}{\omega\mu_0}\left[\left|\underline{\vec{E}}_{0,\vec{k}}\right|^2\vec{k}^* - \left(\underline{\vec{E}}_{0,\vec{k}}\cdot\vec{k}^*\right)\underline{\vec{E}}^*_{0,\vec{k}}\right]\exp\left(2\vec{\alpha}\cdot\vec{r}\right) \qquad \text{(A.5)}
\end{aligned}$$

This equation can be simplified for many cases by evaluation of the second term in the bracket. Since $\underline{\vec{E}}$ and $\vec{k}$ are orthogonal [47] in every point $\vec{r}$

$$\underline{\vec{E}}(\vec{r})\cdot\vec{k} = \underline{\vec{E}}_{0,\vec{k}}\exp\left(-j\vec{k}\cdot\vec{r}\right)\cdot\vec{k} = 0$$

it follows that

$$\underline{\vec{E}}_{0,\vec{k}}\cdot\vec{k} = 0. \qquad \text{(A.6)}$$

In case of a homogeneous plane wave $\vec{k} = \vec{\beta}$ is real and thus the second bracket term in (A.5) and the exponential term vanish, yielding

$$\underline{\vec{S}}(\vec{r}) = \frac{1}{\omega\mu_0}\left|\underline{\vec{E}}_{0,\vec{k}}\right|^2\vec{\beta}. \qquad \text{(A.7)}$$

This well known result gives a real Poynting vector and the energy flow is in direction of $\vec{k} = \vec{\beta}$.

In case of an inhomogeneous plane wave $\vec{k} = \vec{\beta} + j\vec{\alpha}$ is complex and thus the second bracket term does not necessarily vanish, yielding an energy flow direction that might not be in direction of $\vec{\beta}$. However, if $\underline{\vec{E}}_{0,\vec{k}}$ is proportional to a real vector, i.e. $\underline{\vec{E}}_{0,\vec{k}} = \underline{c}\vec{E}_{0,\vec{k}}$ with $\underline{c}$ a complex scalar and $\vec{E}_{0,\vec{k}}$ a real vector, one can show that

$$\underline{\vec{E}}_{0,\vec{k}}\cdot\vec{k}^* = \left(\underline{\vec{E}}^*_{0,\vec{k}}\cdot\vec{k}\right)^* = \left(\underline{c}^*\vec{E}_{0,\vec{k}}\cdot\vec{k}\right)^* = \left(\frac{\underline{c}^*}{\underline{c}}\underline{c}\vec{E}_{0,\vec{k}}\cdot\vec{k}\right)^* = \left(\frac{\underline{c}^*}{\underline{c}}\underline{\vec{E}}_{0,\vec{k}}\cdot\vec{k}\right)^* \overset{(A.6)}{=} 0. \qquad \text{(A.8)}$$

The complex Poynting vector (A.5) then simplifies to

$$\underline{\vec{S}}(\vec{r}) = \frac{1}{\omega\mu_0}\left|\underline{\vec{E}}_{0,\vec{k}}\right|^2\left(\vec{\beta} - j\vec{\alpha}\right)\exp\left(2\vec{\alpha}\cdot\vec{r}\right). \qquad \text{(A.9)}$$

The real part of the Poynting vector (A.9) then gives an energy flow (2.6) in direction of $\vec{\beta}$, as in the case of a homogeneous plane wave.

Appendix B

Goniophotometer's angular response function - Approximation

The goniophotometer's inverse problem Eq. (4.4) can be approximated by an integral over the emission angle θ if assumptions about the sample extent, the sample-fiber distance and the sample emission are made. Eventually, such a formulation allows the definition of an angular response function as will be shown in the following.

Recall the assumption that

$$\begin{aligned} l &\gg d_\mathrm{s}, d_\mathrm{f}\,, \\ \Delta x_\mathrm{s}, \Delta x_\mathrm{f} &\ll d_\mathrm{s}, d_\mathrm{f}\,, \end{aligned} \tag{B.1}$$

where Δx_s and Δx_f are the extents in x-direction of sample and fiber, respectively. Note that due to our assumptions, the sample and fiber are neither quadratic nor circular but small stripes of length d_s and d_f, respectively. The solid angle $\Omega_{\vec{r}_0,\,\theta_0}$ is thus small in x-direction and assumed as independent of the $\vec{r}_0$ x-coordinate. Let us replace the integration over $\Omega_{\vec{r}_0,\theta_0}$ by an integration over the fiber end surface. $\mathrm{d}\Omega$ is subtended by an infinitesimal surface area on the fiber end and described as

$$\mathrm{d}\Omega = \frac{\mathrm{d}x\,\mathrm{d}\theta}{r}, \tag{B.2}$$

where r is the distance between the $\mathrm{d}A$ on the sample surface and the infinitesimal surface area on the fiber end described by $\mathrm{d}x$ and $\mathrm{d}\theta$. The integration boundary in x-direction is Δx_f and independent of $\vec{r}_0$, the position

of $\mathrm{d}A$. Denoting the θ-region of integration by $\theta_{\vec{r}_0,\theta_0}$, Eq. (4.4) becomes

$$\Phi_f(\theta_0) \approx \int_{A_\mathrm{s}} \int_{\theta_{\vec{r}_0,\theta_0}} \int_{\Delta x_\mathrm{f}} L_\mathrm{s}\left(\vec{r}_0,\Theta\right) \cos\theta \frac{1}{r} \,\mathrm{d}\theta \,\mathrm{d}x \,\mathrm{d}A. \tag{B.3}$$

According to our assumptions Eq. (B.1), $L_\mathrm{s}\left(\vec{r}_0,\Theta\right)$ can be approximated by its value in φ_0-direction $L_{\mathrm{s},\varphi_0}\left(\vec{r}_0,\theta\right)$, which depends only on the θ-direction. Neglecting further the x-dependence of r as we integrate over the small Δx_f region on the fiber, Eq. (B.3) becomes

$$\Phi_f(\theta_0) \approx \Delta x_\mathrm{f} \int_{A_\mathrm{s}} \int_{\theta_{\vec{r}_0,\theta_0}} L_{\mathrm{s},\varphi_0}\left(\vec{r}_0,\theta\right) \cos\theta \frac{1}{r} \,\mathrm{d}\theta \,\mathrm{d}A. \tag{B.4}$$

Similiarly, the sample area integral is split into an y- and x-integral and Eq. (B.4) yields

$$\Phi_f(\theta_0) \approx \Delta x_\mathrm{s} \Delta x_\mathrm{f} \int_{d_\mathrm{s}} \int_{\theta_{\vec{r}_0,\theta_0}} L_{\mathrm{s},\varphi_0}\left(y,\theta\right) \cos\theta \frac{1}{r} \,\mathrm{d}\theta \,\mathrm{d}y, \tag{B.5}$$

according to our approximation. In order to obtain an integration over θ first, we will change the order of integration. This requires to adjust the integration boundaries. While in Eq. (B.5) the inner integral's region is the θ-range that reaches the fiber for a given $\vec{r}_0$ and θ_0, after change of the integration order, the inner integral's region is the sample y-range that contributes to the radiant flux at the fiber for a given θ and θ_0. We call this sample y-range $d_{\mathrm{s},\theta,\theta_0}$. The outer integral now spans from $\theta = -\pi$ to $\theta = -\pi$ and we obtain

$$\Phi_f(\theta_0) \approx \Delta x_\mathrm{s} \Delta x_\mathrm{f} \int_{-\pi}^{\pi} \int_{d_{\mathrm{s},\theta,\theta_0}} L_{\mathrm{s},\varphi_0}\left(y,\theta\right) \cos\theta \frac{1}{r} \,\mathrm{d}y \,\mathrm{d}\theta. \tag{B.6}$$

For a sample with position-independent radiance

$$L_{\mathrm{s},\varphi_0}\left(y,\theta\right) = L_{\mathrm{s},\varphi_0}\left(\theta\right) \neq f(y), \tag{B.7}$$

L can be brought outside the inner integral, finally yielding the relation between the measured signal $\Phi_f(\theta_0)$ and the function of interest $L_{\mathrm{s},\varphi_0}\left(\theta\right)\cos\theta$

$$\begin{aligned}\Phi_f(\theta_0) &\approx \Delta x_\mathrm{s} \Delta x_\mathrm{f} \int_{-\pi}^{\pi} L_{\mathrm{s},\varphi_0}\left(\theta\right) \cos\theta \int_{d_{\mathrm{s},\theta,\theta_0}} \frac{1}{r} \,\mathrm{d}y \,\mathrm{d}\theta \\ &\approx \Delta x_\mathrm{s} \Delta x_\mathrm{f} \int_{-\pi}^{\pi} L_{\mathrm{s},\varphi_0}\left(\theta\right) \cos\theta \; f_\mathrm{E}(\theta,\theta_0) \,\mathrm{d}\theta,\end{aligned} \tag{B.8}$$

with the function definition

$$f_{\mathrm{E}}(\theta, \theta_0) = \int\limits_{d_{\mathrm{s},\theta,\theta_0}} \frac{1}{r}\, \mathrm{d}y. \tag{B.9}$$

The function $f_{\mathrm{E}}(\theta, \theta_0)$ is the goniophotometer's instrument response function. Note that the integral in Eq. (B.8) resembles a convolution if f_{E} is dependent only on the argument difference $\theta_0 - \theta$.

Appendix C

Trigonometric calculation of approximate $f_{\mathrm{E}}(\theta, \theta_0)$

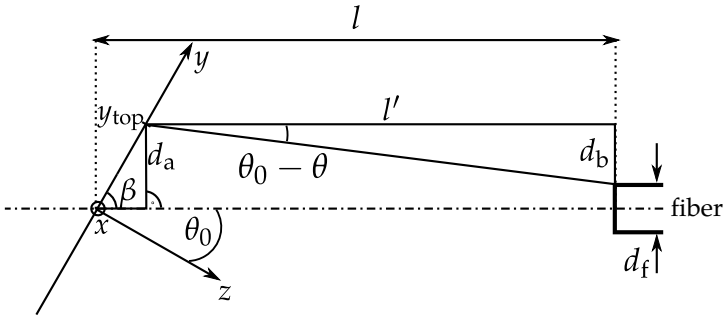

Figure C.1: Angles and lengths needed for the trigonometric calculation of the sample region contributing to the fiber flux depending on sample tilt θ_0 and emission direction θ.

This Appendix derives the limits y_{top} and y_{bottom} that define the region in the sample plane potentially contributing to the fiber flux. The length of this region actually filled by the sample is $d_{\mathrm{s},\theta,\theta_0}$, which is proportional to the goniophotometer's instrument response function $f_{\mathrm{E}}(\theta, \theta_0)$ according to Eq. (4.8). The calculation is based on the two-dimensional approximation described in 4.2.2. The limits y_{top} and y_{bottom} depend sample tilt θ_0 and emission direction θ.

Consider the right-angled triangle with hypotenuse along the y-axis from the sample center (coordinate system origin) to the sought y_{top} and angle

$$\beta = 90^\circ - \theta_0. \tag{C.1}$$

Its opposite side is

$$d_{\mathrm{a}} = y_{\mathrm{top}} \sin\beta = y_{\mathrm{top}} \cos\theta_0. \tag{C.2}$$

In the right-angled triangle with hypotenuse along the emission direction, d_{b} is the opposite side to the angle $\theta_0 - \theta$ and

$$l' = l - y_{\mathrm{top}} \cos\beta = l - y_{\mathrm{top}} \sin\theta_0 \tag{C.3}$$

the adjacent side. Thus,

$$d_{\mathrm{b}} = l' \tan(\theta_0 - \theta) \tag{C.4}$$

and

$$d_{\mathrm{a}} = d_{\mathrm{f}}/2 + d_{\mathrm{b}}. \tag{C.5}$$

Combining Eq. (C.2)-(C.5) and rearrangement yields

$$y_{\mathrm{top}} = \frac{d_{\mathrm{f}}/2 + l \tan(\theta_0 - \theta)}{\cos\theta_0 + \tan(\theta_0 - \theta) \sin\theta_0}. \tag{C.6}$$

Calculation of y_{bottom} is equivalent, but instead of $d_{\mathrm{f}}/2$, $-d_{\mathrm{f}}/2$ has to be used in Eqs. (C.5) and (C.6). The goniophotometer's instrument response function $f_{\mathrm{E}}(\theta, \theta_0)$ is proportional to the overlap of the sample with the y-range defined by y_{bottom} and y_{top} as described in Sec. 4.2.2.

Appendix D

Fabricated compound binary gratings

Group A

2-periodic $\Lambda_1 = 350\,\text{nm}$; $\Lambda_2 = 450\,\text{nm}$; $\Lambda_t = 3150\,\text{nm}$

Min ridge [nm]	Min groove [nm]	field	$l_{rd,1}$[nm]	$l_{rd,2}$[nm]	f_{dc}
50	50	01	50	150	0.429
100	50	02	100	150	0.524
150	50	03	150	150	0.619
200	50	04	200	150	0.714
50	50	05	50	100	0.333
100	50	06	100	100	0.444
100	50	07	150	100	0.556
200	50	08	200	100	0.667
50	50	09	175	-	0.5

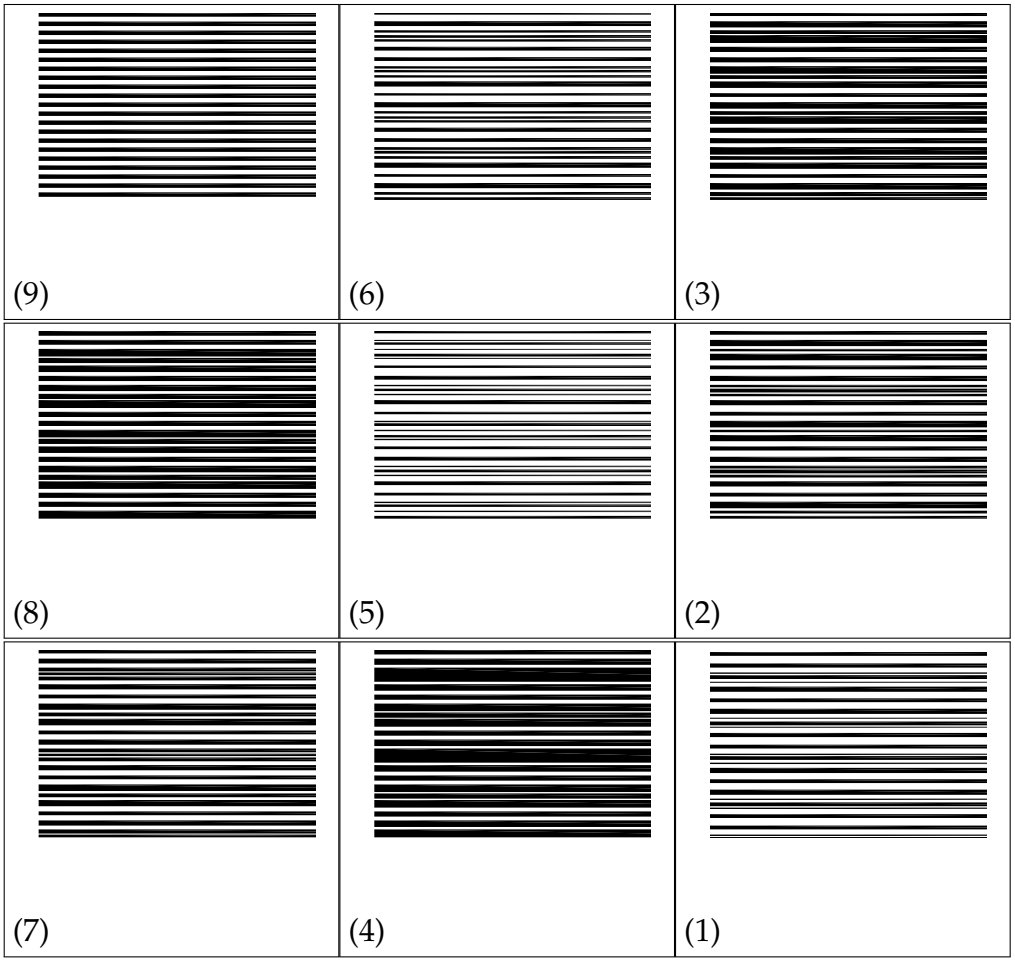

Group B

3-periodic $\Lambda_1 = 350\,\text{nm}$; $\Lambda_2 = 400\,\text{nm}$;$\Lambda_3 = 450\,\text{nm}$; $\Lambda_t = 25200\,\text{nm}$

Min ridge [nm]	Min groove [nm]	field	$l_{rd,1}$[nm]	$l_{rd,2}$[nm]	$l_{rd,3}$	f_{dc} [nm]
50	50	01	50	100	150	0.571
100	50	02	100	100	150	0.643
100	50	03	150	100	150	0.714
200	50	04	200	100	150	0.786
50	50	05	50	100	100	0.5
50	50	06	100	100	100	0.583
100	50	07	150	100	100	0.667
200	50	08	200	100	100	0.750
50	50	09	-	-	225	0.500

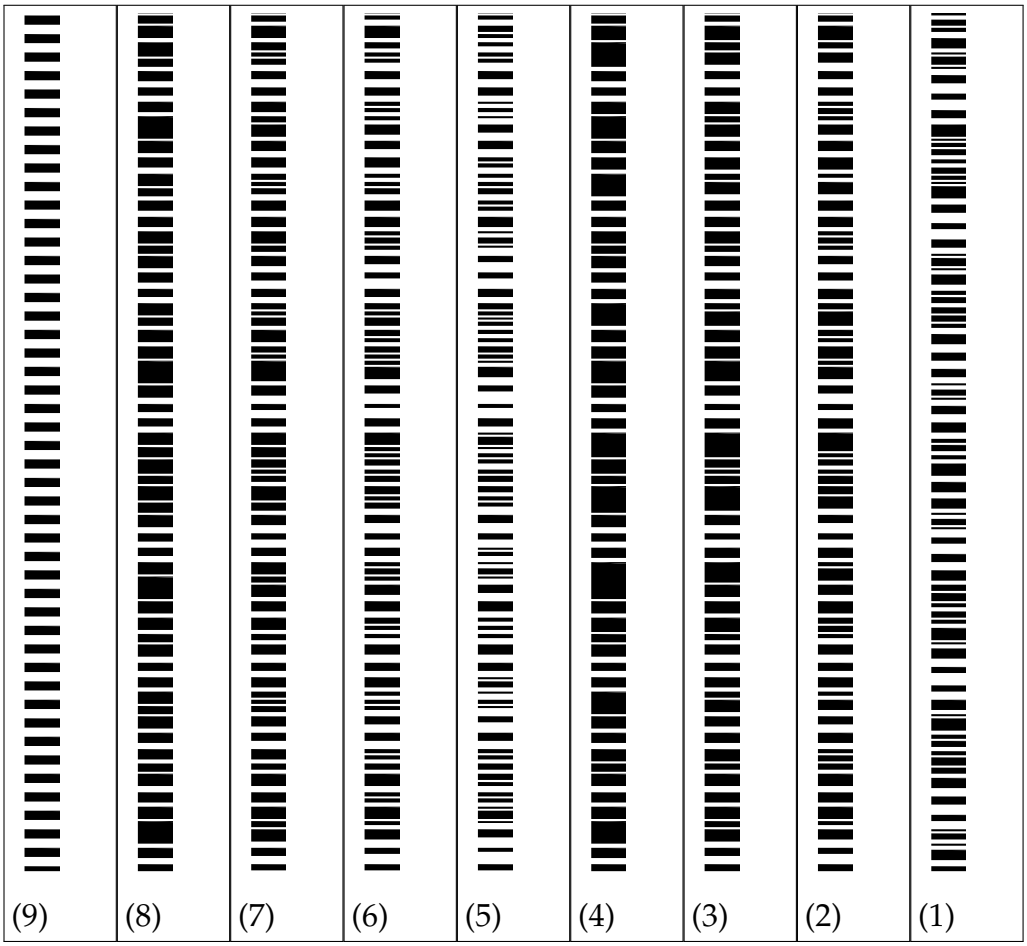

Group C

3-periodic $\Lambda_1 = 300\,\text{nm}$; $\Lambda_2 = 400\,\text{nm}$;$\Lambda_3 = 500\,\text{nm}$; $\Lambda_t = 6000\,\text{nm}$

Min ridge [nm]	Min groove [nm]	field	$l_{rd,1}$ [nm]	$l_{rd,2}$ [nm]	$l_{rd,3}$ [nm]	f_{dc}
50	50	01	50	100	150	0.550
100	50	02	100	100	150	0.650
150	50	03	150	100	150	0.725
200	50	04	200	100	150	0.825
50	50	05	50	100	100	0.500
100	100	06	100	100	100	0.600
150	100	07	150	100	100	0.700
200	100	08	200	100	100	0.800
50	50	09	-	200	-	0.500

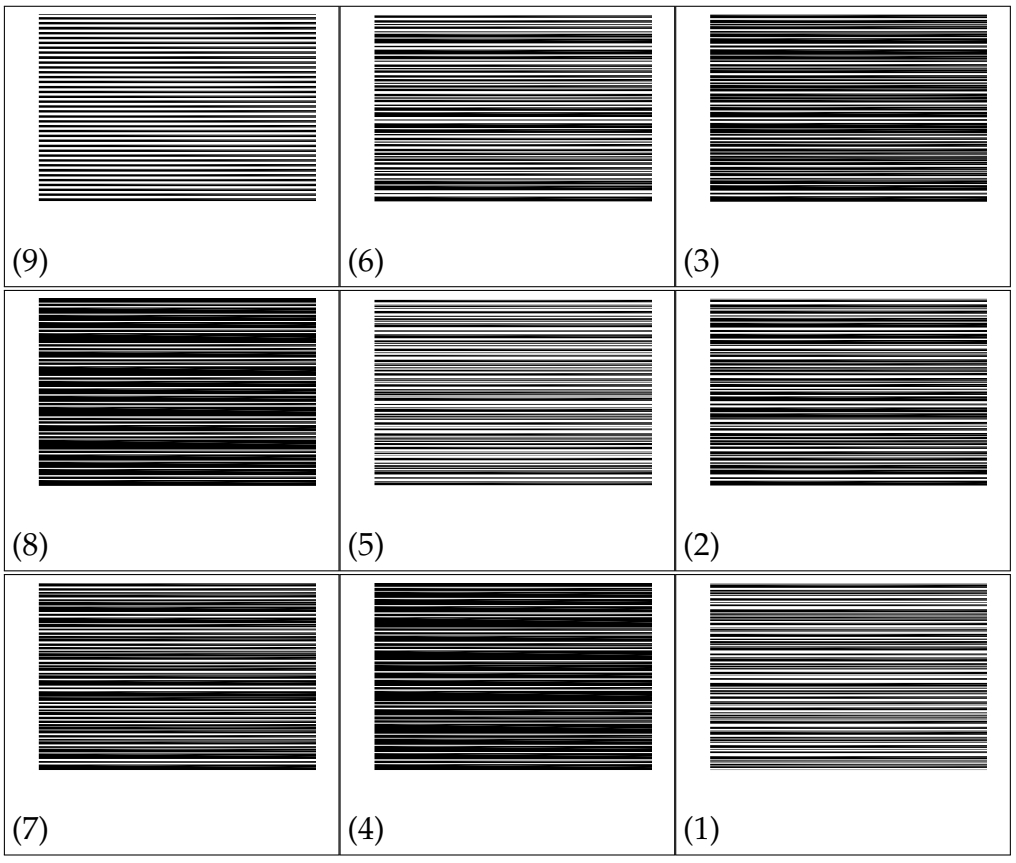

Group D

field	periods [nm]	l_{rd} [nm]	Λ_t [nm]
01	300/400/500/600	50/100/150/200	6000
02	300/350/400/500/600	50/50/100/150/200	42000
03	300/350/400/450/500/600	50/50/100/100/150/200	126000
04	300	150	300
05	500	250	500
06	600	300	600
07	196/392	80/100	392
08	196/392	80/120	392
09	196/490	98/98	980

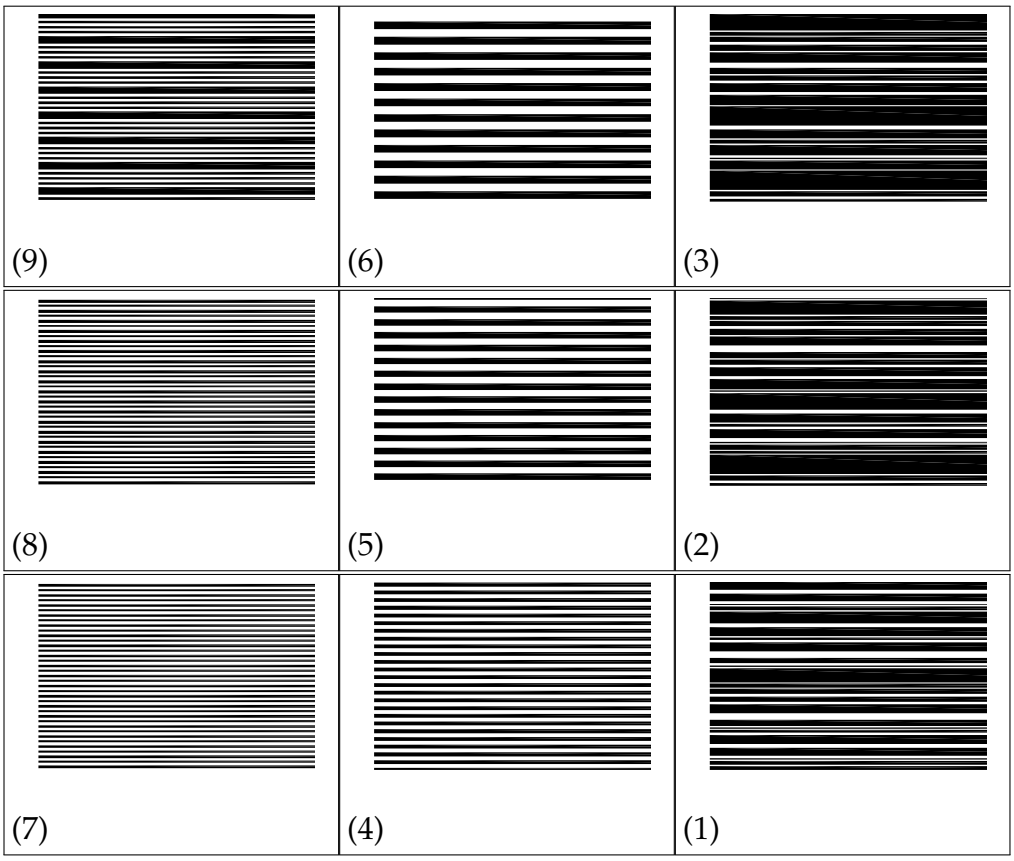

List of relevant samples

Sample	NIL master	SY / toluene	spincoat. 1	spincoat. 2	SiO
K12	05009-4	5 mg/ml	5s@500rpm	60s@1000rpm	100nm
K13	05009-4	5 mg/ml	5s@500rpm	60s@1000rpm	100nm
K14	05009-4	5 mg/ml	5s@500rpm	60s@1000rpm	100nm
K15	05009-4	3 mg/ml	5s@500rpm	60s@1000rpm	100nm
K16	05009-4	3 mg/ml	5s@500rpm	60s@900rpm	100nm

Appendix E

Compound binary gratings

E.1 Peak positions

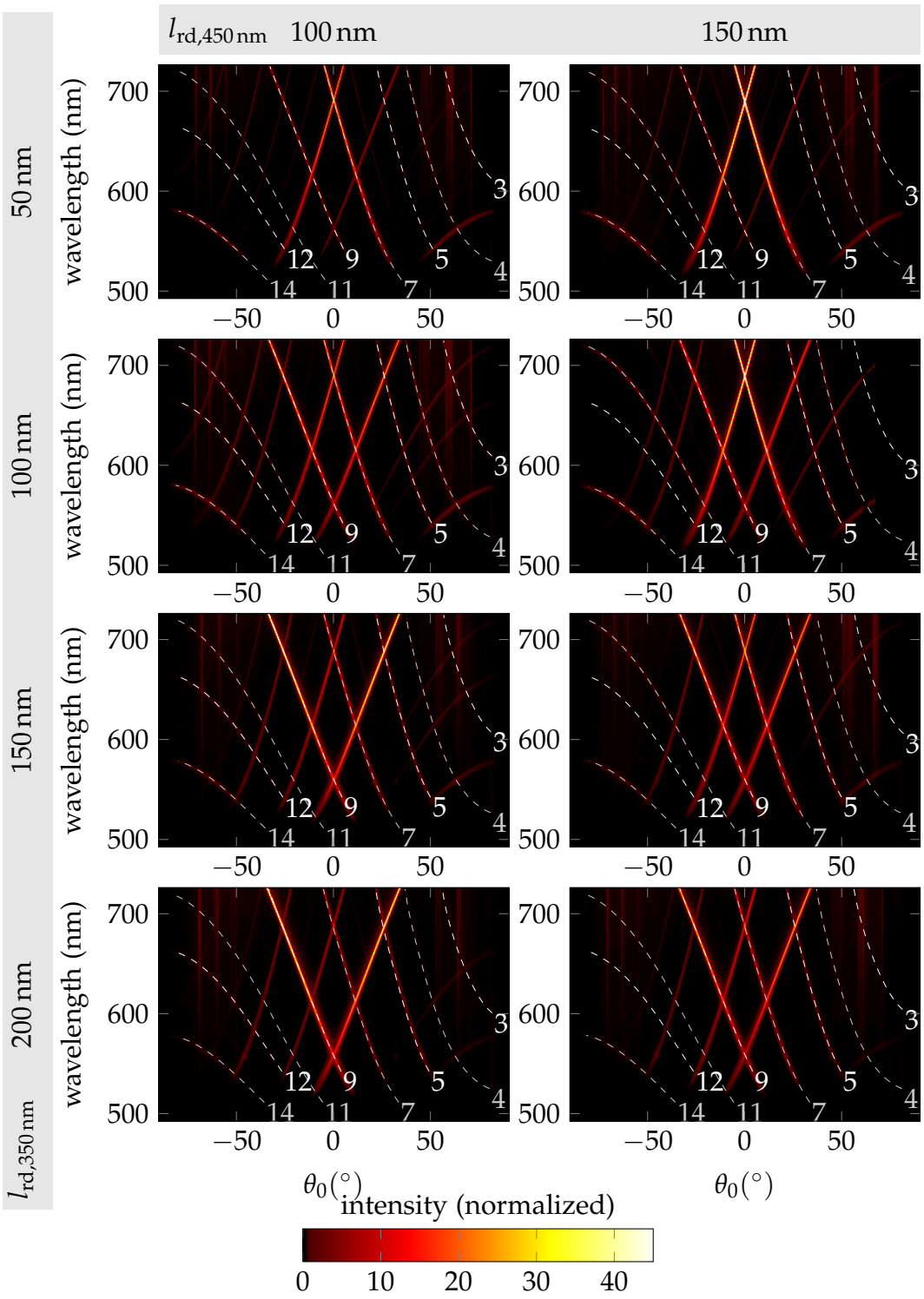

Figure E.1: Field A: compound binary grating 350|450.

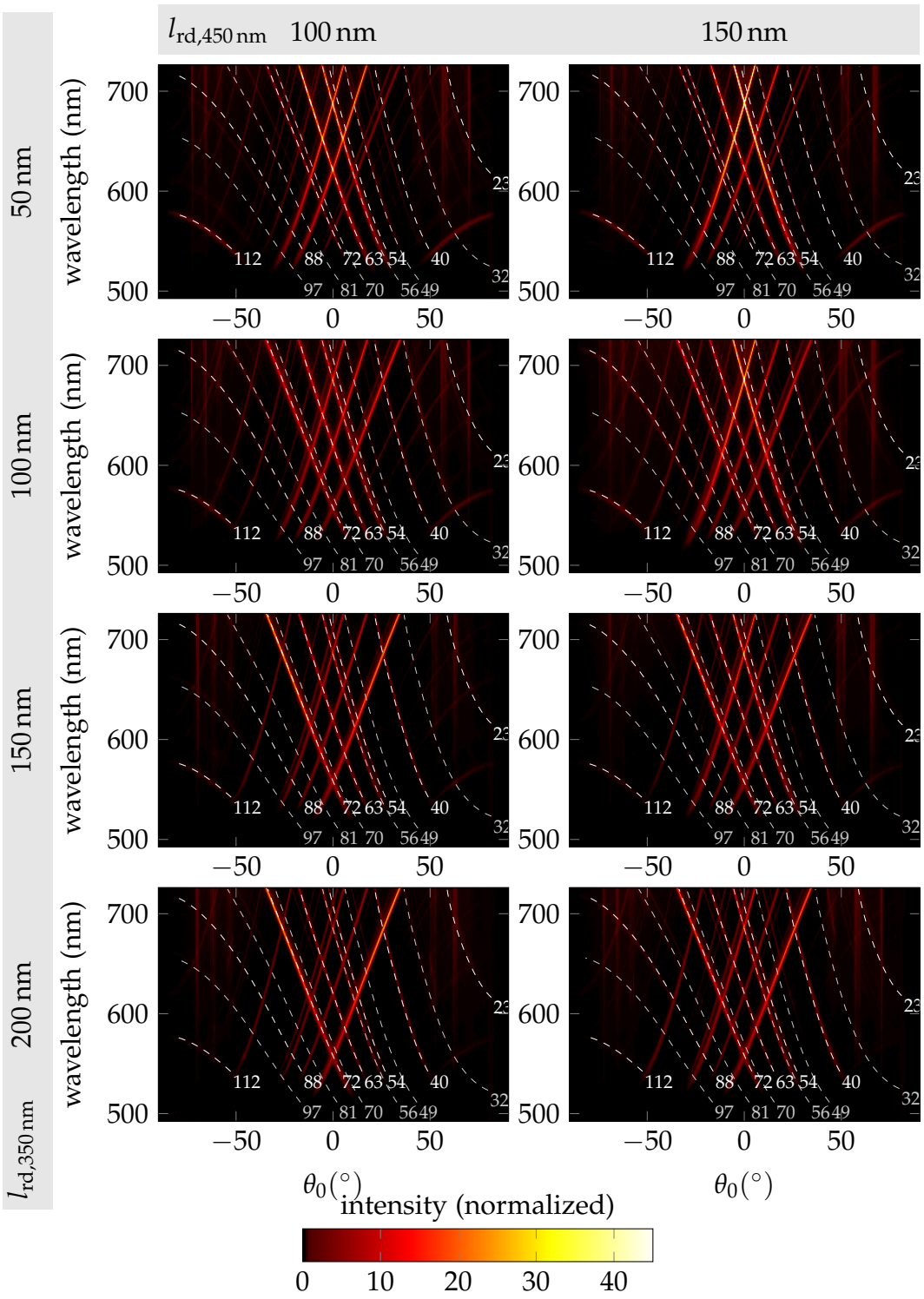

Figure E.2: Group B: compound binary grating 350|400(100)|450.

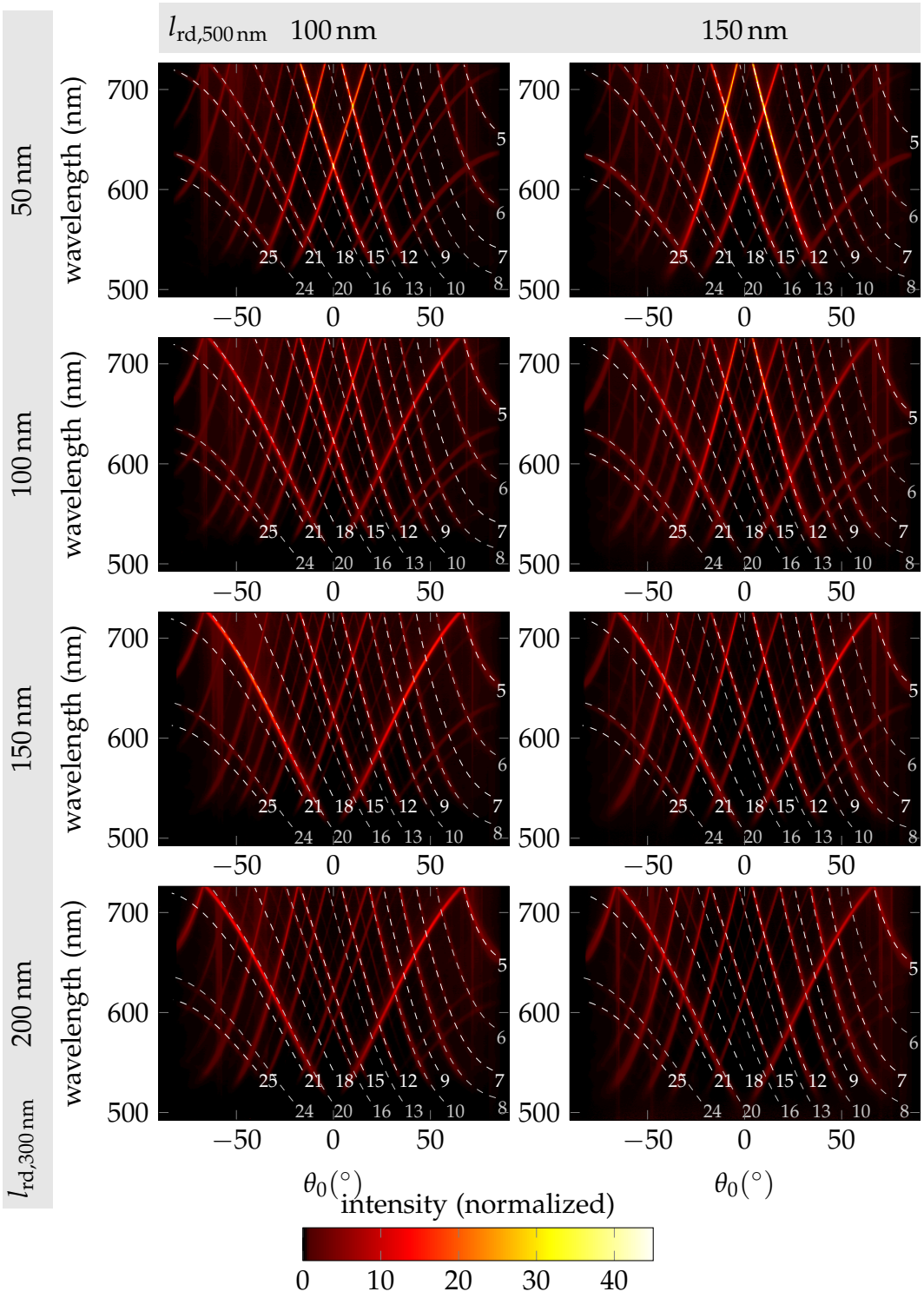

Figure E.3: Group C: compound binary grating 300|400(100)|500.

E.2 Relative peak intensities

E.2.1 Group B

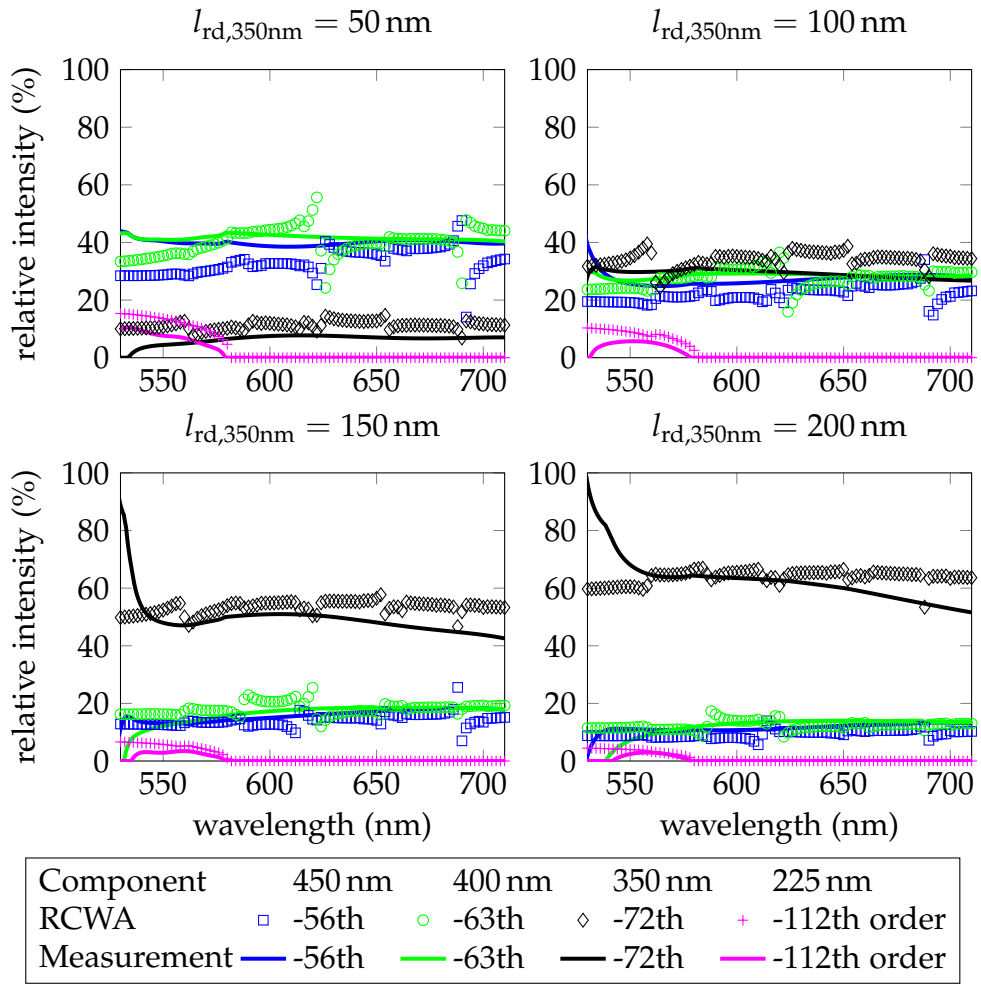

Figure E.4: Relative measured peak intensities (solid lines) and simulated diffraction efficiencies (markers) for the grating $350(l_{rd,350\,nm})|400(100)|450(100)$ with total period $\Lambda_t = 25\,200\,nm$

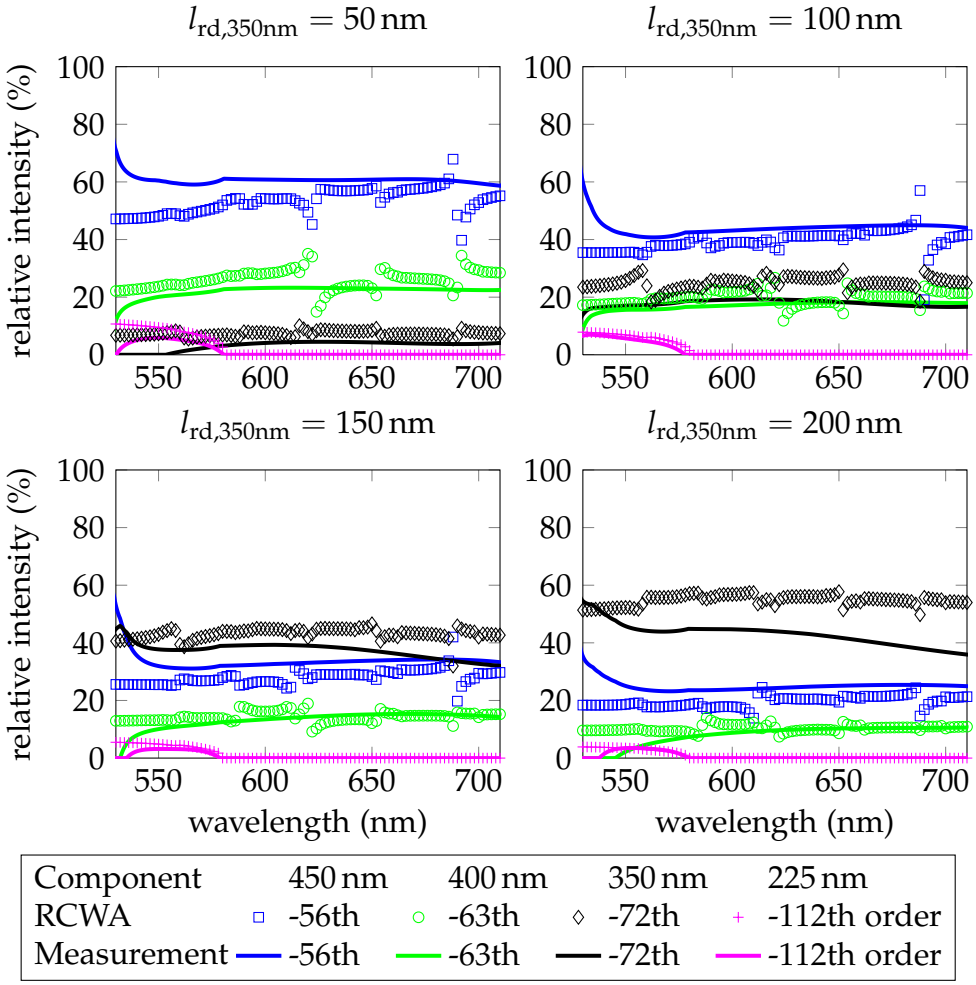

Figure E.5: Relative measured peak intensities (solid lines) and simulated diffraction efficiencies (markers) for the grating $350(l_{\mathrm{rd,350\,nm}})|400(100)|450(150)$ with total period $\Lambda_t = 25\,200\,\mathrm{nm}$

E.2.2 Group C

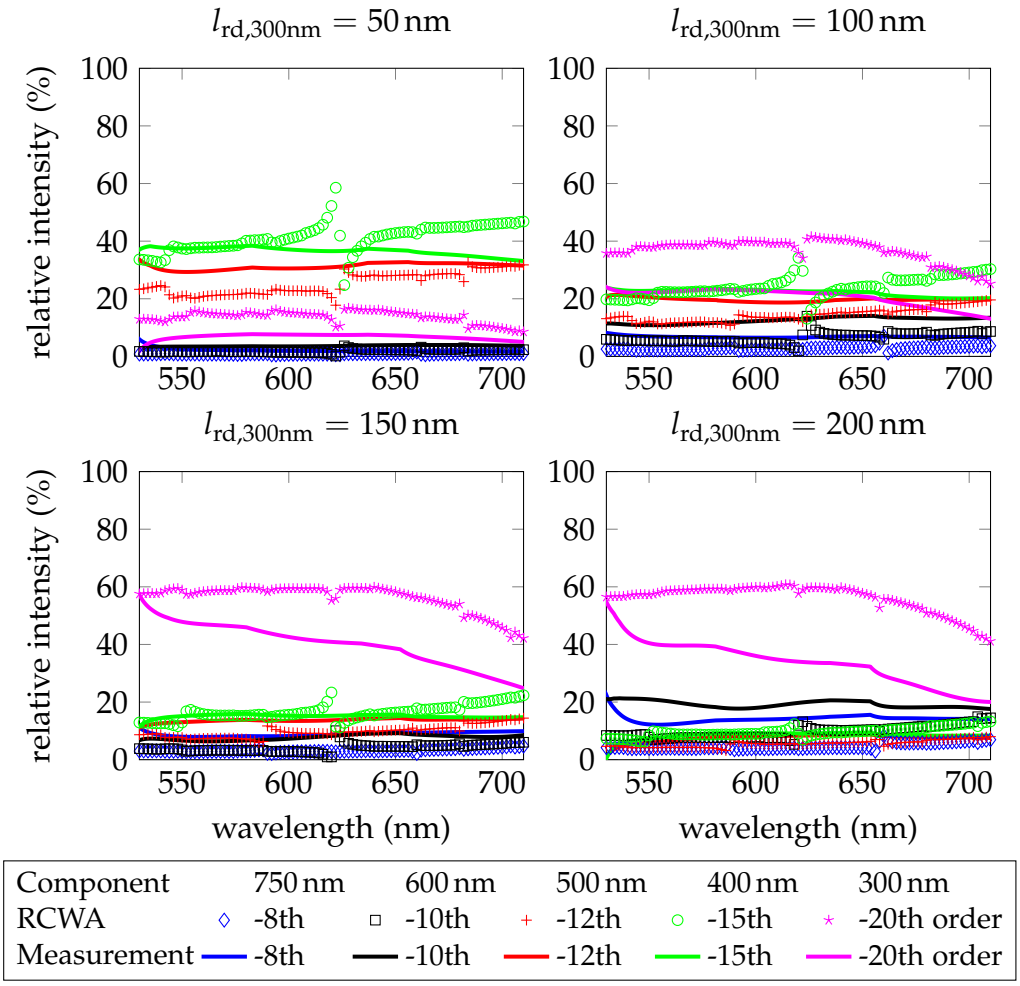

Figure E.6: Relative measured peak intensities (solid lines) and simulated diffraction efficiencies (markers) for the grating $300(l_{\mathrm{rd,300\,nm}})|400(100)|500(100)$ with total period $\Lambda_t = 6000\,\mathrm{nm}$

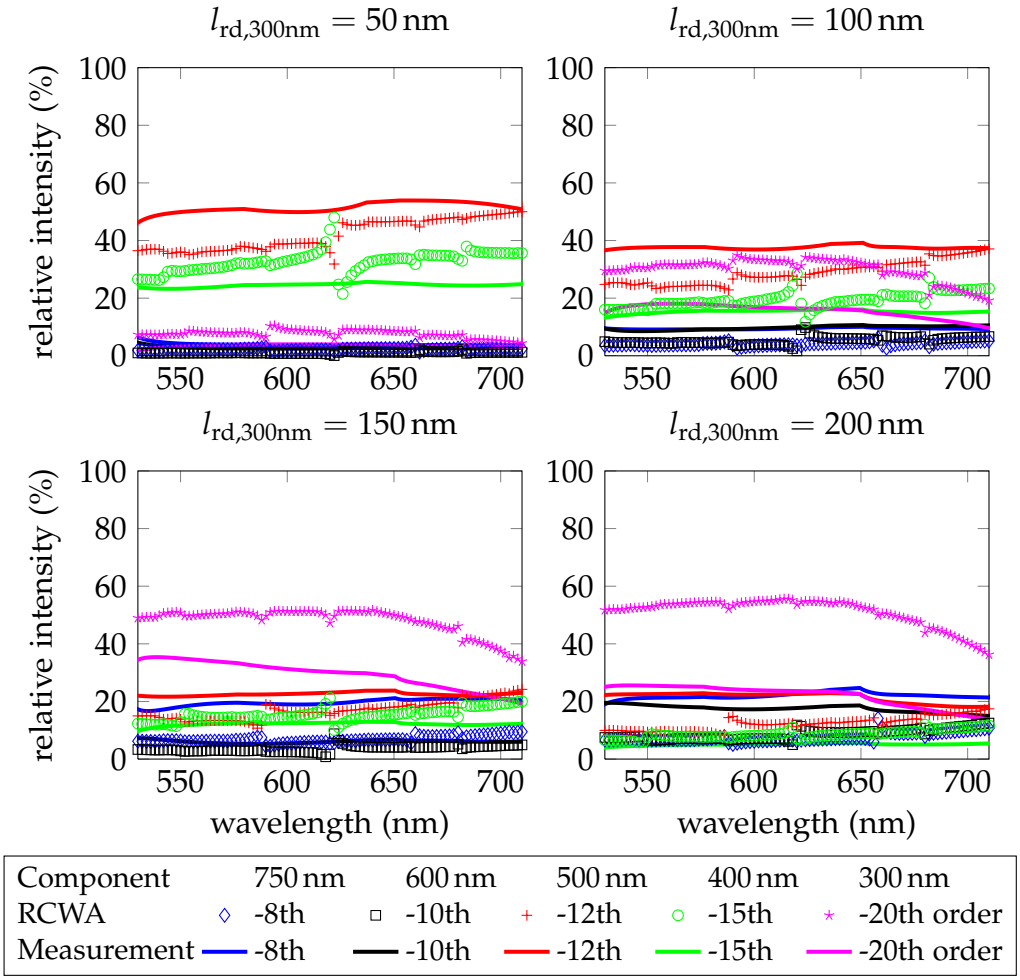

Figure E.7: Relative measured peak intensities (solid lines) and simulated diffraction efficiencies (markers) for the grating $300(l_{rd,300\,nm})|400(100)|500(150)$ with total period $\Lambda_t = 6000\,nm$

Bibliography

[1] G. Lister. The drive for energy efficient lighting. Opt. Photon. News, 15(1):20–25, 2004.

[2] M. Schwoerer and H. C. Wolf. Organische molekulare Festkörper: Einführung in die Physik von π-Systemen. Wiley-VCH-Verl., Weinheim, 2005.

[3] M. R. Krames, O. B. Shchekin, R. Mueller-Mach, G. O. Mueller, L. Zhou, G. Harbers, and M. G. Craford. Status and future of high-power light-emitting diodes for solid-state lighting. J. Disp. Technol., 3(2):160–175, 2007.

[4] M. H. Crawford. LEDs for solid-state lighting: Performance challenges and recent advances. IEEE J. Sel. Top. Quantum Electron., 15(4):1028–1040, 2009.

[5] C. W. Tang and S. A. VanSlyke. Organic electroluminescent diodes. Appl. Phys. Lett., 51(12):913–915, 1987.

[6] J. H. Burroughes, D. D. C. Bradley, A. R. Brown, R. N. Marks, K. Mackay, R. H. Friend, P. L. Burns, and A. B. Holmes. Light-emitting diodes based on conjugated polymers. Nature, 347(6293):539–541, 1990.

[7] R. H. Friend, R. W. Gymer, A. B. Holmes, J. H. Burroughes, R. N. Marks, C. Taliani, D. D. C. Bradley, D. A. D. Santos, J. L. Brédas, M. Lögdlund, and W. R. Salaneck. Electroluminescence in conjugated polymers. Nature, 397(6715):121–128, 1999.

[8] F. So, J. Kido, and P. Burrows. Organic light-emitting devices for solid-state lighting. MRS Bull., 33(07):663–669, 2008.

[9] G. J. McGraw. High Resolution Organic Vapor Jet Printing of Phosphorescent Organic Light Emitting Diode Arrays. PhD thesis, University of Michigan, 2013.

[10] Y. Fukuda, T. Watanabe, T. Wakimoto, S. Miyaguchi, and M. Tsuchida. An organic LED display exhibiting pure RGB colors. Synth. Met., 111-112:1–6, 2000.

[11] G. Gustafsson, Y. Cao, G. M. Treacy, F. Klavetter, N. Colaneri, and A. J. Heeger. Flexible light-emitting diodes made from soluble conducting polymers. Nature, 357(6378):477–479, 1992.

[12] B. W. D'Andrade and S. R. Forrest. White organic light-emitting devices for solid-state lighting. Adv. Mater., 16(18):1585–1595, 2004.

[13] K.-S. Shin, Y.-H. Kim, K.-K. Paek, J. Park, E.-G. Yang, T.-S. Kim, J.-Y. Kang, and B.-K. Ju. Characterization of an integrated fluorescence-detection hybrid device with photodiode and organic light-emitting diode. IEEE Electron Device Lett., 27(9):746–748, 2006.

[14] A. Pais, A. Banerjee, D. Klotzkin, and I. Papautsky. High-sensitivity, disposable lab-on-a-chip with thin-film organic electronics for fluorescence detection. Lab Chip, 8(5):794–800, 2008.

[15] J. Shinar and R. Shinar. Organic light-emitting devices (OLEDs) and OLED-based chemical and biological sensors: an overview. J. Phys. D: Appl. Phys., 41(13):133001, 2008.

[16] M. Ramuz, D. Leuenberger, R. Pfeiffer, L. Bürgi, and C. Winnewisser. OLED and OPD-Based mini-spectrometer integrated on a single-mode planar waveguide chip. Eur. Phys. J. Appl. Phys., 46(01):12510–12510–5, 2009.

[17] E. L. Ratcliff, P. A. Veneman, A. Simmonds, B. Zacher, D. Huebner, S. S. Saavedra, and N. R. Armstrong. A planar, chip-based, dual-beam refractometer using an integrated organic light-emitting diode (OLED) light source and organic photovoltaic (OPV) detectors. Anal. Chem., 82(7):2734–2742, 2010.

[18] M. Ramuz, D. Leuenberger, and L. Bürgi. Optical biosensors based on integrated polymer light source and polymer photodiode. J. Polym. Sci., Part B: Polym. Phys., 49(1):80–87, 2011.

[19] D. Threm, Y. Nazirizadeh, A. Pradana, M. Rädler, J. Mikat, and M. Gerken. Integrated organic optoelectronic system for refractometric measurements. In 2011 International Conference on Optical MEMS and Nanophotonics (OMN), pages 113–114, 2011.

[20] F. Lefèvre, A. Chalifour, L. Yu, V. Chodavarapu, P. Juneau, and R. Izquierdo. Algal fluorescence sensor integrated into a microfluidic chip for water pollutant detection. Lab Chip, 12(4):787–793, 2012.

[21] J.-S. Kim, P. K. H. Ho, N. C. Greenham, and R. H. Friend. Electroluminescence emission pattern of organic light-emitting diodes: Implications for device efficiency calculations. J. Appl. Phys., 88(2): 1073–1081, 2000.

[22] M.-H. Lu and J. C. Sturm. Optimization of external coupling and light emission in organic light-emitting devices: modeling and experiment. J. Appl. Phys., 91(2):595–604, 2002.

[23] A. Chutinan, K. Ishihara, T. Asano, M. Fujita, and S. Noda. Theoretical analysis on light-extraction efficiency of organic light-emitting diodes using FDTD and mode-expansion methods. Org. Electron., 6(1):3–9, 2005.

[24] J. M. Ziebarth and M. D. McGehee. A theoretical and experimental investigation of light extraction from polymer light-emitting diodes. J. Appl. Phys., 97(6):064502–064502–7, 2005.

[25] J. Frischeisen, D. Yokoyama, A. Endo, C. Adachi, and W. Brütting. Increased light outcoupling efficiency in dye-doped small molecule organic light-emitting diodes with horizontally oriented emitters. Org. Electron., 12(5):809–817, 2011.

[26] B. J. Matterson, J. M. Lupton, A. F. Safonov, M. G. Salt, W. L. Barnes, and I. D. W. Samuel. Increased efficiency and controlled light output from a microstructured Light-Emitting diode. Adv. Mater., 13(2): 123–127, 2001.

[27] C. Adachi, M. A. Baldo, M. E. Thompson, and S. R. Forrest. Nearly 100% internal phosphorescence efficiency in an organic light-emitting device. J. Appl. Phys., 90(10):5048–5051, 2001.

[28] S. Reineke, F. Lindner, G. Schwartz, N. Seidler, K. Walzer, B. Lüssem, and K. Leo. White organic light-emitting diodes with fluorescent tube efficiency. Nature, 459(7244):234–238, 2009.

[29] J. M. Lupton, B. J. Matterson, I. D. W. Samuel, M. J. Jory, and W. L. Barnes. Bragg scattering from periodically microstructured light emitting diodes. Appl. Phys. Lett., 77(21):3340, 2000.

[30] J. M. Ziebarth, A. K. Saafir, S. Fan, and M. D. McGehee. Extracting light from polymer light-emitting diodes using stamped bragg gratings. Adv. Funct. Mater., 14(5):451–456, 2004.

[31] U. Geyer, J. Hauss, B. Riedel, S. Gleiss, U. Lemmer, and M. Gerken. Large-scale patterning of indium tin oxide electrodes for guided mode extraction from organic light-emitting diodes. J. Appl. Phys., 104(9): 093111–093111–5, 2008.

[32] J. Hauss, B. Riedel, S. Gleiss, U. Geyer, U. Lemmer, and M. Gerken. Periodic nanostructuring for guided mode extraction in organic light-emitting diodes. J. Photon. Energy, 1(1):011012, 2011.

[33] J. Frischeisen, Q. Niu, A. Abdellah, J. B. Kinzel, R. Gehlhaar, G. Scarpa, C. Adachi, P. Lugli, and W. Brütting. Light extraction from surface plasmons and waveguide modes in an organic light-emitting layer by nanoimprinted gratings. Opt. Express, 19(S1):A7–A19, 2011.

[34] C. Fuchs, T. Schwab, T. Roch, S. Eckardt, A. Lasagni, S. Hofmann, B. Lüssem, L. Müller-Meskamp, K. Leo, M. C. Gather, and R. Scholz. Quantitative allocation of bragg scattering effects in highly efficient OLEDs fabricated on periodically corrugated substrates. Opt. Express, 21(14):16319–16330, 2013.

[35] Y.-J. Lee, S.-H. Kim, J. Huh, G.-H. Kim, Y.-H. Lee, S.-H. Cho, Y.-C. Kim, and Y. R. Do. A high-extraction-efficiency nanopatterned organic light-emitting diode. Appl. Phys. Lett., 82(21):3779, 2003.

[36] Y. R. Do, Y.-C. Kim, Y.-W. Song, and Y.-H. Lee. Enhanced light extraction efficiency from organic light emitting diodes by insertion of a two-dimensional photonic crystal structure. J. Appl. Phys., 96(12): 7629–7636, 2004.

[37] A. Adawi, R. Kullock, J. Turner, C. Vasilev, D. Lidzey, A. Tahraoui, P. Fry, D. Gibson, E. Smith, C. Foden, M. Roberts, F. Qureshi, and N. Athanassopoulou. Improving the light extraction efficiency of polymeric light emitting diodes using two-dimensional photonic crystals. Org. Electron., 7(4):222–228, 2006.

[38] W. H. Koo, S. M. Jeong, F. Araoka, K. Ishikawa, S. Nishimura, T. Toyooka, and H. Takezoe. Light extraction from organic light-emitting diodes enhanced by spontaneously formed buckles. Nat. Photonics, 4 (4):222–226, 2010.

[39] B. Riedel. Effizienzsteigerung in organischen Leuchtdioden. PhD thesis, Karlsruher Institut für Technologie, 2011.

[40] B. Riedel, J. Hauss, M. Aichholz, A. Gall, U. Lemmer, and M. Gerken. Polymer light emitting diodes containing nanoparticle clusters for improved efficiency. Org. Electron., 11(7):1172–1175, 2010.

[41] M. D. Fina. Electrical and Optical Enhancement in Internally Nanopatterned Organic Light-Emitting Diodes. PhD thesis, University of California, Berkeley, 2012.

[42] P. Bienstman, P. Vandersteegen, and R. Baets. Modelling gratings on either side of the substrate for light extraction in light-emitting diodes. Opt. Quantum Electron., 39(10-11):797–804, 2007.

[43] B. Riedel, J. Hauss, U. Geyer, J. Guetlein, U. Lemmer, and M. Gerken. Enhancing outcoupling efficiency of indium-tin-oxide-free organic light-emitting diodes via nanostructured high index layers. Appl. Phys. Lett., 96(24):243302, 2010.

[44] J. Hauss, T. Bocksrocker, B. Riedel, U. Lemmer, and M. Gerken. On the interplay of waveguide modes and leaky modes in corrugated OLEDs. Opt. Express, 19(S4):A851–A858, 2011.

[45] S. T. Peng, T. Tamir, and H. L. Bertoni. Theory of periodic dielectric waveguides. IEEE Trans. Microwave Theory Tech., 23(1):123–133, 1975.

[46] H. Benisty, R. Stanley, and M. Mayer. Method of source terms for dipole emission modification in modes of arbitrary planar structures. J. Opt. Soc. Am. A, 15(5):1192–1201, 1998.

[47] D. L. Lee. Electromagnetic principles of integrated optics. Wiley, New York, 1986.

[48] M. Born and E. Wolf. Principles of Optics: Electromagnetic Theory of Propagation, Interference and Diffraction of Light. Cambridge University Press, New York, 1999.

[49] T. Tamir. Beam and waveguide couplers, volume 7. Springer, Berlin, Heidelberg, 1975.

[50] E. Hecht. Optics. Addison-Wesley, San Francisco, 2002.

[51] H. Benisty, H. de Neve, and C. Weisbuch. Impact of planar microcavity effects on light extraction-Part I: basic concepts and analytical trends. IEEE J. Quantum Electron., 34(9):1612–1631, 1998.

[52] R. Baets, P. Bienstman, and R. Bockstaele. Basics of dipole emission from a planar cavity. In H. Benisty, C. Weisbuch, J.-M. Gérard, R. Houdré, and J. Rarity, editors, Confined Photon Systems, volume 531 of Lecture Notes in Physics, pages 38–79. Springer, Berlin, Heidelberg, 1999.

[53] D. Delbeke, R. Bockstaele, P. Bienstman, R. Baets, and H. Benisty. High-efficiency semiconductor resonant-cavity light-emitting diodes: a review. IEEE J. Sel. Top. Quantum Electron., 8(2):189–206, 2002.

[54] D. Marcuse. Theory of Dielectric Optical Waveguides. Academic Press, New York, 2 edition, 1991.

[55] G. Lifante. Integrated Photonics: Fundamentals. Wiley, Chichester, 2003.

[56] A. Hessel. General characteristics of traveling-wave antennas. In R. E. Collin and F. J. Zucker, editors, Antenna theory - Pt. 2, pages 151–258. McGraw-Hill, New York, 1969.

[57] T. Tamir and S. T. Peng. Analysis and design of grating couplers. Appl. Phys. (Berlin), 14(3):235–254, 1977.

[58] H. Nishihara, M. Haruna, and T. Suhara. Theory of gratings in waveguide structures. In R. E. Fischer and W. J. Smith, editors, Optical Integrated Circuits, McGraw-Hill Optical and Electro-optical Engineering Series, pages 62–94. McGraw-Hill, New York, 1989.

[59] A. Yariv. Propagation and coupling of modes in optical dielectric waveguides - periodic waveguides. In Optical Electronics in Modern Communications, pages 491–540. Oxford University Press, New York, 5. edition, 1997.

[60] T. Tamir. Beam and waveguide couplers. In T. Tamir, editor, Integrated Optics, volume 7, pages 83–137. Springer, Berlin, Heidelberg, 1975.

[61] K. Handa, S. T. Peng, and T. Tamir. Improved perturbation analysis of dielectric gratings. Appl. Phys. (Berlin), 5(4):325–328, 1975.

[62] S. Peng and G. M. Morris. Resonant scattering from two-dimensional gratings. J. Opt. Soc. Am. A, 13(5):993–1005, 1996.

[63] J. D. Joannopoulos, S. G. Johnson, J. N. Winn, and R. D. Meade. Photonic crystals: molding the flow of light. Princeton University Press, Princeton, 2nd edition, 2008.

[64] G. A. Turnbull, P. Andrew, M. J. Jory, W. L. Barnes, and I. D. W. Samuel. Relationship between photonic band structure and emission characteristics of a polymer distributed feedback laser. Phys. Rev. B, 64(12):125122, 2001.

[65] M. T. Wlodarczyk and S. R. Seshadri. Analysis of grating couplers in planar waveguides for waves at oblique incidence. J. Opt. Soc. Am. A, 2(2):171–185, 1985.

[66] W. S. Park and S. R. Seshadri. Analysis of the reflection grating couplers for waves at oblique incidence. J. Opt. Soc. Am. A, 4(6): 1001–1020, 1987.

[67] M. Gerken. Wavelength multiplexing by spatial beam shifting in multilayer thin-film structures. PhD thesis, Stanford University, 2003.

[68] A. Ghatak, K. Thyagarajan, and M. Shenoy. Numerical analysis of planar optical waveguides using matrix approach. J. Lightw. Technol., 5(5):660 – 667, 1987.

[69] M. Nevière. The homogeneous problem. In P. R. Petit, editor, Electromagnetic Theory of Gratings, number 22 in Topics in Current Physics, pages 123–157. Springer, Berlin, Heidelberg, 1980.

[70] S. S. Wang, R. Magnusson, J. S. Bagby, and M. G. Moharam. Guided-mode resonances in planar dielectric-layer diffraction gratings. J. Opt. Soc. Am. A, 7(8):1470–1474, 1990.

[71] E. Anemogiannis, E. N. Glytsis, and T. K. Gaylord. Determination of guided and leaky modes in lossless and lossy planar multilayer optical waveguides: Reflection pole method and wavevector density method. J. Lightwave Technol., 17(5):929, 1999.

[72] D. L. Brundrett, E. N. Glytsis, T. K. Gaylord, and J. M. Bendickson. Effects of modulation strength in guided-mode resonant subwavelength gratings at normal incidence. J. Opt. Soc. Am. A, 17(7):1221–1230, 2000.

[73] M. D. Salik and P. Chavel. Resonant excitation analysis of waveguide grating couplers. Opt. Commun., 193(1-6):127–131, 2001.

[74] D. Pietroy, A. V. Tishchenko, M. Flury, and O. Parriaux. Bridging pole and coupled wave formalisms for grating waveguide resonance analysis and design synthesis. Opt. Express, 15(15):9831, 2007.

[75] J. C. Lagarias, J. A. Reeds, M. H. Wright, and P. E. Wright. Convergence properties of the nelder–mead simplex method in low dimensions. SIAM J. Optim., 9(1):112–147, 1998.

[76] I. N. Bronstein, K. A. Semendjajew, G. Musiol, and H. Mühlig. Taschenbuch der Mathematik. Harri Deutsch, Frankfurt am Main, 5th edition, 2000.

[77] H. J. Dirschmid. Mathematische Grundlagen der Elektrotechnik. Vieweg, Braunschweig, 1988.

[78] P. B. Partha, J. Jarem, and P. P. Banerjee. Computational Methods for Electromagnetic and Optical Systems. CRC Press, Boca Raton, 2nd edition, 2011.

[79] M. G. Moharam, E. B. Grann, D. A. Pommet, and T. K. Gaylord. Formulation for stable and efficient implementation of the rigorous coupled-wave analysis of binary gratings. J. Opt. Soc. Am. A, 12(5): 1068–1076, 1995.

[80] T. Gaylord and M. Moharam. Analysis and applications of optical diffraction by gratings. Proc. IEEE, 73(5):894–937, 1985.

[81] G. H. Golub and C. F. Van Loan. Matrix computations. The Johns Hopkins Univ. Press, Baltimore, 2nd edition, 1989.

[82] K. Inkalä. Homogeneous least squares problem. Photogrammetric J. Finland, 19(2):34–42, 2005.

[83] P. Bienstman. Rigorous and efficient modelling of wavelength scale photonic components. PhD thesis, University of Gent, 2001.

[84] CAMFR home page - http://camfr.sourceforge.net.

[85] M. Gerken. Nanostructuring OLEDs to increase efficiency. In Organic Light-Emitting Diodes (OLEDs): Materials, Devices And Applications, pages 235–261. Woodhead, Cambridge, 2013.

[86] J. Frischeisen. Light extraction in organic light-emitting diodes. PhD thesis, Universität Augsburg, 2011.

[87] H. Hoppe, N. S. Sariciftci, and D. Meissner. Optical constants of conjugated polymer/fullerene based bulk-heterojunction organic solar cells. Mol. Cryst. Liq. Cryst., 385(1):113–119, 2002.

[88] D. Yokoyama. Molecular orientation in small-molecule organic light-emitting diodes. J. Mater. Chem., 21(48):19187–19202, 2011.

[89] J. Frischeisen, B. J. Scholz, B. J. Arndt, T. D. Schmidt, R. Gehlhaar, C. Adachi, and W. Brütting. Strategies for light extraction from surface plasmons in organic light-emitting diodes. J. Photon. Energy, 1(1): 011004, 2011.

[90] P. A. Hobson, J. A. Wasey, I. Sage, and W. L. Barnes. The role of surface plasmons in organic light-emitting diodes. IEEE J. Sel. Top. Quantum Electron., 8(2):378–386, 2002.

[91] S. Nowy, B. C. Krummacher, J. Frischeisen, N. A. Reinke, and W. Brutting. Light extraction and optical loss mechanisms in organic light-emitting diodes: Influence of the emitter quantum efficiency. J. Appl. Phys., 104(12):123109–123109–9, 2008.

[92] W. L. Barnes. Electromagnetic crystals for surface plasmon polaritons and the extraction of light from emissive devices. J. Lightwave Technol., 17(11):2170, 1999.

[93] T. Tamir and S. Zhang. Modal transmission-line theory of multilayered grating structures. J. Lightw. Technol., 14(5):914 –927, 1996.

[94] A. Hessel and A. A. Oliner. A new theory of wood's anomalies on optical gratings. Appl. Opt., 4(10):1275–1297, 1965.

[95] Y. Li, F. Li, J. Zhang, C. Wang, S. Zhu, H. Yu, Z. Wang, and B. Yang. Improved light extraction efficiency of white organic light-emitting devices by biomimetic antireflective surfaces. Appl. Phys. Lett., 96 (15):153305–153305–3, 2010.

[96] T. Bocksrocker, J. B. Preinfalk, J. Asche-Tauscher, A. Pargner, C. Eschenbaum, F. Maier-Flaig, and U. Lemmer. White organic light emitting diodes with enhanced internal and external outcoupling for ultra-efficient light extraction and lambertian emission. Opt. Express, 20 (S6):A932–A940, 2012.

[97] W. L. Barnes. Spontaneous emission and energy transfer in the optical microcavity. Contemp. Phys., 41(5):287–300, 2000.

[98] V. Bulović, V. B. Khalfin, G. Gu, P. E. Burrows, D. Z. Garbuzov, and S. R. Forrest. Weak microcavity effects in organic light-emitting devices. Phys. Rev. B, 58(7):3730, 1998.

[99] S.-H. Kloss. Ein Goniophotometer zur Messung des Lichtstromes und der Lichtstärkeverteilung von hohlen Lichtleitern. PhD thesis, Technische Universität Berlin, 2001.

[100] M. Lindemann and R. Maass. Photometry and colorimetry of reference LEDs by using a compact goniophotometer. MAPAN-J. Metrol. Soc. I., 24(3):143–152, 2009.

[101] R. F. Stamm, M. L. Garcia, and J. J. Fuchs. The optical properties of human hair I. Fundamental considerations and goniophotometer curves. J. Soc. Cosmet. Chem., 28(9):571–599, 1977.

[102] P. Apian-Bennewitz and J. von der Hardt. Enhancing and calibrating a goniophotometer. Sol. Energy Mater. Sol. Cells, 54(1–4):309–322, 1998.

[103] S. Twomey. Introduction to the Mathematics of Inversion in Remote Sensing and Indirect Measurements. Courier Dover Publications, Mineola, 2002.

[104] F. G. Dijkman and J. H. Van Der Maas. Dependence of bandshape and depolarization ratio on slitwidth. Appl. Spectrosc., 30(5):545–546, 1976.

[105] V. N. Kumar and D. N. Rao. Determination of the instrument function of a grating spectrometer by using white-light interferometry. Appl. Opt., 36(19):4535–4539, 1997.

[106] F. Pedrotti, L. Pedrotti, W. Bausch, and H. Schmidt. Optik für Ingenieure. Springer, Berlin, Heidelberg, 2008.

[107] Radiant Zemax - Zemax optical and illumination design software - http://radiantzemax.com.

[108] G. K. Wertheim, M. A. Butler, K. W. West, and D. N. E. Buchanan. Determination of the Gaussian and Lorentzian content of experimental line shapes. Rev. Sci. Instrum., 45(11):1369, 1974.

[109] Faddeeva Package by Steven G. Johnson. `http://ab-initio.mit.edu/wiki/index.php/Faddeeva_Package`. Retrieved on Jul. 10, 2013.

[110] V. Mazet, C. Carteret, D. Brie, J. Idier, and B. Humbert. Background removal from spectra by designing and minimising a non-quadratic cost function. Chemom. Intell. Lab. Syst., 76(2):121–133, 2005.

[111] M. Nevière, E. Popov, and R. Reinisch. Electromagnetic resonances in linear and nonlinear optics: phenomenological study of grating behavior through the poles and zeros of the scattering operator. J. Opt. Soc. Am. A, 12(3):513–523, 1995.

[112] D. Rosenblatt, A. Sharon, and A. Friesem. Resonant grating waveguide structures. IEEE J. Quantum Electron., 33(11):2038 –2059, 1997.

[113] S. M. Norton, T. Erdogan, and G. M. Morris. Coupled-mode theory of resonant-grating filters. J. Opt. Soc. Am. A, 14(3):629–639, 1997.

[114] L. Devys, G. Dantelle, V. Kubytskyi, H. Benisty, and T. Gacoin. Characterization of the guided light/photonic crystal coupling by absorbance. In Proc. SPIE, volume 8818, pages 88180N–88180N–8, 2013.

[115] B. Riedel, Y. Shen, J. Hauss, M. Aichholz, X. Tang, U. Lemmer, and M. Gerken. Tailored highly transparent composite hole-injection layer consisting of Pedot:PSS and SiO2 nanoparticles for efficient polymer light-emitting diodes. Adv. Mater., 23(6):740–745, 2011.

[116] C.-H. Chang, K.-Y. Chang, Y.-J. Lo, S.-J. Chang, and H.-H. Chang. Fourfold power efficiency improvement in organic light-emitting devices using an embedded nanocomposite scattering layer. Org. Electron., 13(6):1073–1080, 2012.

[117] C. Kluge, M. Rädler, A. Pradana, M. Bremer, P.-J. Jakobs, N. Barié, M. Guttmann, and M. Gerken. Extraction of guided modes from organic emission layers by compound binary gratings. Opt. Lett., 37 (13):2646–2648, 2012.

[118] L. Tutt and J. F. Revelli. Distribution of radiation from organic light-emitting diode structures with wavelength-scale gratings as a function of azimuth and polar angles. Opt. Lett., 33(5):503–505, 2008.

[119] A. Isphording and M. Pralle. Quantifying angular color stability of organic light-emitting diodes. Org. Electron., 11(12):1916–1919, 2010.

[120] A. Othonos, X. Lee, and R. Measures. Superimposed multiple bragg gratings. Electron. Lett., 30(23):1972–1974, 1994.

[121] A. Talneau, J. Charil, and A. Ougazzaden. Superimposed bragg gratings on semiconductor material. Electron. Lett., 32(20):1884–1885, 1996.

[122] I. A. Avrutsky, D. S. Ellis, A. Tager, H. Anis, and J. M. Xu. Design of widely tunable semiconductor lasers and the concept of binary superimposed gratings (BSG's). IEEE J. Quantum Electron., 34(4): 729–741, 1998.

[123] W.-C. Tan, J. Sambles, and T. Preist. Double-period zero-order metal gratings as effective selective absorbers. Phys. Rev. B, 61(19):13177–13182, 2000.

[124] D. C. Skigin and R. A. Depine. Diffraction by dual-period gratings. Appl. Opt., 46(9):1385–1391, 2007.

[125] Y.-B. Chen and M.-J. Huang. Infrared reflectance from a compound grating and its alternative componential gratings. J. Opt. Soc. Am. B, 27(10):2078–2086, 2010.

[126] S. C. Kitson, W. L. Barnes, and J. R. Sambles. Surface-plasmon energy gaps and photoluminescence. Phys. Rev. B, 52(15):11441–11445, 1995.

[127] W. L. Barnes, T. W. Preist, S. C. Kitson, and J. R. Sambles. Physical origin of photonic energy gaps in the propagation of surface plasmons on gratings. Phys. Rev. B, 54(9):6227–6244, 1996.

[128] C. Fattinger. The bidiffractive grating coupler. Appl. Phys. Lett., 62 (13):1460, 1993.

[129] C. P. Fattinger, C. Mangold, M. Gale, and Schütz, H. Bidiffractive grating coupler: universal transducer for optical interface analytics. Opt. Eng., 34(9):2744, 1995.

[130] S. T. Peng. Rigorous analysis of guided waves in doubly periodic structures. J. Opt. Soc. Am. A, 7(8):1448–1456, 1990.

[131] S. Y. Chou, P. R. Krauss, and P. J. Renstrom. Imprint lithography with 25-nanometer resolution. Science, 272(5258):85–87, 1996.

[132] K. Ishihara, M. Fujita, I. Matsubara, T. Asano, S. Noda, H. Ohata, A. Hirasawa, H. Nakada, and N. Shimoji. Organic light-emitting diodes with photonic crystals on glass substrate fabricated by nanoimprint lithography. Appl. Phys. Lett., 90(11):111114, 2007.

[133] dxfwrite - A Python library to create DXF R12 drawings. https://pypi.python.org/pypi/dxfwrite. Retrieved on Sep. 13, 2013.

[134] C. Vannahme, S. Klinkhammer, A. Kolew, P.-J. Jakobs, M. Guttmann, S. Dehm, U. Lemmer, and T. Mappes. Integration of organic semiconductor lasers and single-mode passive waveguides into a PMMA substrate. Microelectron. Eng., 87(5-8):693–695, 2010.

[135] A. Boudrioua, P. Hobson, B. Matterson, I. Samuel, and W. Barnes. Birefringence and dispersion of the light emitting polymer MEH–PPV. Synth. Met., 111–112:545–547, 2000.

[136] L. A. Pettersson, S. Ghosh, and O. Inganäs. Optical anisotropy in thin films of poly(3,4-ethylenedioxythiophene)–poly(4-styrenesulfonate). Org. Electron., 3(3–4):143–148, 2002.

[137] M. Campoy-Quiles, P. G. Etchegoin, and D. D. C. Bradley. On the optical anisotropy of conjugated polymer thin films. Phys. Rev. B, 72 (4):045209, 2005.

[138] C. W. Y. Law, K. S. Wong, Z. Yang, L. E. Horsburgh, and A. P. Monkman. Observation of in-plane optical anisotropy of spin-cast rigid-rod electroluminescent polymer films. Appl. Phys. Lett., 76(11): 1416–1418, 2000.

[139] G. Hass and C. D. Salzberg. Optical properties of silicon monoxide in the wavelength region from 0.24 to 14.0 microns. J. Opt. Soc. Am., 44 (3):181–183, 1954.

[140] Refractive index database. http://refractiveindex.info. Retrieved on Jul. 16, 2013.

[141] S. J. Martin, D. D. C. Bradley, P. A. Lane, H. Mellor, and P. L. Burn. Linear and nonlinear optical properties of the conjugated polymers PPV and MEH-PPV. Phys. Rev. B, 59(23):15133–15142, 1999.

[142] R. P. Singh and S. D. Sapre. Communication systems: analog & digital. McGraw-Hill Higher Education, New Delhi, 2007.

[143] J. W. Cooley and J. W. Tukey. An algorithm for the machine calculation of complex fourier series. Math. Comput., 19(90):297, 1965.

[144] F. P. Payne and J. P. R. Lacey. A theoretical analysis of scattering loss from planar optical waveguides. Opt. Quantum Electron., 26(10): 977–986, 1994.

[145] H. Becker, S. E. Burns, and R. H. Friend. Effect of metal films on the photoluminescence and electroluminescence of conjugated polymers. Phys. Rev. B, 56(4):1893–1905, 1997.

[146] K. B. Mogensen, H. Klank, and J. P. Kutter. Recent developments in detection for microfluidic systems. Electrophoresis, 25(21-22):3498–3512, 2004.

[147] J. G. E. Gardeniers and A. van den Berg. Lab-on-a-chip systems for biomedical and environmental monitoring. Anal. Bioanal. Chem., 378 (7):1700–1703, 2004.

[148] S. Balslev, A. M. Jorgensen, B. Bilenberg, K. B. Mogensen, D. Snakenborg, O. Geschke, J. P. Kutter, and A. Kristensen. Lab-on-a-chip with integrated optical transducers. Lab Chip, 6(2):213–217, 2006.

[149] C. Monat, P. Domachuk, and B. J. Eggleton. Integrated optofluidics: A new river of light. Nat. Photonics, 1(2):106–114, 2007.

[150] D. Threm, Y. Nazirizadeh, and M. Gerken. Photonic crystal biosensors towards on-chip integration. J. Biophotonics, 5(8-9):601–616, 2012.

[151] F. Vollmer and S. Arnold. Whispering-gallery-mode biosensing: label-free detection down to single molecules. Nat. Meth., 5(7):591–596, 2008.

[152] M. Ramuz, L. Bürgi, R. Stanley, and C. Winnewisser. Coupling light from an organic light emitting diode (OLED) into a single-mode waveguide: Toward monolithically integrated optical sensors. J. Appl. Phys., 105(8):084508, 2009.

[153] M. C. Gather, F. Ventsch, and K. Meerholz. Embedding organic light-emitting diodes into channel waveguide structures. Adv. Mater., 20 (10):1966–1971, 2008.

[154] K.-Y. Chu and A. R. Thompson. Densities and refractive indices of alcohol-water solutions of n-propyl, isopropyl, and methyl alcohols. J. Chem. Eng. Data, 7(3):358–360, 1962.

[155] Y. Shindo and K. Kusano. Densities and refractive indices of aqueous mixtures of alkoxy alcohols. J. Chem. Eng. Data, 24(2):106–110, 1979.

[156] E. Abbe. Neue Apparate zur Bestimmung des Brechungs- und Zerstreuungsvermögens fester und flüssiger Körper. Jenaische Zeitschrift für Naturwissenschaft, 8:96–174, 1874.

[157] J. Cooper, A. Glidle, and R. De La Rue. Photonic crystal structures in molecular biosensing. Opt. Photon. News, 21(9):26–31, 2010.

[158] N. Skivesen, A. Têtu, M. Kristensen, J. Kjems, L. H. Frandsen, and P. I. Borel. Photonic-crystal waveguide biosensor. Opt. Express, 15(6): 3169–3176, 2007.

[159] W. C. H. Choy and C. Y. Ho. Improving the viewing angle properties of microcavity OLEDs by using dispersive gratings. Opt. Express, 15 (20):13288–13294, 2007.

Nomenclature

Abbreviations

CAMFR	Cavity Modelling Framework. An eigenmode solver for Maxwell's equations.
CCD	charge-coupled device
CIE	Commission Internationale de l'Eclairage
CMOS	complementary metal–oxide–semiconductor
FDTD	finite-difference time-domain
IRF	instrument response function
LED	(inorganic) light-emitting diode
NIL	nanoimprint lithography
OLED	organic light-emitting diode
PL	photoluminescence
PML	perfectly matched layers
pTMM	perturbation source transfer matrix method
RCWA	rigorous coupled wave analysis
RIU	refractive index unit
TE	transverse-electric
TIR	total internal reflection
TM	transverse-magnetic

Symbols

ϵ_0	free-space permittivity
μ_0	free-space permeability
j	imaginary constant
$\vec{e}_x$,$\vec{e}_y$, $\vec{e}_z$	cartesian unity vectors
$\vec{r}$	position in space
t	time*

x, y, z ..... cartesian coordinates

$\vec{\alpha}$ ..... amplitude vector (imaginary part of the wave vector)
$\vec{\beta}$ ..... phase vector (real part of the wave vector)
$\vec{B}$ ..... magnetic flux density
$\vec{D}$ ..... electric displacement
$\vec{E}$ ..... electric field strength
$\vec{H}$ ..... magnetic field strength
$\vec{J}$ ..... current density
$\vec{k}$ ..... wave vector
$\vec{S}$ ..... Poynting vector

ϵ ..... permittivity
λ_0 ..... wavelength in vacuum
ω ..... angular frequency
ρ ..... space charge density
n ..... refractive index

δ_0 ..... Dirac delta function
$\mathbb{F}$ ..... a set of duty cycles
$\mathbb{Z}$ ..... the set of integers
$\vee$ ..... logical disjunction operator
u ..... Heaviside step function

Λ ..... grating period
NA ..... numerical aperture
ϕ ..... field phase change
d_{fi} ..... thickness of the film layer
d_{gr} ..... thickness of the grating layer
f_{dc} ..... duty cycle of a binary grating
l_{rd} ..... ridge width of a binary grating
n_{fi} ..... refractive index of film (waveguide core)
n_{II} ..... refractive index of region II (substrate)
n_{I} ..... refractive index of region I (waveguide cladding)
v_{Airy} ..... cavity Airy factor
$\theta_m^{(l)}$ ..... propagation angle to the surface normal in layer l
ζ ..... standing wave factor of a field source in front of a reflector
r ..... amplitude reflection coefficient*
t ..... amplitude transmission coefficient*

Materials

Alq3	tris (8-hydroxy quinioline) aluminum
ITO	indium-tin-oxide
PEDOT	poly(3,4-ethylenedioxythiophene)
SiO	silicon monoxide
Superyellow	phenylene substituted poly(para-phenylenevinylene) derivative

* symbols with more than one meaning in different contexts

Publications

Journal Articles

(1) **C. Kluge**, J. Adam, N. Barié, P.-J. Jakobs, M. Guttmann, and M. Gerken, "Multi-periodic nanostructures for photon control," Opt. Express **22**, pp. A1363-A1371 (2014).

(2) A. Pradana, **C. Kluge**, and M. Gerken, "Tailoring the refractive index of nanoimprint resist by blending with TiO2 nanoparticles", Opt. Mater. Express **4**, pp. 329-337 (2014).

(3) **C. Kluge**, M. Rädler, A. Pradana, M. Bremer, P.-J. Jakobs, N. Barié, M. Guttmann, and M. Gerken, "Extraction of guided modes from organic emission layers by compound binary gratings", Opt. Lett. **37**, pp. 2646-2648 (2012).

(4) **C. Kluge**, N. Galler, H. Ditlbacher, and M. Gerken, "Modeling of electrically actuated elastomer structures for electro-optical modulation", Applied Physics A: Materials Science & Processing **102**, pp. 407-413 (2011).

Conference Contributions

(1) **C. Kluge**, L.T. Neustock, J. Adam, M. Gerken, "Wavelength dependency of outcoupling peak intensities for emission layers with multi-periodic photonic crystals," *Proc. 16th International Conference on Transparent Optical Networks (ICTON)*, Graz / Austria (2014).

(2) **C. Kluge**, M. Paulsen, L.T. Neustock, N. Barié, P.-J. Jakobs, J. Adam, and M. Gerken, "Emission tailoring for organic emitter layers with compound binary gratings," *MRS Spring Meeting Symposium F*, San Francisco / USA (2014).

(3) A. Pradana, **C. Kluge**, and M. Gerken, "Nanostructured, ITO-free electrodes for OLED emission control," *MRS Proceedings* **1699**, San Francisco / USA (2014).

(4) **C. Kluge**, L.T. Neustock, J. Adam, and M. Gerken, "Calculation of leaky-wave radiation from compound binary grating waveguides," *Proc. XXI International Workshop on Optical Wave & Waveguide Theory and Numerical Modelling*, Enschede / The Netherlands (2013).

(5) **C. Kluge**, P. Metz, A. Pradana, Y. Nazirizadeh, M. Rädler, and M. Gerken, "Influence of waveguide thickness on the angular color impression of nanostructured organic emission layers," *Proc. 16th European Conference on Integrated Optics*, Sitges / Spain (2012).

(6) A. Pradana, **C. Kluge**, M. Bremer, M. Rädler, and M. Gerken, "Multiperiod Gratings in a High Refractive Index Material for Enhanced OLED Outcoupling", *Proc. OSA Solid-State and Organic Lighting (SOLED)*, paper SDWC2, Austin / USA (2011).

(7) **C. Kluge**, P. Metz, B. Ripke, Y. Nazirizadeh, and M. Gerken, "Integrated refractometer design with directional light source," *Proc. IEEE Photonics Conference (PHO)*, pp. 471-472, Arlington / USA (2011).

(8) **C. Kluge**, D. Threm, Y. Nazirizadeh, P. Metz, and M. Gerken, "Integrated optical biosensors with nanostructures," *6th International Summer School, New Frontiers in Optical Technologies*, Tampere / Finland (2011).

Students Advised

Bachelorthesis: ”Simulation und Charakterisierung von Wellenleitern mit multi-periodischen Gittern“, **Lars Thorben Neustock** (2013).

Bachelorthesis: ”Charakterisierung nanostrukturierter Emissionsschichten für Chiplabore mit verbesserter Empfindlichkeit“, **Roger Kwee** (2012).

Bachelorthesis: ”Entwicklung eines Messsystems für die Effizienz von organischen Leuchtdioden mit multi-periodischen Gittern“, **Susanna Wigger** (2012).

Bachelorthesis: ”Empfindlichkeit und Detektionsgrenze von Chiplaboren für optische Brechungsindexmessungen“, **Beate Ripke** (2011).